UNIVERSITY OF AGDER

Optical Modelling for Photovoltaic Panels

Anders Steen-Nilsen Dynge
Asbjørn Orheim Stoveland

Supervisor

Dr. Thomas J. J. Meyer

This Master's Thesis is carried out as a part of the education at the University of Agder and is therefore approved as a part of this education. However, this does not imply that the University answers for the methods that are used or the conclusions that are drawn.

University of Agder, 2013

Faculty of Engineering and Science

Department of Engineering – Renewable Energy

Disclaimer

The content and commentary reflects the opinion of the individual contributing authors. Even if commercial products' names are cited all data used for making models are the authors' own approximations. The results do not necessarily reflect actual performance of the products.

Abstract

A novel approach to predict the performance of anti-reflective glasses on PV panel is presented in this thesis. Anti-reflective glass, such as deeply textured and thin film coated glass, has shown to increase the annual energy production relative to plain glass cover by 2-5%. The type of glass cover is an important factor for the performance of photovoltaic panels, and if properly optimized, glasses can turn into a cost-effective active component in the design of PV panels. Common practice for evaluating anti-reflective glass covers today is to evaluate measurements performed under standard test conditions (STC). However these measurements fail to quantify performance under different incidence angles and diffuse irradiance. Outdoor measurements take these effects into account, but local atmospheric and terrestrial effects greatly influence the results. In consequence outdoor measurements cannot be used to predict the performance of a specific glass cover in a different location. Therefore comprehensive evaluation tools are essential for optimal design of PV panel installations for specific geographical locations. In this study optical models that take in account angular and spectral variation under direct and diffuse light are presented. In ray tracing simulations the performance under both direct and diffuse irradiance for five different anti-reflective glass designs is investigated under equal conditions.

It is found that inverted pyramids and cube corners textured glass as well as thin film coated glass result in increase of both power and annual produced energy. Under direct irradiation thin film ARC coating resulted in the highest gain, approximately 4%, for incidence angles up to 60 degrees. However the study under diffuse irradiance showed that thin film ARC coating were outperformed by textured glass (e.g. inverted pyramids and cube corners textured).

Using the optical simulation results and PVsyst, yearly power generation simulations were performed and despite the fact that ARC thin films were the optimum design under direct irradiance the overall results showed that the textured glass, e.g. inverted pyramids and cube corners result in respectively, 6.2% and 6.6% gain in annual energy production, while thin film ARC results in 4.2%. The location chosen for the PVsyst simulation was Singapore.

Such results implies that “STC” parameters measured under normal incidence are not sufficient in the design process of a PV panel since diffuse irradiation plays a role in the generated power. As the diffuse fraction of global irradiance varies from one location to the next, the glass cover should be optimized for a given location.

Executive summary

Increasing the cost-efficiency of photovoltaic solar panels by reducing reflection losses is a major field of study in the solar glass market. The type of glass cover is an important factor for the performance of photovoltaic panels as it can turn out to be an active component in the design of PV panels. Indeed, different glass covers perform very differently under direct and diffuse irradiance. Optically modelling the behaviour of a PV panel under location correlated irradiation allows the selection of the optimal glass cover.

Anti-reflective glass, such as deeply textured glass and thin film coated glass, is believed to potentially increase the annual energy production by 2-5% relative to plain float glass cover. Researchers and manufacturers of such products have reported gains based on a wide range of different test conditions, as summarized in Figure 1.

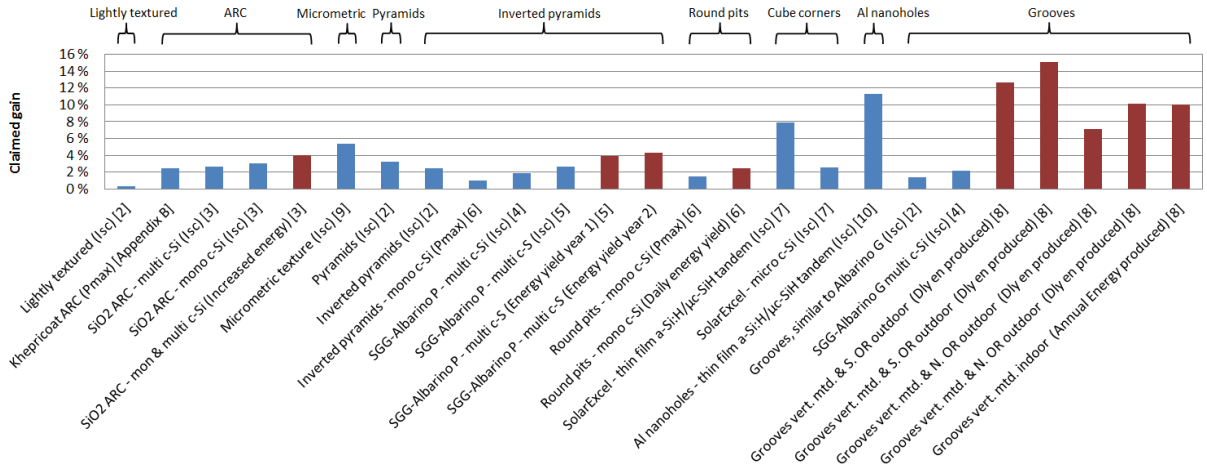

Figure 1: Claimed gains for anti-reflective glasses compared with plain glass on PV panels, found in the literature review.

Most published results are measured under standard test conditions (STC), failing to quantify performance under different incidence angles and diffuse irradiance. A comparison of these results is not straightforward, as different locations experience different local atmospheric effects, ambient and cell temperature, diffuse share of global irradiance, etc. In addition, results are highly dependent on the type of cell in the PV panel tested.

Therefore this study aims to evaluate five anti-reflective glass covers (see schematics below) under the same conditions against a reference plain glass. Optical modelling and ray tracing is used in this study to investigate the effects of these glass covers on PV panel performance under direct and diffuse irradiance:

Inverted pyramids texture (e.g. Albarino P)	Pyramidal grooved texture (e.g. Albarino G)	Cube corners texture (e.g. SolarExcel)	Rough glass (e.g. MT11050)	Thin film anti-reflective coating
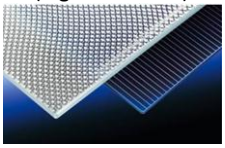	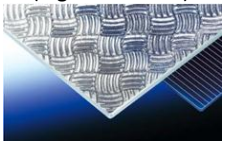	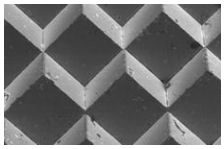	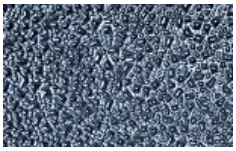	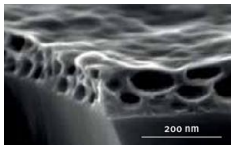

At first a simple optical model for a PV panel is studied, this simple PV model has the following assumptions:

- The solar cell absorbs light according to EQE data
- Light that is not absorbed, is reflected diffusely from the surface
- The reflected light on the solar cell follows a Lambertian scattering distribution

The solar cell optically modelled in this simple model is tested against a more complex optical cell model based on bulk and surface optical data of crystalline silicon. It is shown in this thesis that both models returns different results but the difference in between is negligible in some cases.

Four irradiance models are developed to mimic realistic light conditions, under which the performance of the PV model is evaluated:

- Direct irradiance: A series of light sources that takes into account the sun's apparent trajectory across the sky, the path length of direct light through the atmosphere, and the correlating solar spectrum.
- Diffuse irradiance: The CIE standard for sky luminance distribution under three sky conditions are used to model three diffuse spectra across the sky, replicating the multidirectional nature of diffuse irradiance. Within each model four solar zenith angles are presented which, together with the sky condition parameters, determines the irradiance distribution. The sky conditions are:
    - Clear sky
    - Partly cloudy sky
    - Overcast sky

The results for the PV model with the different glass covers under direct irradiance are shown in Figure 2. The light transmission factor is the absorbed flux in the PV cell divided by the incident flux on the PV panel surface.

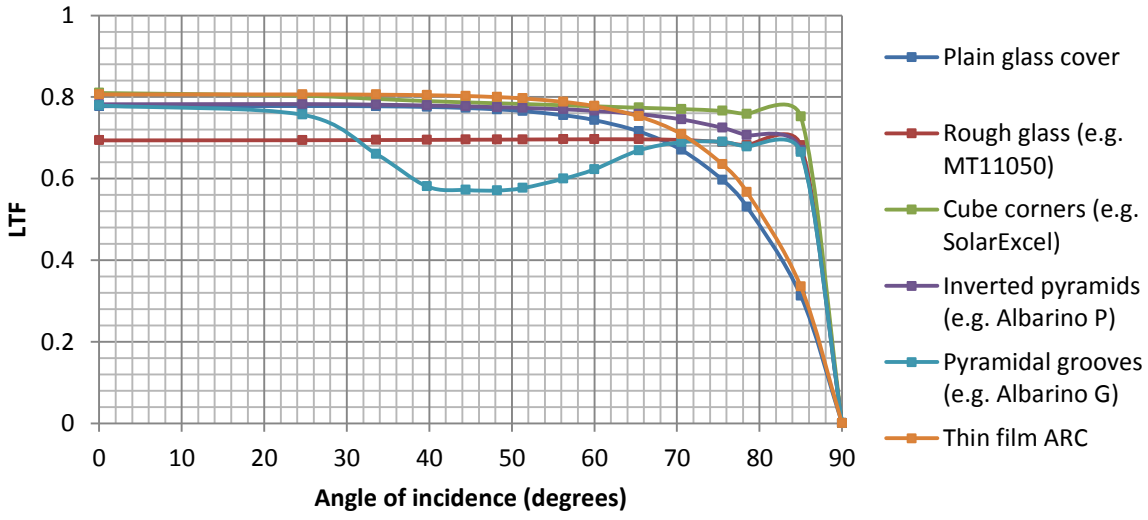

Figure 2: Light transmission factor as a function of angle of incidence for the PV model with the different glass covers.

Pyramidal grooves and rough glass performs poorly in the simulations. Thin film ARC performs best up to 60 degrees, while texture performs particularly well from 60 to 90 degrees.

The results for an example of a glass cover that performed well under diffuse irradiance are shown in Figure 3, where LTF is plotted as a function of solar zenith angle for cube corner textured glass and the reference plain glass, under clear, partly cloudy and overcast sky conditions.

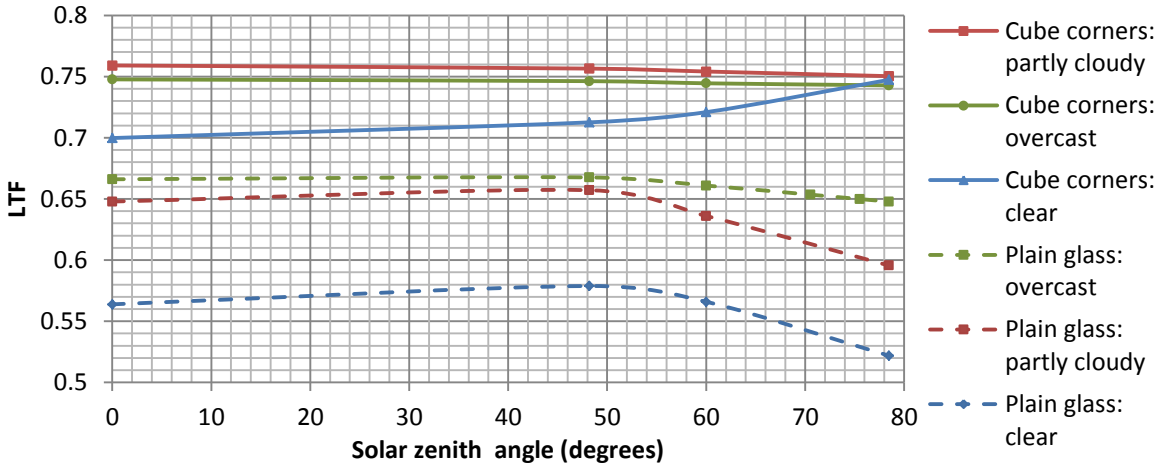

Figure 3: Light transmission factor as a function of solar zenith angle for plain and cube corners textured glass under diffuse irradiation.

It is shown that the LTF is weakly affected by solar zenith angle, especially for textured glass. This indicates that for future studies only one or two solar zenith angles need to be studied. However, the importance of using the correct solar spectrum in the models is also shown. E.g. at normal irradiance plain glass resulted in LTF of 0.56 and 0.67 under clear sky and overcast sky, respectively, a 20 % difference. The weak dependence for LTF on solar zenith angle leads to the conclusion that this is caused by spectral effects.

For the glass covers that resulted in positive gain in LTF, the resulting gains under direct and diffuse irradiance (represented by overcast sky) are shown in Figure 4.

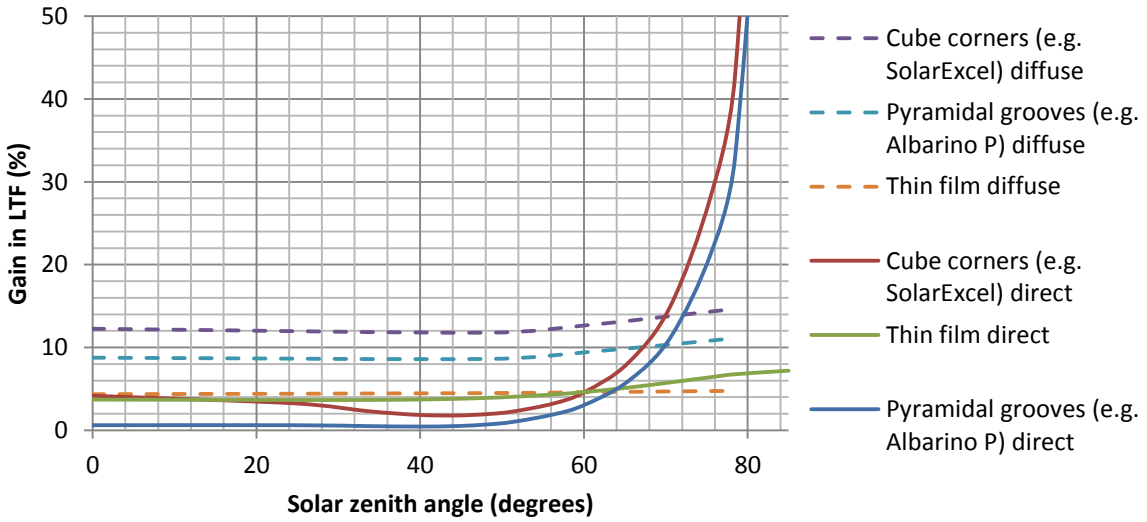

Figure 4: Gain in LTF as a function of solar zenith angle under direct and diffuse irradiance.

From the abovementioned results, input parameters for commercial software like PVsyst can be extracted (incidence angle modifier and maximum power). PVsyst then calculates the annual energy production for each glass. The resulting annual energy production gains, compared with optical annual energy simulations based on direct irradiance in Tracepro Solar Utility, are shown in Figure 5.

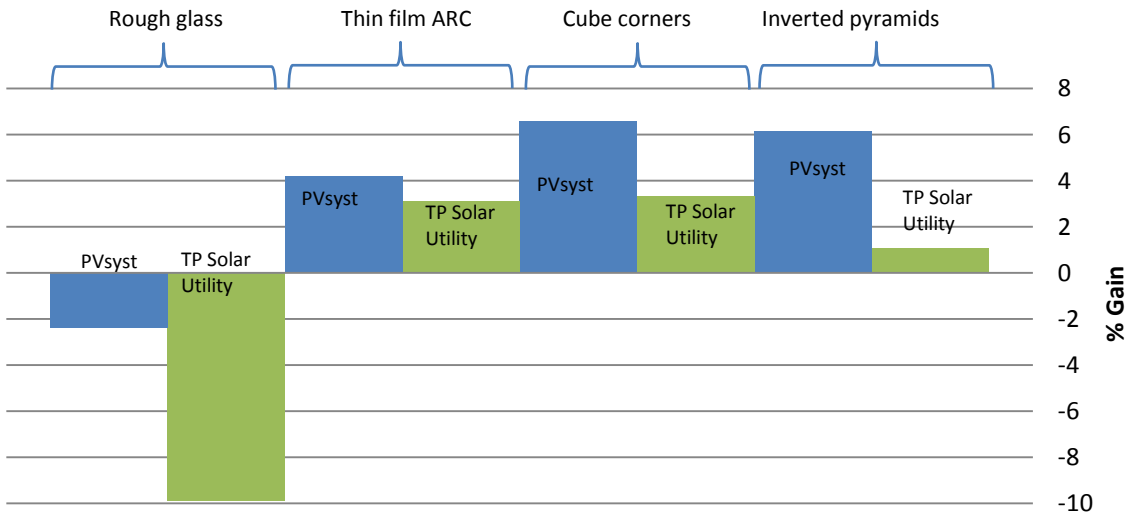

Figure 5: Annual gain in energy production in PVsyst and TP Solar Utility.

The simulation results show in general a gain in PV panel performance when using anti-reflecting glass covers relative to plain float glass. Textured glass surface is particularly effective under high angles of incidence, and therefore also diffuse irradiance, which indicates that it can be of extra value in locations experiencing high share of overcast sky conditions (e.g. northern Europe).

Performance gains as high as 12 % were found for cube corner textured glass under overcast sky conditions. Thin film ARC is shown to perform better than the tested inverted pyramids texture under normal irradiance (3.7% versus 0.6%), however the texture glass return more gain in annual energy production from PVsyst because of the performance under diffuse irradiance (6.2% and 4.2% for inverted pyramids and thin film ARC, respectively). This indicates that parameters under normal incidence are not sufficient in the design process of a PV panel. In addition, the diffuse fraction of global irradiance varies from one location to the next, and hence an optimal glass cover should be chosen for a given location.

Acknowledgements

We are very grateful for the help and guidance from Dr. Thomas J. J. Meyer, who has in spite of a busy schedule always taken the time to advise us, meet us weekly to discuss the project, and further correspond with us by e-mail. His insight into the scientific community has provided us contacts, understanding and a level of detail into thesis writing far beyond what we had prior to this project. We want to thank Teknova for providing us with office space in Grimstad where we have been able to stay and work from early in the morning to late at night, working days and weekends, borrow extra computers for the simulations, and for the patience of our co-workers there and all the coffee. We also want to thank Vetro Solar. Thank you to Lambda Research Corporation for providing us student licences for TracePro Expert, and support from Jack Hlavaty, as well as IronCAD for providing us student licenses for IronCAD 2013. Thanks to Steve Eckhardt for helping us with CAD models of glass cover texture and to Aron Habte for support using SMARTS. We also want to thank prof. Tor Oscar Sætre, our internal advisor from UiA, for guidance and help with taking SEM images of photovoltaic cells in the lab.

Nomenclature

c	Velocity of light in a vacuum	($2.998*10^{8}$ m/s)
dL_S	Scattered radiance	(W/m^2sr)
dE_i	Incident irradiance	(W/m^2)
h	Planck's constant	($6.626*10^{-34}$ Js)
k	Boltzmann's constant	($1.381*10^{-23}$ $m^2kg\,s^{-2}$)
k_e	Extinction coefficient	
m	Air mass ratio	
n	Refractive index	
n_e	Flux of electrons per unit time	(s^{-1})
n_{ph}	Incident flux of photons of wavelength λ per unit time	(s^{-1})
n_{ideal}	Ideality factor	
q	Electron elementary charge	($1.602*10^{-19}$ C)
t	Glass thickness	(m)
x	Distance into the material	(m)
A_{cell}	Area of the solar cell	(m^2)
E_{ph}	Energy of a photon	(J)
E_λ	Global irradiance on a horizontal surface	(W/m^2)
$E_{d\lambda}$	Diffuse irradiance	(W/m^2)
$E_{bn\lambda}$	Beam (direct) irradiance	(W/m^2)
$E_{dR\lambda}$	Component from Rayleigh scattering	(W/m^2)
$E_{da\lambda}$	Component from aerosol scattering	(W/m^2)
$E_{d\lambda}$	Component from ground/sky backscattering	(W/m^2)
EQE	External quantum efficiency	
F	Spectral irradiance	($W/m^2/nm$)
FF	Fill factor of the solar cell	
G_{e-h}	Generation rate	($m^{-3}s^{-1}$)
H	Daily insolation received on a horizontal surface	(J/m^2)
H_0	Extra-terrestrial daily insolation on a horizontal surface	(J/m^2)
I	Effective irradiance	(W/m^2)
I_0	Light intensity at the top surface	(W/m^2)
IQE	Internal quantum efficiency	
$I_{D,0}$	Dark saturation current of the solar cell	(A)
I_L	Light generated current	(A)
I_{mpp}	Current at maximum power	(A)
V_{mpp}	Voltage at maximum power	(V)
I_{SC}	Short circuit current	(A)
J_{SC}	Short circuit current density	(A/m^2)
L_γ	Luminance of a sky element	(cd/m^2)
L_Z	Zenith luminance	(cd/m^2)
L_a	Luminance of an arbitrary sky element	(cd/m^2)
N_0	Photon flux at the top surface	($m^{-2}s^{-1}$)
P_{in}	Spectral incident light power	(W)
R	Reflectance	

SR	Spectral response	(A/W)
T	Transmittance	
T_{CELL}	Absolute temperature	(K)
V_{OC}	Open circuit voltage of the solar cell	(V)
Z_s	Zenith angle of the sun	(°)
α	Absorption coefficient	(m^{-1})
α_a	Azimuth angle of the sky element	(°)
$\alpha_{a,S}$	Solar azimuth angle	(°)
λ	Wavelength of light	(m)
γ	Elevation angle of the sky element above the horizon	(°)
θ_z	Zenith angle	(°)
f	Scattering indicatrix	
χ	Angular distance between a sky element and the sun	(°)
φ	Luminance gradation function	

List of abbreviations

Al	Aluminium
AM	Air mass
APCVD	Atmospheric-pressure chemical vapour deposition
ARC	Anti-reflective coating
ASTM	American Society for Testing and Materials
BSDF	Bidirectional scattering distribution function
BRDF	Bidirectional reflection distribution function
BTDF	Bidirectional transmission distribution function
CIE	International Commission on Illumination
c-Si	Crystalline silicon
DLARC	Double layer anti-reflective coating
EQE	External quantum efficiency
EVA	Ethylene vinyl acetate
IAM	Incidence angle modifier
IQE	Internal quantum efficiency
ISO	International Organization for Standardization
KOH	Potassium hydroxide
LTF	Light transmission factor
NREL	National Renewable Energy Laboratory
OR	Orientation
PECVD	Plasma chemical vapour deposition
PV	Photovoltaic
SLARC	Single layer anti-reflective coating
SMARTS	Simple model of the atmospheric radiative transfer of sunshine
STC	Standard testing conditions

List of figures

List of tables

Contents

1 Introduction

1.1 Thesis Aim and Objectives

In this study we seek to use simulation software to quantify the incidence angle dependence on power generation of a solar panel using anti-reflective cover glasses. Nowadays standard parameters are solely measured under direct irradiance at normal incidence, but for a panel utilizing anti-reflective glasses the largest benefit, in some cases, lies at high angles of incidence. It is believed that an increase of 5 % to 8 % annual energy production can be achieved by selecting the appropriate glass cover. Hence for an accurate evaluation of different antireflective techniques this angular dependency must be considered.

In addition we aim to better understand the effects of diffuse radiation, and thus get one step closer to determine optimal solar panel design for parts of the world (e.g. northern Europe) where the diffuse fraction of the global radiation is large. As pointed out by Torres et al. (2008) the importance of the diffuse fraction is commonly underestimated. In latitudes from 40 to 60° N this fraction may represent 40% to 60% of the yearly radiation received on a horizontal plane because of frequent overcast skies [1].

This study is carried out in three steps.

1. Step one is to generate irradiance models to represent both direct and diffuse irradiance, each of which simulates different angles of incidence and solar spectra.
2. Step two is to create a simple optical model of a photovoltaic panel and evaluate it with different types of glass covers. In this thesis regular float glass, thin film anti-reflective coated glass and deeply textured glass are evaluated.
3. Step three is to run numerical ray tracing to obtain results for the different glass covered panels under the different irradiance models. These results will be fed into PVsyst, a well-known commercial software, to return calculated annual energy production, which are compared to energy production measurements based on direct irradiance in ray tracing. Comparisons with experimental data can be made.

1.2 Thesis Outline

Prior to presenting the results of this study, irradiance models and a solar panel had to be developed and optically modelled. In the following points the structure of this thesis is presented and each chapter is briefly described.

Chapter 1 presents the aim and objectives of this thesis and a literature review comparing the different claims made by researchers and commercial companies selling structured or coated glass covers.

Chapter 2 explains the relationship in between light absorption and power generation at both normal and oblique irradiance.

Chapter 3 describes optical modelling of sky radiation. In this thesis ray tracing simulations are used to model properties of light under different angles of incidence and air mass ratio so to accurately replicate normal operating conditions for a solar panel in the terrestrial environment. In this chapter, one direct and three diffuse irradiation models are explained and developed.

Chapter 4 describes how light interacts with the different layers in a standard c-Si solar panel. The respective optical properties of each layer is described and illustrated. In addition two models replicating the optical behaviour of a c-Si solar cell are developed and validated.

Chapter 5 discusses anti-reflecting and light trapping techniques utilized on the front surface of solar panels. Today a wide range of methods and products are commercially available, and in this chapter they will be categorized and addressed. Altogether six glass cover types are investigated as part of the optical PV panel model described in Chapter 4.

Chapter 6 presents performance of the solar panel developed in chapter 4 under the direct and diffuse radiation models. The solar panel is tested with the various anti-reflecting glass cover models developed in chapter 5. In addition, annual energy production simulations are performed at a specific location with the ray tracing software used in this thesis (TracePro). The results are subsequently compared with a similar simulation using PVsyst.

Chapter 7 summarizes and identifies the contribution made by the present study. Recommendations for future research are also discussed.

1.3 Literature Review

Cost efficiency of photovoltaic solar panels is subject to a lot of research aiming to make solar power an economically attractive choice. Increasing the efficiency by reducing optical losses is a field of study with promising prospects.

At normal incidence approximately 4% of the incident sunlight is reflected off the front surface of a flat glass solar panel. As the light incident angle increase across the day the reflection losses become more substantial (e.g at an incidence angle of 70 degrees 45% of the light is reflected [2])

Thin film anti-reflective coatings (ARC) and textured glass surfaces are methods that can be applied to increase the optical efficiency and increase the energy yield. In recent studies these methods have been investigated both through experiments and simulations. To give the reader some perspective a brief review of recent research trends and claims for antireflective techniques on solar glass is presented.

BP solar has tested the benefits from adding a thin film layer of SiO_2 ARC on the front surface of both a mono and multi c-Si solar panel [3]. An indoor flash test performed under standard test conditions (STC) showed improved short circuit current (I_{sc}) of 2.8% and an increased max power (P_{max}) of 2.7% for the multi c-Si solar panel compared with a standard plain glass covered solar panel. The mono c-Si solar panel showed an increased P_{max} of 3%. In addition, the study also included an outdoor test which indicated that the energy gain may be in excess of the STC gain, the outdoor measurements

showed 4% increased energy produced for both the mono and multi c-Si solar panels when compared with reference panels.

Another thin film ARC manufactured by DSM called KhepriCoat, produces, under normal incident light, a gain in relative power of 2.5% according to the manufacturer. No details regarding how these measurements where produced and what type solar panel was used has been specified by the manufacturer.

Saint-Gobain has developed a series of glass products for the PV industry, namely Albarino G, P, T and S. Albarino S and T are lightly patterned, while G and P have deep textures. In recent studies Albarino G and P have proven to increase the I_{sc} compared with Albarino T and S. However some results are inconsistent, in a paper by Nositschka et al. (2009) the STC measured I_{sc} showed an increase of approximately 2.15% and 1.9% for Albarino G and P respectively for a multi c-Si solar panel [4]. But another study show a gain in STC measured I_{sc} of 2.7% for Albarino P [5]. This test was also performed with a multi c-Si solar panel. The difference in measurements is interesting and after corresponding with the author of these studies (Nositschka) the source of the discrepancy was identified as the result of two factors. Firstly different solar simulators were used. Secondly different suppliers for solar cells were used. In addition to the indoor test outdoor measurements continuing for 2 years have been performed. The measurements showed that a poly c-Si solar panel fitted with Albarino P outperformed a reference panel. The measured increase in energy produced was 3.9% and 4.3%, respectively for the first and second year.

Duell et al. (2010) studied 4 different antireflective glasses with the following structure; lightly textured, pyramids, inverted pyramids and grooves (similar to Albarino G). Indoor tests were performed with a solar simulator for incident light normal to the PV panel surface. The results showed increased I_{sc} generation of respectively 0.3%, 1.4%, 2.5% and 3.2% when compared with a flat glass solar panel [2]. Type cell used in the panels was not been specified.

In a study by Sanchez-Friera et al. (2006) two glass structures; inverted pyramids and round pits were investigated [6]. Indoor tests for light incident normal to a mono c-Si solar panel performed with a solar simulator showed a nominal power boost of 1.5% and 1% respectively, when compared to a flat glass solar panel. However, the authors noted that this gain is only partially a result of the structures, also the “better infrared response in the glasses under evaluation” improves the results i.e. better optical properties in the infrared region. In addition to the indoor tests, outdoor tests were also performed with the rounded pit structured glass and for comparisons with a panel covered with flat glass. The test showed that at the early and late hours of the day the structured glass increased the power by up to 18 %, during the central hours of the day a more consistent gain of 1.7% was observed. Over a time period of 7 months the rounded pits structured glass increased daily energy yield by 2.5-3.5%.

SolarExcel has developed a polymeric sheet with a cube-corner geometric texture and in a study by Ulbrich et al. (2012) the structure was tested on a micro c-Si solar panel in a solar simulator under STC. The cube-corner structure showed increased I_{sc} of 2.6% compared with a flat glass [7]. An amorphous silicon/microcrystalline silicon tandem thin film solar panel was also tested with the cube-corner texture and showed an increased I_{sc} of 7.9% compared with a similar flat glass panel. This structure is further discussed in chapter 5.

Tachikawa et al. (2000) studied the effect of using a v-grooved structure on the front glass surface of a vertically oriented (wall mounted) solar panel. Solar cell type used in this study was not specified. Their study used a solar simulator to measure how the generated power depends on the angles of the two axes of a PV module. By adjusting the angles so that they correspond to altitude and direction of the sun, they simulated the amount of direct sunlight the module would receive at any given time on any given day. Together with reflection values as a function of incidence for the air/glass interface the annual energy production was calculated. The test showed an increase of 10% in annual energy production compared with a PV panel with flat glass. Outdoor measurements was done with a panel facing south and a panel facing north, they generated respectively 12.7% and 7.13% more energy compared with a flat glass module on a sunny day [8]. The theoretical calculated improvements were respectively 15.1% and 10.1%.

The previous techniques can be considered to represent conventional forms of anti-reflection methods. Following are two new methods that have been tested.

- Escarre et al. (2011) has studied the effect of a micrometric pyramidal texture at the air/glass interface for an amorphous silicon/microcrystalline silicon tandem thin film solar module. The structure is based on the pyramidal shapes produced by etching mono c-Si with KOH. A mold of the etched surface is taken and the structure is imprinted on a coating. This coating, with refractive index of 1.518 at 635 nm, optically behaves as glass. The antireflective technique produced a STC measured I_{sc} gain of up to 5.4% compared with a similar thin film solar module with plain glass front cover [9].
- Son et al. (2013) investigated the effect of adding a thin layer (250 nm) of aluminium with nanostructures (e.g. nanoholes) on the front surface of the glass cover of a PV panel. Measurements in a solar simulator showed an impressive increase of 11.34% in I_{sc} compared with a flat glass module [10]. Type cell used in the solar panel was not specified.

These studies demonstrate that structured glass can increase I_{sc} generation in a PV panel by several percent. Compared with a flat surface, a structured surface also effectively increases the area of the front surface of a PV panel. In a study by Duell et al. (2010) it was found that structured glass lowered the cell temperature by up to 3.5 degrees at higher wind speeds resulting in a reduction in V_{oc} losses [2]. This effect was attributed to an increased convective cooling of the structured glass. In a similar study by Saint–Gobain the positive temperature effects from structured glass is claimed to produce a gain in V_{oc} of up to 1.2% [11].

A drawback of structured glass is the potential for dirt accumulation from the environment which can block incident rays from reaching the solar cell. Alfasolar, a module manufacturer, has tested their own pyramidal structured glass in an outdoor test lasting more than 12 months [12]. The location for the test was not specified. The test showed virtually no increase in dirt accumulation over the time period. In comparison with a flat glass module also tested, they experienced increased output. It was believed that the structured glass directed the dirt into the depressions, letting the ridges stay clear. In contrast a flat glass module will have the dirt distributed evenly across the surface. For both modules the dirt was eventually removed by wind and rain. These results correspond well with a study by Sanchez-Friera et al. (2006) performed in Malaga (Spain) where it was also shown that structured glass panels do not necessarily accumulate more dust than a flat glass panel. Figure 1 shows a histogram summarizing the results from the literature review carried on in this thesis. There

have been numerous studies measuring energy yield for solar panels with structured glass outdoors, and as shown in the histogram energy yield results tend to outperform STC measurements. Unfortunately the data from these measurements are only applicable for the location and light conditions the panels experienced. It is impossible to replicate similar settings, and thus the only parameters valid for comparisons are the ones measured indoor under STC. For the above mentioned reasons this study test a range of anti-reflective glass covered PV panels under the same conditions using ray tracing.

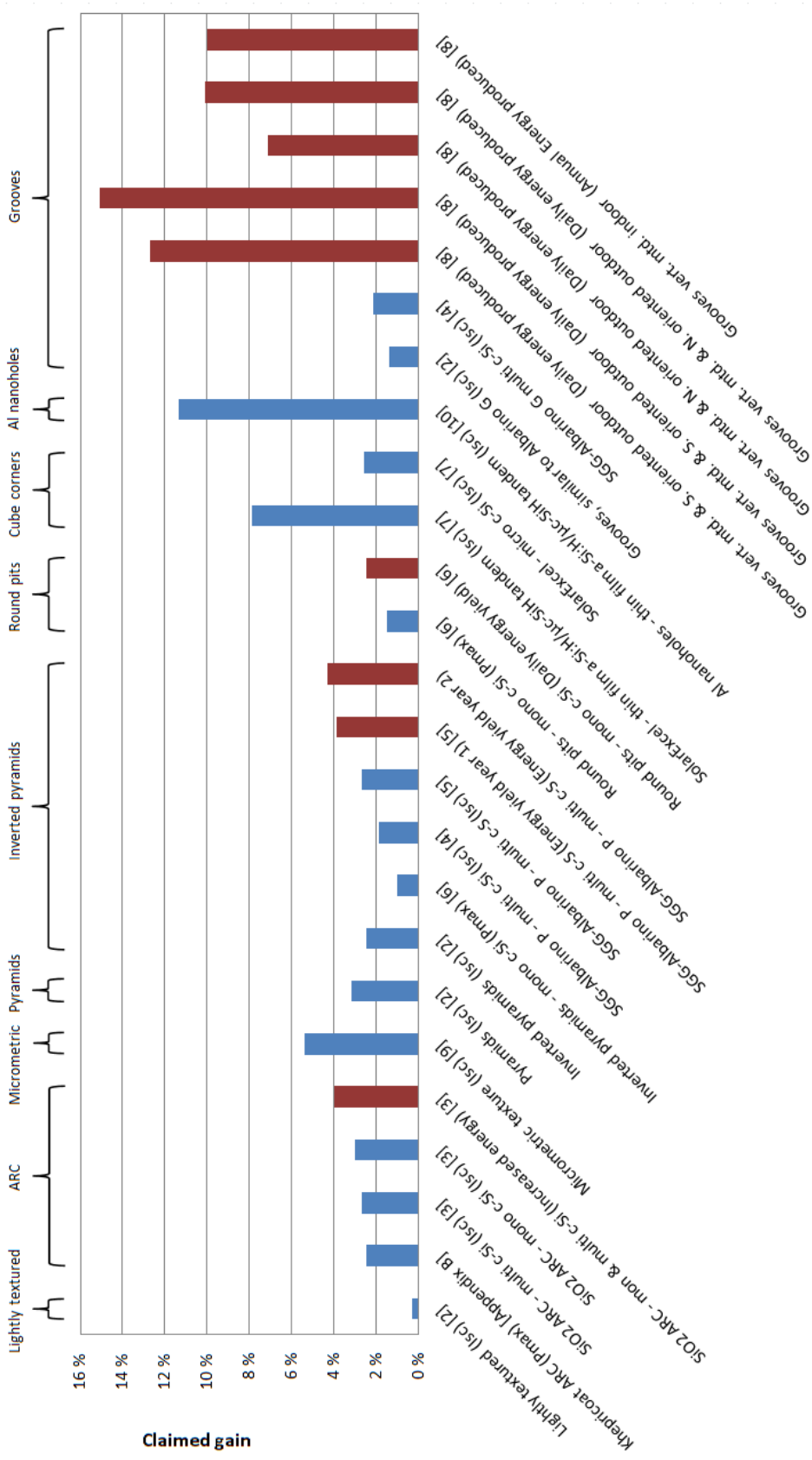

Figure 1: Different claims reported in this literature review. Each claim is represented by anti-reflective technique name and type solar cell used under testing, when this has been specified. The blue columns represent I_{sc} and P_{max}. The red columns represent energy.

In summary, indoor and outdoor experiments tend to deviate, in addition as clearly illustrated in a paper by Grunow et al. results from indoor experiments are dependent on; simulator, set-up, etc. [13]. For textured glass, outdoor experiments tend to result in higher gains than indoor experiments. This could be explained by diffuse radiation and the textured panel's ability to absorb radiation from high angles of incidence [6]. Or by the effect of cell temperature drop due to increased surface area. Unfortunately simulation models available today fail to replicate these effects.

Today modelling of solar panel performance is mostly carried out under direct irradiance; this might be a good approach for analysing energy production on locations such as Spain and California. In contrast, for large parts of the year northern Europe suffers from cloudy weather which causes the suns incident light to be diffusely scattered.

2 Power generation from light absorption

This chapter briefly describes how light absorption, and hence optical modelling, is translated into power generation. Because of the scope of this study, and focus on optical properties, simple equations for ideal cases are used when calculating electrical parameters.

- Light absorption in the photovoltaic cell directly influences the short circuit current, I_{SC}.
- The open circuit voltage, V_{OC}, is determined from the short circuit current.
- The fill factor, FF, is determined from the open circuit voltage.

From these parameters a PV panel's efficiency and power generation is determined. In addition to normal incident light conditions, the effect of oblique angles of incidence on light absorption are analytically modelled and described by the incidence angle modifier. Such parameters are important for estimating the annual energy production simulations.

2.1 Light absorption

This study is based on classical crystalline silicon solar cells where a p-doped silicon region is separated from a n-doped silicon region by a p-n junction. Incoming photons of light that have equal or larger energy content than that of the band gap created by the p-n junction can excite an electron and produce e-h pairs.

Incident photons of light have an energy content given by Equation(1):

$$E_{ph}(\lambda) = \frac{hc}{\lambda} \tag{1}$$

Where:

E_{ph} is the amount of energy in a photon of light (J).
h is Planck's constant, which equals $6.626*10^{-34}$ (Js).
c is the speed of light in a vacuum, which equals $2.998*10^{8}$ (m/s).
λ is the wavelength of the light (m).

The band gap of silicon is about 1.1 eV, which corresponds to a photon with a wavelength of 1.13 µm. Incoming photons of light with more energy than the band gap will dissipate this excess energy as heat. Photons of wavelength above 1.13 µm will not contribute to power generation. Applying some margin and decimal convenience, the upper boundary of the relevant solar spectrum in this study is set at 1.2 µm, i.e. incident solar spectra and material properties will be investigated for wavelengths up to this value. The lower boundary is set to 0.28 µm in this study, because below this value the spectral irradiance and spectral response of the cell is low.

The absorption coefficient of silicon describes the wavelength dependency of the light absorption. The absorption length the light propagates into the silicon wafer is the inverse of the absorption coefficient. The absorption coefficient is related to the wavelength and the extinction coefficient as given by Equation(2):

$$\alpha(\lambda) = \frac{4\pi k_e}{\lambda} \tag{2}$$

Where:

α is the absorption coefficient (m^{-1}).

k_e is the extinction coefficient.

The absorption depth of silicon can be seen in Figure 2 (left) and is defined as the distance into the material at which the light is reduced by a factor of 1/e, or to 36.8% [14]. Blue light is absorbed close to the surface, whereas red and near infrared light are absorbed throughout more evenly throughout the cell. At 1200 nm the cell would have to be 0.45 meters thick to be included in the absorption depth threshold, which is out of the question for practical and economic reasons. The high cost of silicon manufacturing necessitates compromises. Increasing the path length of light in this region by rendering the direction of light and utilizing light trapping is a more viable alternative.

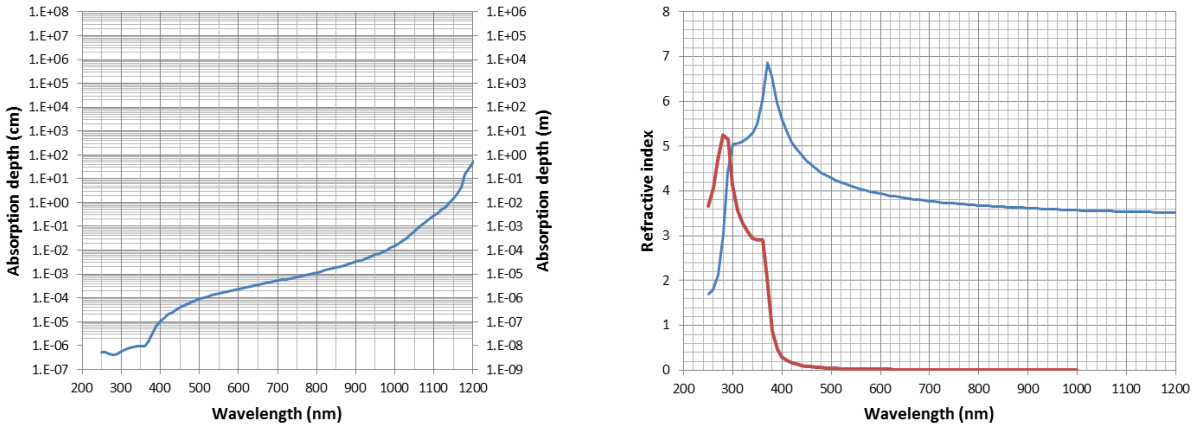

Figure 2: Left: The absorption depth for silicon as a function of wavelength is the inverse of the absorption coefficient. Blue light is absorbed near the surface of the cell while red and near infrared light propagates further. Right: The complex refractive index of silicon. The blue line shows the real part n. The red line shows the imaginary parameter k_e, or the extinction coefficient, which is related to the absorption coefficient [14].

The refractive index of silicon, said to be the second most important optical property in solar panel design, is a complex number on the form $n - ik_e$ where k_e is the mentioned extinction coefficient and n is the real part which determines the reflection and refraction [15]. The refractive index of silicon is shown to the right in Figure 2.

These optical properties for silicon are crucial when modelling the absorption, reflection and transmission in solar panels. As light propagates through the material the intensity of light, I, at any point or depth into the material is given by:

$$I = I_0 e^{-\alpha x} \tag{3}$$

Where:

I_0 is the light intensity at the top surface.

x is the path length of light in the material.

Thus, as the light is absorbed and generates e-h pairs, this generation rate $G_{e\text{-}h}$ at any depth into the material can be given by differentiating Equation(3):

$$G_{e-h} = \alpha N_0 e^{-\alpha x} \tag{4}$$

Where:

N_0 is the photon flux at the top surface (photons/unit-area/sec).

Texturing the surface of the PV cell not only reduces reflectivity, but also contributes to light trapping effects where incident light is refracted by oblique surfaces in a much wider range of angles and hence increases the light path length within the absorbing material. Indeed, the internal reflectivity in the silicon is higher due to the increased light angles. This increase in path length of the light inside the solar cell increases the absorption probability significantly. Such texturing can be done at the front surface, at the back reflector, or both.

2.2 Spectral response

This section briefly describes the spectral response of silicon solar cells related to external and internal quantum efficiency. It gives the generated current under no load conditions, or I_{SC}, per incident power on the solar cell. This parameter is important as it describes limits to the solar cell efficiency as well as a performance indication.

The spectral response SR(λ) in (A/W) of a solar cell is linked to the external quantum efficiency by:

$$SR(\lambda) = \frac{I_{SC}}{P_{in}(\lambda)} = \frac{qn_e}{\frac{hc}{\lambda} n_{ph}} = \frac{q\lambda}{hc} EQE(\lambda) \tag{5}$$

Where:

I_{SC} is the short circuit current (A).

$P_{in}(\lambda)$ is the spectral incident light power(W).

q is the electron elementary charge equal to $1.602*10^{-19}$ C.

n_e is the flux of electrons per unit time.

n_{ph} is the incident flux of photons of wavelength λ per unit time.

EQE is the external quantum efficiency of the cell.

The external quantum efficiency includes reflection losses, while internal quantum efficiency excludes reflection losses. The reflection as a function of wavelength, R(λ), is given as:

$$R(\lambda) = \frac{(n(\lambda)-1)^2}{(n(\lambda)+1)^2} \tag{6}$$

Where n is the refractive index of silicon and the medium from which the light is transmitted is air, with refractive index equal to 1. The transmitted light into the solar cell would then be the amount of light not reflected from the top surface, (1-R). Subtracting light that is transmitted, T, through the back of the cell (often disregarded), EQE is then given as:

$$EQE = IQE(1 - R - T) \tag{7}$$

IQE is the number of e-h pairs generated per incident photon of light that has not been reflected or transmitted through the cell. Reducing the reflection to increase the external quantum efficiency, and hence the solar cell performance, through optical modelling, is the aim of this study. Chapter 4 shows that simple models for PV cells can be made from existing EQE data, but IQE data are required for more complex optical models.

2.3 Power generation

A standard way to determine the maximum power output P_{mp} from a photovoltaic panel is given by:

$$P_{mp} = FFI_{SC}V_{OC} \tag{8}$$

Where:
FF is the fill factor of the solar cell.
V_{OC} is the open circuit voltage of the solar cell.

These parameters necessary to determine the power output from the solar cell are provided typically by measurements under standard test conditions (STC), which are:

- AM1.5 solar spectrum, normalized to 1000 W/m^2
- Operating cell temperature of 25 degrees Celsius, maintained by flash testing
- Normal irradiance

V_{OC}, I_{SC} and FF are typically defined at normal irradiance and therefore only valid for a very short time period during the day, if any time period at all.

However, having standards for testing conditions is important for comparisons of devices but as stated previously are only valid for a certain set of conditions. Solar cells operate in very different conditions throughout the world and this limits the basis for comparison under the standard set.

2.3.1 Parameters measured under normal irradiance

2.3.1.1 Short circuit current, I_{SC}

Short circuit current I_{SC} is often regarded as the most critical parameter in optical modelling of photovoltaic panels because it is directly linked to the number of e-h pairs generated, and hence to the number of incoming photons and therefore to the optical transmissions in the panel and the available sunlight. I_{sc} is the current that flows through the solar cell when it is short circuited and the voltage across the cell is zero. It is the maximum current the tested solar cell can produce under a specific illumination. For an active area of the cell, the short circuit current per unit area, or short circuit current density J_{SC} (A/m^2), can be expressed by:

$$J_{SC} = \int_{\lambda_1}^{\lambda_2} SR(\lambda)F(\lambda)T_g(\lambda)(1-R_g(\lambda))T_{EVA}(\lambda)d\lambda \quad (9)$$

And

$$I_{SC} = J_{SC}A_{cell} \quad (10)$$

Where:

$\lambda_{1\text{-}2}$ is the spectral range of wavelengths (nm).
$F(\lambda)$ is the spectral irradiance per unit area ($W/m^2/nm$).
$T_g(\lambda)$ is the transmission of the glass cover, or fraction of light not absorbed.
$R_g(\lambda)$ is the reflectivity of the glass cover.
$T_{EVA}(\lambda)$ is the transmission of the encapsulant EVA.
A_{cell} is the area of the solar cell (m^2).

The use of J_{SC} is convenient as it eliminates the dependency of the results on the solar cell area. I_{SC} can also be expressed in terms of electron flux:

$$I_{SC} = q \cdot n_e \quad (11)$$

The flux of electrons is a result of generation rate and recombination rate. The resulting I_{SC} can then be measured with an ampere meter. For all the reasons cited above, some studies only examine the gains in I_{SC} when optically optimizing the silicon solar cell.

2.3.1.2 Open-Circuit Voltage, V_{OC}

The V_{OC} is the maximum voltage for a solar cell, which is when no load is connected to the cell, i.e. zero current, and increases logarithmically with increased sunlight [16]. As shown by Mazer (1997), at zero current:

$$0 = I_{SC} - I_{D,0}\left(e^{\frac{qV}{n_{ideal}kT_{CELL}}} - 1\right) \tag{12}$$

And:

$$V_{OC} = \frac{kT_{CELL}}{q}\ln\left(\frac{I_{SC}}{I_{D,0}} + 1\right) \tag{13}$$

Where:

n_{ideal} is the ideality factor, equal to 1 here.
k is Boltzmann's constant equal to $1.381*10^{-23}$ ($m^2 kg\, s^{-2}$).
T_{CELL} is the cell absolute temperature (K).
$I_{D,0}$ is the dark saturation current of the solar cell.

The V_{OC} will therefore not be greatly influenced by higher light absorption and current gains. Giving $I_{D,0}$ a value of 10^{-10} A [17], a plot of V_{OC} as a function of I_{SC} can be seen in Figure 3.

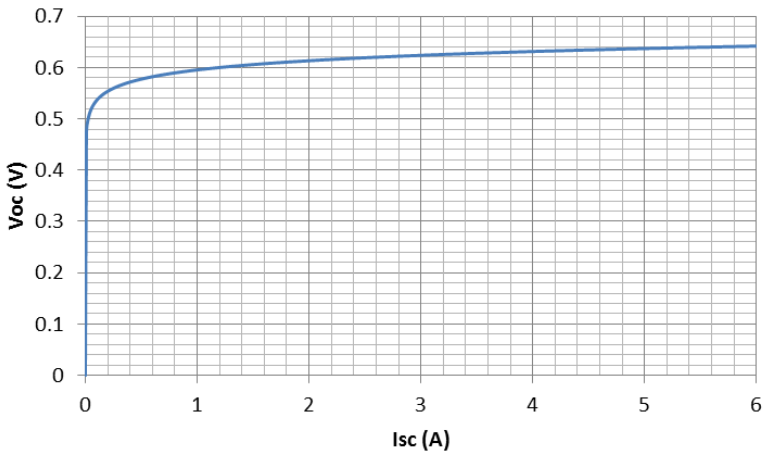

Figure 3: The open circuit voltage as a function of the short circuit current at 300K and with $I_{D,0}$ equal to $1*10^{-10}$. This graph shows that V_{OC} is a logarithmic function of I_{SC}, and henceforth has weak dependence on increasing current.

2.3.1.3 Fill Factor, FF

The fill factor FF is the ratio of the area of the maximum power point current I_{mpp} and voltage V_{mpp} product, and the product of the I_{SC} and V_{OC}. This is seen in Figure 4.

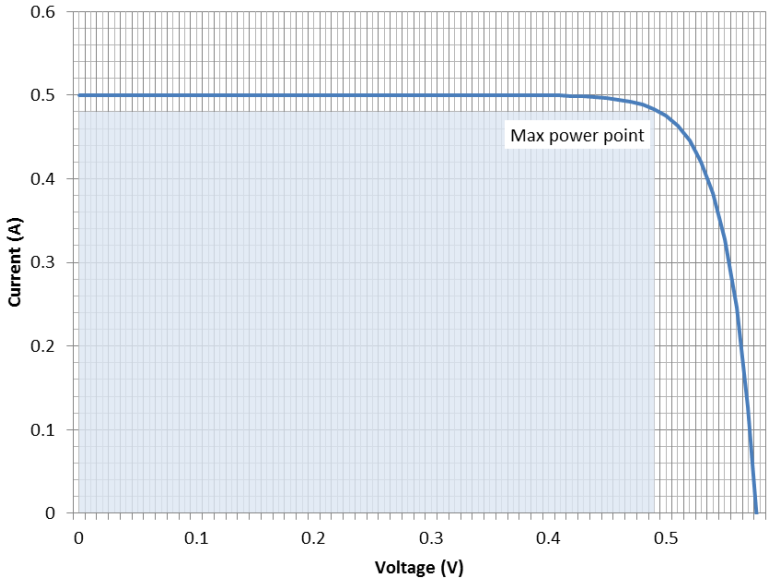

Figure 4: The I-V curve for a solar cell has a maximum operating power output where the product of voltage and current is at peak value. Where the voltage is zero, the current value of the curve is I_{SC}, while the point of zero current is the open circuit voltage. The area of I_{SC} multiplied by V_{OC} divided by the maximum power point area marked in blue is equal to the fill factor of the cell [18].

At zero voltage the current is equal to I_{SC}. At zero current the voltage is equal to V_{OC}. At the maximum power point the current is slightly below I_{SC} and the voltage is slightly below V_{OC}. Green (1982) showed that as FF is ideally a function of V_{OC} only, it can be derived an approximate empirical expression of the ideal fill factor FF_0 [18]:

$$FF_0 = \frac{\frac{V_{OC}q}{kT_{CELL}} - \ln\left(\frac{V_{OC}q}{kT_{CELL}} + 0.72\right)}{\frac{V_{OC}q}{kT_{CELL}} + 1} \tag{14}$$

This equation applies to ideal cases only where there are no parasitic losses, and is supposed to be accurate to about one digit in the fourth decimal place for these cases. As irradiance conditions only weakly affect the V_{OC}, FF_0 is also weakly affected by different irradiance conditions.

The strong dependency of Isc on different irradiance conditions combined with the weak dependency of Voc and FF under different irradiance conditions allows for the following approximation: short circuit current gain can be translated as power gains.

However precise results would require obtaining these parameters from each individual solar cell under investigation.

2.3.2 Parameters taking in account oblique irradiance

2.3.2.1 Annual energy yield

Throughout the year the static solar panel is irradiated by the sun which follows a trajectory across the sky during the day. This trajectory changes with the seasons because of the tilt of the earth's axis of rotation. I.e. the solar panel under regular operation experiences very little normal irradiance. The position of the sun under clear sky conditions determines how much atmospheric gas the light must propagate through and this affects the solar spectrum reaching the solar cell. Local weather and surrounding factors (e.g. albedo) also affect the irradiance and cell operating temperature.

Predicting the annual energy yield requires models that take numerous complex factors into account. Yet despite these inherent difficulties, yield predictions are the most useful data for commercial implantation of solar parks.

Annual energy yield is the produced energy divided by the rated peak performance of the solar panel (kWh/kW_p) [5]. This parameter is useful in that manufacturers rating of their own products will affect the results inversely, i.e. a realistic performance rating is more likely.

2.3.2.2 Incidence Angle Modifier, IAM

The incidence angle modifier (IAM) is a parameter that is very useful when working out the amount of light transmitted to the solar cell. It can be fed as input to simulation software (e.g. PVsyst) to calculate the performance of solar cells, which is done in this study.

The IAM factor describes reflectivity and absorption and is a function of the angle of incidence only. The geometrical cosine factor (covered in section 1.4), that takes into account the spreading of the incident light across the surface as the angle of incidence increases, is not accounted for in the definition of the IAM factor[19]. This is done by assuming an infinite collector surface area. Incoming photons that are incident on a photovoltaic panel surface have a certain probability to be reflected. Higher angles of incidence on plain surfaces leads to more reflected photons. In addition, there is an increase of absorption probability for the photons in each layer as they experience longer path lengths through different materials before reaching the solar cell. The IAM factor is the ratio of the light transmission at an incident angle θ_i and the light transmission that would have occurred at normal incidence (i.e. the angle of incidence equals zero, $\theta_0 = 0$).

A simple analytical model can be used to demonstrate this. Consider a perfect absorber in the form of a thin sheet. Covering this perfect absorber is a glass cover of thickness t, absorption coefficient α, and refraction index n_{glass}. The IAM factor can be expressed from the Beer-Lambert Law, Snell's Law and Fresnel's Law:

$$IAM(\theta_i) = \frac{(1 - R(\theta_i))e^{\frac{-\alpha t}{\cos(\theta_2)}}}{(1 - R(\theta_0))e^{-\alpha t}} \tag{15}$$

Where:

α is the absorption coefficient of the glass.

t is the glass thickness.

θi is the angle of incidence.

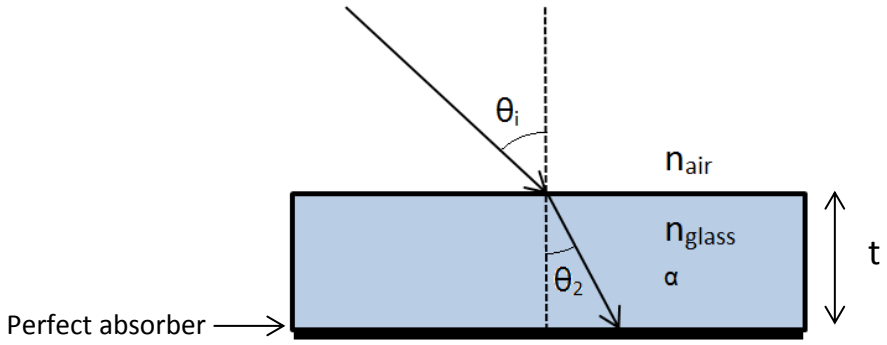

Figure 5: The simple model for analytically deriving an IAM factor consists of a glass plate of the same type as used as solar cell cover. The bottom consists of a perfect absorber, and the optical effect of $n_{glass} > n_{air}$ according to Snell's law of refraction is shown.

Multiple reflections within the glass cover are not taken into account, and the surfaces are assumed to be perfectly smooth. Using Snell's Law for refraction:

$$n_{air}\sin(\theta_i) = n_{glass}\sin(\theta_2) \tag{16}$$

And Fresnel's Law for reflection (of unpolarized radiation, as described by Yamada et al. (2001) [20]:

$$R(\theta_i) = \frac{1}{2}\left(\frac{\sin^2(\theta_2-\theta_i)}{\sin^2(\theta_2+\theta_i)} + \frac{\tan^2(\theta_2-\theta_i)}{\tan^2(\theta_2+\theta_i)}\right) \tag{17}$$

And substituting θ_2 by Snell's Law:

$$R(\theta_i) = \frac{1}{2}\left(\frac{\sin^2\left(\sin^{-1}\left(\frac{n_{air}}{n_{glass}}\sin(\theta_i)\right)-\theta_i\right)}{\sin^2\left(\sin^{-1}\left(\frac{n_{air}}{n_{glass}}\sin(\theta_i)\right)+\theta_i\right)} + \frac{\tan^2\left(\sin^{-1}\left(\frac{n_{air}}{n_{glass}}\sin(\theta_i)\right)-\theta_i\right)}{\tan^2\left(\sin^{-1}\left(\frac{n_{air}}{n_{glass}}\sin(\theta_i)\right)+\theta_i\right)}\right) \tag{18}$$

+

The IAM factor can be derived as a function of θ_i, keeping the expression for $R(\theta_i)$ separated for convenience:

$$IAM(\theta_i) = \frac{(1-R(\theta_i))e^{\frac{-\alpha t}{\cos\left(\sin^{-1}\left(\frac{n_{air}}{n_{glass}}\sin(\theta_i)\right)\right)}}}{(1-R(\theta_0))e^{-\alpha t}} \tag{19}$$

At normal incidence the IAM calculation results in an error, because in the equation for reflectivity in the analytically derived model for the IAM factor there will be division by zero ($\theta_i = \theta_0 = 0$). This error is avoided by calculating R at very small values for θ_i instead of zero.

There are numerous approaches developed to describe the IAM factor in analytical terms. The simulation software PVsyst operates with the IAM factor as input parameter. The function used is based on the ASHRAE-standard 93-77 and is given by Wiggelinkhuizen (2001) [21], as stated by the developers of PVsyst on their web page.

$$IAM(\theta_i) = 1 - b_0 \left(\frac{1}{\cos(\theta_i)} - 1 \right) \tag{20}$$

Where:

b_0 is an incidence angle modifier coefficient, usually with a value of 0.05 for photovoltaic modules.

The advantage of the ASHRAE model is its simplicity in that there is only one parameter that needs to be determined. This advantage is at the expense of its accuracy. PV Evolution Labs states on their webpage (31.01.2013):"PVsyst provides default values for IAM. However, these values are often inaccurate, particularly for modules with anti-reflective coatings, textured glass, or other features designed to capture more light at higher angles of incidence. The result of using PVsyst's default IAM value can be an error of up to 1% of total system performance." Given the uncertainties and complexity in modelling and predicting solar cell performance under oblique irradiance this is most certainly an understatement, but the advantage of model simplicity stands.

Soto et al. (2006) used an IAM factor, developed by King et al. (1998), as part of a 5 parameter model made to predict the current-voltage curve of a solar cell. In their paper the incidence angle modifier is given by:

$$IAM(\theta_i) = b_0 + b_1\theta_i + b_2\theta_i^2 + b_3\theta_i^3 + b_4\theta_i^4 + b_5\theta_i^5 \tag{21}$$

Where:

b_0 to b_5 are constant coefficients that need to be determined for the individual cases.

Soto et al. (2006) listed coefficient values for silicon thin-film, single-crystalline, poly-crystalline, and three-junction-amorphous solar cells.

Figure 6 shows plots of the different IAM factors from the analytical approach, King et al. (1998) and ASHRAE. The analytical IAM is represented for incident light of 0.5 µm wavelength. The constant parameters for each model are listed in Table 1:

Table 1: IAM factor parameters for the analytically derived King et al. and ASHRAE model. The IAM factors are compared in Figure 6.

Analytical	King et al.	ASHRAE
n_{air} = 1	b_0 = 1	b_0 = 0.05
n_{glass} = 1.59	b_1 =-4.6445E-3	
t = 0.0032 m	b_2 =5.8607E-4	
α = 0.4 m^{-1}	b_3 =-2.3108E-5	
	b_4 =3.7843E-7	
	b_5 =-2.2515E-9	

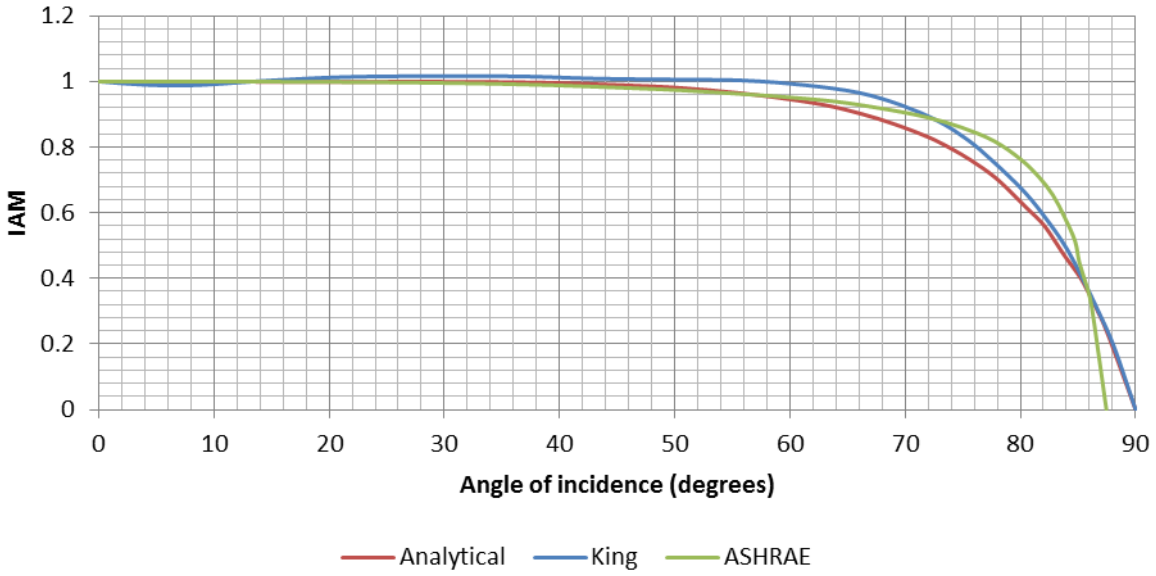

Figure 6: Comparison of analytically expressed IAM models. In general there are small differences for angles of incidence up to 50 degrees. Above this limit the models differ enough to potentially affect the results considerably.

Analytical models provide a quick and simple tool to model the behaviour of simple objects under oblique light incidence. However as the geometry of the flat glass cover is replaced by more complicated geometrical structures the analytical expression quickly become complex and henceforth the use of numerical tool is preferred in this thesis to model the IAM factor.

A comparison of the IAM factor from the analytical model and a numerical model made in TracePro are shown in Figure 8, as well as comparison with an empirical IAM factor based on measurements.

The reader should note that the analytical model for the IAM factor derived here is solely dependent as a function of the angle of incidence only, i.e. IAM(θ).However, in reality and in the numerical model both the refractive index and the absorption coefficient of the material are wavelength dependent and taken in account.

For the comparison to be valid, light of the same wavelength is used so that the two models will have the same absorption coefficient and index of refraction. A wavelength of 0.5 µm is used, approximately corresponding to the peak in the solar spectrum. The following material from the database in TracePro7.3 is used for comparison of the two models. The values are valid for 0.5 µm wavelength:

Table 2: Parameters for the analytical model and the numerical model in TracePro. The IAM factors represented by these two models are shown in Figure 8.

Glass cover details		Analytical symbol
Name	BAF3	
Catalogue	SCHOTT	
Refractive Index	1.58992	n_{glass}
Absorption Coefficient	0.000400401 mm^{-1}	α
Thickness	3.2 mm	t

The numerical simulation traces 10000 rays at 0.5 µm wavelength from 19 different light sources placed at increasing angles (from normal incidence, i.e. where the angle of incidence equals zero, stepped every 5 degrees from 0 to 90 degrees). A screenshot from the TracePro model is shown in Figure 7 where a number of these sources are highlighted. For illustration purposes the traced rays from grid source 11 are displayed. The reflected rays from the glass cover surface can be seen as blue, indicating a reduction in intensity. The red rays, propagating through the glass cover are absorbed in the perfect absorbed located at the bottom surface of the glass cover (see Figure 5).

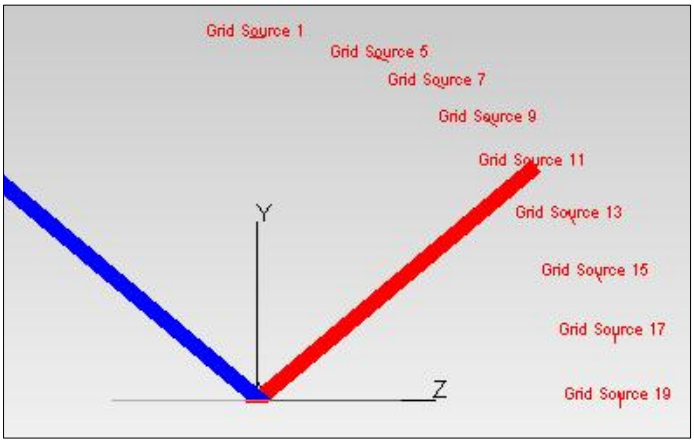

Figure 7: Screenshot from the numerical model in TracePro. A selection of the light sources is highlighted, ranging from Grid Source 1 at normal incidence to Grid Source 19 at horizontal irradiance.

The results from the numerical simulation plotted against the analytical IAM model, are shown in Figure 8. Normalised I_{sc} measurements are also shown [19]. The close relationship between the number of transmitted photons and short-circuit current is again demonstrated here.

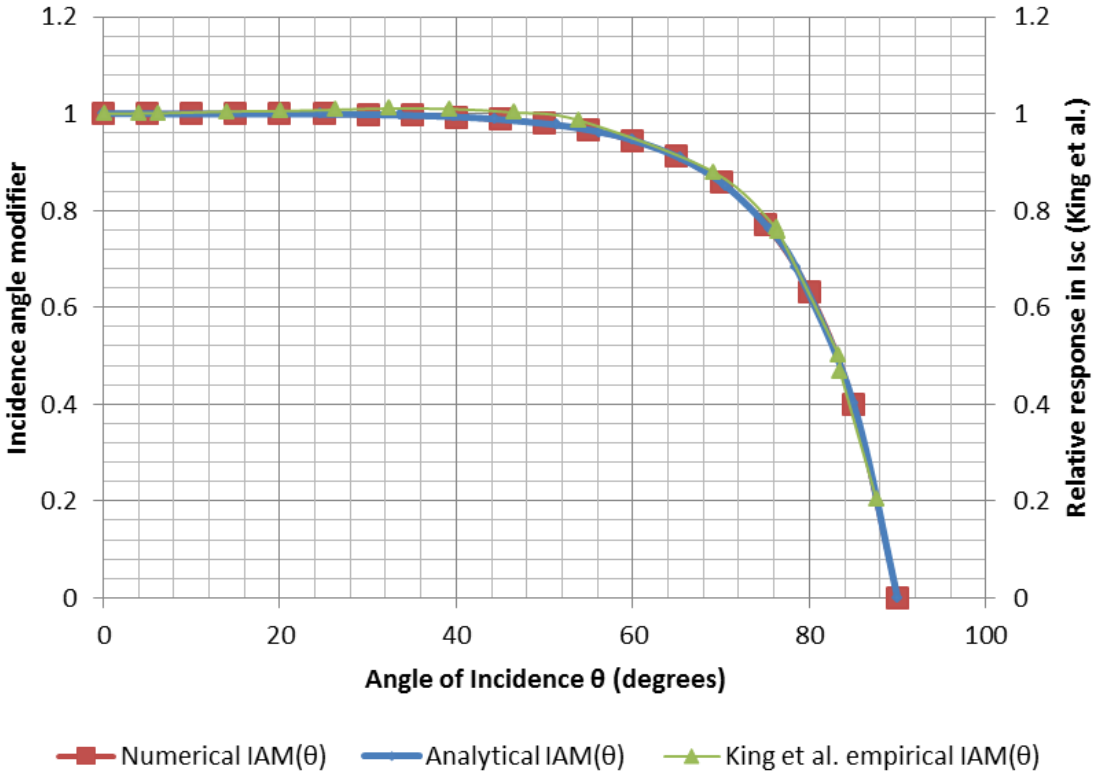

Figure 8: Numerical IAM model run in TracePro compared to the analytically derived model from Equation (19) and an empirical model based on measured normalised response in I_{SC}. The three curves are in good agreement.

The measured data in Figure 8 is for a crystalline silicon solar cell covered by glass, illuminated by light of the AM1.5 spectrum and is extracted from a study by King et al. (2004) [19]. The influence of optical reflectance losses is lower for angles of incidence below 55 degrees for flat-plate modules.

The numerical ray trace model agrees very well with the analytical model validating our numerical approach. In chapter 6 the IAM factors are calculated for complex structures including textured glass surfaces, anti-reflective coatings, EVA, etc., as well as spectral irradiance dependency.

2.3.2.3 Light transmission factor, LTF

The light transmission factor (LTF) describes the transmitted light reaching the solar relative to the incident amount of light at the top surface. It is sometimes referred to as the transmission coefficient in physics when wave propagation in a medium containing discontinuities is considered. It can describe the amplitude, intensity, or total power of a transmitted light wave relative to an incident wave. The previously covered IAM(θ_i) factor can be regarded as a normalized LTF(θ_i) to the value at normal irradiance (θ_i=0).

The LTF as a function of wavelength and incidence angle can be directly combined with irradiance data and spectral response of the photovoltaic panel to calculate the spectral short circuit current I_{SC},at any light incident angle.

2.4 The cosine effect

At oblique angles of incidence light rays are distributed across a larger surface and thus the incident power per unit area is reduced. This is commonly referred to as the cosine-effect and must be added to optical losses like reflection, etc.

The incident power per unit area, or irradiance, on a surface is determined by the incident irradiance and the angle between the light rays and the normal to the surface plane:

$$I = I_0 \cos(\theta_i) \tag{22}$$

The cosine effect is displayed graphically in Figure 9.

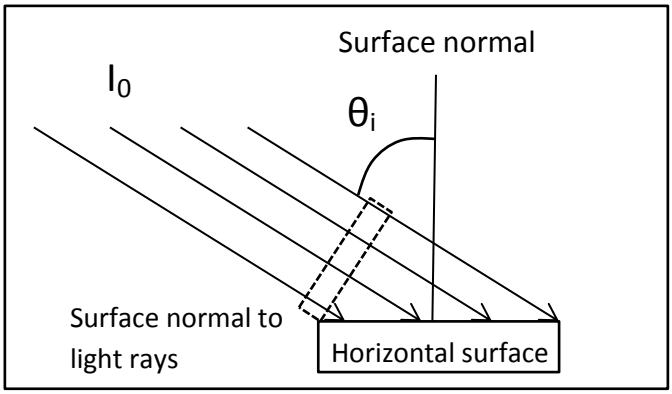

Figure 9: The cosine effect describes how light at an angle of incidence will spread out over a larger surface area than a hypothetical surface normal to the sun's rays, thereby reducing the incident power per unit area.

The rotation of the earth around its axis causes an apparent motion of the sun across the sky each day and makes the incident power dependent on the time of the day. Also, the height of the sun's trajectory in the sky varies throughout the year because of the earth's trajectory around the sun and the earth's tilt relative to the plane of earth's trajectory around the sun. Thus, complete modelling of the sun's angle to a fixed position or surface on earth requires the latitude, longitude, day of the year and time of the day or more precisely the solar time. Numerical software like PVsyst and TracePro Solar Utility do these types of calculations.

2.5 Conclusion

Parameters used to determine and predict photovoltaic panels' performance are limited to testing conditions because of the dependency on numerous variables such as the spectral irradiance, angles of incidence, etc. Optical modelling is linked to light absorption, which is linked to the short circuit current and hence the performance of the device. Analytical expressions for the angular and spectral dependence, i.e. the IAM factor, have been derived and compared to a numerical version. The IAM factors used in this thesis (shown in chapter 6) represents the solar panel developed in chapter 4 with the different anti-reflective glasses developed in chapter 5.

3 Optical modelling of sky radiation

Simulation tools are continuously being developed allowing for performance predictions of PV technology without relying on measurements from demanding and time-consuming field studies. This study utilizes ray tracing simulation software to model the properties of light. Direct and diffuse solar radiation is modelled separately to investigate the performance of photovoltaic devices under different sky conditions. A brief description of solar irradiance and our models used to reproduce it in ray tracing is given in this chapter. The following irradiance models for investigation of solar panel performance are presented:

- Direct irradiance model
- Clear sky diffuse irradiance model
- Partly cloudy sky diffuse irradiance model
- Overcast sky diffuse irradiance model

3.1 Properties of sunlight

Light has been described as waves propagating in the electromagnetic field through space. The speed of light gives the relationship between the wavelength of the light and its frequency. However, light also inhibits particle-like properties that the wave model does not account for. Light can be seen as massless energy elements, or quanta of energy. As mentioned in chapter 2 each particle of light contains a finite amount of energy determined by the frequency, or wavelength, of the light.

Therefore energy of a photon is proportional to its frequency, or inversely proportional to its wavelength. The photoelectric effect, which is a key element in the field of photovoltaic technology, is an example of a phenomenon well described by the particle model of light. Thus, depending on the situation, light can be regarded either as a wave or as a particle. This is called the “wave-particle duality”. In ray tracing light is represented as distinct rays parallel to the direction of the propagating light waves, which can be subject to absorption, specular reflection and refraction, diffraction and scattering after being emitted from a source. Each ray will hold properties like wavelength and intensity.

The solar spectrum outside the earth’s atmosphere is shown in Figure 10 [22]. The solar spectrum is sometimes simplified as a black body radiation source at 6000 K at the distance of the sun. This does give the advantage of having an analytical function for the solar spectrum. However, in this study it is desirable to have solar spectra as accurate as possible. Thus, the black body approximation is considered not accurate enough for this thesis. Spectra based on actual measurements are considered instead.

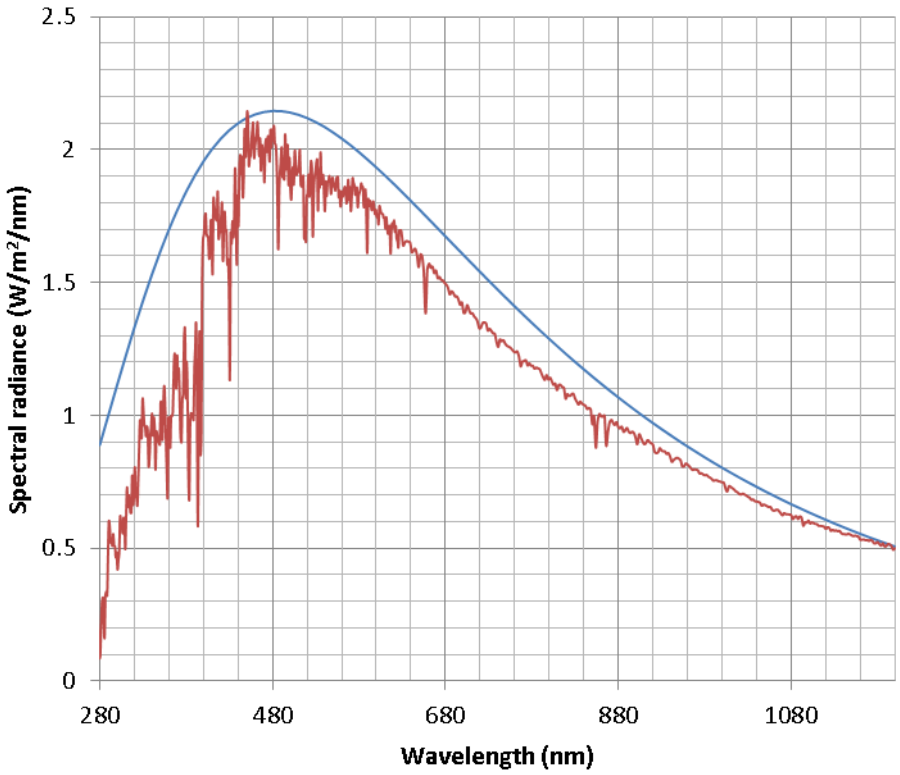

Figure 10: The red line shows the solar spectrum on top of the earth's atmosphere (AM0 given by the ASTM E-490 Standard Spectrum). The blue line is the spectral irradiance for the sun being approximated by black body radiation at a temperature of 6000 K located $1.5*10^{11}$ m away.

The spectral transmission for the atmosphere determined by the different compounds under a set of given atmospheric conditions can be seen in the section about the program SMARTS2, used to provide irradiance data. How the atmosphere alters the extra-terrestrial spectrum determines the irradiance at ground level. Measured spectral data are used when SMARTS2 cannot provide these data, namely under overcast and partly cloudy sky conditions.

The total integrated power density at the top of the earth's atmosphere per surface area perpendicular to the direction of the light is about 1.36 kW/m^2 and varies slightly throughout the year because of the variable distance between the earth and the sun. However, for a given spectrum this value is often referred to as the "solar constant".

3.2 Global radiation

Global radiation is the total solar radiation, i.e. the sum of direct and diffuse radiation, on a terrestrial surface at sea level and can be measured using a pyranometer. Atmospheric effects will affect the solar radiation reaching the earth's surface by altering the solar spectrum and reducing the total irradiance.

The solar radiation is affected by:

- Scattering from clouds and the earth's surface
- Atmospheric scattering
- Absorption in the atmosphere, caused among others by CH_4, N_2O, O_2, O_3, CO_2 and H_2O. In the visible area of the spectrum the atmosphere is close to transparent. However, at wavelengths below 300 nm solar radiation is completely absorbed at sea level by absorption in O, O_2, O_3 and N_2 gases and above 1200 nm the atmosphere is almost completely opaque [23].

The absorption in the atmosphere further contributes to the previously mentioned selection of relevant range of the solar spectrum.

As light passes through the atmosphere it is also subject to scattering. One type of scattering caused by molecules in the atmosphere called Rayleigh scattering especially affects light of short wavelengths (the blue end of the visible spectrum). In addition to Rayleigh scattering, aerosols and dust particles contributes to scattering of sunlight. The scattering divides the sunlight into direct radiation and diffuse radiation as direct light is scattered and produces a smooth distribution of diffuse light throughout the sky. Local variations in weather, cloud cover, dust, humidity, etc. continually affect the amounts of direct and diffuse radiation on any location.

3.2.1 Air mass ratio

The air mass (AM) ratio describes the distance of atmosphere the light has to travel through. Because the top of the atmosphere is not well defined in terms of distance, it is more practical to consider the mass of atmosphere the light will travel through. A standard mass of atmosphere (AM1) will be encountered by a direct beam at normal incidence passing through the atmosphere at normal pressure (101.325 kPa), clear sky with no cloud, dust or air pollution at sea level. AM0 refers to no atmosphere, i.e. extra-terrestrial irradiance. AM1 refers to atmosphere at solar zenith. AM1.5, where the light is incident at a zenith angle of 48.2 degrees, is an often used standard for testing of solar cells. The air mass ratio, with symbol m, is given by:

$$m = \sec(\theta_z) \tag{23}$$

Where:

θ_z is the zenith angle, i.e. the angle between the incoming light flux and the solar zenith.

The air mass ratio is displayed graphically in Figure 11.

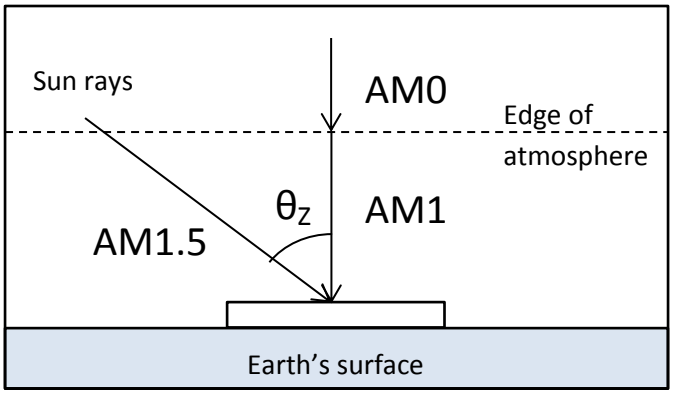

Figure 11: AM0 represents solar radiation outside the earth's atmosphere. AM1 represents solar zenith radiation, and AM1.5 represents 1.5 atmospheres for the light to go through.

Standard spectra are defined in standards, e.g. American Society for Testing and Materials (ASTM) or International Organization for Standardization (ISO), or can be calculated using software that takes the spectral transmittance of the atmosphere into account, e.g. SMARTS2. For ASTM there are two standard spectra for AM1.5 given in ASTM G159-99: direct (AM1.5d) radiation normal to the surface and global (AM1.5g) radiation incident on a 37 degrees tilted surface to the horizontal, and one for extra-terrestrial solar radiation (AM0) given in ASTM E-490 [24].

Reference spectra described in ASTM G-159 is based on an extra-terrestrial AM0 spectrum given by Wehrli [25], the United States Standard Atmosphere (USSA) [26] and atmospheric aerosol profiles of Shettle [27], as presented by Myers and Emery [24]. The atmospheric conditions specified in ASTM G159-99 are summarized as follows:

- 1976 USSA profiles of temperature, pressure, air density and molecular species density specified in 33 layers starting from sea level
- Absolute air mass ratio of 1.5 (solar zenith angle of 48.10 degrees) at sea level
- Aerosol Optical Depth (AOD), or "turbidity" of 0.27 at 500 nm wavelength
- Constant surface albedo of 0.2, assuming Lambertian reflectivity profile
- Total precipitable water vapour content of 1.42 cm
- Total ozone content of 0.34 atm-cm

Myers and Emery showed in their work that direct normal reference spectra for flat-plate and concentrating PV applications do not represent appropriate spectral conditions, and embarked on a program to select an appropriate spectral model to produce a more representative reference combination of hemispherical and direct reference spectra. Modern terrestrial spectral radiation models, knowledge of atmospheric physics, and measured radiometric quantities are continually applied to develop new and precise reference spectra since having representative standard spectra is important for comparative studies.

SMARTS2, described later in this report, produces spectra based on atmospheric conditions with satisfying accuracy. The same inputs as in ASTM G-159-99 can be used to produce spectra in SMARTS2.

Figure 12 shows two global solar spectra on the surface of the earth at AM1.5, representing the global radiation in AM1.5g and the direct radiation in AM1.5d, compared to the solar spectrum outside of the atmosphere (AM0). The data are derived from SMARTS2 for a 37 degrees tilted plane.

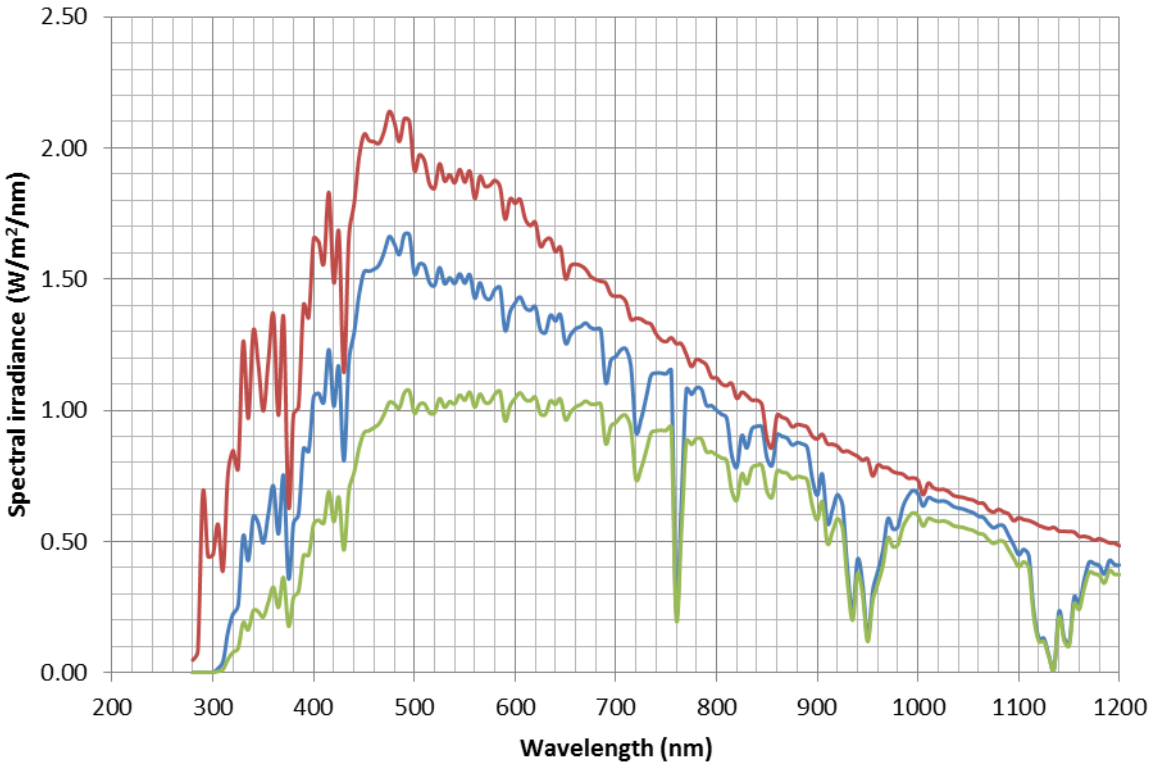

Figure 12: The solar spectra at AM1.5 for global (AM1.5g) (blue line) and direct (AM1.5d) radiation (green line) compared to the spectrum on top of the earth's atmosphere (AM0) for normal incidence (red line).

The spectral areas where the atmosphere causes reduced radiation on earth compared to outside the atmosphere is visible in Figure 12 as the areas where there is considerable difference between the AM0 and AM1.5 values. The difference is most visible from 280 to 880 nm, as well as sections, or bands, at e.g. 760 nm, 920 to 960 nm and 1120 to 1160 nm, caused by different atmospheric compounds. The difference between the AM1.5g and AM1.5d is mostly visible from 300 to 880 nm, caused by scattering.

3.3 Direct radiation

The direct radiation is the portion of the light which is unaffected by scattering. Direct radiation is near parallel rays of light and can be measured with a pyrheliometer by blocking out incoming diffuse radiation from any other angle than what comes directly from the sun. The direct portion of the solar spectrum can be seen in Figure 13.

Direct light is easier to model in ray tracing software because of the near parallel direction of the rays that enables use of simple light sources for simulations. The direct irradiance reaching the earth is weakened through absorption and scattering in the atmosphere. These effects are wavelength dependent, thus the solar spectrum is changed. Figure 13 shows the direct normal irradiance at different air mass ratios, ranging from 1 to 5. Normal irradiance from different solar zenith angles is obtained by calculating irradiance for a plane perpendicular to the rays, like a solar tracker. The air mass still changes as the light has to propagate through more atmosphere for each increase in solar zenith angle.

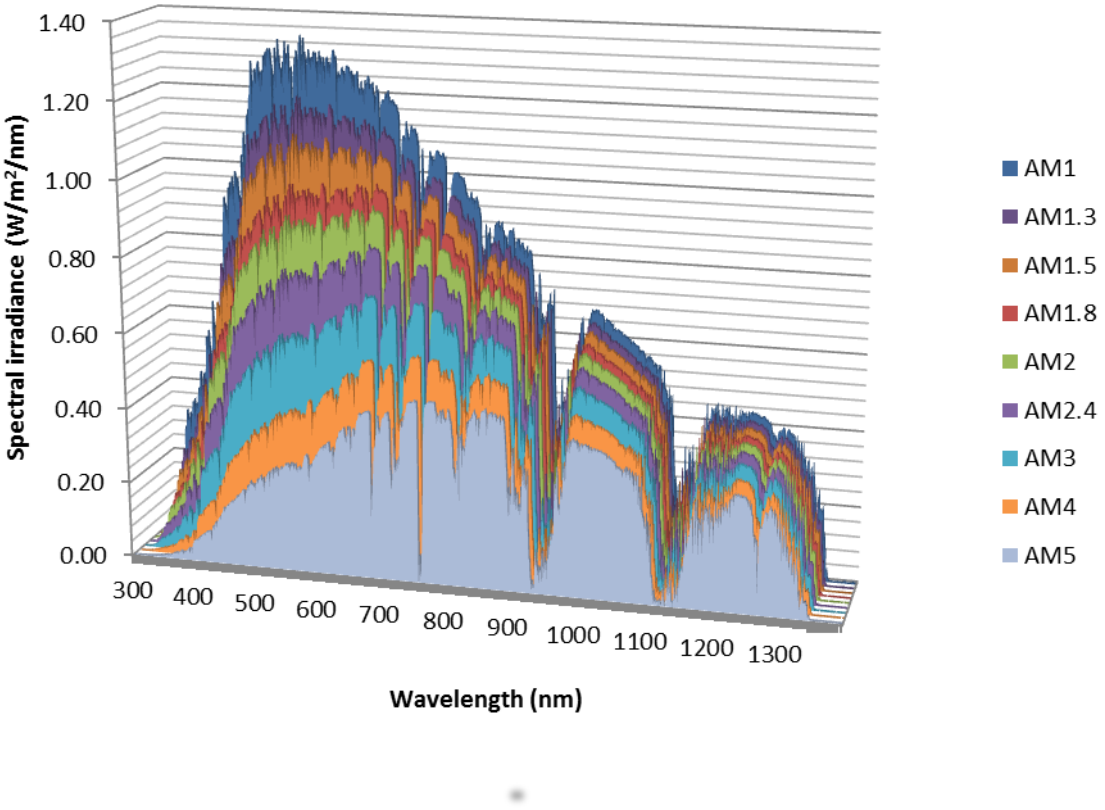

Figure 13: Spectral direct irradiance normal to the receiver surface for air mass ratios ranging from 1 to 5 as derived from SMARTS. AM1 corresponds to solar zenith, e.g. a zenith angle of zero degrees while AM5 corresponds to a zenith angle of 78.5 degrees. The absorption bands are clearly visible. It can be seen how the reduction is wavelength dependent; the blue end of the visible spectrum is affected most.

Figure 13 shows how the direct irradiance spectrum at different air mass ratios, or zenith angles, is affected differently at different wavelengths. As predicted the effects from scattering affect the blue end of the visible spectrum most. A considerable fraction of the light lost in that spectral region will still be incident at ground level in the form of diffuse radiation, which will be modelled independently.

3.4 Diffuse radiation.

The diffuse radiation incident from all directions is a result of light scattering by molecules or aerosols in the atmosphere and by reflection from surroundings (albedo). The scattering processes, namely the Rayleigh scattering and the Mie scattering, can be seen as phenomena where light is deviated from its path without being absorbed and with no change in wavelength. If the particles are small compared to the wavelength of the light, Rayleigh scattering occurs. If the scattering particles are approximately the same size as the wavelength of the light or bigger, Mie scattering occurs, which is described as the scattering of light by a sphere.

Rayleigh scattering is when light is scattered by molecules of the constituent gases in the atmosphere by an angle that is wavelength dependent. Blue light, with relative short wavelength, will be scattered more strongly than red light, with longer wavelength. Hence the blue colour of the clear sky at daytime. The Rayleigh laws predict the variation of the intensity of scattered light with direction. One of the results is symmetry in the patterns of forward scattering and backward scattering from a single particle [28].

The diffuse multi-directional spectral irradiance on a horizontal surface under clear sky conditions on a horizontal surface compared to the global radiation as derived from SMARTS2 is shown in Figure 14.

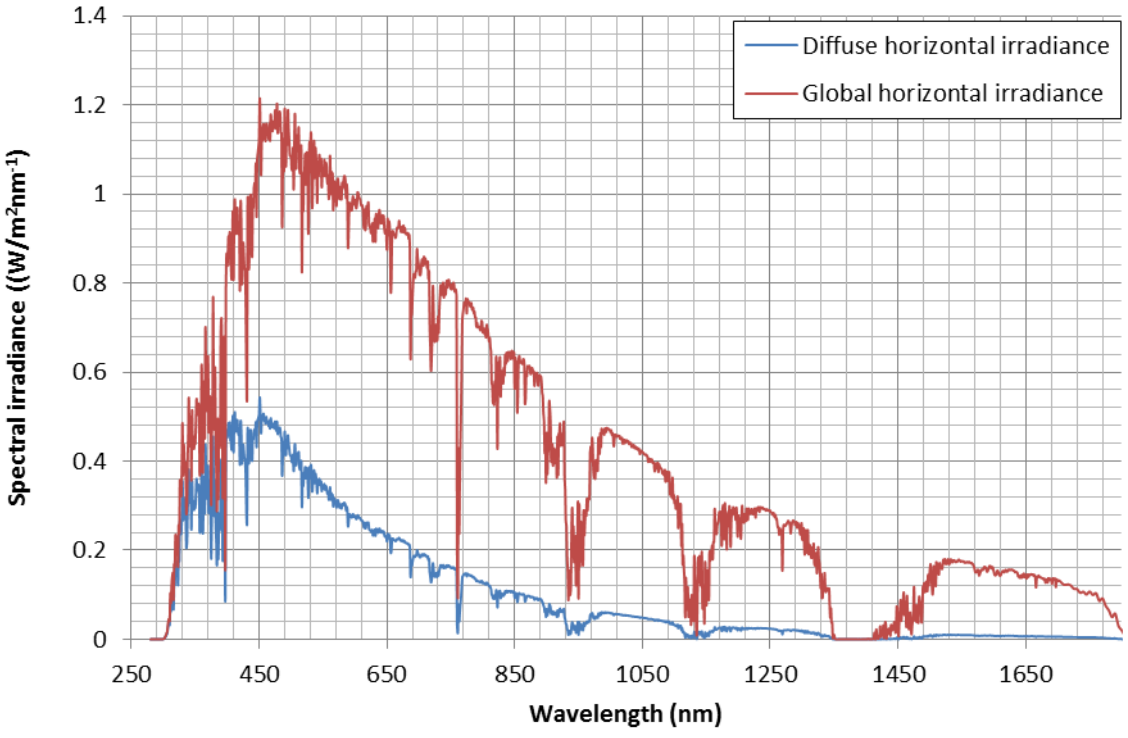

Figure 14: Global (red line) and diffuse (blue line) irradiance on a horizontal plane at sea level. The diffuse radiation from scattered light is mostly represented in the blue end of the visible solar spectrum and is notably low in intensity compared to the total global irradiance.

The diffuse irradiance in Figure 14 does not describe the angular distribution of the light, i.e. how the light changes in intensity from near the solar angle to the horizontal. The diffuse light is most intense

near the direction of the sun because of Rayleigh forward scattering. The solar spectrum depending on the solar angle for diffuse radiation should also be described. However lack of available data necessitates an assumption for diffuse irradiance. In this thesis it is assumed that the diffuse irradiance spectrum is the same from all directions, and that only the intensity, or integral, has a non-uniform distribution across the sky.

The diffuse spectral irradiance under cloudy sky conditions also needs to be investigated as different intensities and spectra are found, which affect the results in this study. A comparison of the diffuse irradiance under clear, partly cloudy and overcast sky conditions is shown in Figure 15.

The overcast spectrum is extracted from Myers et al. (2009) [29]. The diffuse global spectrum is derived from SMARTS2 with ASTM Standard G-159 atmosphere. Both these cases are for a south facing surface tilted 40 degrees and AM1.3 (39.7 degrees solar zenith angle).

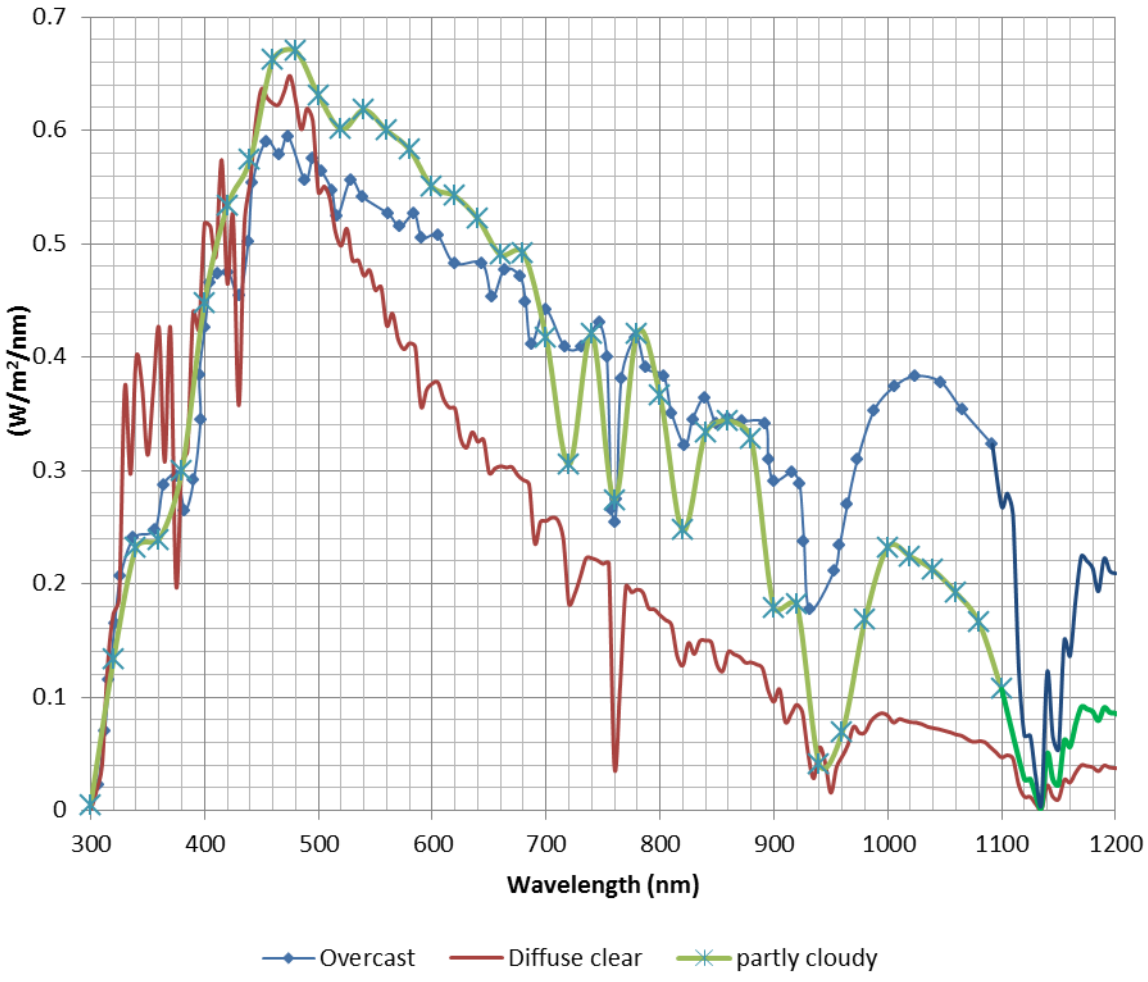

Figure 15: Diffuse spectral irradiance at clear, partly cloudy and overcast sky conditions. The blue line shows diffuse irradiance on overcast sky conditions for a south oriented surface tilted 40 degrees. The red line shows the diffuse irradiance under clear sky conditions derived from SMARTS2 on a similar surface. Both spectra are at AM1.3. The spectra have not been normalized. There is a general similarity for the spectra up to 520 nm. However, above this value, the spectra differ in that the overcast light is more evenly distributed while the clear diffuse light is more reduced. The elevated levels in the upper end of the spectrum for overcast irradiance are referred to by Myers et al. (2009) as "cloud enhancement".

The partly cloudy sky spectrum is gathered from the NREL Spectral Solar Radiation Database for Florida Solar Energy Center (FSEC). The measurement is from 1986, day number 318, 11.30am at a 28.4° tilted surface facing south [30].

The data for partly cloudy and overcast sky conditions only covers wavelengths up to 1100 nm. Lack of available irradiance data at this point led to an assumed shape of the last range from 1100 to 1200 nm. It is assumed that the data fits the shape of the clear sky spectrum, but the data are normalized so that the entry at the higher end of the original spectra matches the first entry in the lower end of the assumed spectra. It is recommended that full measured spectra are used for future studies.

Note the difference in the distribution of the spectra. In the clear sky diffuse irradiance there is predictably a heavier distribution in the blue end of the visible spectrum, whereas the light is whiter, i.e. more evenly distributed in the overcast case. The performance of photovoltaic panels under diffuse irradiance is of importance in this thesis, and therefore the modelled spectra should be as close to reality as possible. The 3 spectra in Figure 15 are used in the 3 diffuse irradiance models.

Because of data availability, the clear sky model is the only model with different solar spectrum for each solar zenith angle from AM1 to AM5, whereas the partly cloudy and the overcast sky model have constant solar spectra for all four solar zenith angles, as summarized in Table 5.

3.5 Models of sky radiation

Having accurate models for sky radiation is crucial when attempting to predict the nature and magnitude of solar irradiance in any location. In this study models are used both for estimating the performance of photovoltaic cells under different conditions and for estimating location-specific annual energy production under both direct radiation and diffuse radiation.

Powerful computer models like SMARTS2 can accurately calculate spectral direct irradiance and diffuse irradiance but are limited to clear sky conditions. It is emphasized that in locations with a high degree of cloud cover, such simplifications will not be representative enough. Models that include the irradiance for overcast sky conditions must be included.

In most simulation programs the models of the International Commission on Illumination (CIE) overcast and CIE clear sky are applied. E.g. the program SUPERLITE generates the luminance distribution under uniform sky, CIE Overcast Sky, CIE Clear Sky with or without sun [31]. Usually in the simulation programs only the CIE Overcast and CIE Clear Sky are included. These are two extremes that are important for performance determination, but it would be useful to include more steps in between. Nakamura et al. (1985) have classified sky conditions into three groups, namely overcast, clear and intermediate trying to define the luminance distribution of the intermediate sky [32]. Three similar sky radiance cases are considered in this study, namely clear, overcast and partly cloudy sky conditions.

3.5.1 Direct irradiance model

While the diffuse component of sky irradiance is often considered as the largest potential source of computational error, the treatment of the direct component is straightforward and close to error-free for flat surfaces [33]. Modelling direct irradiance can be done for the purpose of predicting the annual direct irradiance on a surface at a specific location, or it can be used to describe the instantaneous direct irradiance for different circumstances.

First the position of the sun on the sky must be calculated, which is a matter of making a geometric model for direct light. The time of year, the time of day, the latitude and longitude of the location must be given. Then the atmospheric conditions are taken in to account and will both reduce the integrated irradiance and render the spectrum as was shown in Figure 13.

Analytical calculation of the direct irradiance spectrum can therefore quickly become complex. Therefore numerical computer tools are used. The geometric calculations that account for time and location and tilt of the receiver surface are easily calculated in e.g. SMARTS2 and TracePro Solar Utility (See appropriate sections). The spectra themselves as received at ground level after atmospheric effects will be output from SMARTS2 and other sources. An example of irradiance on a horizontal surface as given from the direct irradiance model in TracePro is shown in Figure 16.

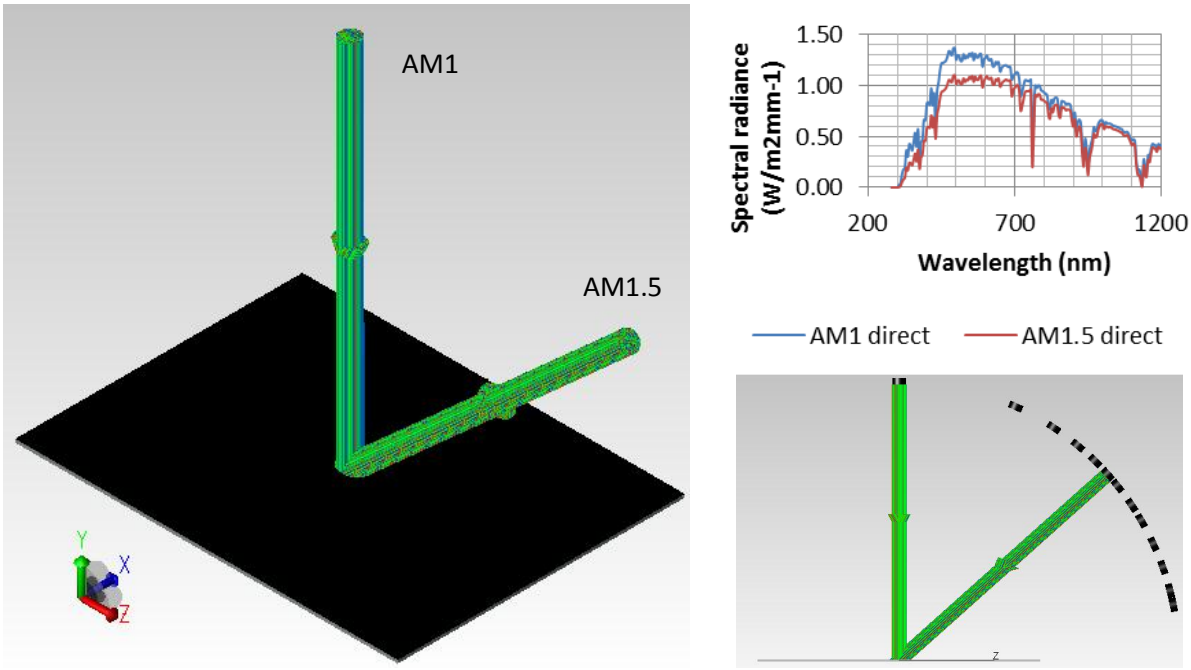

Figure 16: Direct irradiance from two solar positions in the sky as modelled in TracePro. The rays are parallel and irradiant on a horizontal collector. At normal incidence the solar spectrum is as derived from SMARTS2 at ASTM G159 standard atmosphere and AM1. The second case is irradiance at a zenith angle of 48 degrees, i.e. AM1.5 spectrum is used for the same atmosphere. The differences in colour (though green dominates) correspond to differences in intensity at different wavelengths. The spectral plots are for the sources, i.e. the unit area is normal to the rays.

It is important here to point out that the irradiance emitted from these sources is emitted in the same way as is incident on a surface normal to the rays in SMARTS2. That means that the irradiance coming from a non-zero zenith angle will be spread across a larger surface in accordance with the cosine effect and the measured power per unit area on the collector will decrease. However the finite area of the sources keeps the incident power constant. In other words the area of the collector and thus also the cosine effect is disregarded in this direct irradiance model. This is to maintain the focus on reflection losses, etc. For energy yield calculations the cosine effect is easily taken in to account in the simulation software.

Direct irradiance from the following solar angles with corresponding direct solar spectra in the direct irradiance model is listed in Table 3.

Table 3: The solar azimuth angles and the corresponding solar spectra related to the air mass ratio in the direct irradiance model.

Solar zenith angle (°)	Direct spectrum	Solar zenith angle	Direct spectrum
0	AM1	56.3	AM1.8
24.6	AM1.1	60.0	AM2
33.6	AM1.2	65.4	AM2.4
39.7	AM1.3	70.5	AM3
44.4	AM1.4	75.5	AM4
48.2	AM1.5	78.5	AM5
51.3	AM1.6		

For energy production over time, solar source trajectory across the sky needs to be implemented. This is done through TracePro Solar Utility (See own section) and PVsyst, which similarly handles direct irradiance measurements on surfaces (either tilted or horizontal) and does the geometrical calculations needed to describe the solar position on the sky. PVsyst is made for annual energy yield calculations and is therefore limited regarding investigation of instantaneous performance.

3.5.2 Diffuse irradiance models

Depending on the accuracy and simplicity desired, a range of models can be used to describe the diffuse solar radiation. The irradiation is always given at a certain wavelength in this study, i.e. the spectral irradiance must be used because of the wavelength dependent nature of the properties of the solar cell structures investigated in this thesis.

There are two different purposes for a diffuse irradiance model. The first is to be able to predict with accuracy the solar energy irradiant on a given surface, e.g. during a year. This necessitates taking into account the solar trajectory, tilt angle, orientation, atmospheric effects, clearness, cloud cover, local albedo, etc. The second purpose is to replicate the instantaneous diffuse irradiant power to predict the performance of solar panel design. This second purpose is subject to much of our attention as knowledge about solar panel performance under diffuse radiation is limited.

In this section the choice of using the CIE standard (for sky luminance) for modelling diffuse irradiance in this thesis rather than two other widely used models, namely the Perez model and the Liu and Jordan model, is discussed.

3.5.2.1 Simple uniform diffuse radiation model

A simple model as shown in Figure 17 could presumably be accurate enough for some cases. Here, the spectral diffuse irradiance measured at a horizontal surface (see Figure 14) is uniformly distributed across the sky, i.e. uniform sky radiance. The area that covers the sun itself on the sky is excluded, thus also the direct radiation. Any solar spectrum can be distributed in such a way. In this case the spectrum at solar zenith is used.

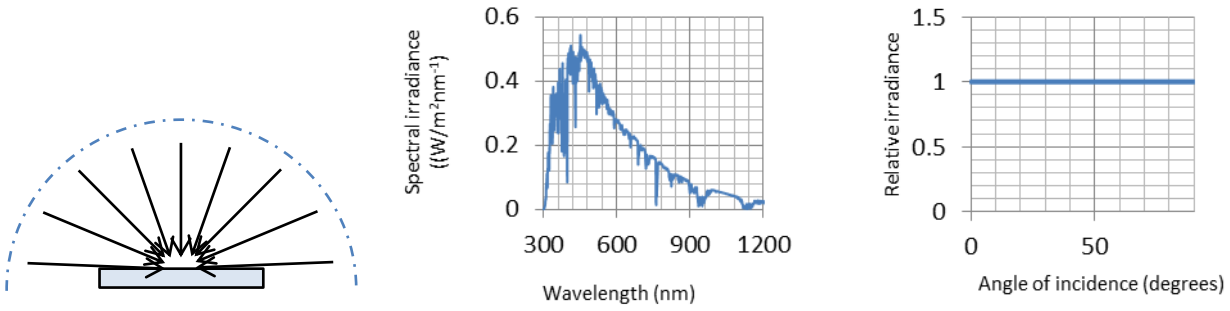

Figure 17: A simple model distributing the diffuse horizontal spectral irradiance (also presented in Figure 14) uniformly across the sky. In this model the inside of a hemisphere can be regarded as a light source with uniform and close to normal radiance.

Using the inside of a hemisphere as a light source makes it possible to replicate the multidirectional nature of diffuse radiation. However, it is important to remember that normal radiance from such a surface would create a focal point at the centre of the sphere, where the modelled solar panel is located. Concentrating the diffuse irradiance in a single point on the panel leads to problems when investigating the effects of textured surfaces and other non-uniform features. Such models should therefore only create near normal rays from the inside of the hemisphere so that the incoming rays on the solar panel will cover a finite suitable area.

This first simple model will not be accurate enough for this study. The performance of photovoltaic cells as a function of the angle of incidence and the wavelength dependent properties of the cell makes it necessary to replicate the diffuse sky radiation in nature as accurately as possible. In reality the diffuse irradiance is not distributed uniformly across the sky but is more intense near the direction of the sun. Also, the direction near the horizontal breaks the uniform radiance pattern.

3.5.2.2 Diffuse radiation models based on CIE sky distribution

This section describes the diffuse sky radiance models based on the CIE standard distribution. First the simplest case is described where the sun is located at zenith and the traditional overcast sky distribution is used. Next, non- zenith solar positions in the sky is taken into account as well as the alternative cloud covers.

The first non-uniform CIE standard for the luminance distribution on an overcast sky where all irradiance is diffuse was suggested in 1942 [31]. The changes of luminance from horizon to zenith in ratio 1:3 were described by the relation:

$$\frac{L_\gamma}{L_Z} = \frac{1+2\sin(\gamma)}{3} = \frac{1+\cos(\theta_Z)}{3} \tag{24}$$

Where:

L_γ is the luminance of a sky element in cd/m^2.
L_Z is the zenith luminance in cd/m^2.
γ is the elevation angle of the sky element above the horizon.

This relation stands as Traditional Overcast Sky Standard in CIE 2002 [34]. So given the zenith luminance the luminance distribution across the sky can be mapped. This equation places the highest light intensity at solar zenith, which might be a good approximation in some locations. The denser the cloud cover, the more justified is the simplification.

Luminance is based on photometry, which takes the perception of the human eye into account. The brightness in terms of luminance therefore is not directly applicable to solar power estimations. However, there are not necessarily critical differences between the sky luminance distribution and the sky radiance distribution, as pointed out by Vartiainen (2000) [35] amongst others. He examined several sky distribution models as well as diffuse radiation models and compared them to measurements.

The performance of the best sky luminance models led to the conclusion that there does not appear to be a significant difference between the sky radiance and the luminance distributions. One should note that the sky distribution is not meant to predict absolute values of irradiance, but only provide a relative distribution. The absolute values are gathered from measurements and derivations from SMARTS2 in this study. Assuming that the CIE traditional overcast sky distribution is representable for instantaneous simulations, the following enhanced model is presented.

This model takes measured diffuse horizontal irradiance (at solar zenith or any desired solar angle or atmosphere) and distributes it across the sky, like the previous model does. But this time the distribution is not uniform, and follows the CIE Traditional Overcast Sky distribution that varies the intensity with zenith angle but not with azimuth angle. In this thesis this model is assumed to be accurate enough to describe the multidirectional nature of diffuse irradiance.

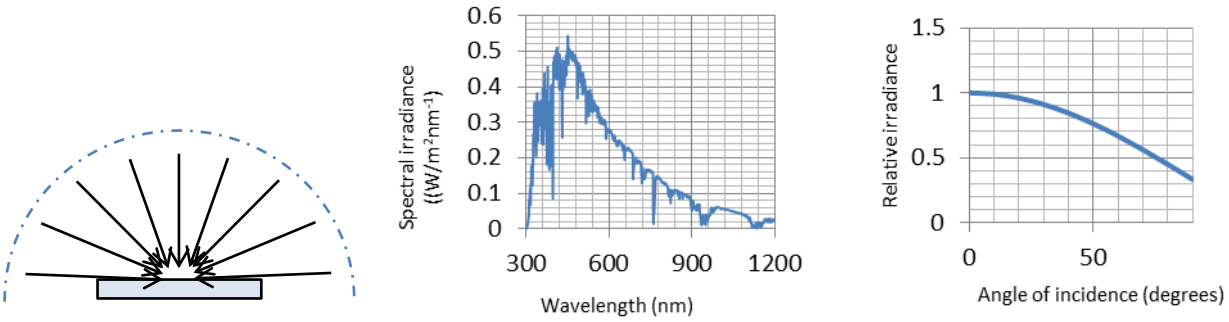

Figure 18: A model distributing the diffuse horizontal spectral irradiance (also presented in Figure 14) across the sky according to the CIE traditional overcast sky distribution where the intensity at any point in the sky follows a 3:1 ratio from solar zenith to the horizon and is azimuthally uniform.

This enhanced model also neglects some effects. Firstly it neglects the special nature of the sky radiance near the horizon where there is substantial multiple Rayleigh scattering and retro-scattering. Secondly it assumes that the spectrum does not depend on the direction, i.e. the diffuse spectrum is constant across the sky, only the integrated magnitude changes. Thirdly Equation (24) for the CIE traditional overcast sky distribution only handles solar zenith, and leads to increased irradiance from the horizon at the opposite direction if the equation is shifted to distribute in relation to another point in the sky than solar zenith, because of the trigonometric nature of the equation. This third simplification can be avoided if desirable as follows.

Adapting this distribution for cases when the sun is located elsewhere in the sky is also described in the CIE standard [34]. The distribution can also be adapted to a number of cloud conditions in addition to the traditional overcast sky by using chosen coefficients as follows.

The ratio of the luminance of an arbitrary sky element to the zenith luminance for any sun position and any cloud cover is given by:

$$\frac{L_a}{L_Z} = \frac{f(\chi)\varphi(\theta_Z)}{f(Z_S)\varphi(0)} \tag{25}$$

Where:

L_a is the luminance of an arbitrary sky element.

f is the scattering indicatrix.

χ is the angular distance between the sky element and the sun.

φ is the luminance gradation function.

Z_s is the zenith angle of the sun.

The luminance gradation function relates the relative luminance to the zenith angle as is given by:

$$\varphi(\theta_Z) = 1 + a \cdot e^{\left(\frac{b}{\cos(\theta_Z)}\right)} \tag{26}$$

Where:

a and b are luminance gradation parameters.

At the horizon, the luminance gradation function equals 1.
The scattering indicatrix relates the luminance to the angular difference between the arbitrary sky element and the sun and is given by:

$$f(\chi) = 1 + c(e^{d\chi} - e^{\left(d\frac{\pi}{2}\right)}) + \mathrm{e} \cdot \cos^2(\chi) \tag{27}$$

Where:

c, d and e are scattering indicatrix parameters.

Beware of the difference between the parameter e and Euler's number in Eq. (27). The angular distance between the sun and the sky element is given as follows:

$$\chi = \arccos\left(\cos(Z_S)\cos(\theta_Z) + \sin(Z_S)\sin(\theta_Z)\cos\left|\alpha_a - \alpha_{a,S}\right|\right) \tag{28}$$

Where:

α_a is azimuth angle of the sky element.

$\alpha_{a,s}$ is the solar azimuth angle.

The parameters for the luminance gradation function and the scattering indicatrix are tabulated in the CIE standard. The parameters are listed in Table 4:

Table 4: The luminance gradation function parameters, and the scattering indicatrix parameters for sky conditions in the CIE standard. The 3 distributions used for diffuse irradiance in this study, namely clear, partly cloudy and overcast, are highlighted in bold letters. These parameters as well as the angles defining the sun position in the sky determines the diffuse sky radiance distribution.

Type	Gradation group	Indicatrix group	a	b	c	d	e	Description of luminance distribution
1	I	1	4.0	-0.7	0	-0.7	0	CIE Standard Overcast sky, Steep luminance gradation towards zenith, azimuthal uniformity
2	I	2	4.0	-0.7	2	-1.5	0.15	**Overcast, with steep luminance gradation and slight brightening towards the sun**
3	II	1	1.1	-0.8	0	-1.0	0	Overcast, moderately graded with azimuthal uniformity
4	II	2	0	-0.8	2	-1.5	0.15	Overcast, moderately graded and slight brightening towards the sun
5	III	1	0	-0.8	0	-1.0	0	Sky of uniform luminance
6	III	2	0	-1.0	2	-1.5	0.15	Partly cloudy sky, no gradation towards zenith, slight brightening towards the sun
7	III	3	0	-1.0	5	-2.5	0.30	**Partly cloudy sky, no gradation towards zenith, brighter circumsolar region**
8	III	4	-1.0	-1.0	10	-3.0	0.45	Partly cloudy sky, no gradation towards zenith, distinct solar corona
9	IV	2	-1.0	-0.55	2	-1.5	0.15	Partly cloudy, with the obscured sun
10	IV	3	-1.0	-0.55	5	-2.5	0.30	Partly cloudy, with brighter circumsolar region
11	IV	4	-1.0	-0.55	10	-3.0	0.45	White-blue sky with distinct solar corona
12	V	4	-1.0	-0.32	10	-3.0	0.45	**CIE Standard Clear Sky, low luminance turbidity**
13	V	5	-1.0	-0.32	16	-3.0	0.30	CIE Standard Clear Sky, polluted atmosphere
14	VI	5	-1.0	-0.15	16	-3.0	0.30	Cloudless turbid sky with broad solar corona
15	VI	6	-1.0	-0.15	24	-2.8	0.15	White-blue turbid sky with broad solar corona

The luminance distributions **CIE Standard clear sky**, **Partly cloudy sky** and **Overcast sky** are used in the 3 diffuse irradiance models in this study. The variable angles used as inputs equations 1-5 can be visualized in Figure 19.

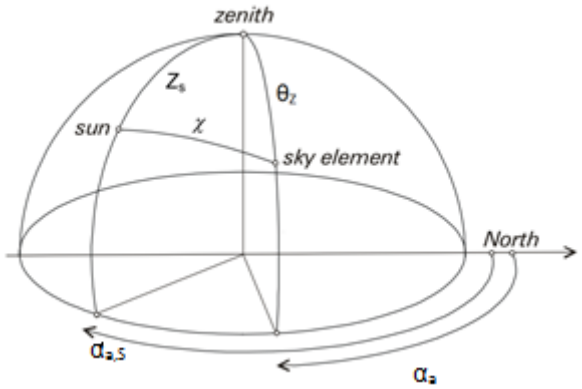

Figure 19: The angles defining the position of the sun and an arbitrary sky element as given in the CIE standard. The distribution of diffuse radiance across the sky is given by these parameters [34]**.**

In this study primarily outputs from SMARTS2 are used as source for absolute irradiation for, thus the sky distributions are only relative distributions. Combining these should make realistic representation of the nature of diffuse irradiance.

How the different sky radiance distributions look like when modelled in the ray tracing software is shown in Figure 20, in the form of polar iso-candela plots as screenshots where the irradiation in watts per steradian is a function of the polar angle and the azimuth angle. The three types of distribution are shown, namely clear sky, partly cloudy sky and overcast sky. Each type is shown at AM1 (solar zenith) and AM1.5 (solar zenith angle of 48.2°). In this thesis AM1, AM1.5, AM2 and AM5 are used for simulations for each sky type that include diffuse radiation.

The same integrated irradiance flux of 1000 W is used for all three cases in the next figure, chosen because of the convenient and often used value. However, the reader should focus on the relative values, not the absolute values, because the point here is to show how a given amount of irradiance is distributed across the sky. In the simulations the absorbed flux in the solar relative to the irradiant flux is investigated.

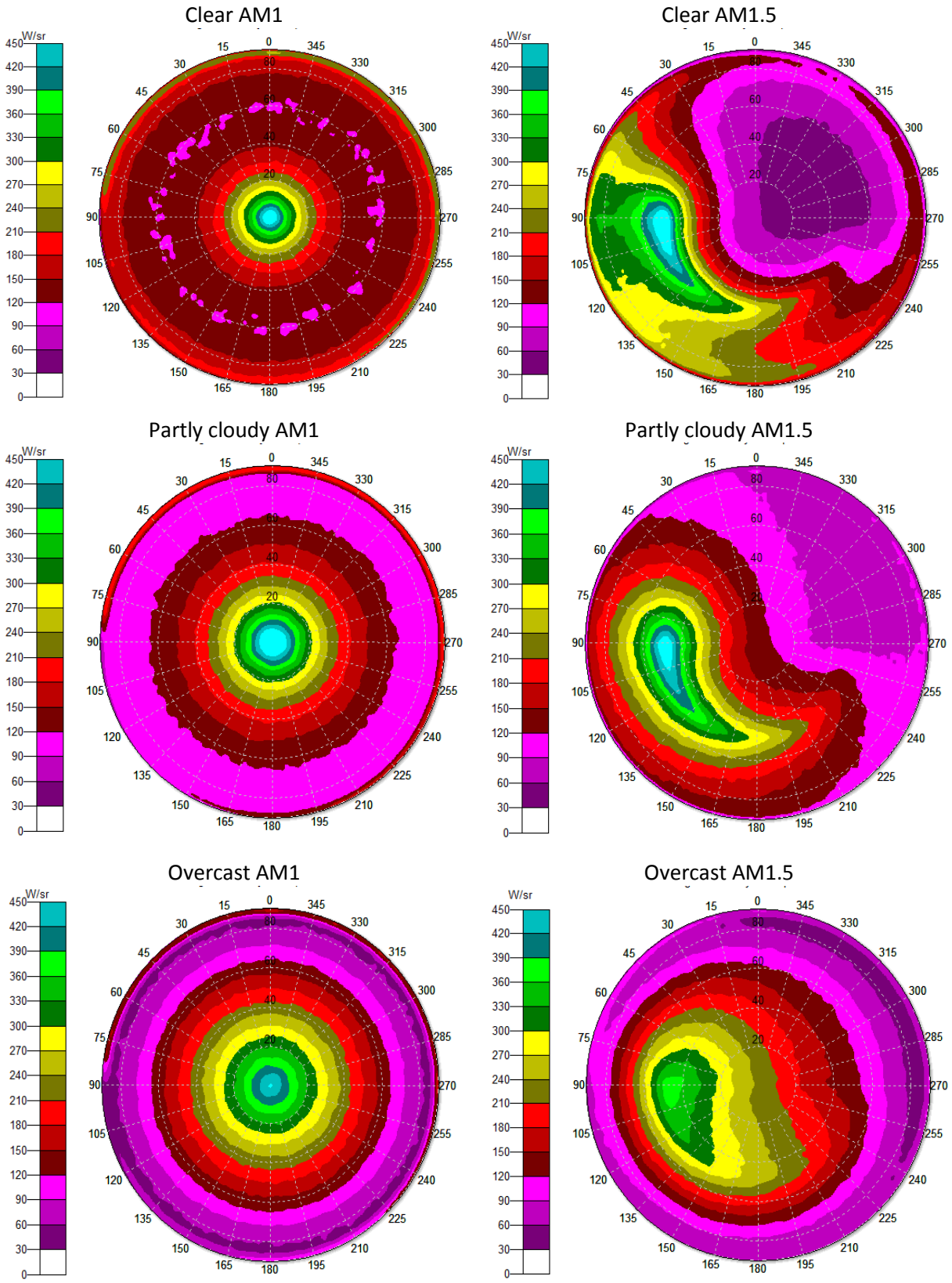

Figure 20: Generated candela plots showing the irradiance from three diffuse sky radiance models used in this thesis for two solar zenith angles each, namely AM1 (0° solar zenith angle) and AM1.5 (48.2° solar zenith angle). Each model also has AM2 and AM5. The irradiance in watts per steradian is shown as a function of solar azimuth angle (0° to 360°) and solar zenith angle (0° to 90°). The total integrated irradiance flux in each case is 1000 W for convenience. However, only the relative values to the incident flux are of importance.

The diffuse solar spectrum chosen to be distributed across the sky should correspond to the solar angle above the horizon. If a solar zenith angle of 60 degrees is used in the model, the diffuse solar spectrum to be distributed must be AM2. Ideally, the actual solar spectrum for the chosen cloud cover should also be used. A limitation to using the SMARTS2 program as source for solar spectra is the restriction to clear sky conditions (see section 3.6). Therefore, as mentioned earlier, measured data was necessary for obtaining spectra for partly cloudy and overcast sky conditions.

3.5.2.3 Jordan and Liu correlation as diffuse irradiance model in PVsyst

PVsyst uses a "robust" version of the Liu and Jordan correlation [36], which results from an experimental correlation of the D/G ratio (diffuse component divided by global component) by respect to the clearness index, K_t:

$$K_t = \frac{H}{H_0} \tag{29}$$

Where:

H is the daily insolation received on a horizontal surface.

H_0 is the extra-terrestrial daily insolation on a horizontal surface.

This model describes a relation between the clearness index and the D/G ratio so that the diffuse insolation can be found given the global insolation from measurements for a location is available. This relation for horizontal surfaces is described in graphs in Jordan and Liu (1960) [37] and built into the PVsyst software.

The model builds on the assumption that the calculated relations between the clearness index and the share of diffuse insolation hold for other locations than where the study was conducted and also that the effects from cloud cover outweighs the effects from other atmospheric compounds. The strength of the model is the simplicity in the need for only one input, namely the total global insolation, at a certain location and time. Hourly measurements were used as basis for the study. The model distributes the diffuse radiance evenly across the sky and is therefore a uniform diffuse sky radiance model [38].

Noorian et al. (2008) evaluated a number of models to estimate diffuse irradiation on inclined surfaces. On a south-facing surface the Liu and Jordan correlation performed with a Root Mean Square Error (RMSE) of 13.4% referred to global irradiance. A more sophisticated model, the Perez model, which performed with a RMSE of 11.17%, was tested for use in PVsyst 5.6, but the increased complexity did not return significantly better results for the program, according to the co-author of the Perez model, and also a worker at the laboratory in which PVsyst was developed, P. Ineichen [36].

3.5.2.4 Perez model

The original Perez diffuse model has been used worldwide to estimate short time step, i.e. hourly or less, irradiance on tilted surfaces based on global and direct irradiance measured at horizontal surfaces, though originally developed to handle instantaneous events [33]. It is an anisotropic diffuse sky radiation model with several parameters to adapt the model for a range of cloud conditions.

The model is based on the following anisotropic pattern. The main sky is isotropic, while a circumsolar cone and a horizon zone superimposed over the isotropic background breaks the pattern and describes areas where the background radiance will be multiplied with a factor. These two zones were made to account for the two most consistent anisotropic effects in the atmosphere, namely forward scattering by aerosols and multiple Rayleigh scattering and retro-scattering near the horizon. Thus there are three zones defining the sky radiance distribution. The parameterization of insolation conditions determines the value of the radiant power originating from the two deviating zones.

The Perez model has been revised several times, been simplified and improved in terms of accuracy [33]. However the mentioned key assumptions defining the model remain basically unchanged. The half-angle of the circumsolar cone is adjusted and the horizontal band is defined as infinitely thin at zero degrees elevation above the horizon. Some of the equations in the model were changed for convenience and Perez et al. have step by step shown how each change rendered the model either more accurate than before, or more simplified. Thus only revised Perez diffuse sky radiance models would be desirable for this study.

Revised Perez models have proven to outperform other diffuse models in terms of accuracy. Noorian et al. concludes that in general, the Perez et al. model shows the best agreement with the measured tilted data in their study. However, the required sheer numbers of parameters needed make this model more time-consuming than the previously reviewed CIE distribution models. Therefore the Perez model was not implemented in this thesis. As mentioned the developers of PVsyst did not find the original Perez model significantly more accurate than the much simpler Liu and Jordan relation. It is supposedly especially suited for very well-measured data. They claim that applying it to synthetic hourly data does not make great sense as opposed to using simpler models.

3.6 SMARTS2

3.6.1 Configuration

Simple Model of the Atmospheric Radiative Transfer of Sunshine (SMARTS) is a spectral model and FORTRAN code developed by Christian A. Gueymard at Solar Consulting Services (USA). It is made to predict the direct beam, diffuse and global irradiance incident on surfaces of any geometry at the Earth's surface. Solar irradiance is calculated from spectral transmittance functions for the main extinction processes in the cloudless atmosphere. These include Rayleigh scattering, aerosol extinction, and absorption by ozone, uniformly mixed gases, water vapour and nitrogen dioxide.

Temperature dependent or pressure dependent extinction coefficients have been developed for these absorbing gases. These are based on recent spectroscopic data obtained either directly from

experimental literature or from MODTRAN2, referred to by Gueymard as a state-of-the-art rigorous code. Version 2.0 of the program was released in 1994, and is described by Gueymard in 1995 [39]. The releases 2.9.2 and 2.9.5 are used as tools in this study.

The program covers solar spectra with wavelengths from 280 to 4000 nm. A range of different sources for the extra-terrestrial solar spectrum is available, together with its corresponding solar constant. A modifiable file for user-defined spectrum is also available. SMARTS2 has a default extra-terrestrial spectrum that is in good general agreement with the ASTM E-490 extra-terrestrial AM0 standard spectrum, although the E490 spectrum has different spectral interval centres and resolution.

Spectroradiometric data measured at Florida Solar Energy Center (FSEC) and National Renewable Energy Laboratory (NREL) were compared with SMARTS2 model results as well by Myers et al. (2002) [24]. For both direct normal and global tilted irradiance the predictions were largely within the instrumental uncertainty, usually in the order of 5% over a spectral range of 400 – 1100 nm. The solar constants are slightly larger than the integrated irradiance over the given spectra because they include contributions from wavelengths outside of the selected range.

The direct radiation is modelled in the following way. The beam irradiance $E_{bn\lambda}$ received at sea level by a surface normal to the sun's rays at wavelength λ is given by:

$$E_{bn\lambda} = E_{on\lambda} T_{R\lambda} T_{o\lambda} T_{n\lambda} T_{g\lambda} T_{w\lambda} T_{a\lambda} \tag{30}$$

Where:

$E_{on\lambda}$ is the extra-terrestrial irradiance.

T_λ is the wavelength dependent transmittance where the subscript R is for Rayleigh scattering, o is absorption by ozone, n is absorption by nitrogen dioxide, g is for absorption by uniformly mixed gases, w is for absorption by water vapour and a is for aerosol extinction. Each of the transmittances is calculated separately.

As in simplified models like SPECTRAL the diffuse radiation in SMARTS2 is obtained based on the assumption that photons not directly transmitted are scattered in all directions and a roughly predictable fraction of these is directed downwards and constitutes the diffuse irradiance at ground level. The diffuse irradiance $E_{d\lambda}$ is considered as the sum of three components: due to Rayleigh scattering, aerosol scattering and ground/sky backscattering. The first two components are corrected to take into account the multiple scattering effects.

$$E_{d\lambda} = E_{dR\lambda} + E_{da\lambda} + E_{db\lambda} \tag{31}$$

Where:

$E_{dR\lambda}$ is the component from Rayleigh scattering.

$E_{da\lambda}$ is the component from aerosol scattering.

$E_{d\lambda}$ is the component from ground/sky backscattering.

SMARTS2 will thus calculate the global irradiance on a horizontal surface E_λ as:

$$E_\lambda = E_{bn\lambda} \cos(\theta_z) + E_{d\lambda} \tag{32}$$

3.6.2 Example of outputs

A demonstration of outputs produced by SMARTS2 is given here, using the same inputs as in ASTM G159-99 described in the Global Radiation section, as well as:

- An atmospheric carbon dioxide content of 370 ppm
- Rural Shettle & Fenn aerosol model
- A solar constant of 1367 W/m^2
- AM1.5 solar spectrum

Figure 21 shows a comparison between global, direct and diffuse irradiance on a horizontal surface.

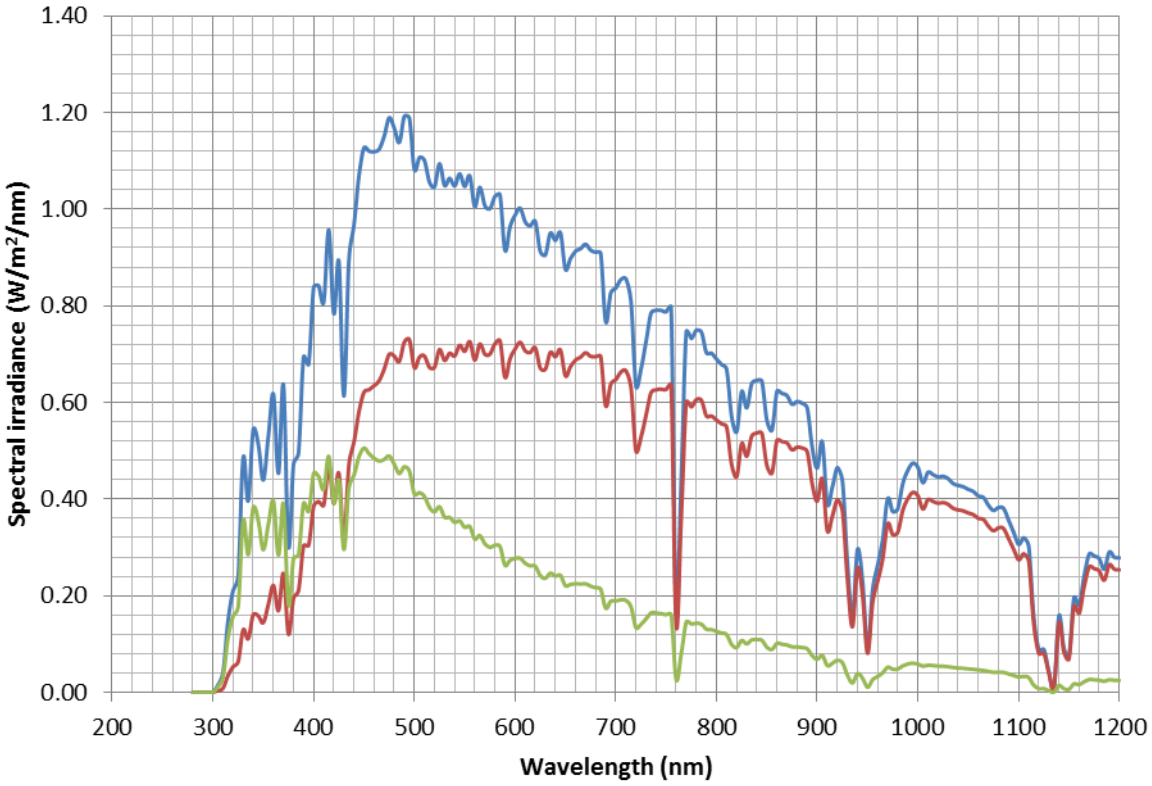

Figure 21: Comparison of global (red), direct (blue) and diffuse (green) spectral irradiance on a horizontal surface as calculated in SMARTS2 with the standard atmospheric condition described in ASTM G-159-99 at AM1.5.

Figure 22 shows spectral transmittances, defined as the fraction of light at a certain wavelength that passes through the atmosphere, for Rayleigh scattering, ozone totals, trace gases, water vapour, mixed gases and aerosol totals. Unity represents total transmission at that wavelength.

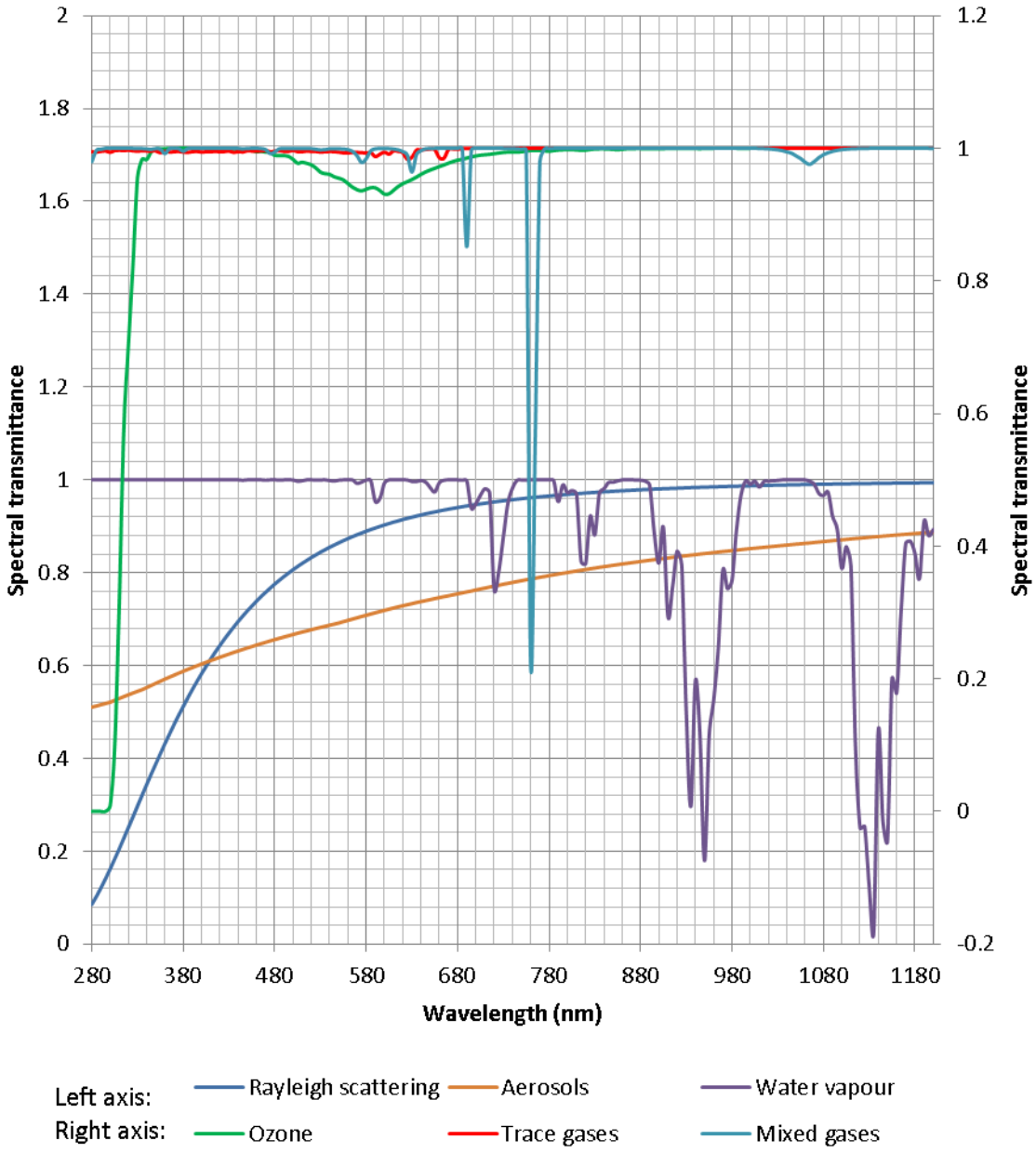

Figure 22: Spectral transmittances for atmospheric compounds as calculated in SMARTS2.

3.6.3 Conclusion

It has been shown that SMARTS2 is a powerful tool embraced by several groups that can calculate useful solar spectra on given a number of input conditions.

An important limitation for this study is the exclusion of overcast sky conditions in SMARTS2. The diffuse radiations are calculated under clear sky conditions. In locations where the diffuse portion of the incident sunlight can be large, e.g. 60%, because of cloud cover. Additional computer models are utilized in this study to achieve desired results, as described under sky radiation models (particularly direct model and diffuse model based on CIE sky distribution).

3.7 TracePro Solar Emulator

TracePro Solar Emulator (TPS) is an automated tool for performing simulations for a specified time and location and calculating incident sunlight. It is a utility in TracePro 7.3, a ray tracing software suited for optics, etc., developed by Lambda Research Corporation.

The sun's trajectory across the sky and the irradiance from it is calculated in TPS. The location is specified in longitude and latitude. The time interval for any simulation is specified in date and time of day from start to end. Figure 23 shows a screenshot of the graphical representation as is given in the Solar Emulator.

The light source in the utility is divided into two options, namely the solar model and the sky model. The Solar model defines the direct radiation while the sky model defines the diffuse light from the sky in photometric units, i.e. illuminance. The direct light can be a predefined solar source in TracePro or a user-defined surface source where the radiance as a function of temperature, wavelength, polar angle and azimuth angle can be specified.

The modelled sun is at a distance from the receiver model specified in the utility by the user. Hence the total incident flux will be determined by a combination of the sun distance, the angular distribution in the source property and the solar constant.

The solar constant specifies the total amount of irradiance from the solar source in watts per square meter. This value can be constant, or modified with Earth Radius Vector (ERV) which is the ratio to the average earth-sun radius, a correction factor for the distance between the earth and the sun.

For simulations the wavelengths for the simulations must be given. For accurate analyses the whole relevant solar spectrum and resolution is specified. The number of rays to be traced is also specified. TracePro is built on the Monte-Carlo simulation method so the accuracy of the ray trace simulation depends on the quantity of rays that are traced.

The results from the simulations are for example irradiance map, candela plots, flux reports, etc. These results can be plotted as a function of time and the annual energy production for different photovoltaic panel designs can be investigated. The option of investigating in detail the irradiance, transmission, reflection, absorption, etc, in detail is a useful feature for this thesis and the reason why it is utilized.

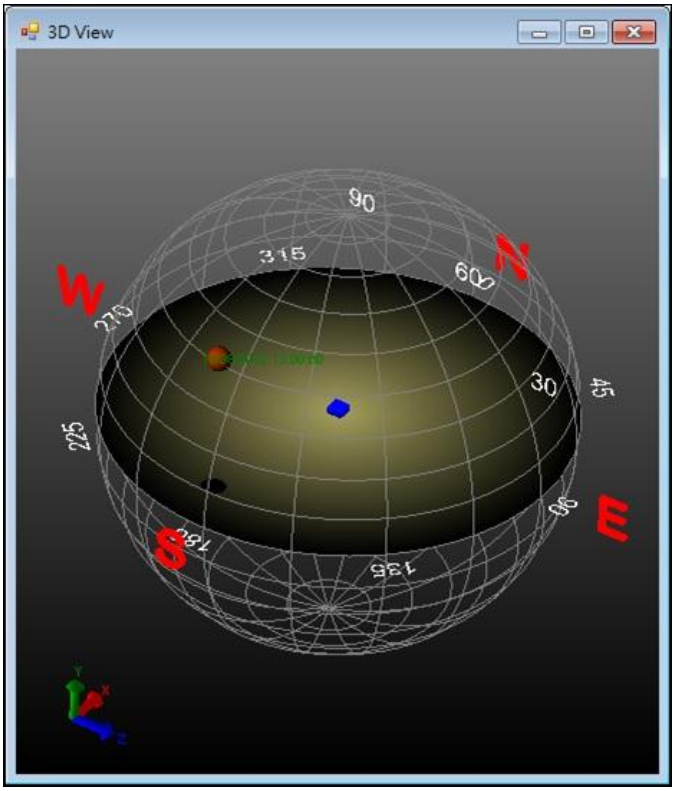

Figure 23: A graphical representation (screenshot) from TracePro Solar Emulator. The solar light source's position and trajectory is given by a solar angle and an azimuth angle. These are decided by time and location of the receiver surface.

The most important limitations for TracePro Solar Utility are as follows. There is lack of dependency on the solar position in the sky of the irradiance. Only the cosine-effect is taken into account. The solar intensity and spectrum remains constant throughout the solar trajectory across the sky. Thus, the solar spectrum is unaffected by atmospheric effects. There is a sky model available in the utility, but it is built on photometric values and does not take the diffuse solar spectrum into account.

3.8 Conclusion

For performance investigations for photovoltaic panels, one direct irradiance model and three diffuse irradiance models will be used separately. At each ray tracing simulation the absorbed flux (W) in the cell as a fraction of the emitted light that enters the top glass cover is obtained as the light transmission factor. The same flux is emitted in each simulation for convenience, however, only the relative figures are important in the optical models. The incident light is modelled in such a way that the whole glass cover front surface is uniformly irradiated.

The direct radiation model implements output direct solar radiation spectra from SMARTS2 into geometrical orientations for a series of ray trace simulations, each with an angle of incidence and corresponding spectrum, ranging from 0 to 85 degrees as given in Figure 16.

The diffuse radiation models used will be measured spectra or output diffuse spectral irradiance distributed across the sky, represented by a hemisphere, according to the CIE standard for luminance. 4 solar zenith angles, with corresponding sky radiance distributions, are used for each diffuse radiation models:

- 0° (AM1)
- 48.2° (AM1.5)
- 60.0° (AM2)
- 78.5° (AM5)

The spectra and parameters for the CIE distributions for the diffuse irradiance models are given in Table 5.

Table 5: Parameters for the CIE diffuse sky radiance distributions used for each diffuse irradiance model in this study.

Diffuse irradiance model	Spectrum	Parameters for Equation (25)				
		a	b	c	d	E
Clear sky	Varies with solar zenith angle	-1.0	-0.32	10	-3.0	0.45
Partly cloudy sky	Constant	0	-1.0	5	-2.5	0.3
Overcast sky	Constant	4.0	-0.7	2	-1.5	0.15

Simulations are done with clear sky diffuse spectral irradiance and overcast sky diffuse spectral irradiance. The solar spectra that correspond to any given solar angle, or solar position, will be used. Hence the atmospheric effects on the solar irradiance will be taken into account in any case.

When investigating how the annual energy production is affected for different solutions TracePro Solar Utility and PVsyst are used. PVsyst takes diffuse irradiance into account, with the use of the Liu and Jordan relation. TracePro Solar Utility offers more freedom to manipulate the nature of the incident direct light, but does not take diffuse irradiance into account

4 Optical modelling of photovoltaic panels and solar cell

In this chapter optical modelling of a standard solar panel is explained. In this optical model objects with specific optical properties (e.g. refractive indexes and absorption coefficients) are assembled to replicate a real solar panel. Advanced ray tracing simulations are then used to investigate the light propagation in the panel.

How light interacts with the optical model is wavelength dependent. Light from the sun contains a wide spectrum and when it strikes a material the material has a tendency, depending on its optical properties, to selectively absorb, reflect or transmit light depending.

Reflected and transmitted light is distinguished by having specular and diffuse components. For specular surfaces, such as glass or polished metal the reflection and transmission will primarily follow one direction. Specular distribution can be calculated by applying Snell's law and Fresnel's equations. For diffuse surfaces, such as matte white the reflection and transmission is scattered multidirectionally. For an ideal diffuse surface light is distributed to all directions, where the light intensity follows a cosine dependency between the scatter angle and the surface normal. Such surfaces are said to be Lambertian. Most real materials show a mixture of both diffuse and specular properties.

The amount of light absorbed, follows the Beer-Lambert law. The law states, that there is a logarithmic dependence in between absorption and transmission of light through a material and absorption in the material

This chapter will cover how the different layers in a solar panel affect light propagation. A solar panel consists of many different materials which serve different needs. In this chapter each material is discussed and presented with its associated optical properties.

- In section 4.1 the different materials that make up the layers surrounding the solar cell are discussed. The goal of this thesis has been to model a standard solar panel with materials and features found in commercial products available today.
- In section 4.2 optical modelling of a c-Si solar cell is discussed. A solar cell is a highly advanced and complex object; subsequently the majority of this chapter is dedicated to producing a representative model.

4.1 Optical structure of classical photovoltaic panel

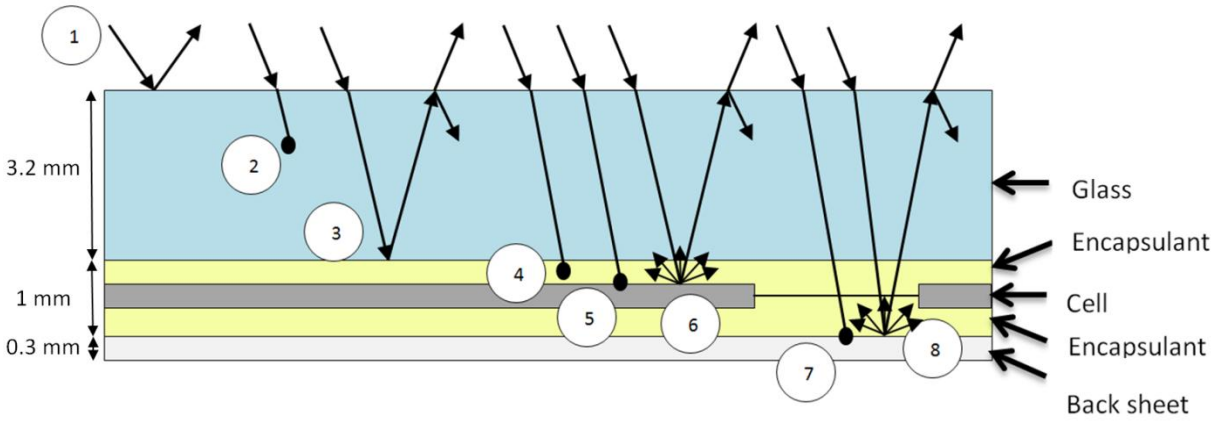

Figure 24: A cross section of a solar panel showing 8 different cases of light propagation. This diagram is reproduced from a paper by McIntosh et al. (2009) [40].

A basic schematic of light propagation through a solar panel is shown in Figure 24. As illustrated an accurate optical assessment is not straightforward. Multiple layers with their own optical properties affect the incoming light differently. How light interacts with a solar panel depends on the wavelength and angle of incidence. In general one distinguishes between absorption, transmission and reflection. To better understand the light propagation in a solar panel, 8 different cases of incoming light are explained in the following points.

1. Rays are reflected, with no transmission.
2. Rays are transmitted at the air-glass intersection and absorbed within the glass layer.
3. Rays are transmitted through the glass layer and reflected at the encapsulant-glass intersection. At the glass-air intersection the rays are both internally reflected and transmitted into the air.
4. Rays are absorbed in the encapsulant layer.
5. The ideal situation is shown; the rays are entirely absorbed in the solar cell.
6. Rays are reflected at the encapsulant-cell intersection.
7. Rays are absorbed in the back sheet.
8. Rays are reflected at the encapsulant-back sheet intersection. Reflection at (6) and (8) is often distinguished by being diffuse.

In the following section of this chapter each layer in the solar panel will be discussed. It is structured in the same manner as light propagates through the panel; starting with the glass and ending with the back sheet.

4.1.1 Optical properties of glass

The key purpose of a glass cover is to protect the solar cells. Solar cells are thin and thus vulnerable to mechanical damage. In addition metal contacts must be protected from rain which can cause corrosion. For most PV applications, soda-lime silica glass made by the 'float' process is the material of choice. For most commercial standard PV modules the thickness varies between 3-6 mm. In this thesis a standard thickness of 3.2 mm is used in the simulations.

4.1.1.1 Glass varieties

Glass manufacturers produce four nominally standardized varieties of glass: clear, grey, bronze and green. Glass is well suited for a variety of functions. Contrary to solar modules some applications require low transmission of light. Grey, bronze and green glasses contain absorbers to reduce the transmittance. The different colours of glass represent different additives introduced in the material composition. Clear glass also called standard glass contains no additives other than those meant to affect the manufacturing process. For PV applications glass containing less iron than standard glass is used. In Figure 25 different absorption coefficients for the above mentioned glasses as a function of wavelength are shown. Low-iron glass has the lowest absorption coefficient over the entire wavelength region and will demonstrate the lowest absorption losses.

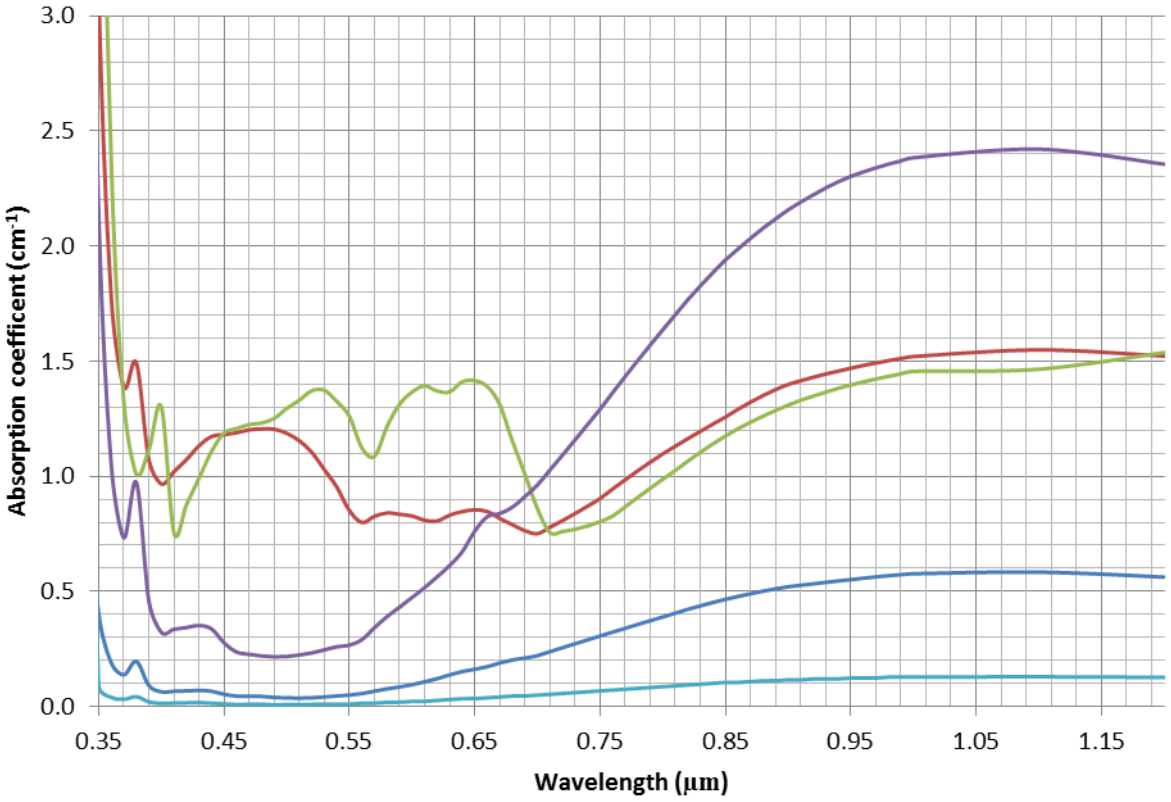

Figure 25: Absorption coefficient for different types of glass as a function of wavelength [41]. The purple line shows a type Green glass. The red line shows a type Bronze glass. The green line shows a type Grey glass. The dark blue line shows a type Clear glass. The light blue line shows a type Low-iron glass.

4.1.1.2 Low iron glass

Transmission varies as a function of wavelength of the incident light. For glass, the transmission depends highly on the amount of iron oxides in the material. Hence in production of low-iron glass some special considerations must be made. Low-iron glasses require raw materials with as little iron content as possible. E.g. low iron sand. Also different iron oxides absorb light in different wavelengths. Ferric oxide absorbs mostly in the ultraviolet region and ferrous oxide absorbs mostly in the high visible and lower infrared region [42]. A reduction in ferric oxide can be achieved through the conversion of ferrous oxide to the higher oxidation state ferric oxide [41][43]. Additionally, iron contamination sources in the whole production process must be given careful attention. Typical content of ferrous in commercial low iron glass is between 100 and 200 ppm [44].

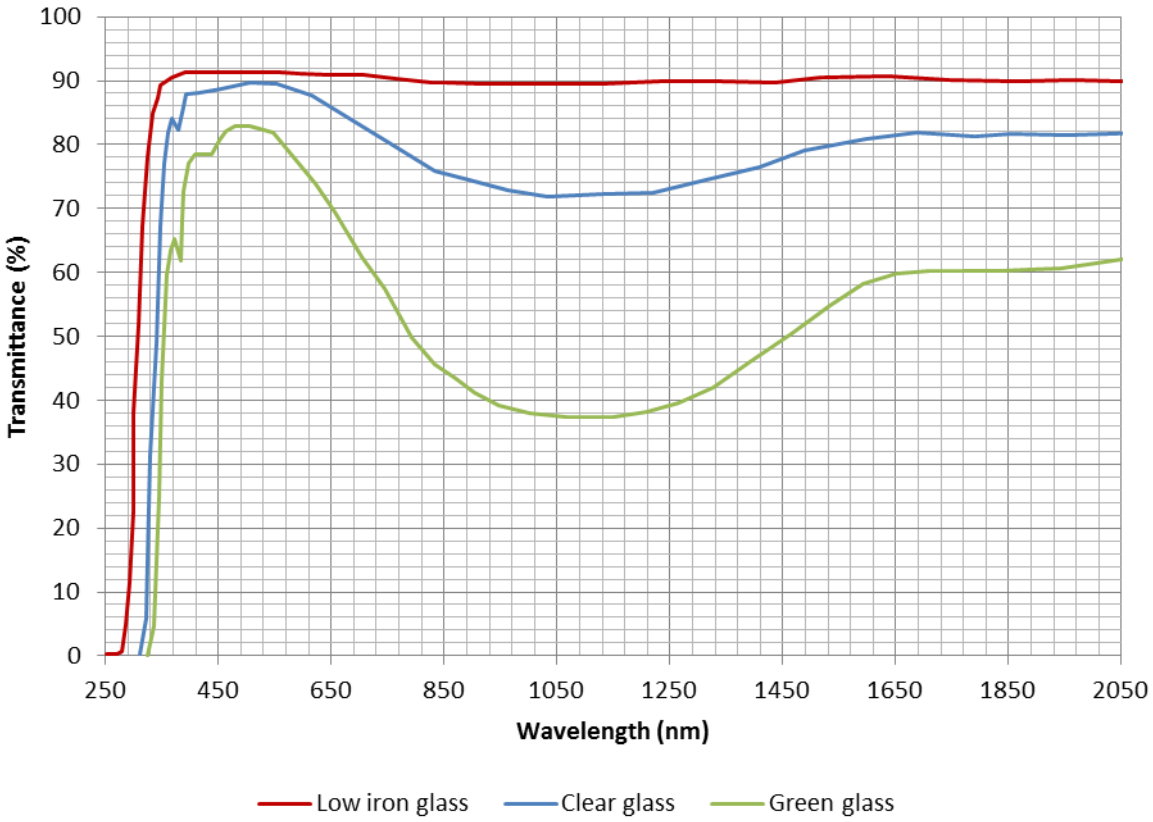

Figure 26: Spectral transmittance for 4mm thick float glass with three different concentrations of ferrous oxide [44]**. The red line represents a glass with low iron content (Fe_2O_3 $100 - 200$ ppm). The blue line represents a standard clear glass (Fe_2O_3 $800 - 1000$ ppm). And the green line represents a glass with high iron content ($Fe_2O_3 app.$ 5000 ppm).**

In Figure 26 the wavelength dependent transmittance of 3 glasses with different iron content is shown. The blue line represents the spectral transmittance of 4 mm thick standard float glass, the red line represents a glass with low iron content and the green line represents a glass with high iron content. As the figure illustrates high iron content produces unfavourable optical properties.

Many factors determine the optical properties of glass. In addition products carrying the same type name may have different properties. This discrepancy is taken into account here. For illustration and discussion three low-iron soda-lime type glasses have been evaluated.

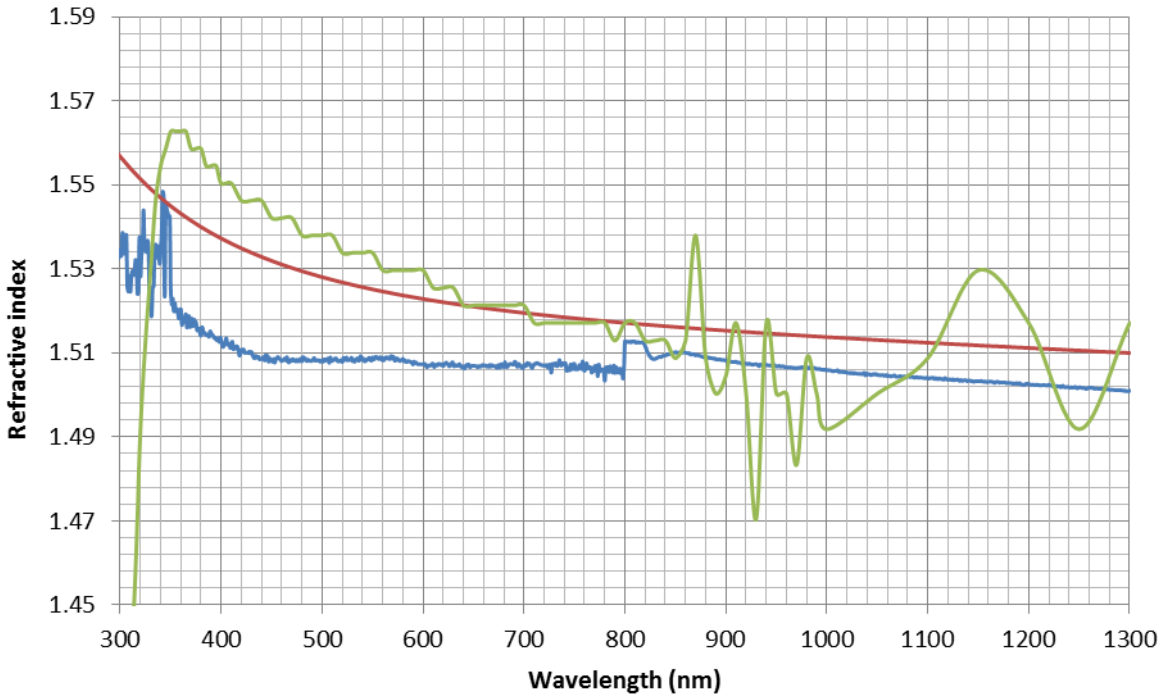

Figure 27: Refractive index for three low-iron soda-lime glasses as a function of wavelength. The blue line represents a Pilkington glass. The red line represents data from Rubin [41]**. And the green line represents a PPG Starphire glass. Optical properties for all three glasses are published in OPAL** [45]**.**

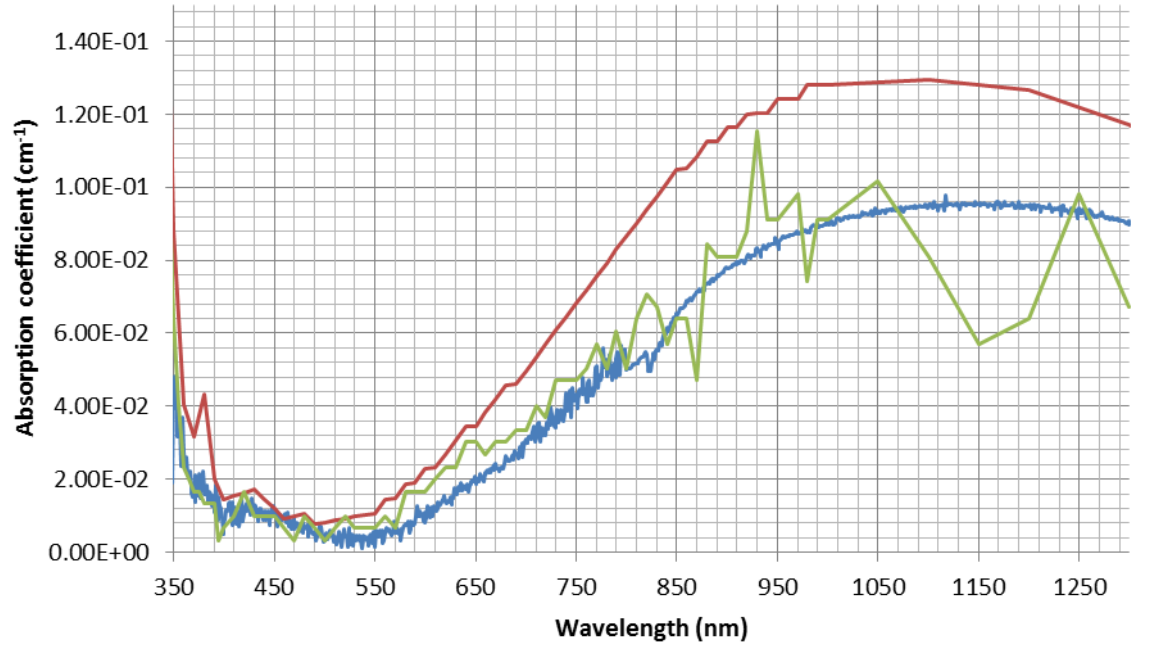

Figure 28: Absorption coefficient for three low-iron soda-lime glasses as a function of wavelength. The blue line represents a Pilkington glass. The red line represents data from Rubin [41]**. And the green line represents a PPG Starphire glass. Optical properties for all three glasses are published in OPAL** [45]**.**

The significance of the different optical properties shown in Figure 27 and Figure 28 require further investigation. Using the ray tracing program OPAL, the effects of the different optical properties can be calculated. A test is performed with the following arrangement: A flat surface glass of thickness

3.2 mm covers a c-Si solar cell (the solar cell's optical properties are presented in section 4.2.2.1). The incident irradiance spectrum is AM1.5 Global and the angle of incidence is normal to the surface.

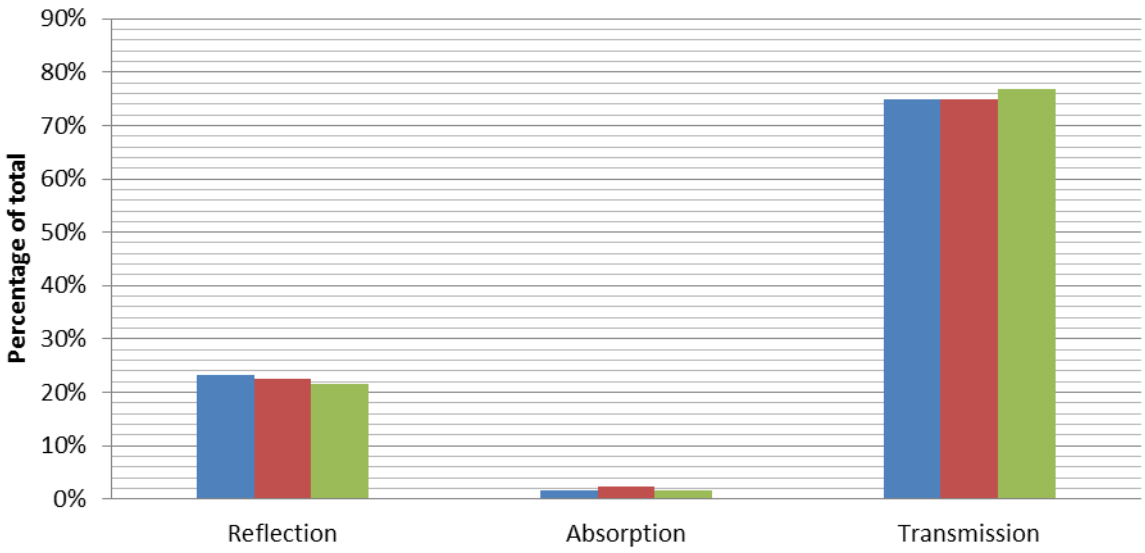

Figure 29: Total reflection, absorption and transmission measurements over the relevant wavelength spectrum. The results are obtained from optical simulation performed on three low-iron soda-lime glasses, the simulation is done in OPAL. The blue columns show results for a Pilkington glass. The red columns show results for optical data from Rubin and the green columns show results for a PPG Starphire glass. Optical properties for all three glasses are published in OPAL[41][45]**.**

PPG Starphire represented by the green columns has the best optical properties according to results in Figure 29. Of special interest is the difference between Rubin (red) and Pilkington (blue). Compared with the glass from Pilkington, Rubin's has higher absorption and lower reflection losses. By applying a textured surface the reflection losses would decrease for both glasses. But the increase in ray path length due to ray's bouncing in the glass would increase absorption losses. Therefore Pilkington would outperform Rubin due to its lower absorption coefficient. However the results are in general not far apart and are most likely within the measurements uncertainty tolerances.

In conclusion glass is a good surface cover for solar applications because of its suitable optical properties and long lifetime. Highest transmission is achieved with low-iron glass. However there are many types of low-iron glass, all with different optical properties. Despite the dissimilarity into optical properties the end results are fairly similar at normal irradiance. For the subsequent calculations and simulations in this thesis Rubin's data for optical properties as shown in Figure 27 and Figure 28 will be used [41].

4.1.2 Encapsulant

The purpose of the encapsulant is to protect the c-Si cells and provide adhesion between the solar cells, the glass and the back sheet. It must provide structural support during handling, storage, transportation, installation, and operation in the (weathering) terrestrial environment. The encapsulant must also achieve and maintain good optical coupling with the surrounding layers in the solar panel. Furthermore the encapsulant must provide electrical isolation for the solar cell circuit elements to meet operational and safety requirements. Because of its low cost and suitable properties *ethylene vinyl acetate* (EVA) is the industry standard encapsulant material today [46]. The typical thickness of one sheet of EVA is 0.45 µm [16][40].

Silicone is another, but more expensive material used as encapsulant. McIntosh et al. (2010) compared optical properties of silicone and EVA encapsulant. Their study showed that silicone can increase the relative efficiency of a c-Si solar cell by 0.5-1.5% [47][40].

Figure 30 shows the wavelength dependent refractive index of both silicone and EVA. The encapsulant, situated between the glass and the solar cell, should ideally have a refractive index that follows the geometrical mean of the adherent layers. Typical refractive index values for low iron glass and silicon are respectively 1.5 and 4. Calculation shows the geometrical mean to be 2.44. Of the two encapsulant materials shown in Figure 30, silicone will have the lowest reflection losses.

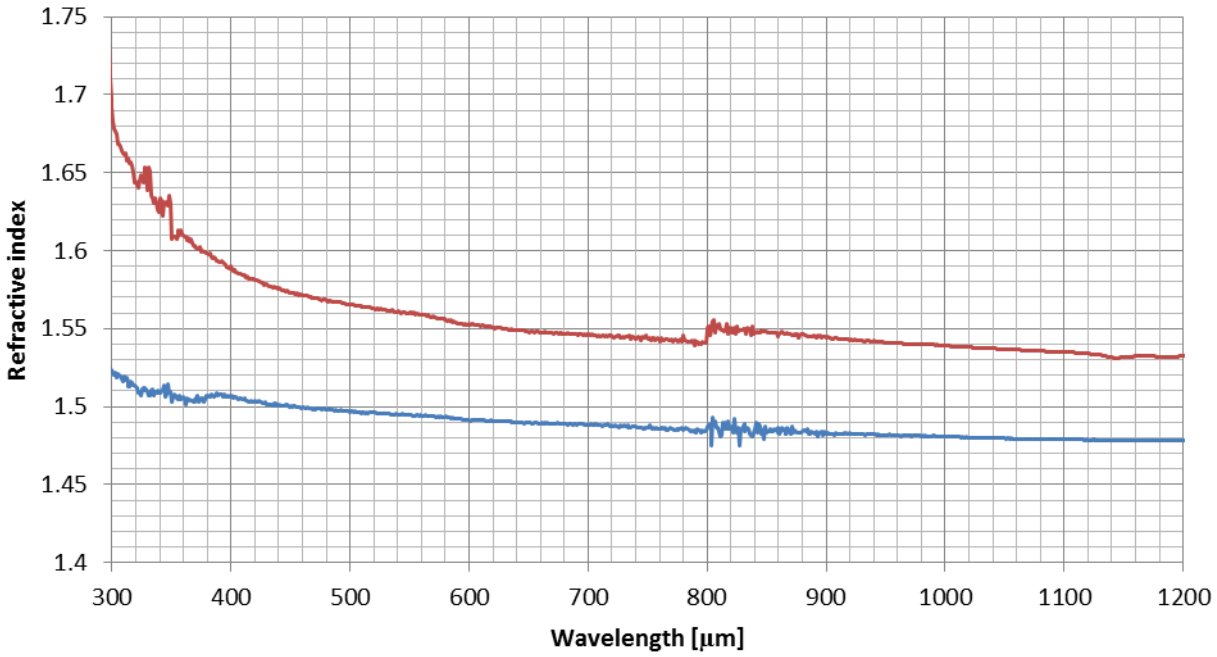

Figure 30: Comparison of refractive index as a function of wavelength for two encapsulant materials. The blue line shows standard EVA and the red line shows standard Silicone. These data are from a study by McIntosh et al. [40].

Figure 31 shows the absorption coefficient of silicone and EVA. In the short wavelength region up to 700 nm silicone has significantly lower absorption characteristics compared with EVA. The wavelength dependent spectral irradiance is highest in the region between 450 nm to 750 nm.

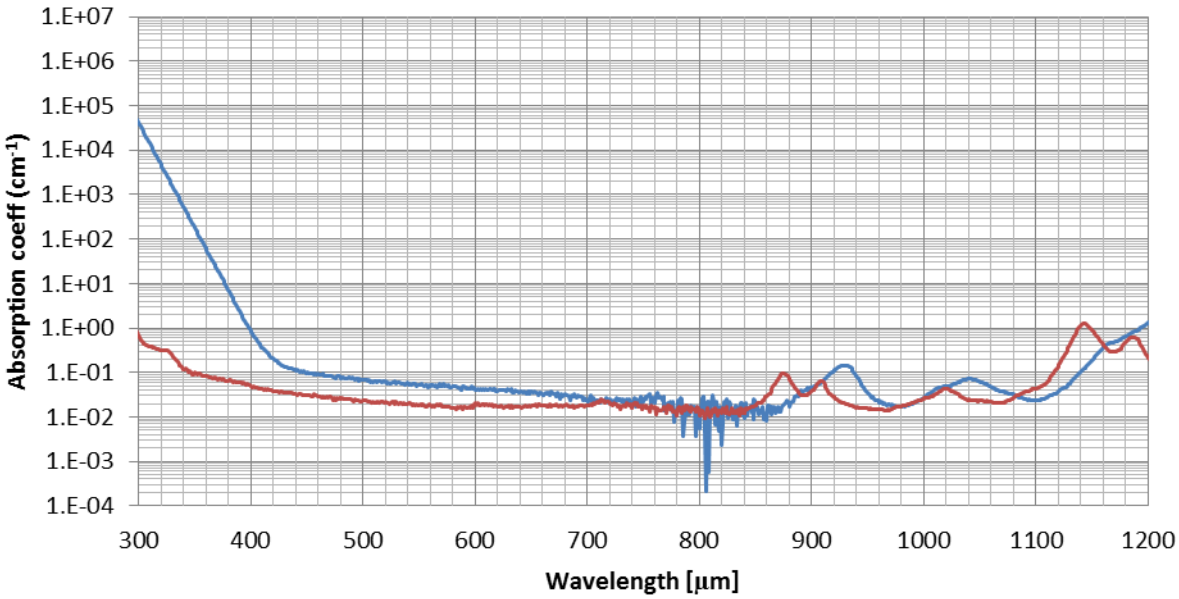

Figure 31: Comparison of absorption coefficient as a function of wavelength for two encapsulant materials. The blue line shows a standard EVA and the red line shows a standard Silicone. The data is from a study by McIntosh et al. [40]**. (Note, the EVA's absorption coefficient has been modified and linearized in the <400nm range to a more realistic characteristic, compared to the data provided in McIntosh study.)**

4.1.3 Metallization

Solar cells feature conductive contacts to collect the e-h pairs. The structure consists of fingers and bus bars on the front side and a flat layer on the back side. Fingers collect electrons and deliver them to the bus bars, the electrons moves from the bus bars and onto the directly connected external c. On the back side a sheet of metal also connected to the external conductors completes the circuit. The front contact material is usually silver (Ag) and the back sheet is usually a thin layer of aluminium (Al).

Figure 32: Front surface of a mono crystalline solar cell with two bus bars and fingers [48]**.**

In Figure 32 the front surface of a solar cell is shown. Two bus bars are running vertically and fingers are crossing horizontally. When designing a solar cell reflection losses from the front contact design and resistive losses from grid spacing must be balanced. Fingers are typically spaced 2.2 mm apart with height 20 µm and width 150 µm. Bus bars are typically 2 mm wide with height 20 µm and

spaced evenly to optimally collect the generated electrons. The back plate typically has a thickness of 100 µm.

Front contacts block the sunlight from reaching the semiconductor, and therefore reduce the efficiency of the solar cell. Typically front contacts cover 9.4% of the solar cell [49]. Not accounting for the shaded area in optical modelling will lead to inaccurate results. In this thesis a front contact covered area of 6.3% is used [50].

Optical properties for Al and Ag are presented in Figure 33. The absorption coefficient is high for both materials. In addition Ag has a very low refractive index.

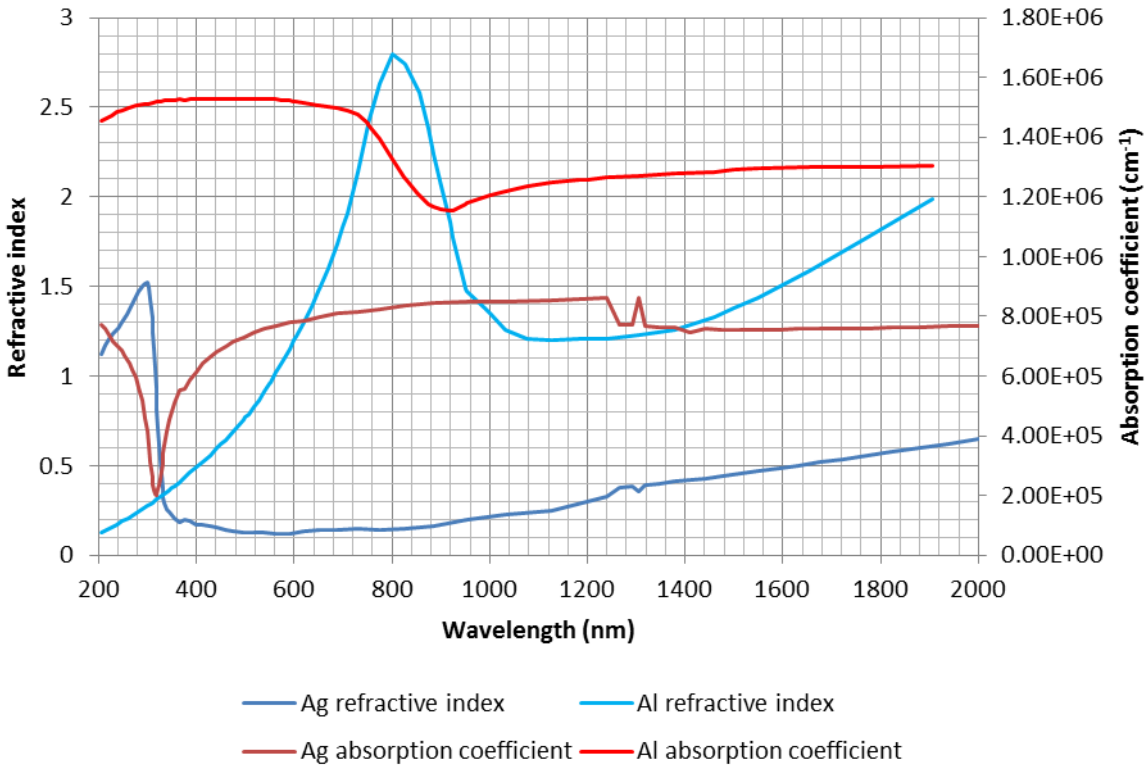

Figure 33: Optical properties for silver (Ag) and aluminium (Al) respectively represented by the blue lines and the red lines. These optical properties are published in OPAL [45]**.**

Metals are well known for having a high reflection. In Figure 34 results from an optical test for Ag and Al are shown. OPAL was used to test how reflective the materials are under the solar spectrum. Results show that both materials have high reflection over the entire solar spectrum. For metallic materials, light reflection is dependent on the surface condition. In this study the following assumptions are made: fingers reflect diffusely, bus bars and the back plate reflect light specular. The reader should note that the back plate can show a diffuse reflection [51]. Due to limitations in the numerical model the reflection was modelled specular.

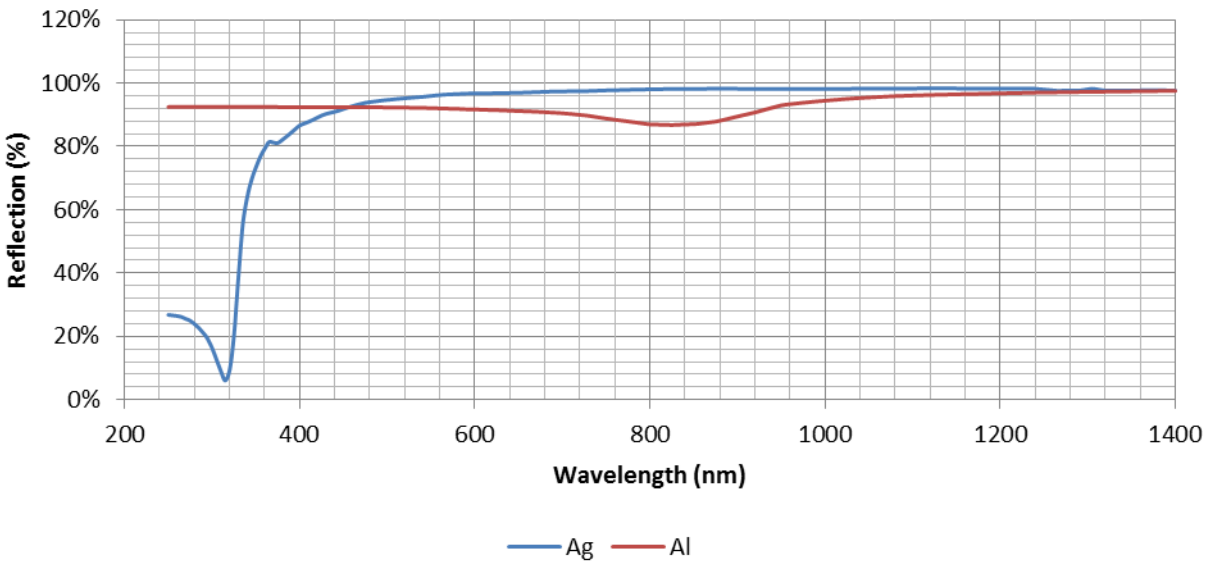

Figure 34: A reflection test performed in OPAL for Al (red line) and Ag (blue line). Both materials where considered to have polished surfaces.

4.1.4 Back sheet

The backside of PV modules is covered by a thin protective material. Important characteristics of the back sheet material are low thermal resistance, good insulating properties, high resistance to weathering, high moisture and rain protection. In most modules a thin polymer sheet is used. The industry standard back sheet material is developed by DuPont and called Tedlar, and it typically has a thickness of 320 µm [52].

The reflection type from the back sheet is dependent on the colour and surface finish. In this the back sheet is considered to have a white colour with a matte finish giving a Lambertian reflection distribution.

In Figure 35 the reflection of Tedlar as a function of wavelength is shown. The blue line shows Tedlar measurement data published in the ray tracing program Tracey, the red line shows published data from DuPont for TPT PV 2001 type Tedlar and the blue line shows published data from DuPont for TPT PV 2111 type Tedlar.

The three Tedlar types shown in Figure 35 have the same characteristic reflectance features. Below approximately 360 nm the reflection is less than 10 % permitting over 90% of the incoming rays to be transmitted. The reflectance is rapidly increased to above 75% for all three at 500 nm. Tracey's Tedlar measurements and TPT PV 2111 show the best reflection properties. In this thesis the measured Tedlar properties published in Tracey will be used in the simulations.

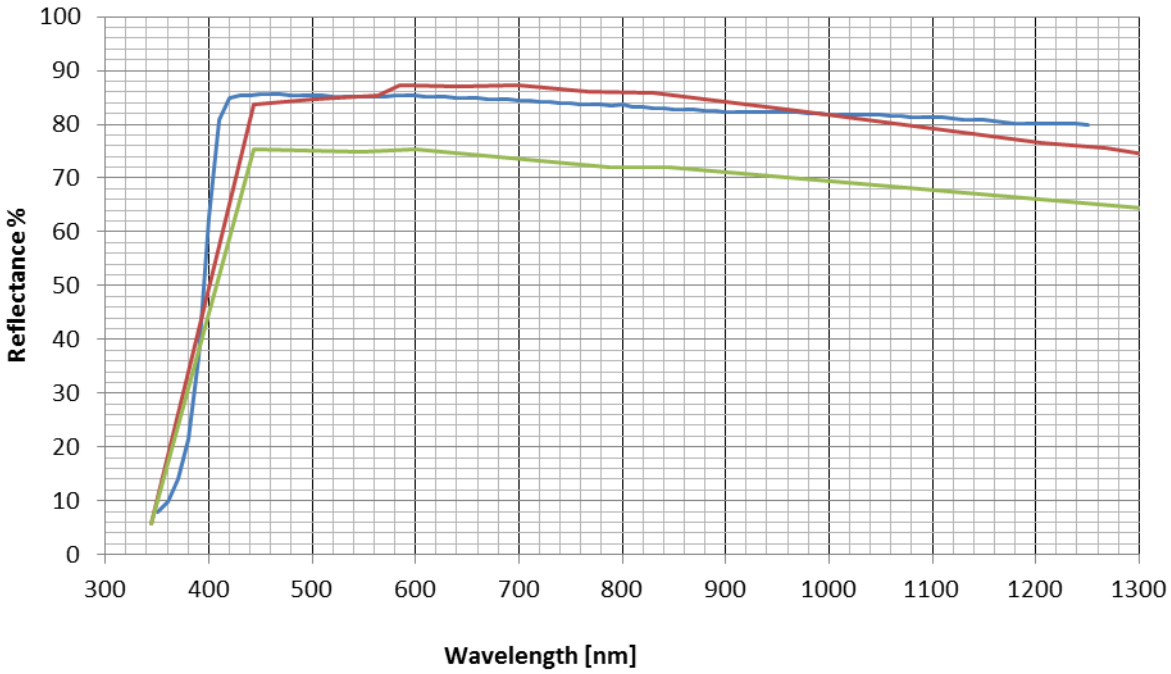

Figure 35: Reflectance of Tedlar as a function of wavelength. The blue line shows Tedlar measurements published in the ray tracing program Tracey [53]. The red line shows published data from DuPont for TPT PV 2001 type Tedlar. The blue line shows published data from DuPont for TPT PV 2111 type Tedlar.

4.2 Detailed structure of a c-Si cell

The solar cell is the most important component in a PV panel, and accordingly it is the most complex. At present most solar cells are silicon based, since this is the most mature technology [18]. Hence this part of chapter 4 will discuss how to optically model a standard c-Si solar cell.

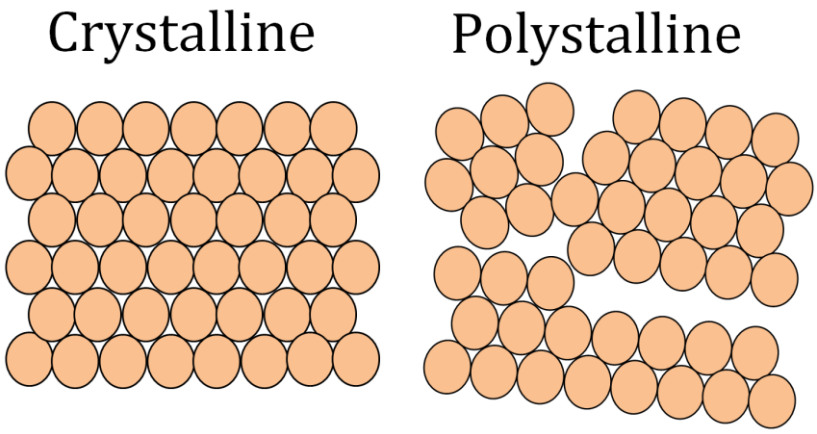

Figure 36: Illustration of monocrystalline (left) and polycrystalline (right) silicon.

Crystalline silicon used for solar cells are generally classified as either monocrystalline or polycrystalline. As shown in Figure 36 monocrystalline silicon has an ordered crystal structure, with each atom ideally lying in a pre-ordained position. It therefore allows for application of theories and

techniques developed for crystalline material and exhibits predictable and uniform behaviour. Polycrystalline, also shown in Figure 36, feature several crystal structures. The crystal boundary, or grain boundary as its more commonly called, reduce the cell performance by blocking carrier flow, allowing extra energy levels in the forbidden gap, thereby providing effective recombination sites, and providing more possibilities for recombination losses [18]. The randomized nature of polycrystalline makes it challenging to model optically.

Silicon solar cells consist of two doped layers of silicon, n-type and p-type. By adding n- and p-type doping to silicon free electrons and holes are introduced. These free charge carriers can absorb photons by so called free-carrier absorption. Hence the absorption coefficient of silicon is a function of doping concentration [15]. In addition solar cells can feature layers of different doping content, often depicted by a + sign, to increase the performance.

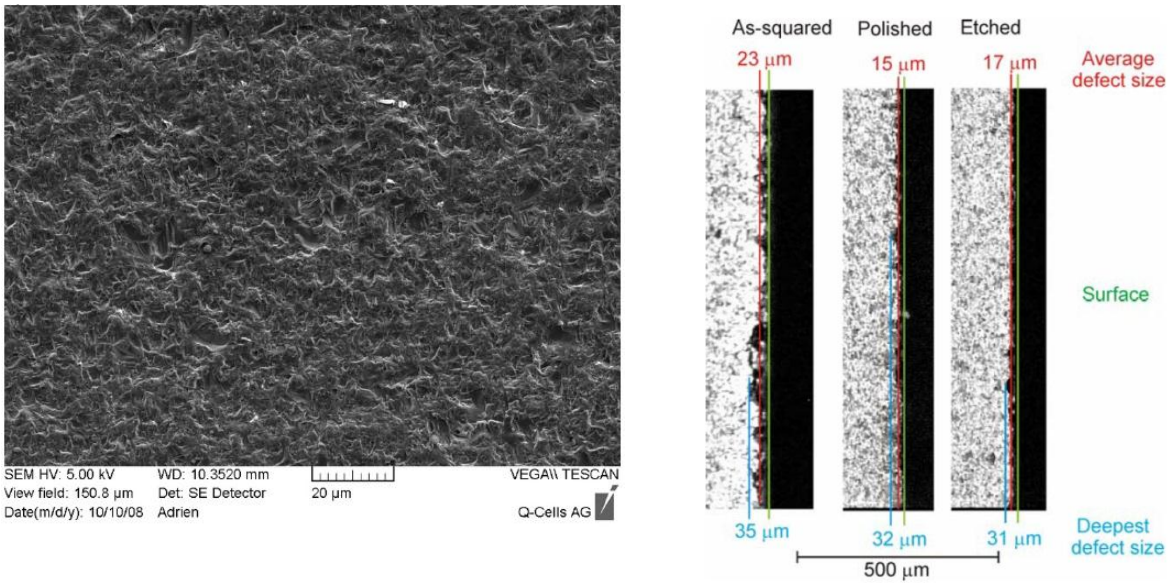

Figure 37: The image on the left shows a SEM picture of an as-cut mono c-Si wafer [54]**. The image on the right shows a cross-section image of an as-cut, polished and etched mono c-Si wafer, the images are obtained using a near-infrared transmission microscopy** [55]**.**

Up until now this section has mainly focused on effects that determine the absorption and e-h pair generation. But the surface of the solar cell is also highly complex. Silicon wafers are mainly manufactured by cutting blocks of silicon with a multi-wire slurry saw. In Figure 37 a SEM image of a mono c-Si as-cut wafer is shown in the left picture. After the cutting process the wafers undergo chemical etching to remove surface damage and to render a desired surface texture to reduce reflection losses (Textured surfaces are discussed more in detail in section 4.2.2.2.1). The right picture in Figure 37 shows a cross-section view of an as-cut, polished and etched mono c-Si wafer.

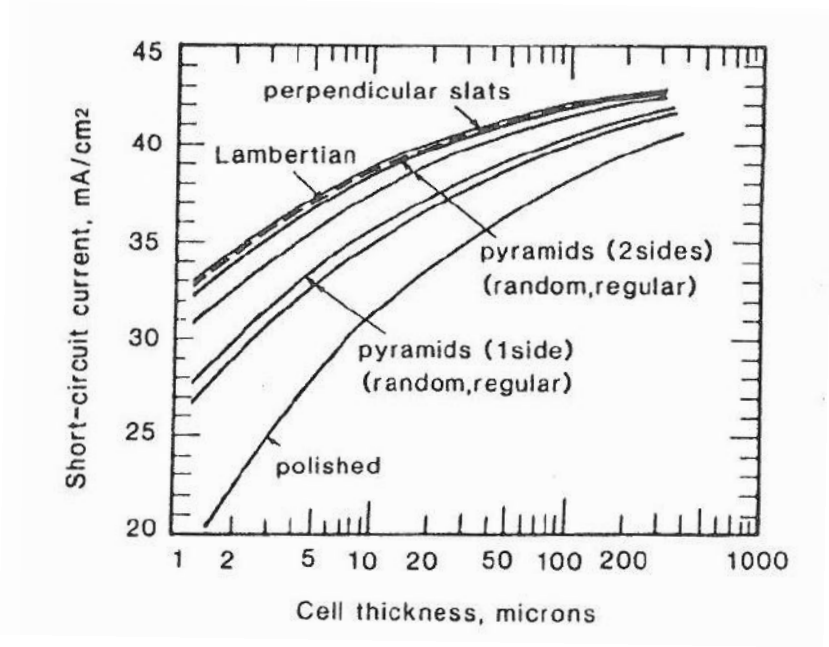

Figure 38: Calculated short-circuit current density as a function of silicon cell thickness for different light trapping geometric schemes. All schemes assume zero front surface reflection and a perfect rear reflector [15]**. The illumination used was AM1.5 global spectrum.**

It is not only on the front side geometric structures can enhance the performance of the cell. Long wavelength photons that are not absorbed during their first passage through the cell can be internally reflected, photons will then have additional opportunities for absorption. This is done by adding geometric schemes and a back surface field which increases the possibility of photons being reflected on the rear surface [18][15]. Together with textured front surface photons can be trapped inside the wafer. In Figure 38 calculations for I_{sc} as function of wafer thickness for different front and rear side geometric schemes are shown. As displayed, when the wafers' thickness is reduced the I_{sc} dependence on the light trapping geometry increases.

In this section the main considerations when modelling a c-Si solar cell optically was briefly described and in the following sections they are further discussed. It is a goal of this thesis to develop an optical model which accurately represents a normal operating solar cell. Accordingly, in the following sections two models are presented:

- A simple model where the front surface of the solar cell is assumed to reflect and absorb light as a Lambertian diffuser
- A more complex model where texturing of the front surface of the cell is optically modelled

4.2.1 A simple optical model of a c-Si cell using a Lambertian reflection approximation

There are many applications where a simple model of a solar cell is of interest. It can reduce design, model and computational time, as well as required computational capacity.

In this study a simplified model has been developed. The considerations and limitations made are presented in the following points.

- The optical response is defined by the EQE of a standard c-Si screen-printed solar cell
- The optical model is represented by a surface property
- Internal light propagation is not considered
- Light is either absorbed or reflected, following the wavelength dependent EQE
- All losses, including optical and recombination losses are modelled as reflection losses. As a result the reflection will be higher than it realistically would be
- The reflection follows a Lambertian distribution
- Angle of incidence is not considered, the simplified model does not distinguish between different angles of incidence

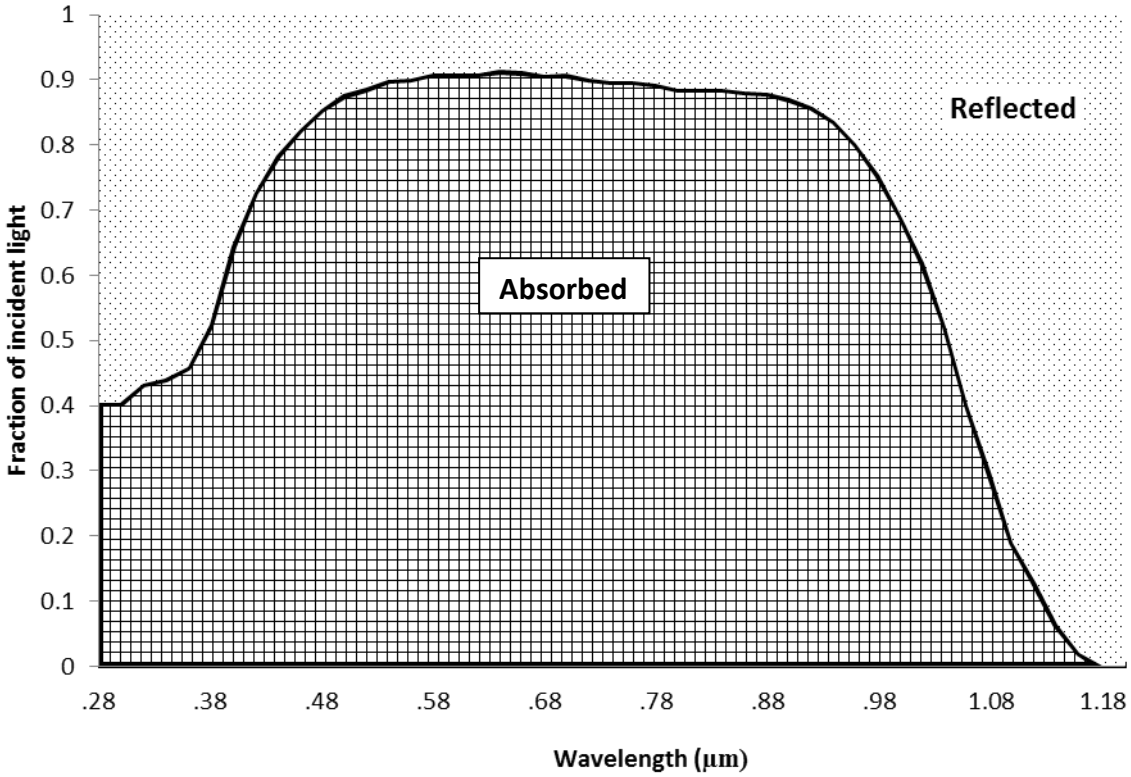

Figure 39: EQE as a function of wavelength for a c-Si solar cell [50].

The main reason for defining the optical response in terms of the EQE is because EQE measurements are readily available. However, note that these measurements are performed for an un-encapsulated cell in an open environment. But a solar cell is usually encapsulated by EVA, and EVA has a higher refractive index than air; consequently and in accordance with Fresnel's equations the reflection will be higher than if the EQE measurements were performed in an EVA environment. Consequently

higher reflection results in lower absorption. To investigate the potential error, simulations were performed using the ray tracing programs OPAL and TRACEY. For the simulations AM1.5 Global spectrum was used as irradiance. The reader should note that in this investigation front metallisation, e.g. fingers and bus bars, has not been added to the calculations resulting in overall lower reflection for the results in Figure 40.

OPAL has been developed by K.R. McIntosh and S.C. Baker-Finch. The program simulates the front-surface optics of a solar cell and can be used to determine the absorption, transmission and reflection for different thin film ARC, glass covers, etc. Tracey has been developed by K.R. McIntosh. It can be used to perform ray tracing simulations on PV panels. Both programs are freely available on the authors website, and have been used and tested in a series of papers, e.g. by K.R. McIntosh and S.C. Baker-Finch [47][40][56].

The setup for the simulation in OPAL was as follows; reflection simulations were performed where a c-Si cell was textured with random upright pyramids and coated with a 75 nm thick SiNx thin film ARC.

1. The first simulation was performed in an EVA environment (only refractive index considered, no absorption)
2. The second simulation in air (atmospheric environment), i.e. with refractive index= 1

Subsequently the reflection results for the two simulations were exported from OPAL and imported into TRACEY. The reflectance data are paired with an IQE (shown in Figure 40) to represent the optical response of a solar cell. In Tracey the simulations were performed to extract EQE and short circuit current for both reflection data in an EVA environment.

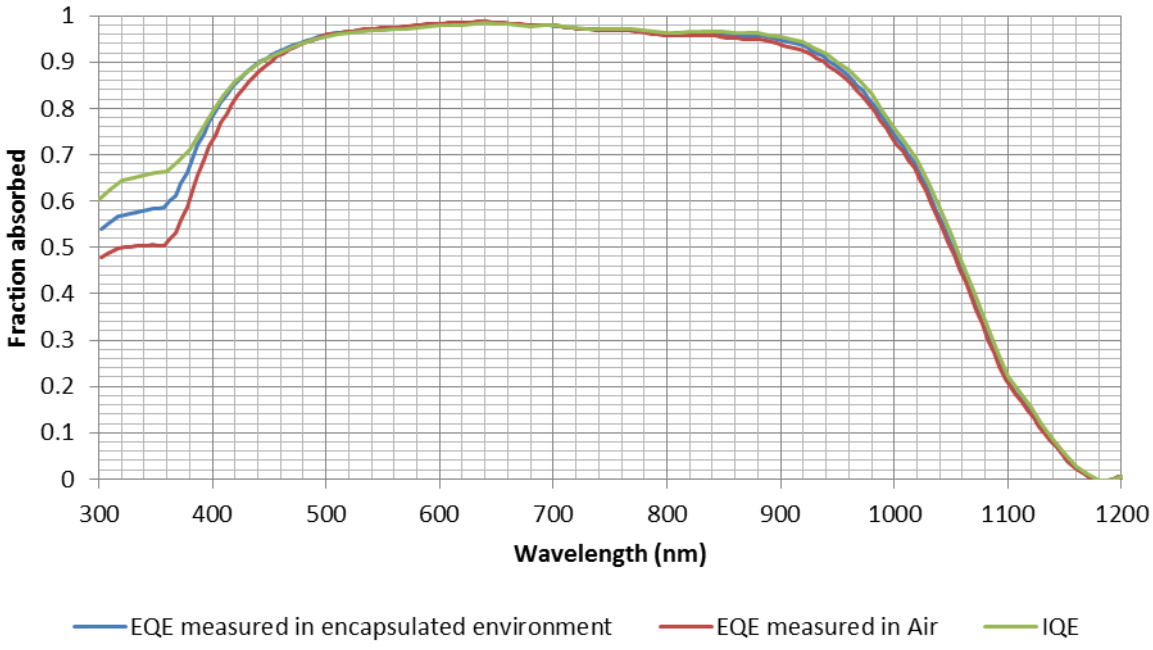

Figure 40: EQE calculations for a solar cell in an EVA environment with cell surface reflection data from simulations in two different environments. The IQE is obtained from a published paper by Thaidigsmann et al. (2009) and combined with the reflection data to obtain the EQEs [50].

In Figure 40 the results from the simulation in Tracey are shown. And as expected the EQE with reflection data from air has lower absorption than the EQE with reflection data from an EVA environment. But in the region from 400 nm and up to the upper cut off wavelength there is hardly any difference between the two. In addition a short circuit current calculation carried out in TRACEY resulted in a difference of only 1%. It is therefore assumed that the EQE measured in a sea level atmospheric environment can produce representable and realistic results.

As stated the optically modelled solar cell distributes reflected light identically to a Lambertian surface. And a Lambertian distribution follows Lambert's cosine law, which states that the intensity of light scattered from a point on a reflecting surface follows a cosine relationship with the angle to the horizontal. In the ray tracing simulation rays striking a Lambertian surface are reflected randomly following Lambert's law (see Figure 41).

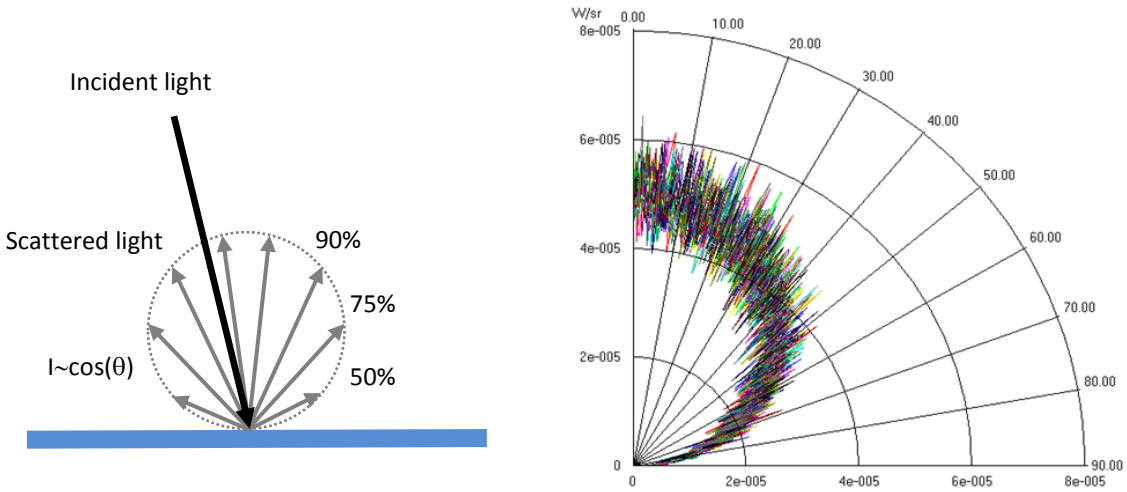

Figure 41: Theoretical representation of a Lambertian reflecting surface is shown on the left. In the right figure, results from a ray tracing simulation on the actual solar cell surface are shown.

Baker-Finch et al. (2010) demonstrated in their study that the Lambertian approximation is not very accurate for a mono c-Si solar cell [57]. In reality the light would be scattered as a function of incident angle. However, Baker-Finch and his colleagues showed that the reflection distribution from the cell surface had a minor influence on the short circuit current. They showed that if 85 % of the initially reflected light where to be internally reflected in the solar panel and transmitted into the solar cell at a second meeting the short circuit would increase by 1%.

In this section a simple model of a solar cell was presented. The model is expected to perform well, but with two major restraints; all losses are modelled as reflection losses and that it does not consider angles of incidence. This leads to the conclusion that a more accurate model is necessary; not only for producing more accurate results, but also as a good tool to explore the limitations of this simple cell model. In section 4.2.3 the simple cell model is compared with a more realistic approach

4.2.2 A more realistic optical approach

In the previous section a simple cell model for representing a solar cell in a ray tracing simulation was developed. In this section a more complex and realistic model is developed based on a mono crystalline solar cell.

4.2.2.1 Optical properties of silicon

Optical properties of intrinsic silicon are presented in Figure 42. As described earlier, doping concentration will in a real solar cell influence the optical properties of pure undoped silicon, therefore in this section the influence of the doped layers with respect to the optical modelling and simulation will are discussed. Another important but challenging factor when using simulation software is accounting for every physical effect a substance experiences. For instance silicon's optical properties are temperature dependent. And it is challenging to account for variation of temperatures in an optical model. As a result, in this chapter it will also be discussed if a c-Si solar cell can be accurately modelled with optical properties of undoped silicon at 300k. This is of interest since simplifying the model can reduce modelling and computational time.

In Figure 42 the absorption coefficients for n-type, p-type and intrinsic (i.e. undoped) silicon are shown as a function of wavelength. As shown p-type doping does not change the absorption coefficient of the material prior to the upper cut-off wavelength. It is therefore believed that p-type doped silicon can be optically modelled with optical properties of intrinsic silicon.

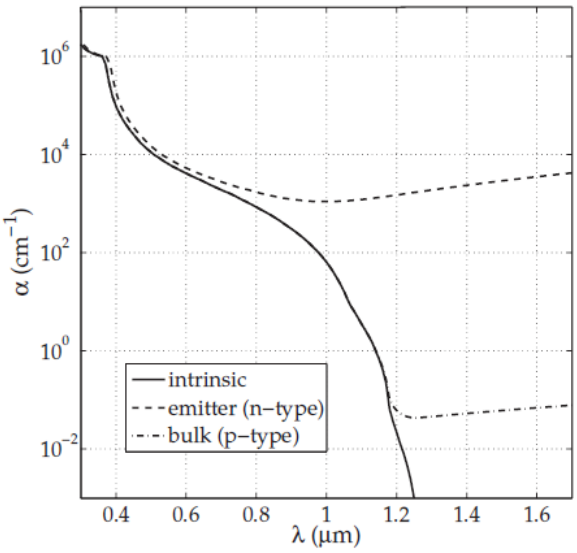

Figure 42: Absorption coefficient of intrinsic, n-type and p-type silicon. The p-type silicon has a doping concentration of $1.0\ x\ 10^{16} cm^{-3}$ and the n-type silicon has a doping concentration of $3.3\ x\ 10^{20} cm^{-3}$ [58].

N-type doping on the other hand dramatically influences the absorption coefficient. Santbergen has in his PhD thesis examined the optical difference between polished, undoped and n-type doped silicon [58]. In Figure 43 two plots show Santbergen's results. By comparing the two plots the following conclusion can be made; the reflection curves show only a limited variance, which is caused

by a higher refractive index in the doped specimen. As Santbergen points out, the doping not only affects the absorption coefficient but also the refractive index. However both specimens show good agreement over the tested wavelength region with noticeable differences only around 0.4 µm, 1µm and above 1.2 µm. It is therefore assumed here that n-type doped silicon also can be optically modelled with optical properties of intrinsic silicon.

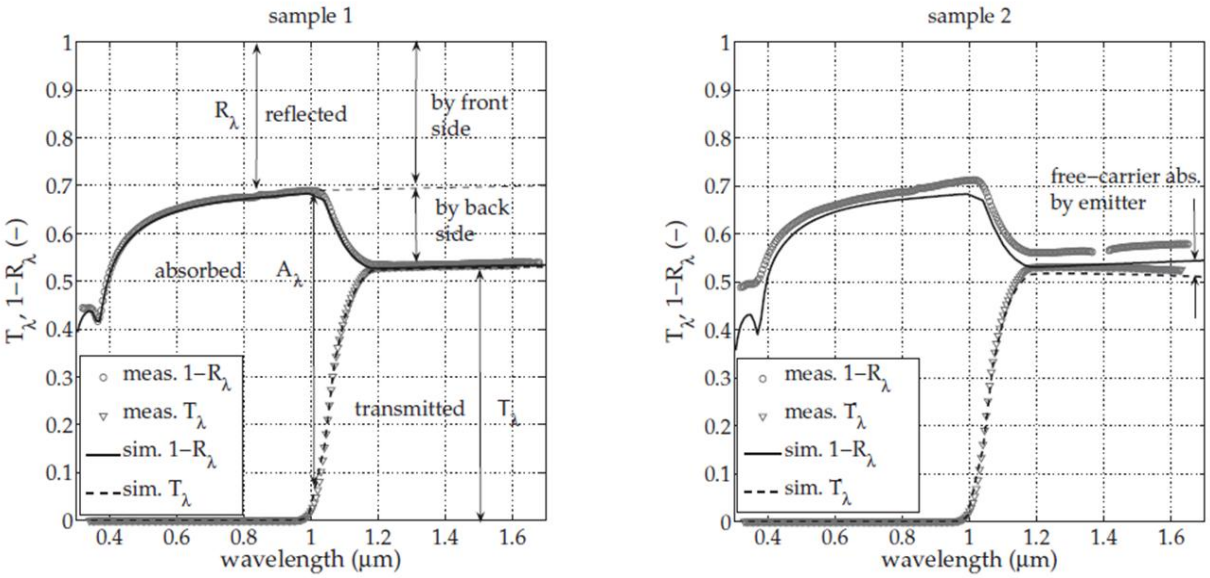

Figure 43: The plot on the left represents both measured and simulated reflectance, absorption and transmittance for polished undoped silicon. The plot on the right represents both measured and simulated reflectance, absorption and transmittance for polished n-type doped silicon [58]**. The measurements illustrates that in the wavelength region below 1 µm the material is opaque (i.e. no light is transmitted) and that the increased reflection above 1.2 µm is caused by internal reflection from the back surface.**

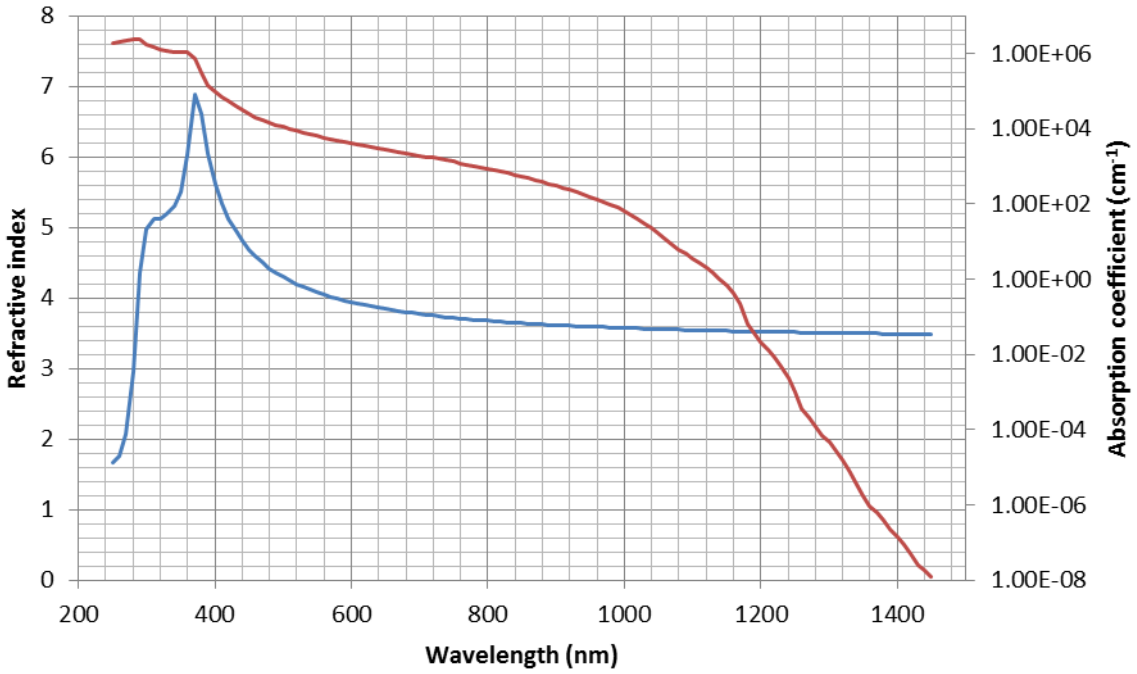

Figure 44: Optical properties of intrinsic silicon [14]**. The red line represents the absorption coefficient and the blue line represents the refractive index.**

In Figure 44 the optical properties of silicon is shown. The blue line represents the refractive index. At approximately 380 nm the refractive index is highest, resulting in high reflection loss. In the wavelength region from 600 nm to 1400 nm the refractive index has a lower dispersion. The absorption coefficient of silicon is high at short wavelengths and low at longer wavelengths. Photons of short wavelengths are easily absorbed and photons with long wavelength are only weakly absorbed.

The solar cell's operating temperature is dependent on ambient temperature, encasement, wind speed and intensity of sunlight [18]. Usually solar panels operate at 60 degrees (333k) and ideally this study would use optically properties for silicon at that temperature, but because data for silicon at this temperature is not available values for 300 k are used.

The biggest contributor to the solar cells temperature is the thermal process going on in the cell. As mentioned in chapter 2 both the short circuit current and the open circuit voltage are temperature dependent. Electrons jump from the valance band to the conduction band when they are excited by incoming photons with energy equal to or greater than the band gap. The excited electrons with energy greater than the band gap quickly relax down to the conduction band edge, releasing the excess energy as thermal energy, causing the solar panel to heat up. The increased temperature in the panel lowers the band gap [15]. Thus lower energy photons are able to generate electron-hole pairs, expressed in the increased absorption coefficient, illustrated in Figure 11 (the reader should note that y-axis scale is logarithmic and therefore there is a significant difference between the graphs displayed).

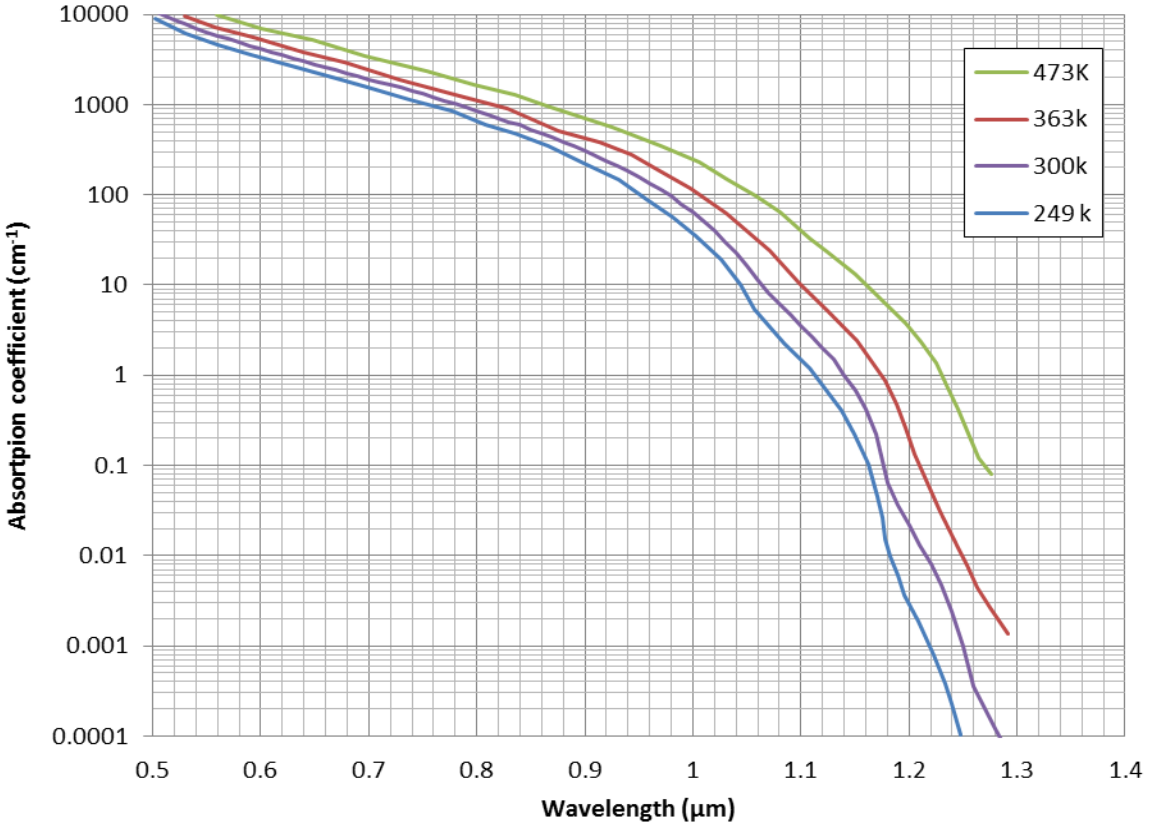

Figure 45: Silicon absorption coefficient dependency on temperature [14].

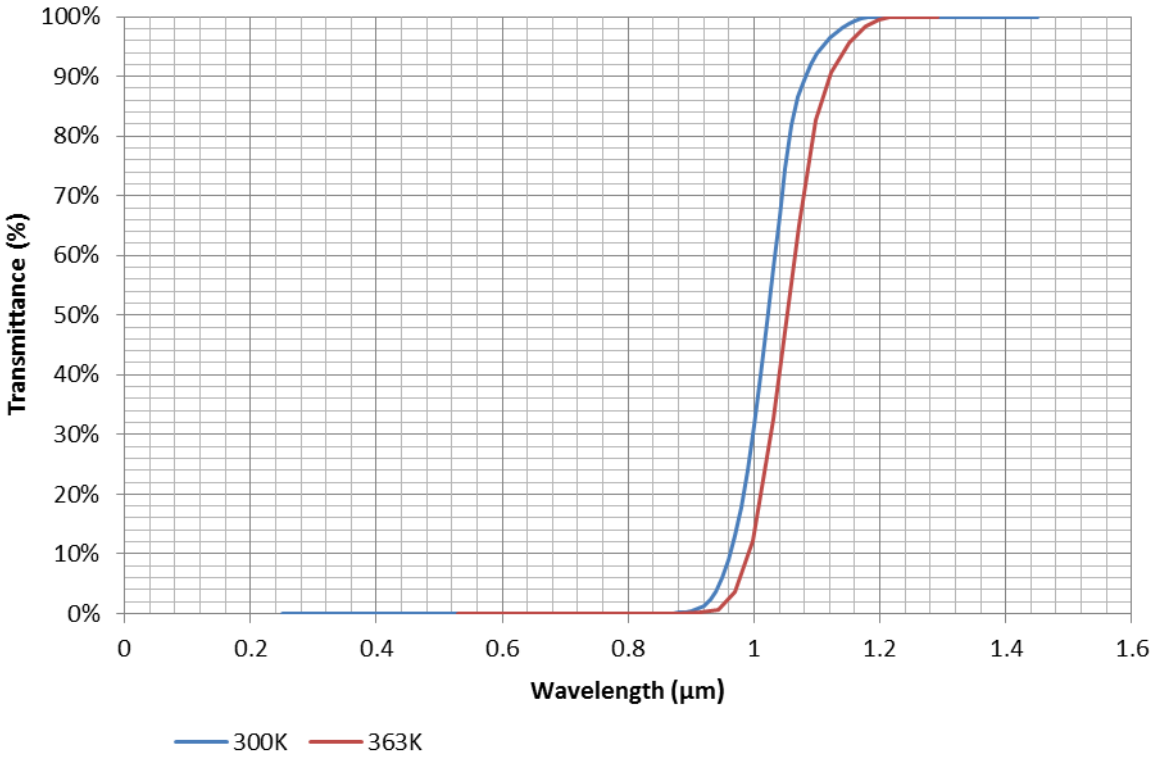

Figure 46: Transmittance for a 180 µm thick wafer with absorption properties of silicon at 300K and 363K. The calculation is carried out by using the Beer-Lambert law.

To quantify the difference in transmittance a calculation using the Beer-Lambert law was carried out for a 180 µm thick wafer with the absorption properties of silicon, at 300K and 363K. The results from the calculation are shown in Figure 46. And as expected the higher temperature silicon (red line) absorbs more than the lower temperature silicon. Results from a calculation with silicon at the desired temperature (333K) would fit somewhere in between these results. The test shows that by using absorption properties of silicon at 300K the absorption will be representable for a normally operating c-Si solar cell in the wavelength region from 0.28-0.9 µm. In the region above 0.9 µm some divergence is expected. In conclusion results from the simulations should produce very representative results in the wavelength region up to approximately 0.9 µm, above 0.9 µm the absorption will be lower compared to a solar cell operating at 333K.

4.2.2.2 *Surface treatment of silicon*

Generally there are two types of losses that reduce the conversion efficiency of silicon, optical losses and electrical losses. Optical losses can be reduced by anti-reflective coating and/or texturing the surface. In Figure 47 the reflection of polished silicon is shown. Because of silicon's high refractive index the reflection is high over the entire solar spectrum. Reducing the surface reflection can increase the short circuit current and thereby increase the conversion efficiency [15].

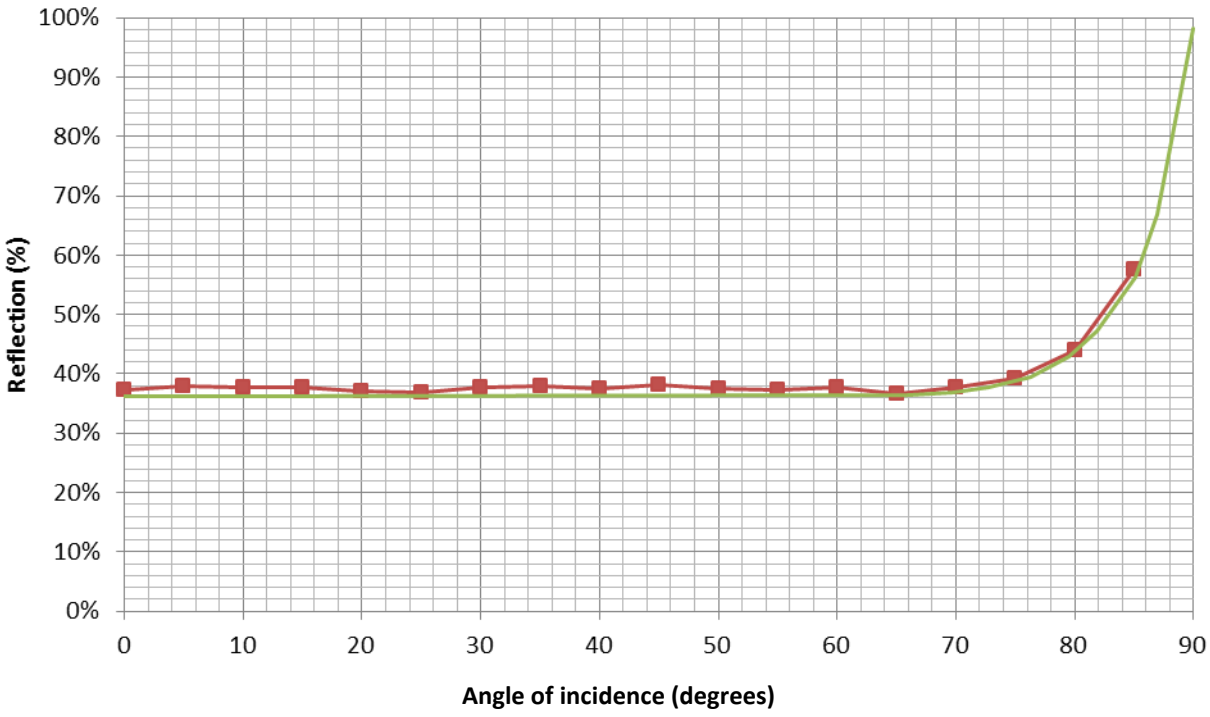

Figure 47: Reflection for polished silicon at the air-silicon interface is shown as a function of angle of incidence. The red line represents simulation results from ray tracing using optical properties shown previously. The green line represents reflection calculation carried out by the applying Fresnel's equations [59].

4.2.2.2.1 *Realistic optical modelling of typical c-Si solar cell surface*

By applying textured structures on the top surface of the c-Si solar cell reflection losses can be reduced. There are many methods to texture silicon surfaces. Chemical etching is the most used technique. Alkali hydroxide etchants, such as potassium hydroxide (KOH) and sodium hydroxide (NaOH), have been widely used to texture mono c-Si solar cells [60][61].

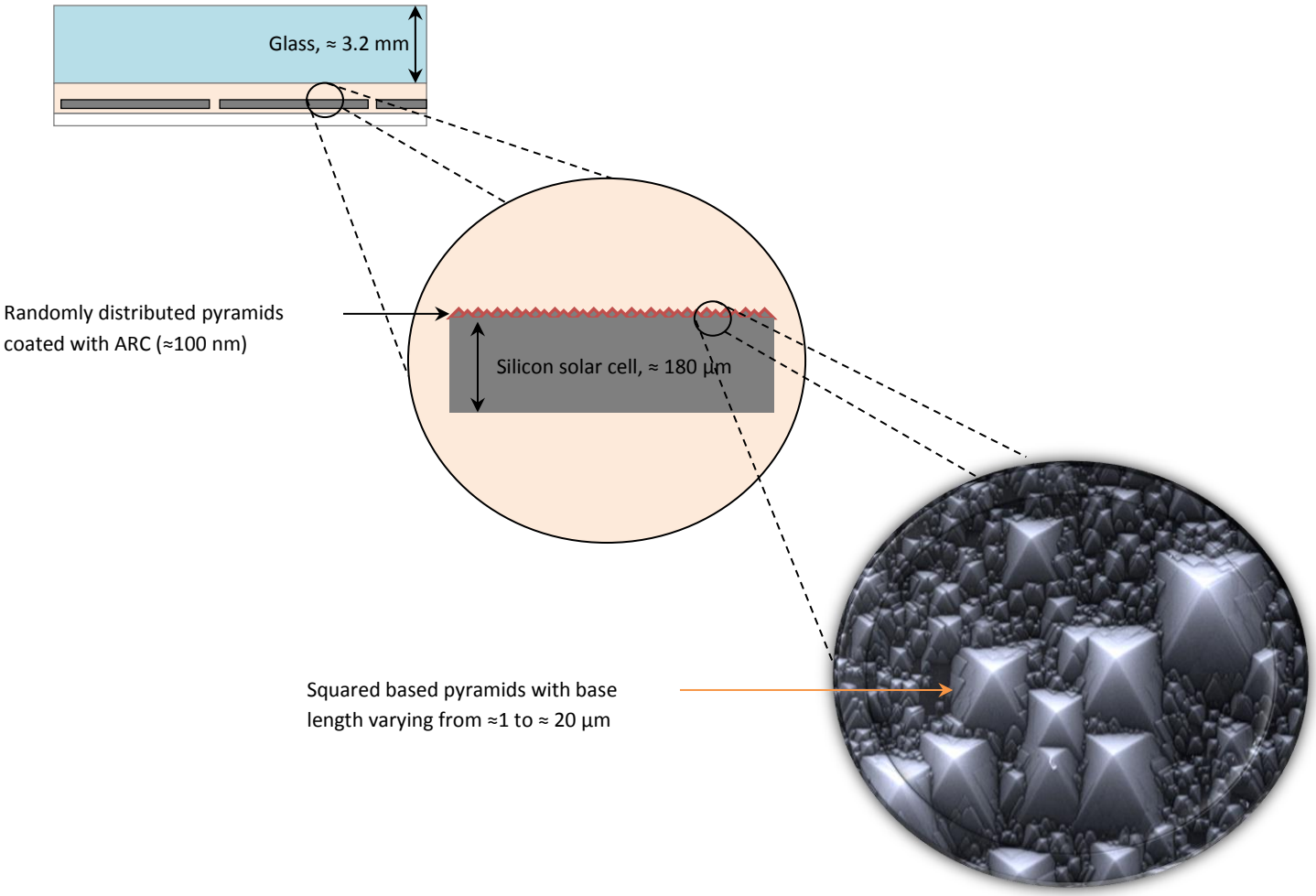

Figure 48: Top: Cross section of a solar cell showing the texturing AR coating layers. Bottom: Example of a mono-crystalline silicon surface after crystallographic (111) wet etching (SEM picture). SEM picture is provided by project owner. SEM pictures taken in this study on a mono c-Si KOH etched wafer can be found in Appendix D.

Silicon has a face centred cubic (FCC) crystal structure. Chemically etching the flat ((100) oriented) silicon wafer exposes almost ideal ((111) faceted) pyramids, as seen in Figure 48. Normally the base angle of the pyramids has been considered to be 54.74 degrees. Baker-Finch et al. (2012) have studied the base angle of the pyramidal textures [62]. They conclude that the base angle is dependent on the etching time, and is normally closer to 50-52 degrees. They also discovered that the textured surface actually consists of hillocks, and not the commonly believed pyramids. However the study proved that this misconception (from a modelling perspective) leads to a 0.2 % difference in photo generated current, if the thin film ARC is optimized.

The size of the pyramids is dependent on the chemical used and etching time. Lien et al. (2011) have done measurements of texture formation and reflection as a function of etching time; the results are presented in Figure 49 [63]. As shown with etching time less than 10 minutes, only small pyramids and planar areas in-between are produced, resulting in high reflection. By increasing the etching time the whole surface is covered with structures, resulting in lowered reflection. After an etching time of more than 40 min the reflection is increased. Due to the smoothing of the surfaces.

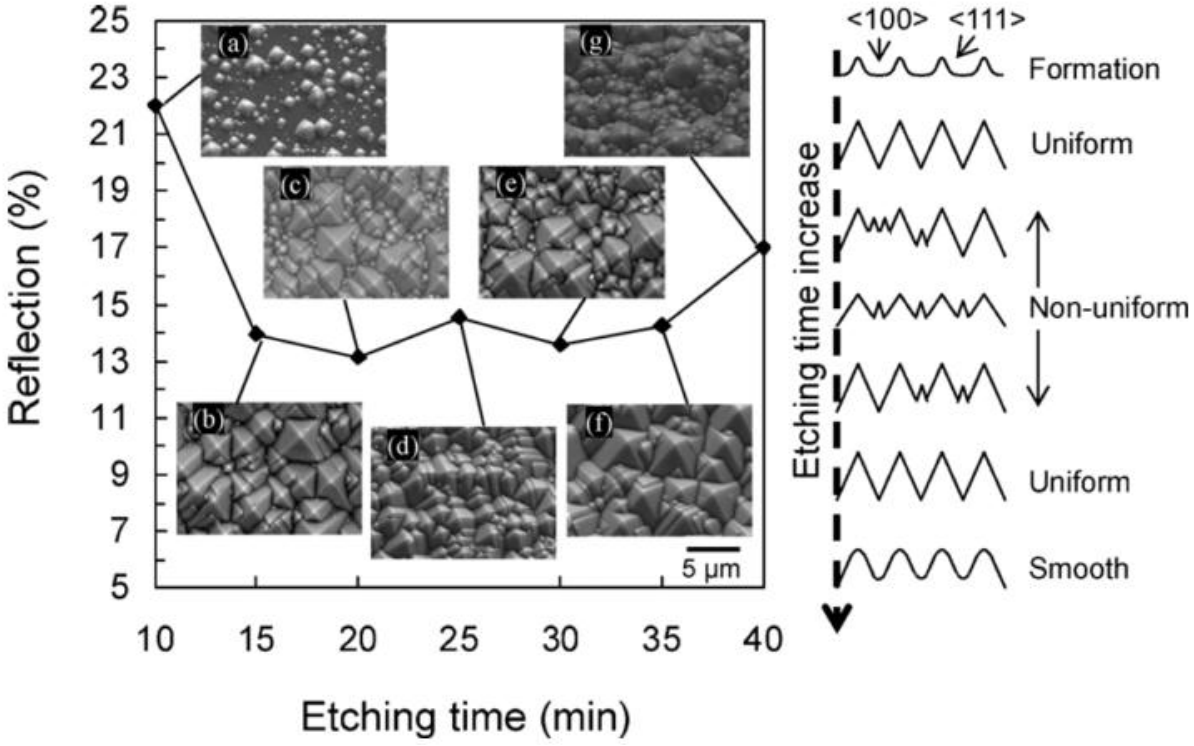

Figure 49: Average reflection of textured structure for different etching times and proposed mechanism of formation of pyramids with KOH etching [63].

Normally the pyramidal structures vary in size between 1-10 µm [57][64]. But if the structures are smaller than ten times the wavelength ray tracing programs will not model optical effects like diffraction correctly. Hence the modelled structures should be larger than 12 µm. It is however expected that using pyramids somewhat larger should not greatly affect the results since the geometrical shape is the same for small and large pyramids. Lien et al. (2011) also studied this and came to the same conclusion.

The designed surface texture used in this study was inspired by Lien's *Mostly Big* texture, shown in Figure 57. The extracted designed texture is shown in Figure 51. The primary pattern consists of large pyramids surrounding small and medium size pyramids. To make sure the texture produces consistent results the primary pattern is duplicated 121 times.

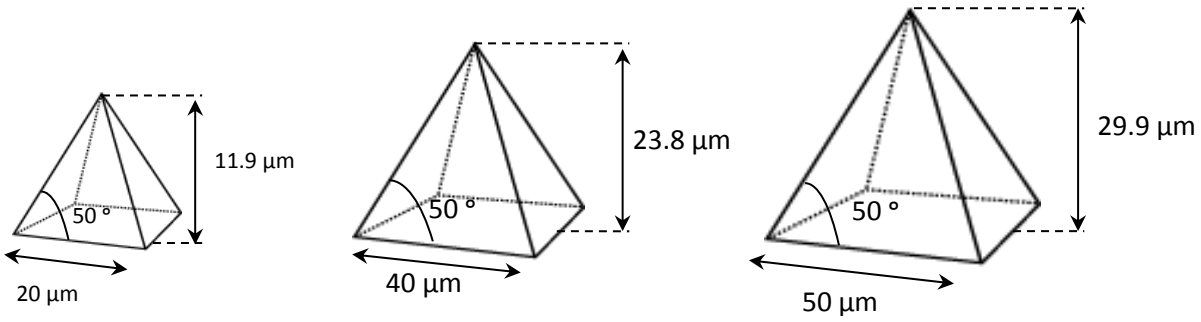

Figure 50: The geometry of the three pyramids used in the texture design.

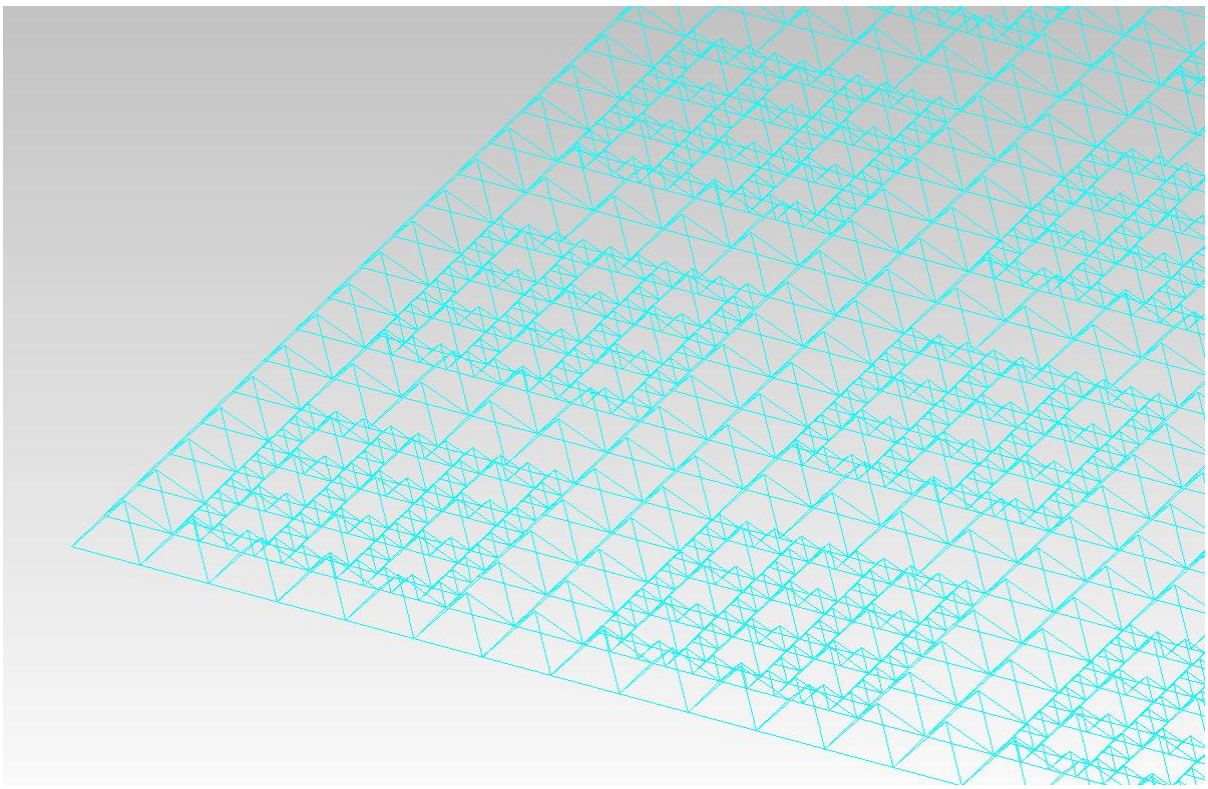

Figure 51: The designed surface texture structure is shown; it is named the Extended mostly big surface texture. As seen, one primary pattern is duplicated to cover a larger area.

Modelling the textured structures accurately is challenging. As seen in Figure 48 the structures are randomly distributed, often with varying size. Additionally the more objects modelled the more computational capacity is required. In the ray tracing software (TracePro) used in this thesis, modelling of the textured structures can be simplified by the use of a feature called Repetitive Tile (RepTile). Where the textured structure can be created in a tile and then that tile can be repeated, over a desired surface. However tests have shown that this modelling simplification is not enough for the computer to work efficiently.

As mentioned previously surface texture structures for mono c-Si solar cell are normally in the size 1-10 µm. Tests have shown that running ray tracing simulations on a full sized solar cell (155mm x 155mm), with surface texture requires very long computational time (weeks). To lower the

computational requirement the surface structure can be simplified. To do so one can measure the incoming ray's angle of incidence and the corresponding direction of the reflectance and transmittance. By exporting data measurements with this connection a surface property following the desired reflectance and transmittance distribution can be made. The model of the desired surface texture need only cover a small area. The reflectance and transmittance distribution can be collected, and applied as a surface property for a much larger surface area. In the following section a method of creating just such a surface property is described.

4.2.2.2.1.1 BSDF

A bidirectional scattering distribution function (BSDF) is a measure of light scattered from a surface in different directions. It is called bidirectional because it is a function of both the incident direction and the scattered (outgoing) direction of light. BSDF is defined as the scattered radiance per unit incident irradiance. The function is expressed in Eq. (33).

$$BSDF(\theta_i, \phi_i, \theta_s, \phi_s) = \frac{dL_s(\theta_s, \phi_s)}{dE_i(\theta_i, \phi_i)} \tag{33}$$

Where:

dL_s is the scattered radiance ($\frac{W}{sr\ m^2}$).

dE_i is the incident irradiance ($\frac{W}{m^2}$).

The angles θ and ϕ represents the angles for respectively the incident and scattered light in spherical coordinates.

An arithmetic calculation proves that the BSDF has units ($\frac{1}{sr}$). In Figure 52 the BSDF is illustrated. Here dA_s represents the illuminated area and $d\Omega_s$ represents the solid angle.

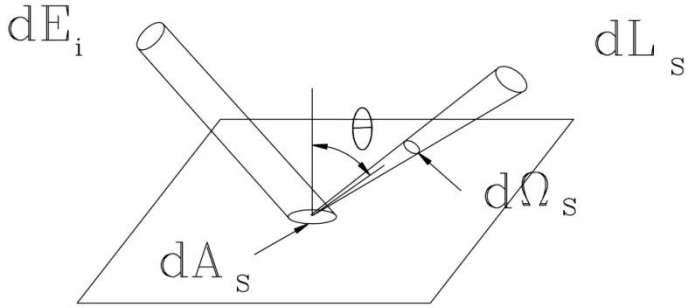

Figure 52: The Angles and dimensions defining the BSDF [65].

More precisely the BSDF is split into reflected and transmitted components, namely bidirectional reflectance distribution function (BRDF) and bidirectional transmittance distribution function (BTDF).

In TracePro the BSDF is shift-invariant with respect to the incident direction. This means that the shape of the BSDF depends only on the difference between the specular direction and the scattered direction. An illustration of how the BSDF is employed in TracePro is shown in Figure 53. Where $\vec{\beta}_0$ is the projection onto the surface of a unit vector r_0 in the specular direction and $\vec{\beta}$ is the projection

onto the surface of a unit vector r in the scattering direction. The magnitude of their difference; $|\vec{\beta} - \vec{\beta_0}|$ is the argument for the BSDF [66]. The reader should note that specular direction is here defined as the direction reflected light would have if incoming and reflected light made the same angle with respect to the surface normal.

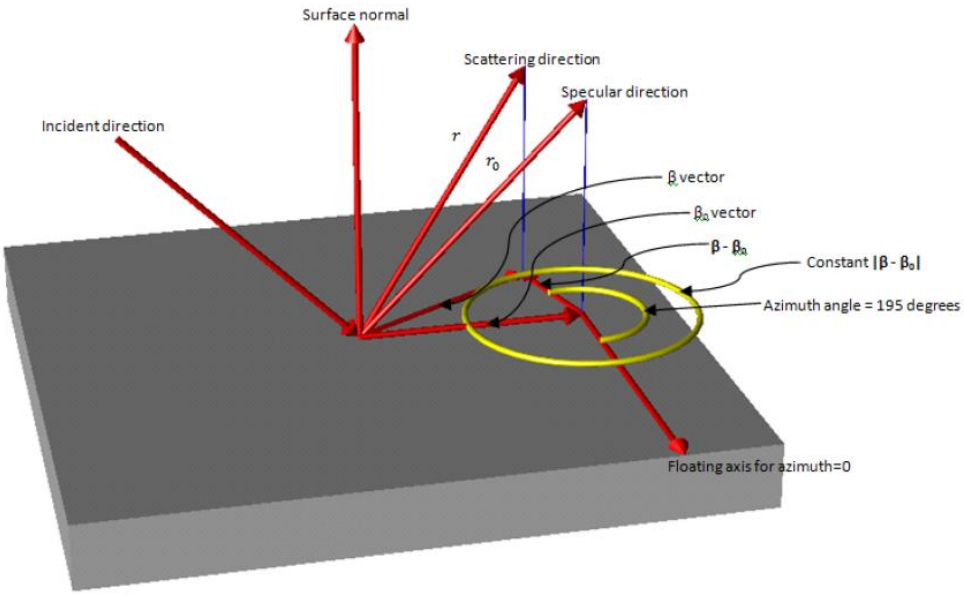

Figure 53: Angles and dimensions defining the BSDF in TracePro [66].

In TracePro the BSDF is defined by a list of azimuth angles and the magnitude $|\vec{\beta} - \vec{\beta_0}|$. For every combination of azimuth and $|\vec{\beta} - \vec{\beta_0}|$ there exist a BRDF and a BTDF value. To illustrate this, consider that the scattering direction vector in Figure 25 represents the magnitude of the BRDF for azimuth angle 195^o and for one value of $|\vec{\beta} - \vec{\beta_0}|$. As further illustrated in Figure 53 a ring of constant $|\vec{\beta} - \vec{\beta_0}|$ has BRDF values for every azimuth angle. For BTDF the same relationship applies in negative y direction.

To test whether the BSDF surface property would produce good results a c-Si solar cell with textured pyramidal structures as displayed in Figure 51 has been optically modelled and tested. The dimensions of the pyramids are displayed in Figure 50. For simplicity the test is only performed for irradiance sources located at 0, 40, 70 degrees to the surface normal and it is only emitting light at 400 nm.

The BSDF surface property is created by the following method. A ray trace simulation is performed with the desired surface texture over a small area with AM1.5 global spectrum and incident irradiance of $1\frac{W}{m^2}$. The surface reflectance and transmittance distribution intensities are extracted via a candela distribution plot and exported from the ray tracing software. A data file is created. TracePro has a freestanding utility, the BSDF converter, which can convert candela distribution data into a BSDF data table. This exercise of exporting and converting is done for each wavelength and angle of incidence. After the conversion the BSDF files for each wavelength and angle of incidence are combined and imported to the ray tracing software as a surface property.

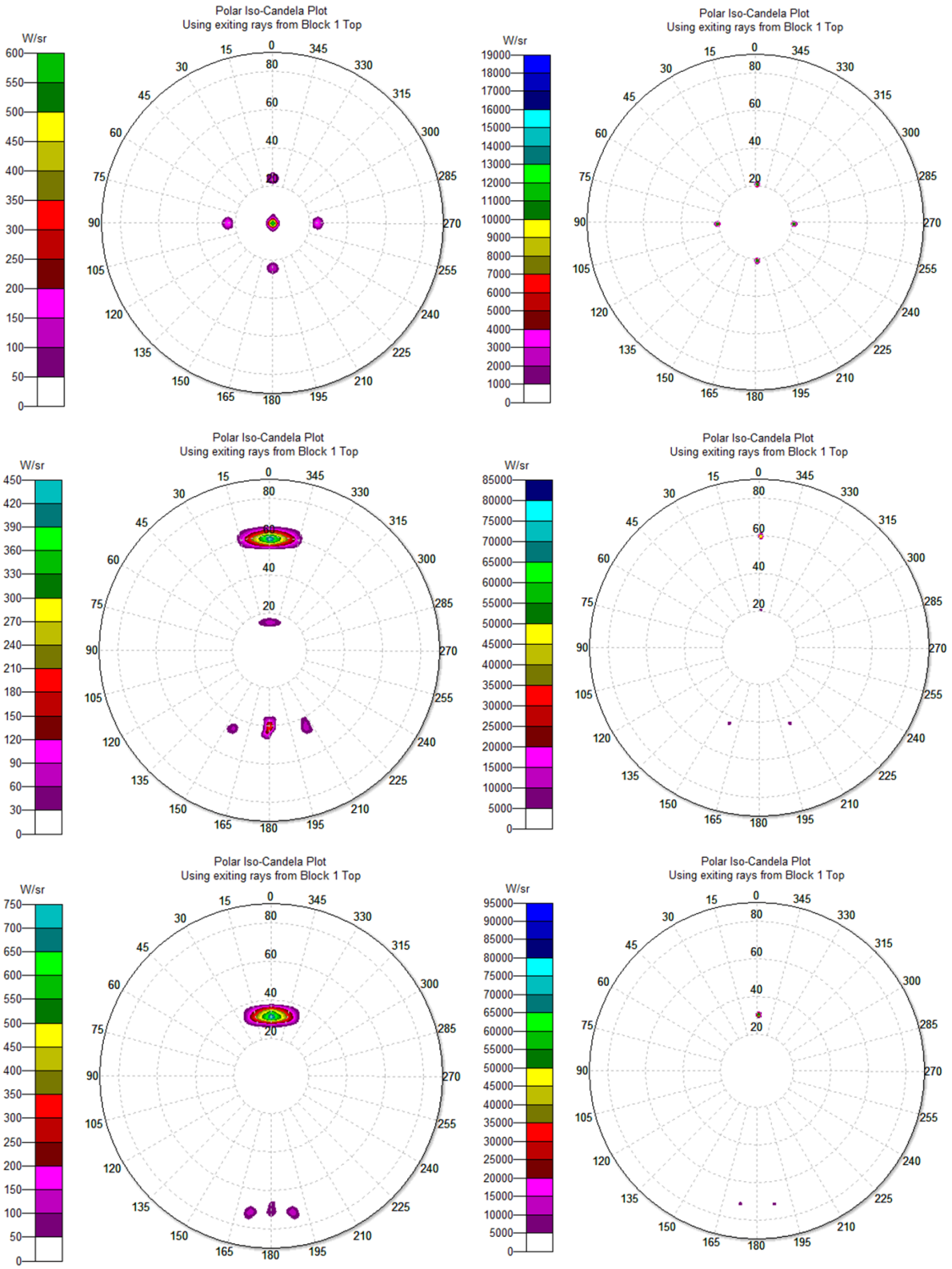

Figure 54: Candela polar plots for the BSDF surface property (left) and the original pyramidal surface structure (right). From top to bottom the plots represent respectively irradiance from 0, 40 70 degrees from the surface normal.

Note, the candela plots for the original surface can be challenging to assess (an explanation of how to assess the plots is presented further down). By viewing the BSDF plots first and then investigating the same impact positions in the original plot the radiant intensity ($\frac{w}{sr}$) can easily be spotted. Although the BSDF plot displays weaker radiant intensity ($\frac{w}{sr}$) it clearly demonstrates good familiarization with the original plot and if the distributed radiant flux was integrated the values would compare. The deviation in radiant intensity is caused by inaccuracy in the data processing when creating the BSDF file.

In conclusion the BSDF surface property gives a good representation of a textured surface. And in this study it will be used to represent the full surface of a textured solar cell.

In Figure 54 the BSDF surface property (left) can be compared with the original pyramidal surface (right). The results are presented in candela plots where the circular placed values represents azimuth angles and the vertical placed values represent the zenith angle. The reflection magnitude is given in radiant intensity ($\frac{w}{sr}$) and is best understood by viewing Figure 55. For a general sphere of radius r, any portion of its surface with area A=r^2 subtends one steradians (sr). The surface area of a sphere is $4\pi r^2$, thus the sphere measures $4\pi = 12.566$ steradians.

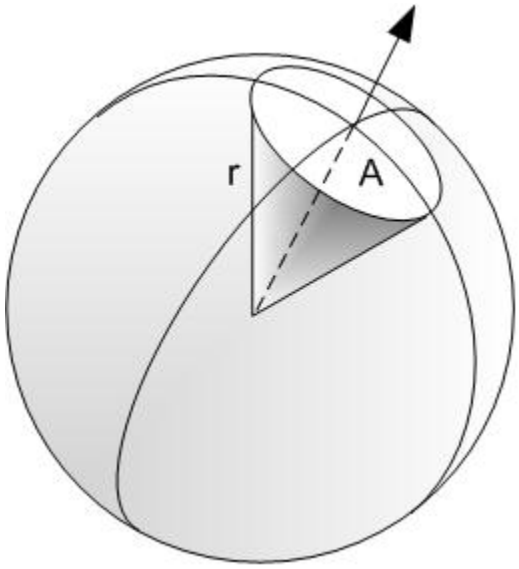

Figure 55: Representation of steradian [67].

4.2.2.2.2 Thin film coating

A thin film of antireflective coating can be used to lower reflection losses at many interfaces in a solar panel. For a single layer ARC (SLAR) optimum antireflection for light of wavelength λ, at normal incidence is achieved when the refractive index for the ARC is equal to the geometric mean of the refractive index for EVA and silicon, expressed in Eq. (34). The optimal thickness is expressed in Eq. (35).

$$n_{ARC} = \sqrt{n_{EVA} n_{Si}} \tag{34}$$

$$d_{ARC} = \frac{\lambda}{4n_{ARC}} \tag{35}$$

Double layer antireflective coatings (DLARs) operate on the same principles as SLARs. With two layers more parameters are available for optimization. And can produce lower reflection over a broader wavelength region [68]. For a DLAR, it can be shown that the optimum refractive indexes, n_1 and n_2, where layer 1 is the top layer, are calculated using Eq. (36) and (37). The corresponding optimum thickness d_1 and d_2 are given by Eq. (38) and (39) [69].

$$n_1^3 = n_0^2 n_{Si} \tag{36}$$

$$n_2^3 = n_0 n_{Si}^2 \tag{37}$$

$$d_1 = \frac{\lambda}{4n_1} \tag{38}$$

$$d_2 = \frac{\lambda}{4n_2} \tag{39}$$

A table showing different optimum properties of the antireflective coating was published in Richards PhD thesis and is reproduced in Table 6 [69]. In the calculations the design wavelength was 600nm. Taking n_{Si} at 600 nm to be 3.491, air-silicon (n_{air}=1) and EVA-silicon (n_{glass}=1.5) interfaces. Normally the design wavelength is chosen to be at the peak in the solar spectrum, i.e. 600 nm.

Table 6: A representation of optimum refractive index and thickness for antireflective coatings [69].

	air-Si	**EVA-Si**	**air-glass**
SLAR n_1	1.985	2.431	1.225
SLAR d_1 (nm)	75.6	61.7	122.5
DLAR n_1	1.580	2.070	1.145
DLAR n_2	2.495	2.856	1.310
DLAR d_1 (nm)	95.0	72.5	131.0
DLAR d_2 (nm)	60.1	52.5	114.5

ARC's are normally deposited by either atmospheric-pressure chemical vapour deposition (APCVD) or plasma chemical vapour deposition (PECVD). Common ARC's are titanium dioxide (TiO_2) n=2.25, silicon dioxide (SiO_2) n=1.45 and silicon nitride (Si_3N_4) n=2-2.2 [16]. Since neither PECVD nitrides and oxides are necessary stoichiometric, they are sometimes represented as SiNx and SiOx [16].

The main benefit of using thermally grown silicon dioxide for an ARC is that it has good passivation features. Recombination at the top surface is due to surface defects like non-terminated dangling bonds. Growing a thermal oxide layer on the surface reduces surface defects and therefore increases quantum efficiency [16].

In this thesis a titanium nitride ARC is used; the optical properties are shown in Figure 56. The optical properties for the ARC where published in a paper by Richards (2002), unfortunately the properties covered only the wavelength region between 350nm and 1320 nm [69]. In this thesis the incident spectrum has wavelengths starting from 280 nm. Therefore the refractive index and extinction coefficient was linearly extended to also cover the region between 280 nm and 350 nm. The extended area is pointed out in the graphs by the dashed lines. In section 4.2.3 this modified ARC will be tested and it is shown that it can be used to accurately represent a typical ARC. The reader should note that the linear extension approach was chosen because optical data for ARC covering the whole solar spectrum is difficult to obtain.

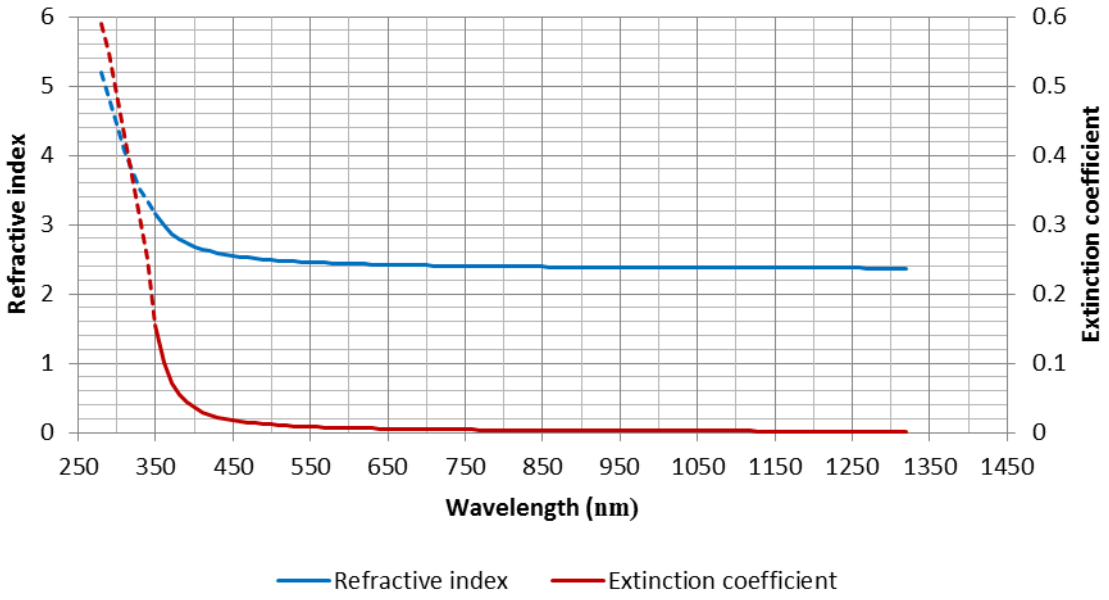

Figure 56: Optical properties of a TiO2 ARC are shown [69]. The properties have been linearly extended in the wavelength region between 280nm and 350 nm.

4.2.3 Comparison of both models with a real solar cell, other models and literature

In this section the two optical models of a c-Si solar cell developed in the previous sections of this chapter are presented. To assess the design limitations the optical models will be validated by comparisons with literature and a commercial product. This process is done in the following order; first results from literature are presented and discussed, subsequently the solar cell models developed in the previous section will be presented.

4.2.3.1 Reflection results from literature

In a study by Lien et al. (2011) experimental reflection measurements for a bare c-Si cell were compared to reflection results from a ray tracing simulation [63]. Lien investigated three different KOH etched surfaces, shown in Figure 57. The textures are categorized as uniform, mostly small and mostly big pyramids. The experimental measurements demonstrate similar spectral reflection with the simulation results from using simplified optically modelled pyramidal structures, as displayed in

the plots. Unfortunately the measurements are limited, covering only the wavelength range between 400 nm and 800 nm.

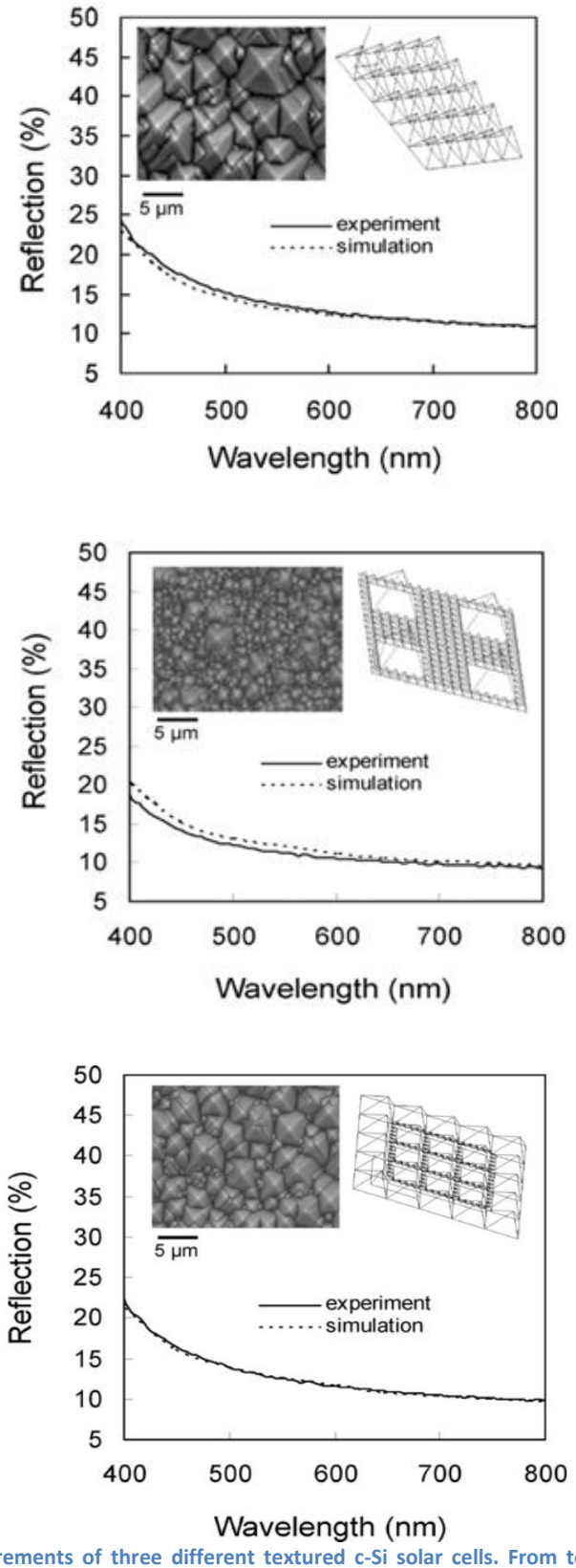

Figure 57: Reflection measurements of three different textured c-Si solar cells. From top to bottom the surfaces are characterised by the following names; regular upwards pyramids, mostly small pyramids and mostly big pyramids. As seen in the plots, ray tracing simulations of the optical models displayed in the right corner (of the plots) show similar spectral reflection compared with the experimental measurements.

In 2010 S.C. Baker and K.R McIntosh introduced OPAL, an excel macro program that simulates the front surface optics of a solar cell [56]. Complex optical structures are normally simulated with more advanced ray tracing software's. However ray tracing programs can require very long computational time. OPAL offers a fast and accurate means to analyse the complicated optics of a solar cell. The program can be used to simulate the effects of ARC, encapsulant, glass and different solar cell surface morphologies.

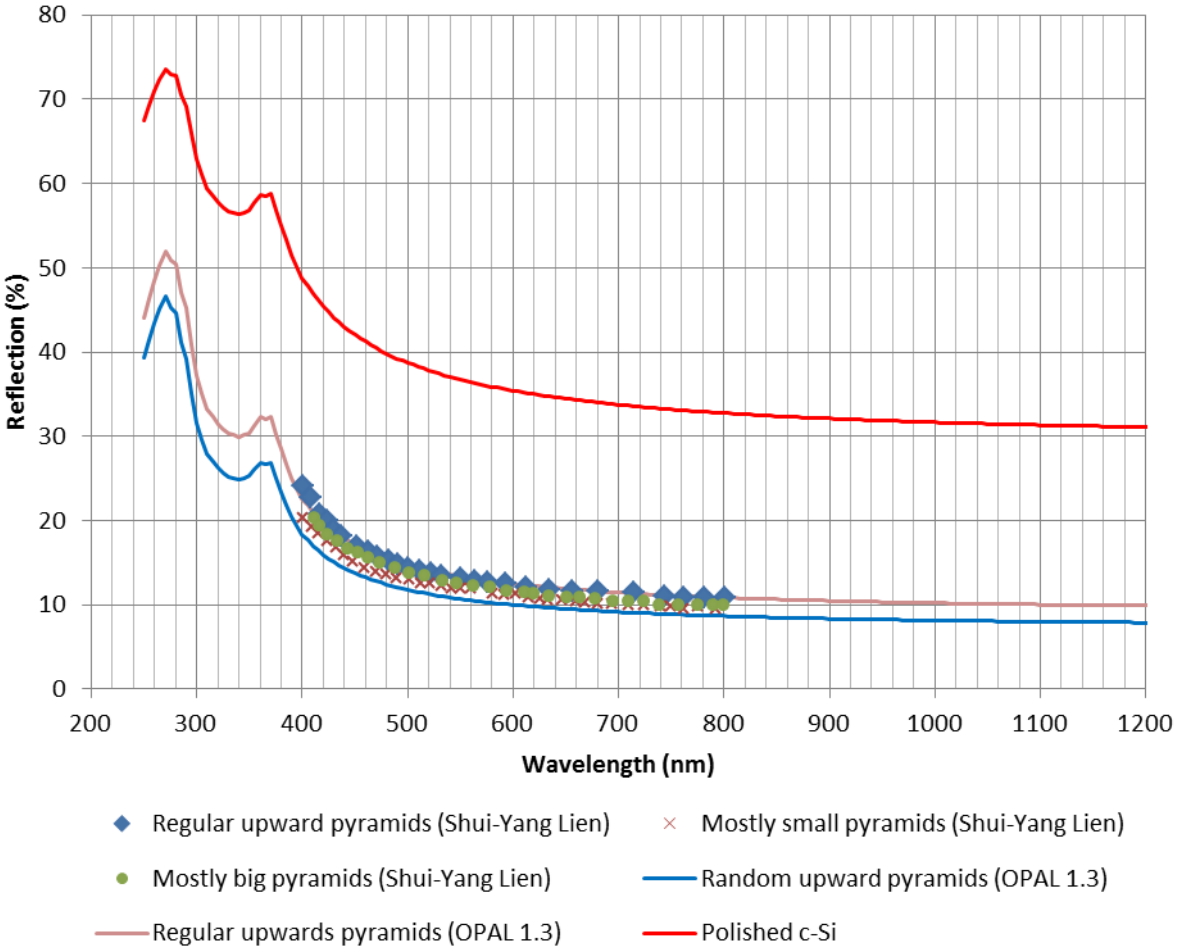

Figure 58: Reflection of different surface structures for a c-Si solar cell. The three dotted lines represent measurements done by Lien et al. [63]**. The red, pink and blue line represent data obtained from a simulation in OPAL** [56]**.**

In Figure 58 reflection for different surface structures on a c-Si solar cell are shown. The simulation results from OPAL correspond well with the measurements performed by Lien et al (2011) and both OPAL and Lien show that a randomized and non-uniform texture has the lowest reflection over the solar spectrum.

In this thesis two models of a c-Si solar cell have been developed (section 4.2.1 and 4.2.2), a simple model with optical response following the EQE with Lambertian reflection, and a more realistic model with optical properties of intrinsic silicon, textured surface and ARC. In the next section the more realistic model will be presented and evaluated by examining reflection losses. The evaluation will be followed by a comparison of both models with regards to light absorption.

4.2.3.2 Reflection simulation of complex cell model

This section is allocated to evaluating the reflection losses from the more realistic model developed in section 4.2.2. Previously a surface texture named Extended mostly big was developed to accurately portray the surface of a bare c-Si solar cell and together with an ARC the reflection from the optical model should exhibit the same behaviour as a real solar cell. Following a reflection test performed with the model in a ray tracing simulation is presented.

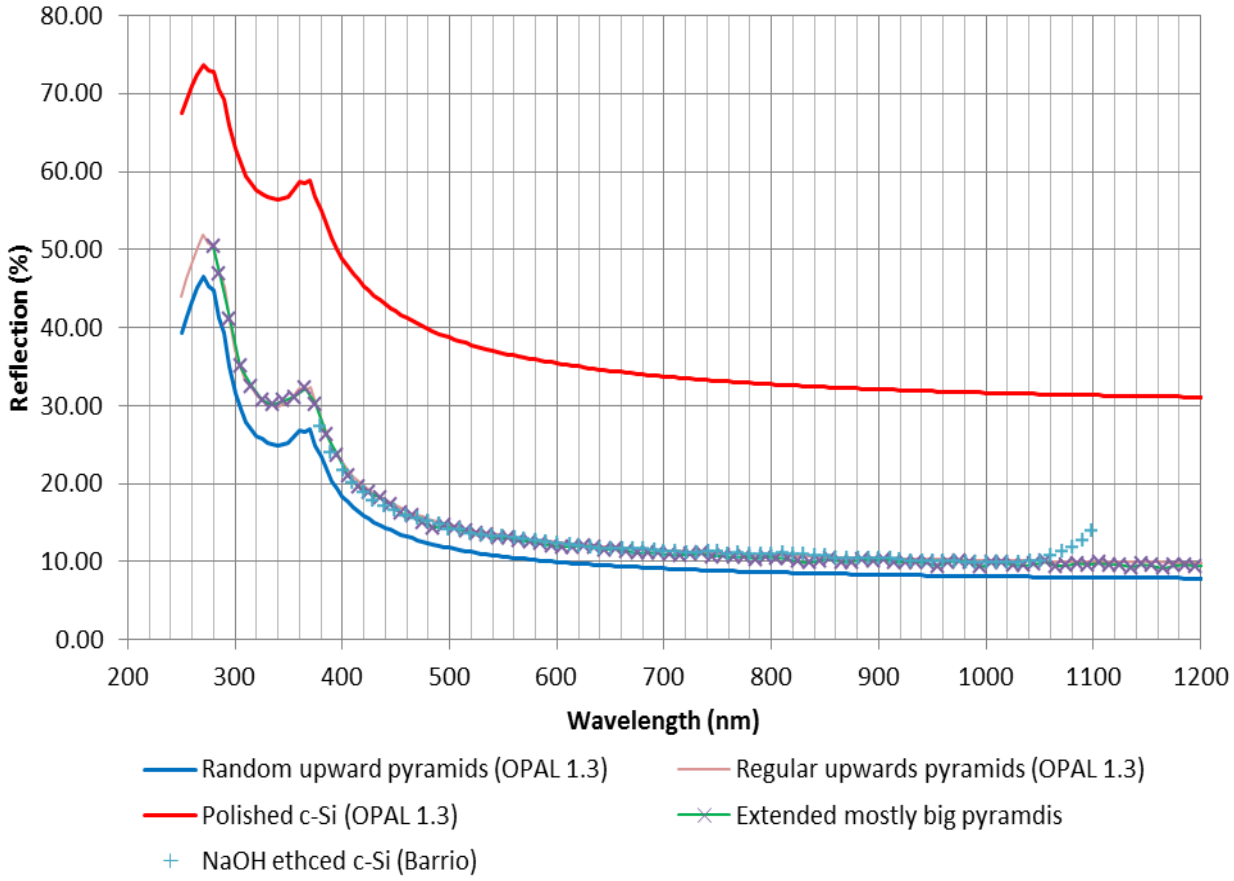

Figure 59: Reflection from textured c-Si solar cells.

In Figure 59 reflection from the optically modelled c-Si solar cell with the Extended mostly big surface texture is shown. Also shown is the simulation results from OPAL and experimental reflection measurements for a mono c-Si textured solar cell from a study by Barrio et al. (2011) [70]. As displayed the complex cell model corresponds very well with the simulations from OPAL and measurements from Barrio.

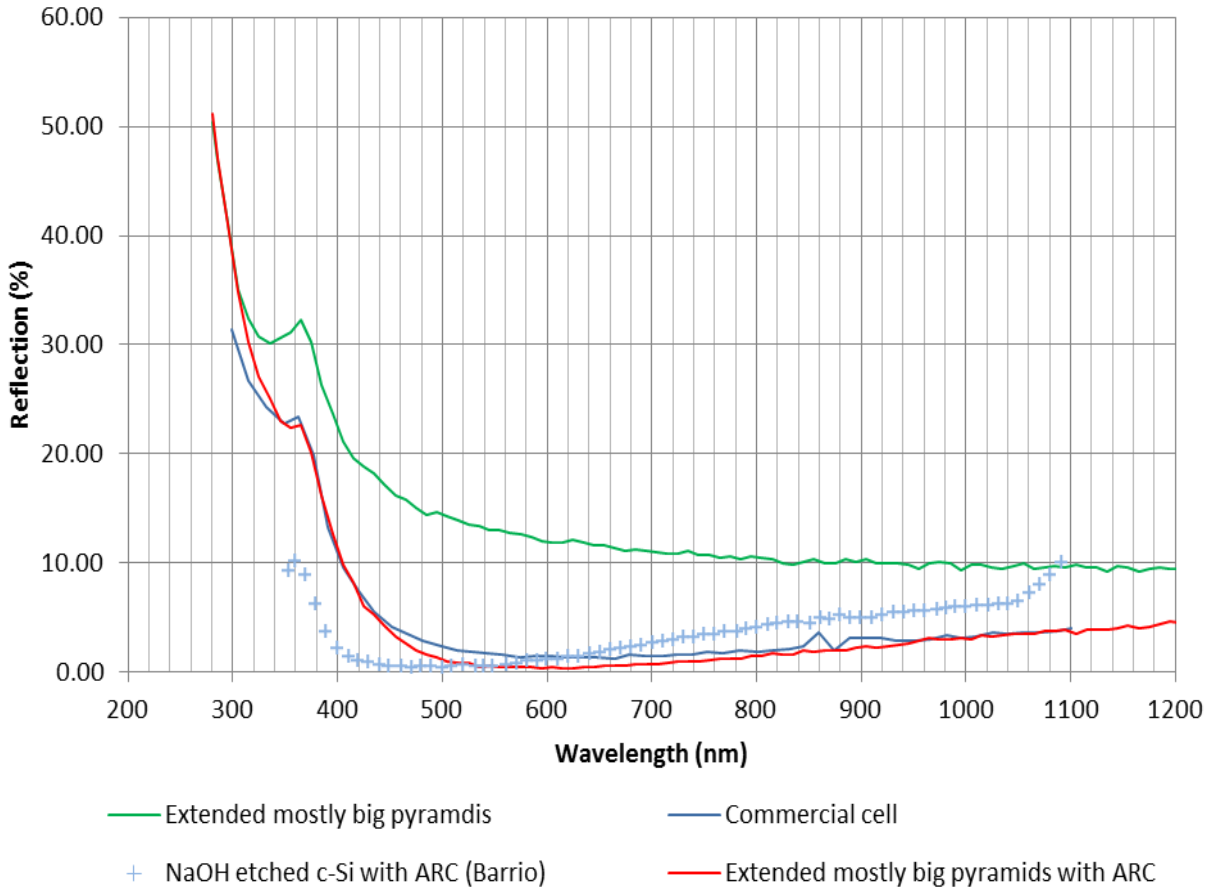

Figure 60: Reflection from textured c-Si solar cells with ARC. The reflection measurement for the commercial cell is from an in-house test.

Normally c-Si solar cells are coated with ARC to further reduce reflection losses. A 65 nm thick TiO2 ARC was applied to the textured surface of the Extended mostly big model, represented by the faded green line in Figure 60. The blue line represents the benchmark, a commercial c-Si solar cell. An inspection shows that the largest difference between the model and the commercial solar cell is about 1% at approximately 550 nm. In conclusion the extended mostly big model compares very well with the commercial model, and it is expected that it will produce realistic results.

4.2.3.3 Simple cell model vs. complex cell model

In the following three figures results from ray tracing simulations for the complex cell model and simple cell model are compared. The solar cells which measure 155mm x 155mm are exposed to three different solar spectrums: AM1, AM1.5 and AM5 each emitting 1000 watts. The angle of incidence for the three spectrums corresponds to the suns altitude at the respective AM. In the simulation incident light is either reflected, transmitted or absorbed in the cells. The results are expressed by I_{SC} as a function of wavelength.

The I_{SC} is calculated by the following method:

1. For the simple cell model, the e-h pairs generated in the cell is the product of EQE and the spectral incident light power (i.e. $EQE(\lambda) * P_{in}(\lambda)$). Solving for I_{SC} in Eq. (5) and performing the calculation for each wavelength returns the current.
2. For the complex cell model, the e-h pairs generated in the cell is the product of what is absorbed (following the Beer-Lambert equation and the absorption coefficient of silicon) and the IQE. Solving for I_{SC} in Eq. (5) and performing the calculation for each wavelength produces the current. The reader should note that Eq. (5) has now been modified, for this calculation $EQE(\lambda) * P_{in}(\lambda)$ is now represented by $IQE(\lambda) * P_{abs}(\lambda)$, where P_{abs} represents absorbed watts in the cell.

The reader should note that the simple model is based on an EQE of a screen-printed c-Si solar cell, therefore the more realistic cell model has been fitted with bus bars and fingers, and now depicted the complex cell model. The design area covered by the metallization is described in section 4.1.3 which corresponds to the same fractional coverage as stated in the paper where the EQE is obtained.

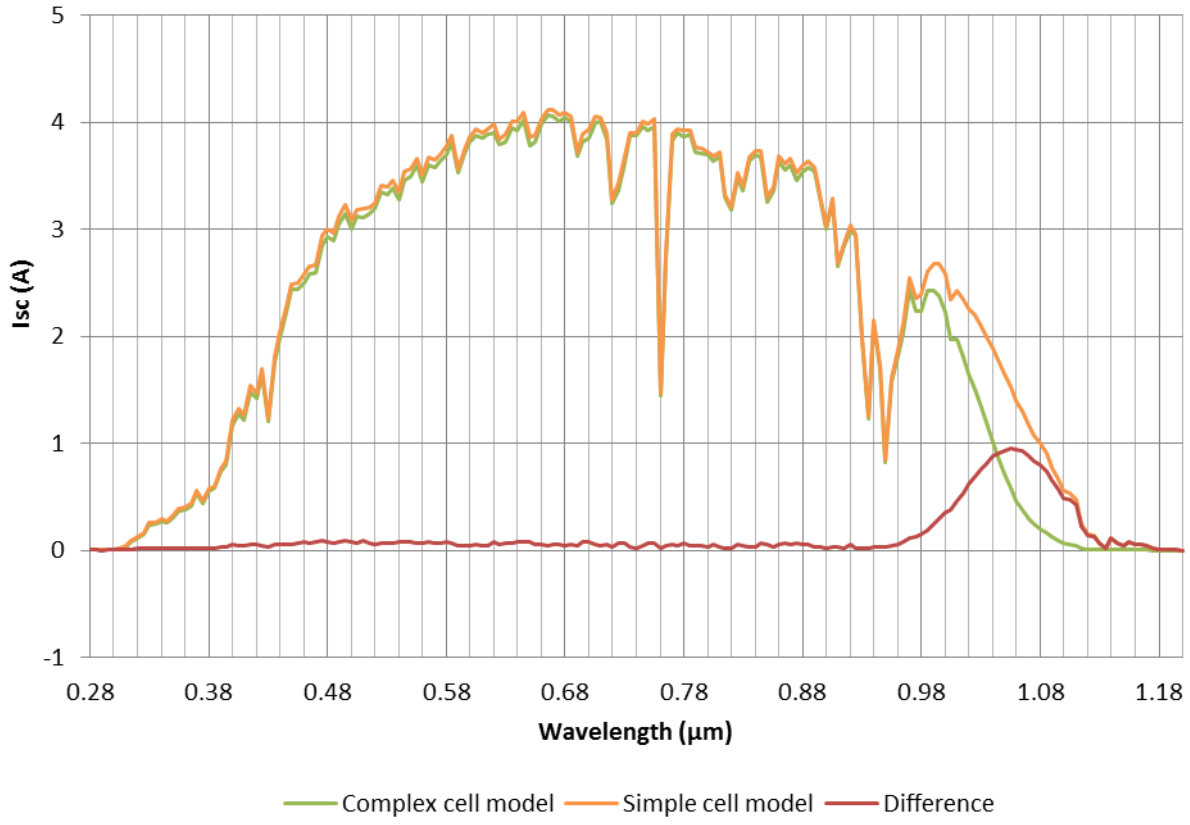

Figure 61: Simple cell model vs. complex cell model under AM 1 spectrum and normal incidence.

In Figure 61 results for the two models from a ray tracing simulation under AM 1 spectrum and normal incidence are shown. The red line, displaying the difference, indicates that the models compare very well up to approximately 0.96 µm. From 0.96 µm and the wavelength region above the complex models reflection is comparably higher, leading to lower absorption.

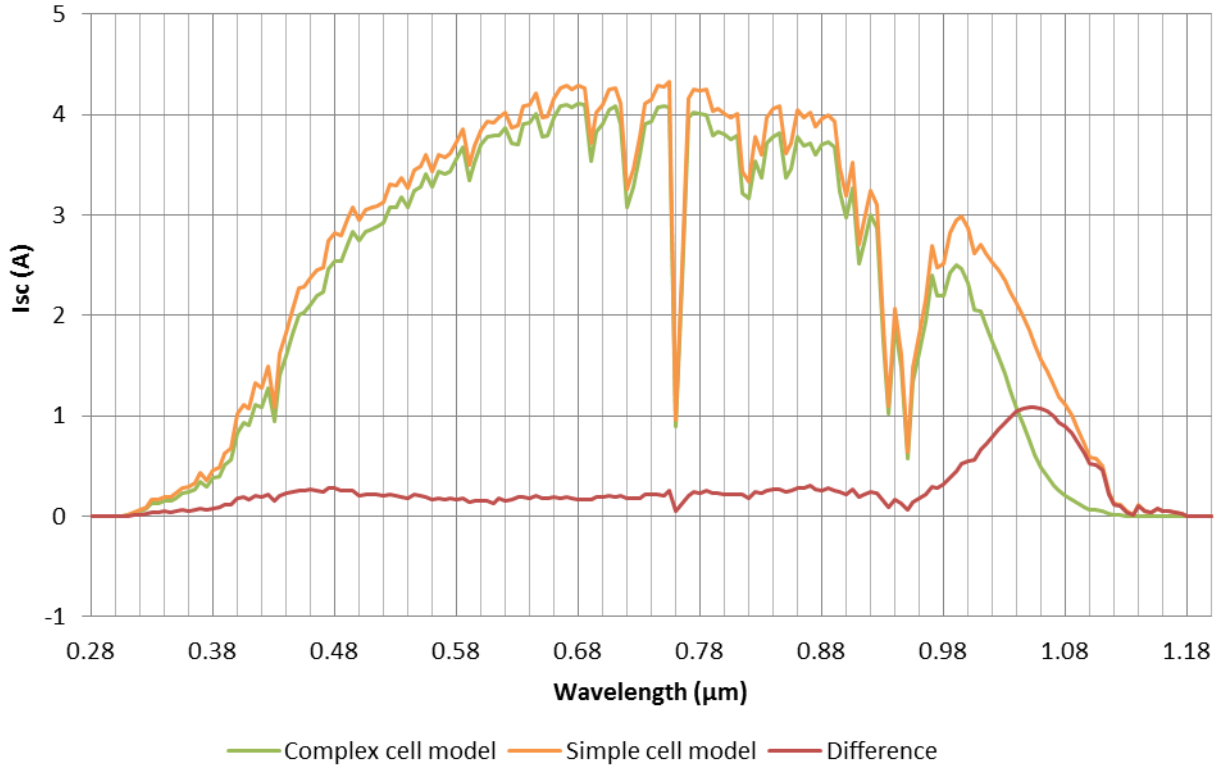

Figure 62: Simple cell model vs. complex cell model under AM 1.5 spectrum and angle of incidence 48.2 degrees.

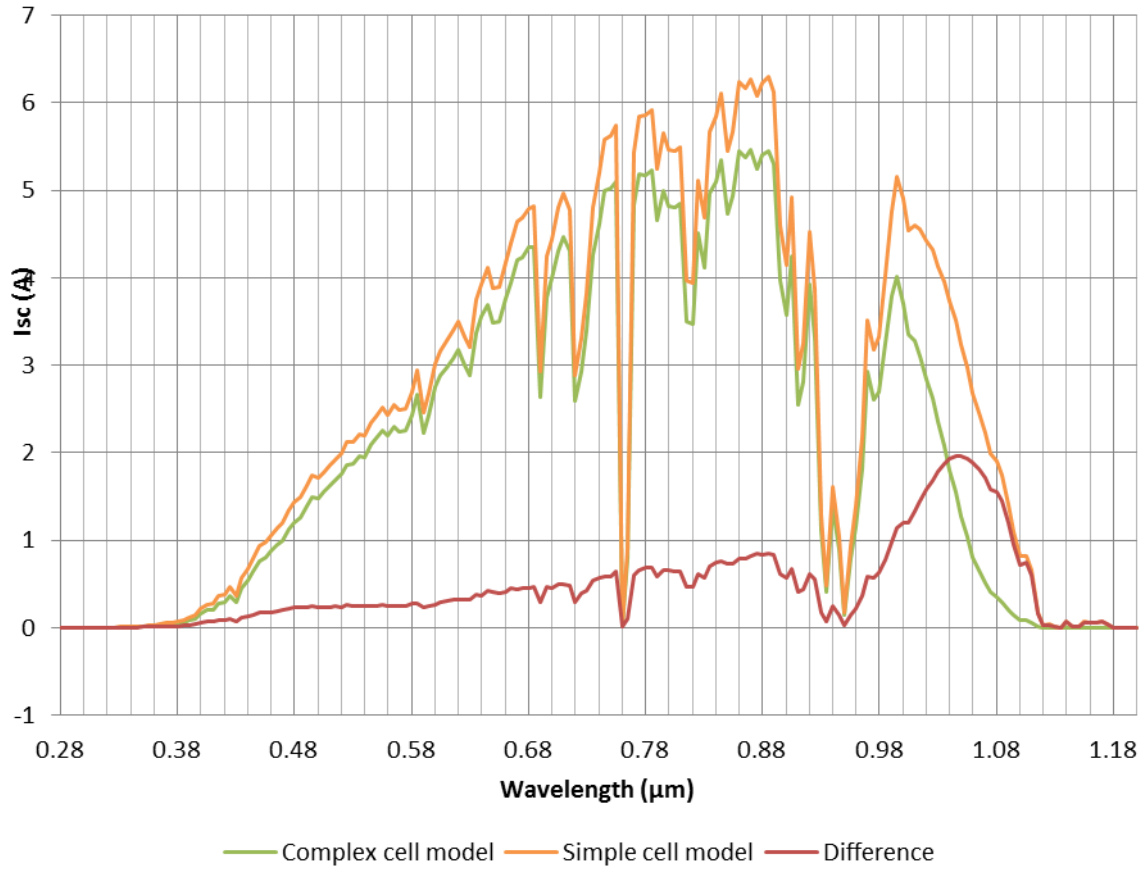

Figure 63: Simple cell model vs. complex cell model under AM 5 spectrum and angle of incidence 78.5 degrees.

Figure 62 and Figure 63 clearly shows that the angle of incidence and AM influences the behaviour of the models. As seen the complex cell model absorbs less with increasing angle of incidence compared to the simple cell model, expressed by the red line. A naturally effect since the simple cell model does not account for angle of incidence. Which means that for the complex cell model reflection losses will increase for higher angles of incidence while for the simple cell model reflection losses stays constant, and is independent of angle of incidence.

4.3 Optical models of a solar panel

By assembling all the materials discussed in this chapter three optical models of a solar panel have been developed. They are descriptively named:

- Simple model
- Extended simple model
- Complex model

4.3.1 Complex model

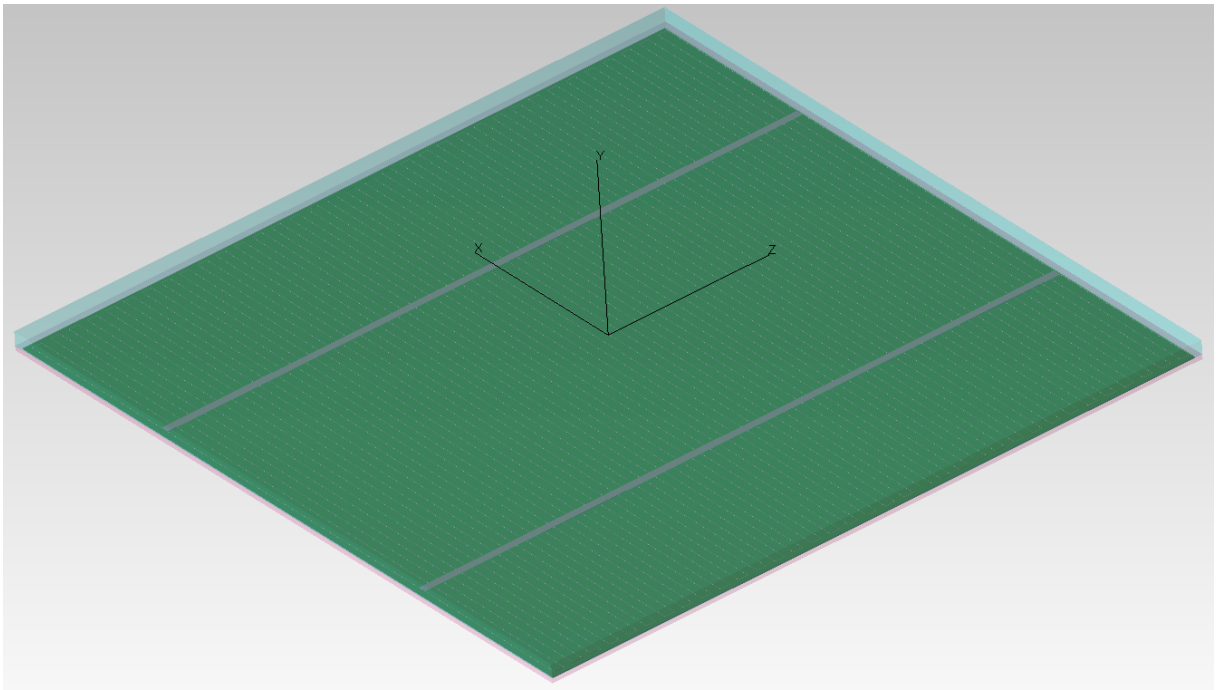

Figure 64: A 3D picture of the complex solar panel model showing glass, bus bars, fingers and the cell

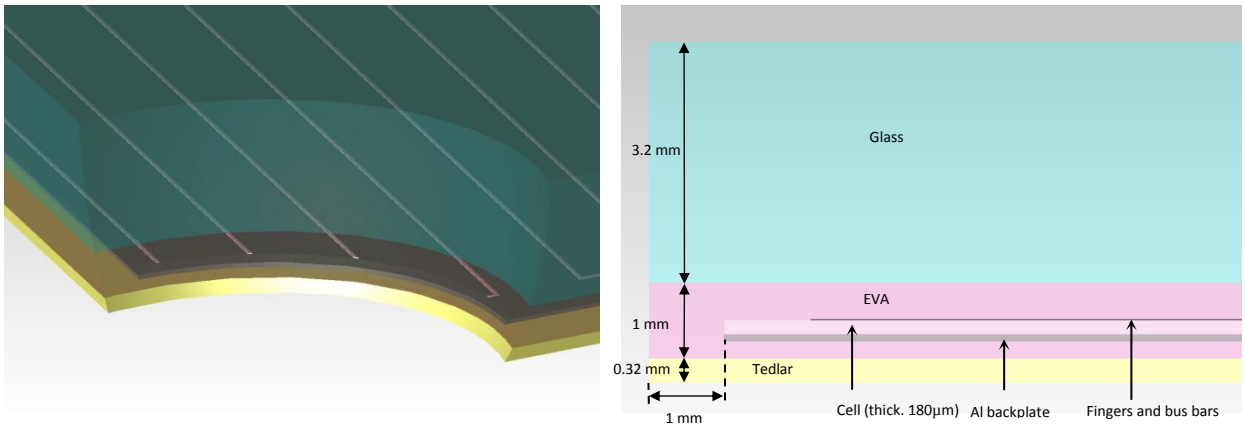

Figure 65: The picture to the left shows a cut out of the complex solar panel model. The picture to the right shows a cross section view of the complex solar panel model.

The complex solar panel model encapsulates all the features in a normal solar panel. To account for the spacing between solar cells in a panel a space of 1mm is added as shown in the figure. Correspondingly the cell and the back plate measures 155mm x 155mm, while the EVA, Tedlar and glass measures 157mm x 157mm. The solar cell model used here is the complex cell model described in section 4.2.2.

4.3.2 Extended simple model

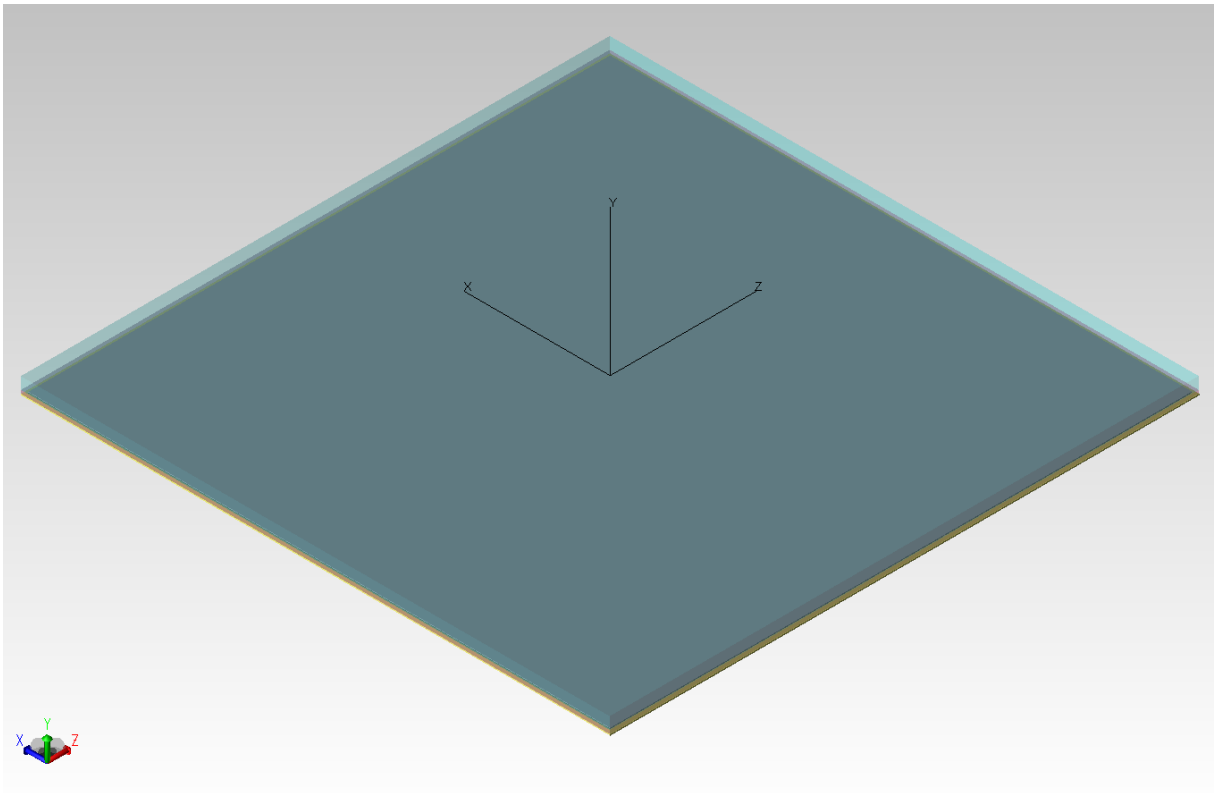

Figure 66: A 3D picture of the extended simple solar panel model showing the glass and the cell.

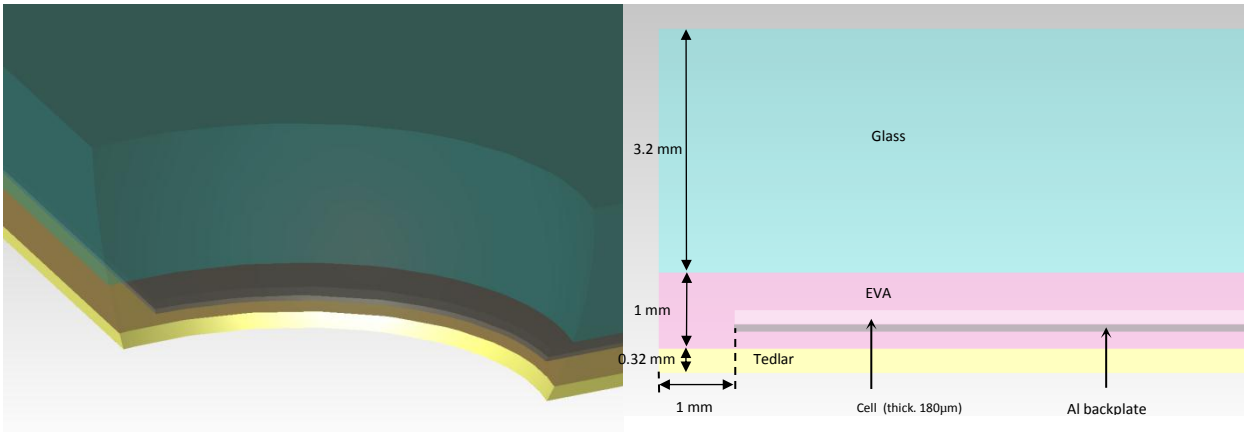

Figure 67: The picture to the left shows a cut out of the extended simple solar panel model. The picture to the right shows a cross section view of the extended simple solar panel model.

The extended simple solar panel model encompasses some of features from the complex model and some of features from the simple model. To account for the spacing between solar cells in a panel a space of 1mm is added as shown in the figure. Correspondingly the cell and the back plate measures 155mm x 155mm, while the EVA, Tedlar and glass measures 157mm x 157mm. The solar cell model used here is the simple cell model described in section 4.2.1. Since this model compared with the simple solar panel model has a 1mm space to account for spacing in between cells it features the properties of the simple cell on the top surface and the sides of the cell.

4.3.3 Simple model

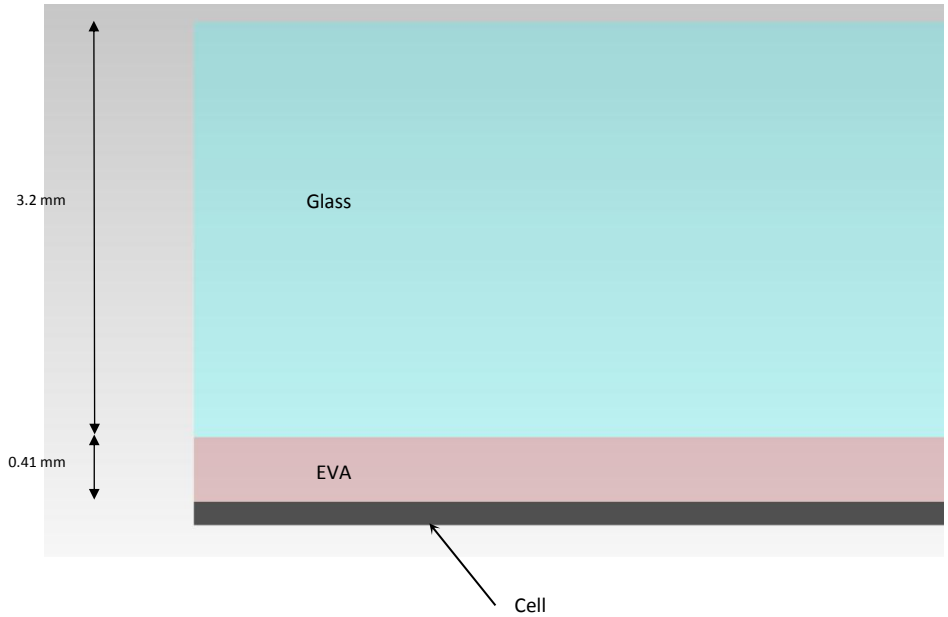

Figure 68: Cross section of the simple solar panel model.

The simple model is the most limited model developed in this thesis. A 3.2 mm top layer of glass is followed by a 0.41 mm thick layer of EVA and on the bottom the solar cell is represented by the simple cell model described in section 4.2.1.

4.3.4 Size reduction for computational time

Initial testing emphasized the need for adjusting the models displayed in the figures above considering the simulation time. Two modifications where imposed:

1. The sides of the model were fitted with perfect mirrors, and therefore the model replicates the behaviour of solar panel of infinite area.
2. Due to symmetry, the modelled solar panels were cut in 4 parts, and only a quarter parts was used in the simulations. An illustration of how the quarter piece was "cut" from the full size model is shown in Figure 69. The sides of the quarter size models where subsequently fitted with perfect mirrors to re-create an infinite area solar panel.

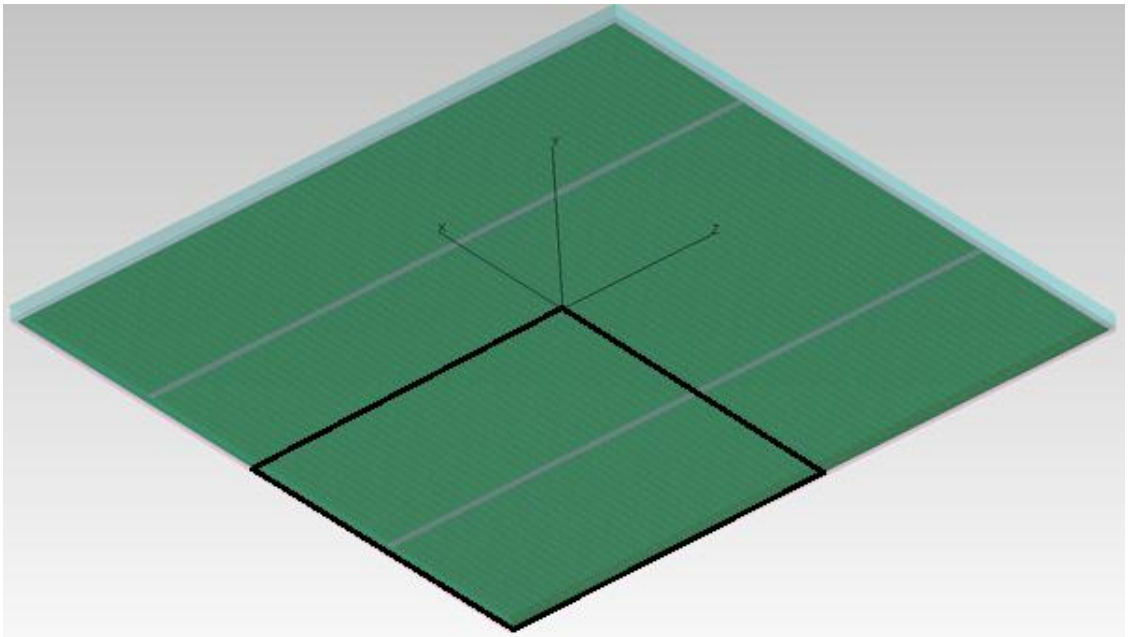

Figure 69: Illustration of how the optical solar panel models are cut (black quadrant) to a quarter size to improve simulation time.

One of the goals of this thesis was to compare the simple solar panel model and the complex solar panel model. And thereby evaluate what level of complexity is necessary to accurately portray a solar panel in an optical simulation. Unfortunately technical issues caused by the models high complexity prevented any full simulations from being performed on the complex solar panel model.

The main contrast between the simple and the complex model is the solar cell. It was shown in section 4.2.3 that the two cells performed relatively similarly under different incidence spectra. The largest shortcoming of the simple cell is that it does not account for angle of incidence, resulting in a higher absorption at increased angles of incidence. Also the simple model does not include the spacing in-between the cells, as a result the extended simple model was developed. In chapter 6 these two models are tested and compared.

5 Enhancing light absorption by optimization of the glass cover

A wide range of methods and products made for reducing reflection by optimization of the glass cover are available today. In Figure 1 typical anti-reflective glasses were presented with the claimed increase in I_{sc}, P_{max} or energy production relative to plain glass cover. In this chapter five available anti-reflective glasses are described in more detail, including deeply textured glass, rough glass and thin film ARC. Several claims have been made in published papers and brochures about the performance of these products, and with the modelling tools used in this study these claims are investigated.

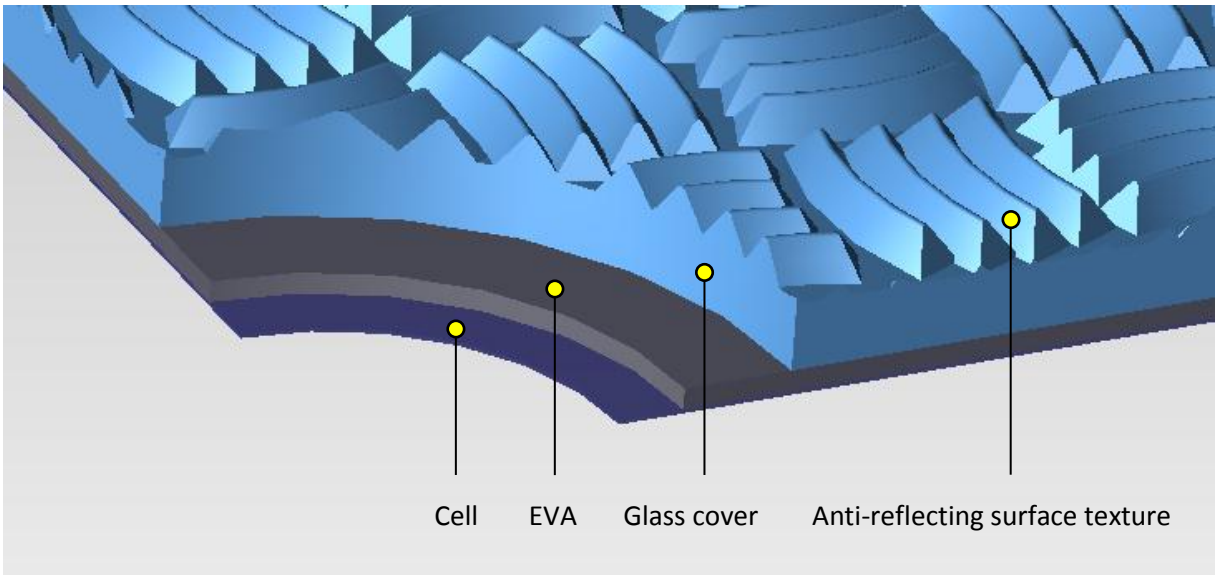

Figure 70: Illustration of textured glass cover on top of a photovoltaic panel structure (screenshot from Tracepro), together with the simple model for a solar panel described in chapter 4, which consists of a glass cover, EVA, and the solar cell in the form of a surface property based on external quantum efficiency data. The texture pattern is pyramidal grooves.

The glass cover of the photovoltaic panel is primarily made as protection for the structure against weather, dust, etc. It is desirable that the cover glass has optimal transmittance properties for light of the solar spectrum. Texturing the glass cover surface as well as using anti-reflective coating (ARC) has been proven effective in reducing reflection and can be done in several ways. The following anti-reflective features are investigated relative to plain glass cover:

- Inverted pyramidal texture
- Pyramidal grooves texture
- Cube corner geometrical texture
- Rough glass
- Thin film anti-reflective coating

5.1 Macro texturing

Macro texturing includes visible texture down to millimetre sized features, which can be random or repetitive patterns. Repeating patterns in the market today include e.g. pyramids, inverted pyramids, sinus shaped, wave shaped, cones, bumps, holes and more. Some of these features can be seen in Figure 71. These repeating patterns can be re-occurring and symmetrical in both x and y direction, or in just one orientation. In the latter case oblong grooves are the result. The texture can be applied by e.g. heating up the glass, force in the pattern by pressure through a roller and then cooling the glass.

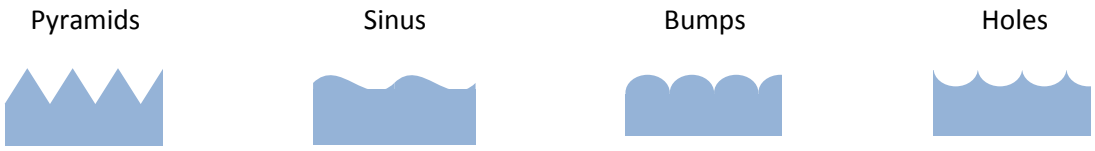

Figure 71: A selection of common texture patterns used on glass surfaces to reduce reflectivity. Pyramids, sinus-shape, bumps and holes are simple geometrical features that can be replicated in ray tracing simulations.

Saint-Gobain have developed glass covers for photovoltaic panels that in addition to manufacturer's brochures are investigated in several published papers[5][71]. Securit Albarino P and Albarino G are examples of such, and are textured as inverted pyramids and pyramidal grooves, respectively. These are shown in Figure 72.

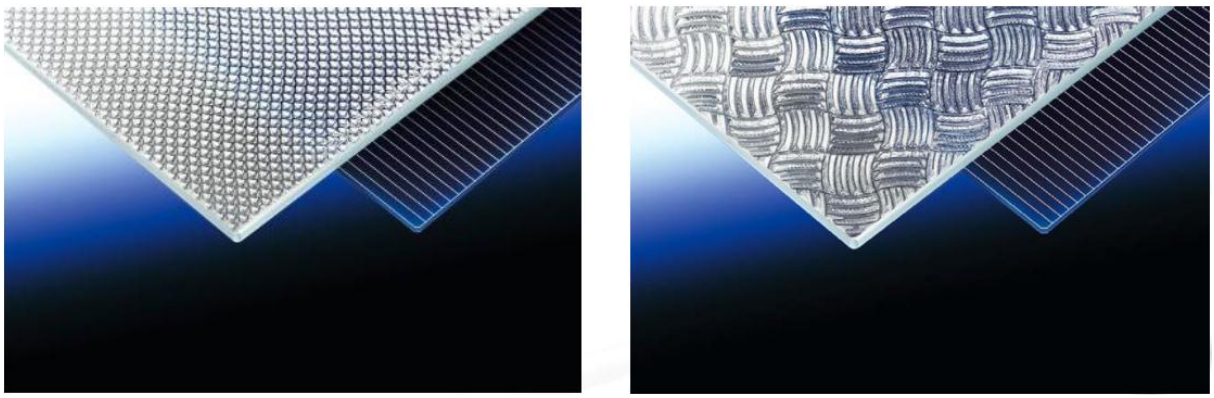

Figure 72: Textured glass cover surfaces by Saint-Gobain. Albarino P to the left is randomized inverted pyramids. Albarino G to the right is bumps as curved grooves which is part of a larger pattern which repeats in both x and y directions. The pictures are from manufacturer's brochures.

For Albarino P the bottom to bottom period is about 2.6mm. The depth of the inverted pyramid holes are about 0.9 mm. For Albarino G the period between the groove peaks is about 2.6 mm while the length of the grooves is about 11 mm. Note that the grooves are curved, increasing the uncertainty in the latter dimension. The height of the grooves is about 1.4 mm.

The geometrical shapes for these products are the authors' approximations. The models are not made directly from manufacturer's data. No guaranties are made regarding the precision of these replicated geometries.

In addition the reference shape of the texture deviates from actual texture shape because of practical limitations in the manufacturing process, as can be seen in Figure 73.

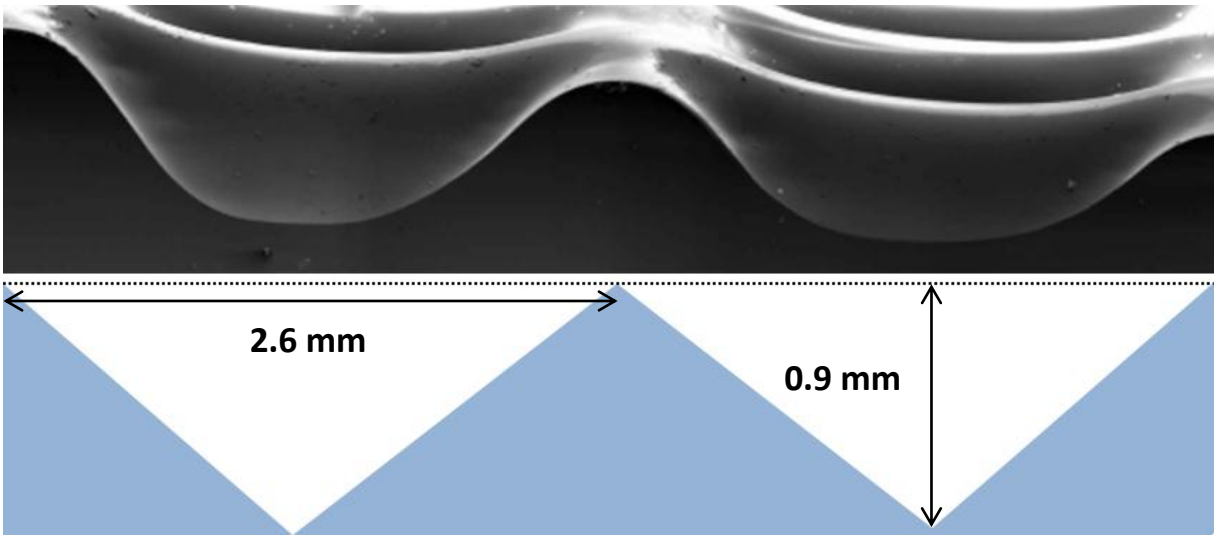

Figure 73: Pyramidal structure in practice compared to principal sketch. Rounding of the edges makes a visibly different shape. The picture on top is a magnified picture of Albarino P cover glass with inverted pyramids, from manufacturer's brochures.

The rounding of the edges of commercially available products can affect the results of the comparisons between computer models, often with "perfect" geometrical patterns, and measurements. These effects are taken into account when modelling textured glass covers in the ray tracing software (see Figure 74).

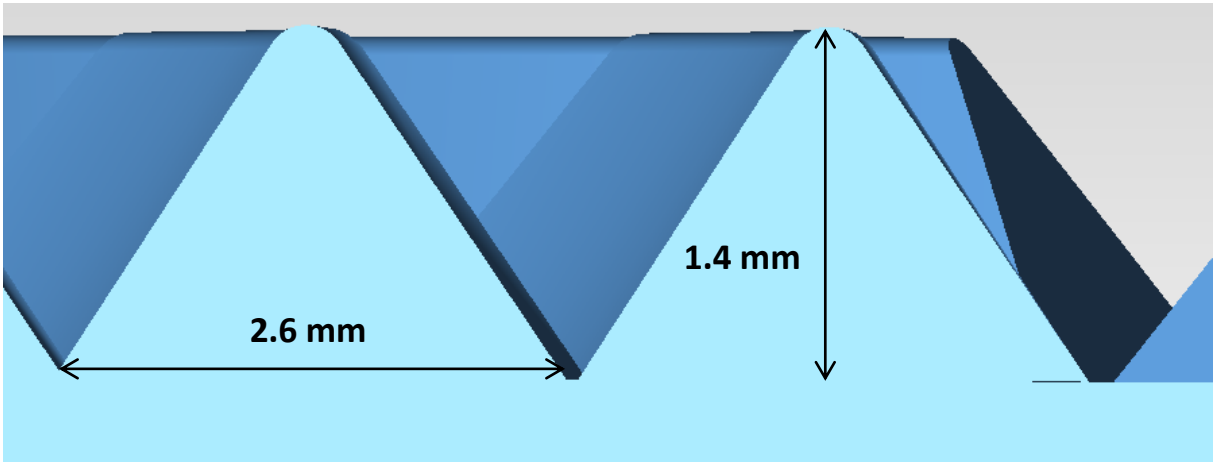

Figure 74: Cross section of the CAD model for Albarino G. These are the authors' estimations and not made directly from St. Gobain's product.

The claimed gain in efficiency for the solar cells with glass cover of the inverted pyramids texture is relative to solar modules with Albarino T glass cover from the same producer and given as follows. The change in short circuit current, I_{SC}, and maximum power, P_{MAX}, under standard test conditions (STC) for Albarino P is 2.7% and 2.9%, respectively [5]. The gain in energy yield for modules tested outdoors one a fixed plane during a two year period is 3.9% and 4.3% for year 1 and year 2, respectively.

The claimed gain in efficiency for clear sky conditions compared to cloudy sky conditions is shown in Figure 75. The data is extracted from Betts et al. [72]. The efficiency is the gain in short circuit current I_{SC} normalized to the irradiance P_{in} relative to the solar panel with plain glass cover (Albarino T).

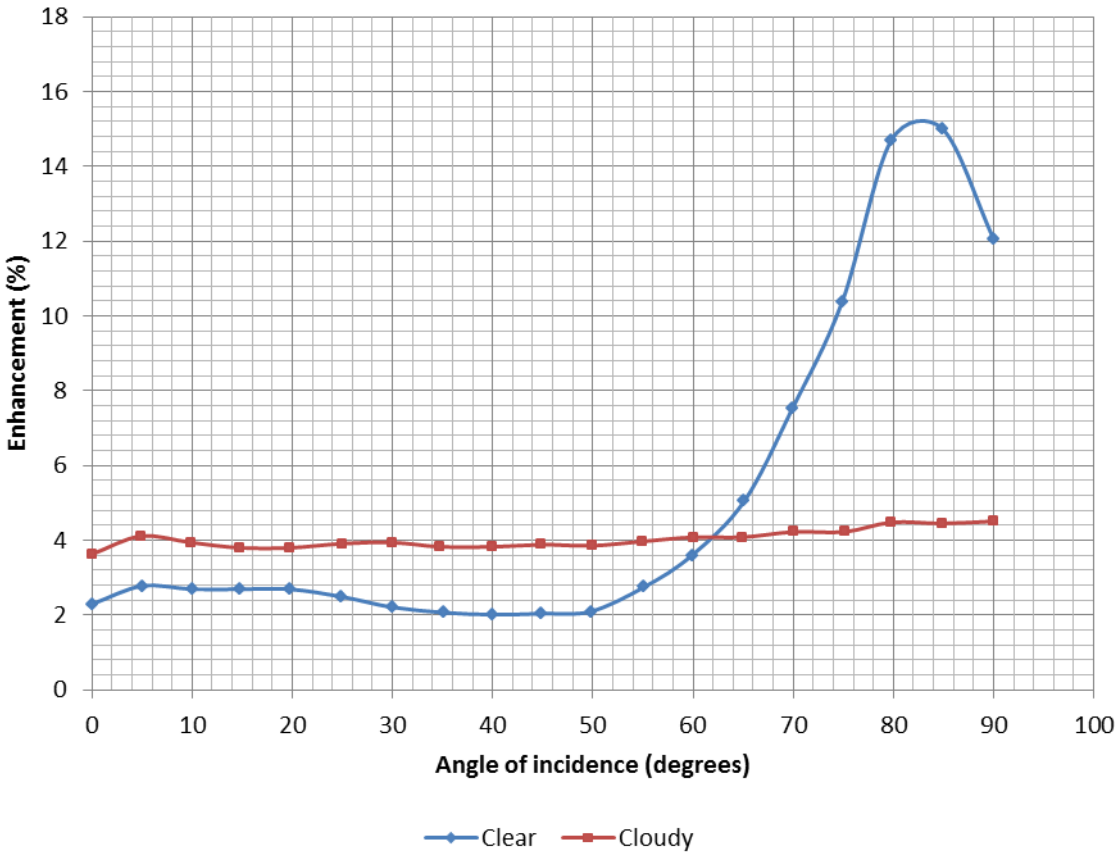

Figure 75: Claimed enhancement of I_{sc}/P_{in} for textured glass covered solar panel relative to plain glass covered panel (Albarino P versus Albarino T cover glass). The blue line shows the enhancement under clear sky conditions and the red line shows the enhancement under cloudy sky conditions [72].

The almost constant gain in normalized I_{SC} of approximately 4% under cloudy sky conditions for solar panels with textured glass covers is of high interest in this thesis. This might have grater implications in choice of solar panel design in areas with high cloud cover than the performance under clear sky conditions.

It is also possible to apply surface texture to a thin layer of acrylic plastic, with refractive index close or equal to that of glass, which is applied to the glass surface. The absorption and reflection effects from this layer are assumed to be equal to that of glass when optically modelling such textures in this thesis.

SolarExcel, recently acquired by DSM Advanced Surfaces, is an example of a manufacturer that develops polymeric sheets with anti-reflective light-trapping texture to be applied to glass covers. The sizes of these textures vary, down to 500 µm height, which is mentioned to be minimum height in the patent that is accessible online [73]. An example of such patent made is described by Ulbrich et al. (2012) and shown in Figure 76 [74].

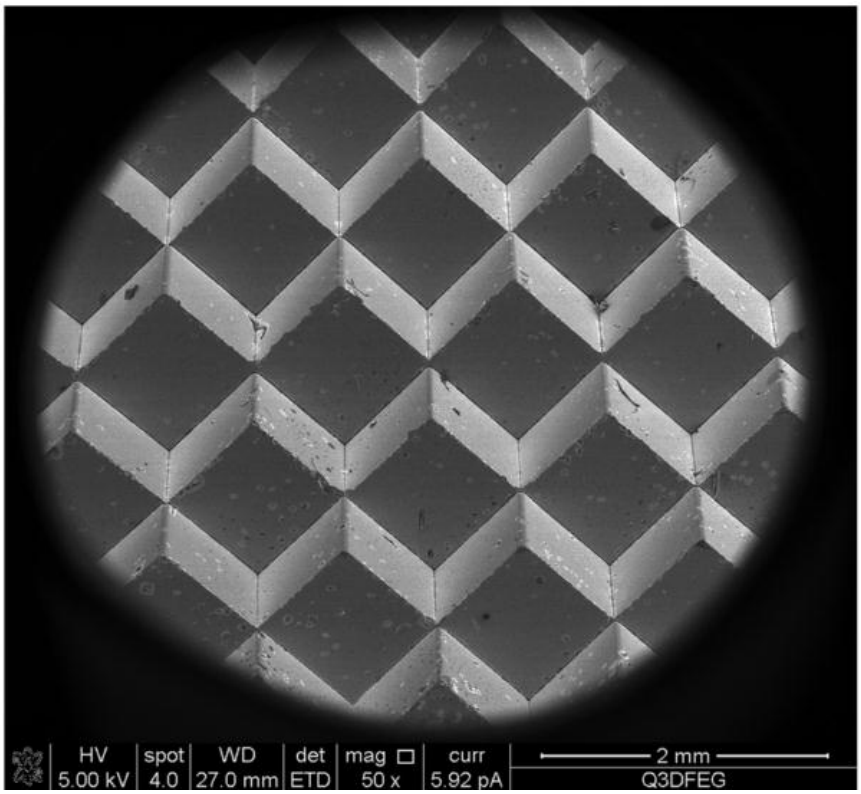

Figure 76: SEM image of a texture sheet surface described by Ulrich et al. (2012) and developed by SolarExcel. Such pattern, resembling stacked cubes, is commonly referred to as cube corner pattern [74].

Figure 77 (a) and (b) shows respectively a photograph and a sketch of one up-scaled element of the texture sheet that was illuminated with a laser to show the light path within the sheet material. The incident laser beam is refracted to oblique angles inside the material, and the beam directed toward the air interface is reflected back onto the structure. This is referred to as retro-reflecting properties.

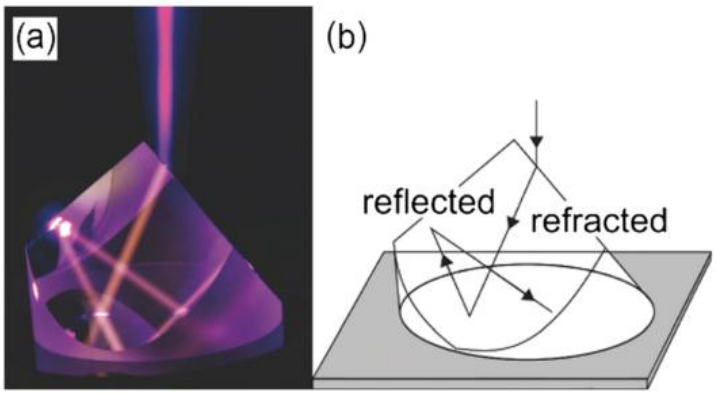

Figure 77: (a) A photograph of a model of the substructure elements of the textured sheet from Figure 76. (b) shows a schematic drawing illustrating the light path and the retro-reflecting properties [74].

Requests for accurate geometrical details were rejected by SolarExcel. The optical model for this texture is therefore based on the following assumptions. The pattern corresponds to cube corners. This shape is hexagonally stacked across the surface, as seen to the left in Figure 79. Seen from above each tile covers a hexagon. This holds as long as the three vertexes corresponding to a corner of a cube is located at the surface plane. Thus the shape is locked in terms of tilt. The faces are perpendicular to each other. A cube corner has a centreline-to-face angle of 35.2644 degrees. The

circular base shown in Figure 77 is assumed to be of exhibition purposes, and not a representation of the actual design of each feature. A circular base would produce a surface texture as illustrated in Figure 78 as modelled in 3D CAD software.

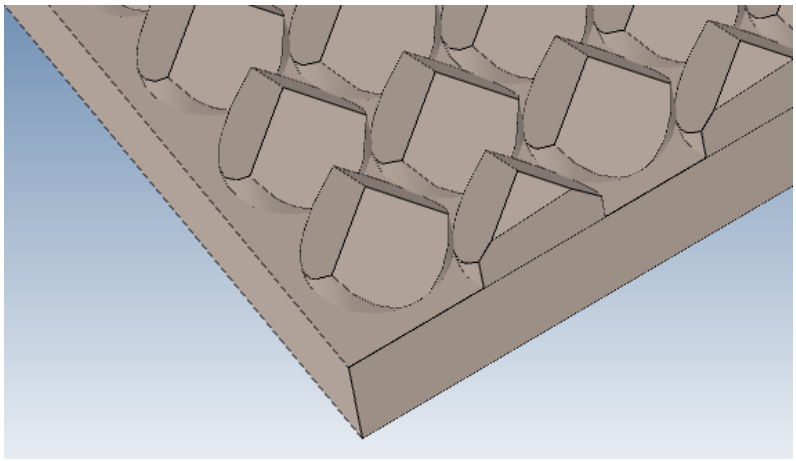

Figure 78: The cube corner pattern with circular base as modelled in 3D CAD software. It is regarded to not make much sense as opposed to hexagonal base as there is horizontal surface area in between the tiles that does not contribute to the anti-reflective texture.

A circular base as opposed to a hexagonal is not sensible as it increases horizontal surface area and thus decreases the working area of the anti-reflective glass texture. The SEM image in Figure 76 shows no sign of such a circular base. It is therefore assumed that the texture is cube corners as represented in Figure 79. This feature needs only to be specified in terms of the tile width, which is read from Figure 76 to be approximately 1.2 mm. A patent made that can be found online shows another illustration of the pattern, as seen in Figure 79.

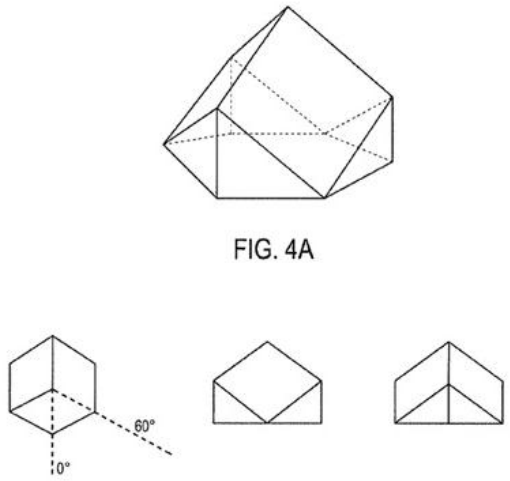

Figure 79: The SolarExcel pattern schematic as given in the patent description [73].

Macro textured glass can be modelled in ray tracing software and/or CAD software that can accurately reproduce the solid shape, size, bulk material properties, etc. Increasing the accuracy, complexity of the pattern features, number of texture tiles per unit area, increases the need for computational power and will increase the computational time in studies. Some ray tracing software has simplified models of these features, which handles many small repeated structures. This

implementation of a functional form for the shape and distribution of the replicated structure should be used with some caution so that severe loss in data accuracy is avoided. Such models assume identical shape of each feature.

In this thesis the following macro textures for the glass cover are investigated. Inverted pyramids and oblong pyramidal grooves are represented by Albarino P and G, respectively, with the dimensions covered earlier. Albarino G is modelled in CAD software while Albarino P and the cube corners of SolarExcel can be modelled by a functional form in TracePro called RepTile.

5.2 Rough glass

As well as by patterned texture, surface reflectivity on the glass cover can be reduced by roughening the surface. As there is no specific definition of rough glass in literature, both random micro texture and the ordinary meaning of a rough surface apply to these features, which are on the microscopic scale. Ground glass and frosted glass are examples of surface treated glass by roughening. This reduces the portion of specular reflection and increases the portion of diffuse reflection. This has practical advantages where reducing gloss is of interest, e.g. at airports, neighbourhoods, etc. It also has the same effect as patterned texture, where the total reflectivity is reduced.

Figure 80 shows images of two examples of glass textures which differ in shape and size. Fonrodona et al. (2005) used these glass textures as masters for texturing polyethylene naphthalate [75]. The first image is of commercially available frosted glass, while the second image is Asahi U (from Asahi Glass). The root mean square (RMS) roughness values are 2.74 µm and 36 nm, respectively.

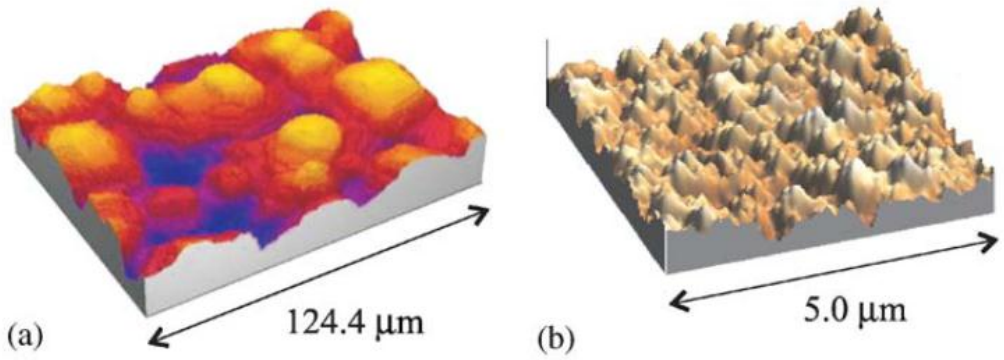

Figure 80: Examples of rough glass surfaces. (a) shows white light interferometry image of frosted glass. (b) shows AFM image of Asahi-U glass surface. The latter can potentially result in problems in ray tracing because the scale of the roughness approaches the wavelength of light [75].

A warning was given by Renhorn et al. in 2008 about inaccuracy in ray tracing when describing scattering processes related to rough surfaces, especially when diffraction is important [76]. However, analytical BRDF models have limited accuracy themselves when the scale of the surface roughness is of the same order of magnitude as the wavelength. Numerical models are in this case an alternative, but the computational complexity limits the calculation to very small surface areas. In this study it is assumed to give accurate enough results to use ray tracing with high resolution (tracing millions of rays) for a small surface area and converting the resulting scattering to BSDFs,

which are quickly applicable to larger surface areas. Using surface roughness of a scale considerably larger than that of light is done in this study to avoid these issues.

BSDF functions for rough surfaces can be obtained in several ways with different accuracy. The preferable method when high accuracy is important is to obtain measured scattering data with scatterometer. These measured data can then be transferred to the software for ray tracing, etc. by curve fitting parameters.

Rough glass with RMS roughness significantly larger than the wavelength of light is modelled in the same matter as above wavelength patterned texture is relative to sub-wavelength texture. Here, the surfaces and geometry of the rough surface determines the BSDFs. Measurements of the scattering functions can, however, be used for fitting the parameters in the ABg BSDF model as a simplification.

Figure 81: Image of rough glass produced by Mold-Tech with different RMS roughness values. The glass appears as matt/ground glass as the surface scatters the light. Source: Correspondence with M. Gauvin from TracePro.

Mold-Tech produces rough surface textures where some of which through light scatter measurements are represented by fitted parameters for the ABg BSDF model for use on surfaces in ray tracing software. The data is from scattering measurements, and was provided in correspondence with M. Gauvin at TracePro (correspondence can be found in Appendix C). MT11050 texture, with RMS roughness of approximately 110 µm, is represented by the parameters:

Table 7: ABg scattering model parameters for rough glass MT11050.

BSDF	A	B	g
BRDF	6.11e-06	3.41e-07	3.76
BTDF	2.90e-2	2.62e-3	2.51

Because of the incoherent random microscopic nature of the surface texture in rough glass, CAD modelling is out of the question. The lack of repeating pattern also excludes functional forms. Thus, the use of BSDF is necessary. BSDF is described more in detail in chapter 4.

5.3 Nano texturing

Texturing of the glass cover of a solar panel can also be done using sub-wavelength of light sized nanostructures. When the surface texture is dense and consisting of surface relief nanostructures with a height and spacing that is small compared to the wavelength of the incident light, the light propagating through the texture will encounter a gradual change of the refractive index in the same manner as thin film ARC. This effect is sometimes referred to as the Moth eye principle [77] when relating to texture. Some problems related to ARC can be avoided with micro texture, e.g. different thermal expansion of the multiple materials.

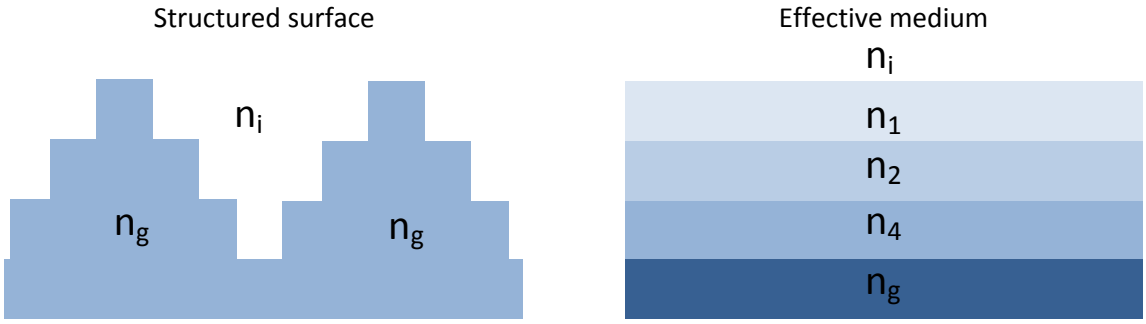

Figure 82: The surface texture and the equivalent refractive index when the structures are at the microscopic scale. n_i and n_g are the refractive indices of the surrounding medium and the glass, respectively. The effect is similar to that of thin film ARC, but referred to as the moth eye effect when relating to texture. The gradual change in refractive index reduces reflectivity.

Effective-medium theories (EMTs), which are functions of the ratio of the incident wavelength to the structure period, and of the indices of refraction of the involved materials, can be used to quantify the effective refractive index synthesized by sub wavelength structured surfaces. These should be accurate enough for principal studies, but not for designs, as they are simplified approximations.

Diffraction from the periodic moth eye texture of light with wavelengths less than the design range can be undesirable. Relatively short wavelength light (of high energy) can add constructively somewhere within the solar panel structure, leading to local increase in temperature. This would negatively affect the performance of any silicon solar cell. Therefore random distribution of the texture features can be desirable. Random texture distribution is also simpler to manufacture, which reduces the price.

An example of manufacturer that develops such solutions is TelAztec. They released a paper in 2007, displaying Scanning Electron Microscope (SEM) photographs of their random texture anti-reflecting microstructure etched into the surface of glass [77]. An example is shown in Figure 83.

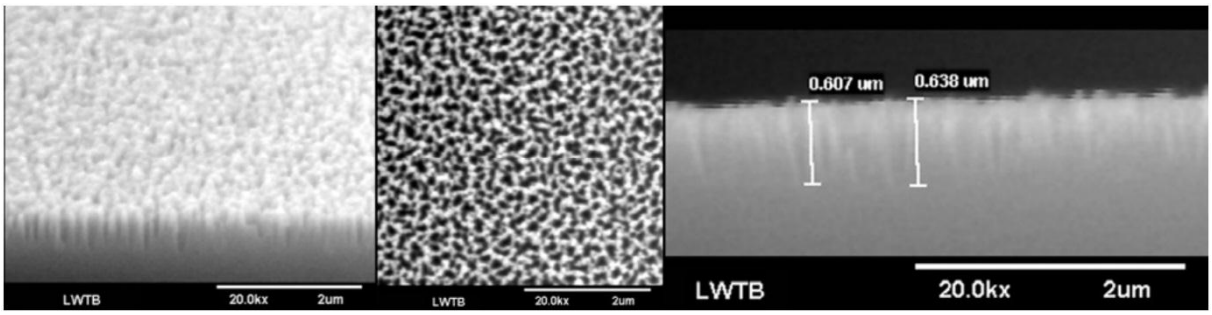

Figure 83: SEM images of randomly distributed surface micro texture features developed by TelAztec. The left image shows an elevated view, the middle shows an overhead view and the right shows a profile view. These carpet-like features are slim and somewhat oblong. The majority of the structures are smaller (in the surface plane directions) than the wavelengths of visible light [77].

Though TelAztec do not investigate potential gain in efficiency for solar panels, the reflectivity as a function of wavelength is given in Figure 84. The data are extracted from the 2007 publication. However, the integrated reflectivity as a function of the angle of incidence is not given.

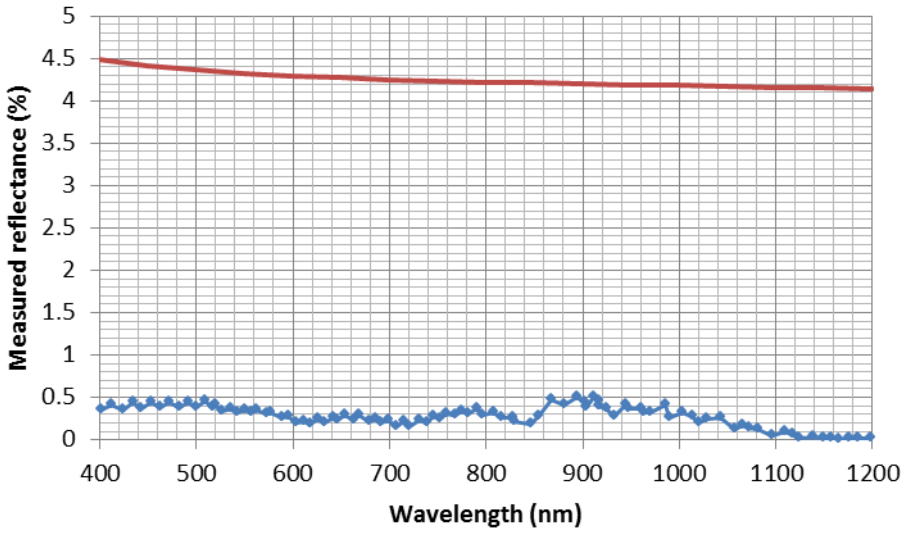

Figure 84: Measured spectral reflectance of glass with randomly distributed anti-reflective texture as given by TelAztec (blue). The producer does not provide comparable reflectance with untreated glass, so plain low-iron reference float glass at normal incidence is provided for comparison (red) [77].

Unfortunately the size of these features are in the same order of magnitude as the wavelength of the incident light and therefore it is not possible to model nano texturing in the ray tracing software used in this thesis.

5.4 Thin film anti-reflective coating, ARC

The principals of thin film anti-reflective coatings (ARCs) are described in chapter 4. Adding one or more of these layers on top of the glass surface reduces the reflectivity. It can be added to plain glass surface or textured glass surface. For a glass cover with refractive index equal to 1.5 the optimal refractive index for the ARC is 1.225 and the optimal ARC thickness is about 120 nm.

Such a commercial example of an ARC product with nano-pores suspended inside a binder material is KhepriCoat, produced by DSM. A scanning electron microscope (SEM) picture of the closed silica surface and suspended nano-pores is shown in Figure 85, as well as a corresponding anti-reflective coating from another manufacturer, EVG. The images are from the respective manufacturer's brochures available in their web pages.

Following the theory of ideal thickness of the anti-reflective coating, the EVG product displayed in the picture to the right in Figure 85 is ideal for a reference wavelength of light of 550 nm, which

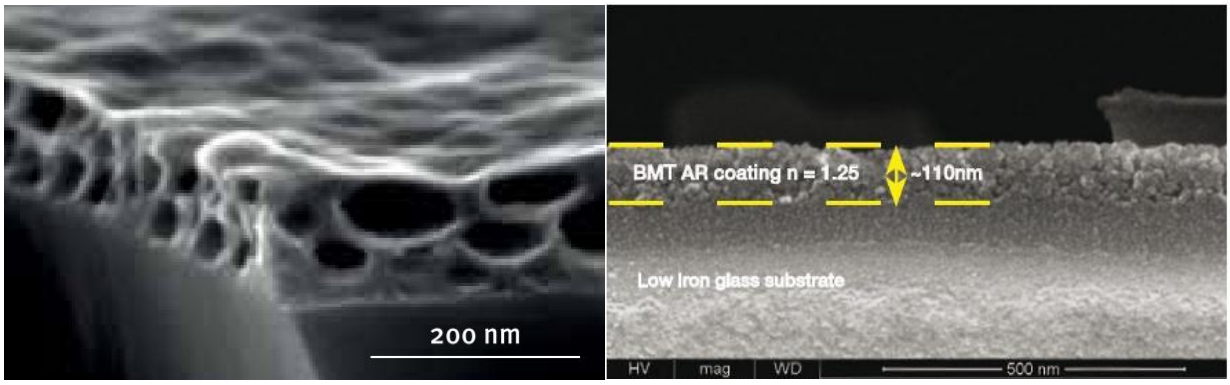

Figure 85: SEM picture of two commercially available anti-reflective coatings showing nano pores and a refractive index in between that of air and glass. The scale is below that of visible light. The picture on the left is from DSM and the picture on the right is from EVG. Both are available on the manufacturers' web pages.

corresponds well to the maximum power density in the solar spectrum. The gain in transmittance as claimed by DSM for the KhepriCoat coating is shown in Figure 86.

The gain in power output for a photovoltaic module from KhepriCoat as claimed by DSM is shown in Figure 87. The gain is relative to an uncoated reference module. The details for conducting the experiments are not published.

Anti-reflective coating, can, like texture, be modelled as solid thin plates in CAD software. However it can be difficult to model when applied to non-uniform surfaces. In TracePro this is done by using thin film stacks, a feature where the coating coherently follows the covered surface. The light behaviour follows the theory from Born & Wolf (1999) [78].

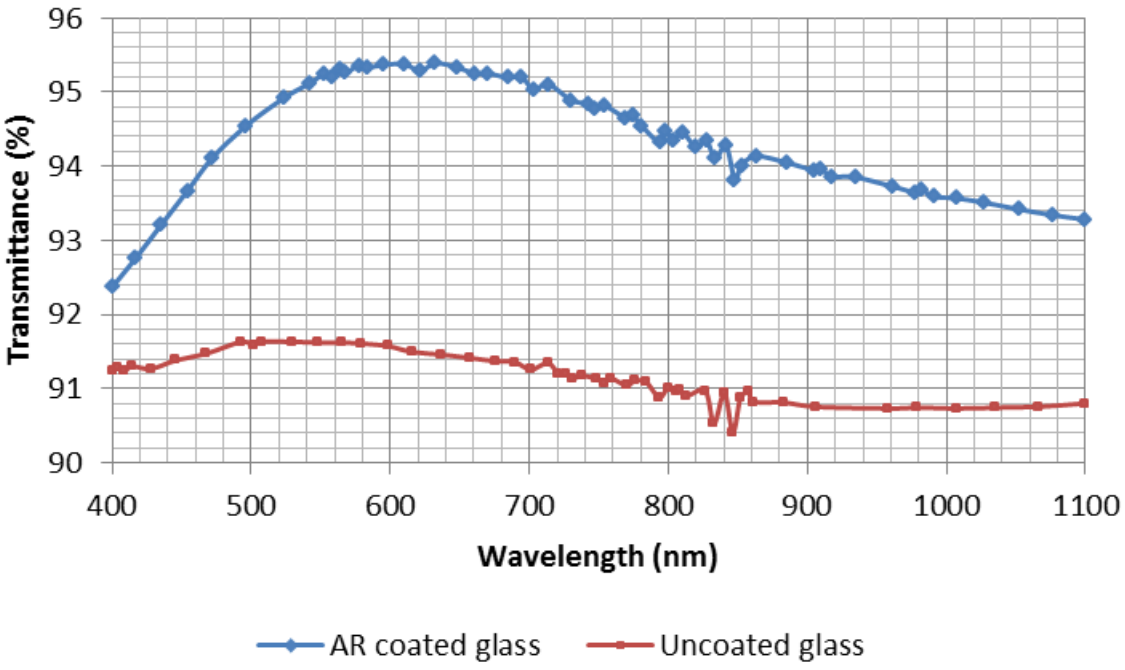

Figure 86: Claimed gain in transmittance from KhepriCoat anti-reflective coating for most of the relevant solar spectrum for PV panels. The peak in transmittance coincides with the peak power density in the solar spectrum around 600 nm. Source: Khepricoat brochure, Appendix B.

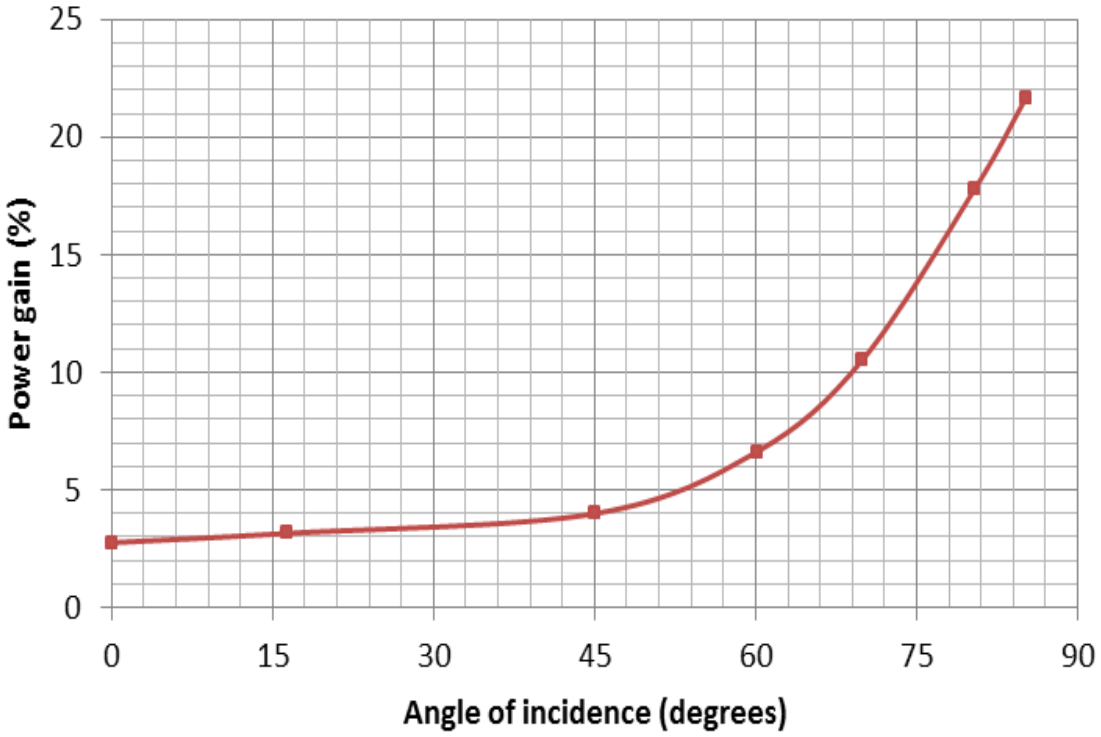

Figure 87: Power gain relative to a reference module for a photovoltaic module with KhepriCoat anti-reflective coated glass cover as claimed by DSM. As the angle of incidence increases, the effect of the ARC becomes more evident. Source: Khepricoat brochure, Appendix B.

5.5 Optical modelling of the glass cover in ray tracing

The features for the glass cover investigated in this study are summarized in Table 8. The geometrical sizes for the textures are summarized in this section.

Table 8: The anti reflective features for the glass cover under investigation in this study. Any gain in efficiency will be relative to a module with plain glass cover.

Feature	Name	Producer
Plain glass (reference)		
Inverted pyramids	Albarino P	St. Gobain Solar
Pyramidal grooves	Albarino G	St. Gobain Solar
Cube corners		SolarExcel
Thin film ARC	KhepriCoat	DSM
Rough glass	MT11050	Mold-Tech

The pyramidal grooves texture of Albarino G shown in Figure 70 is modelled in 3D CAD software (IronCAD) and imported for ray tracing.

Cube corners and inverted pyramids are modelled as functions for repetitive tiles. The latter has geometrical parameters given in Figure 88.

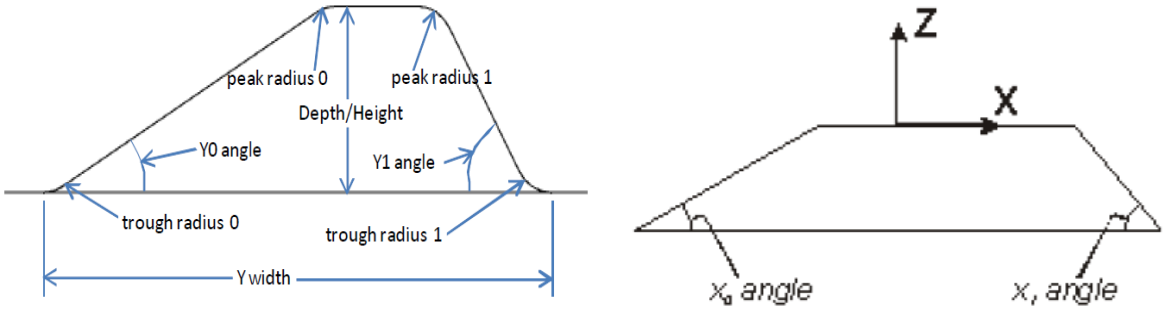

Figure 88: Geometrical dimensions used as inputs for the repetitive tile function for Albarino P. The illustrations are from the producers of TracePro. The dimensions are for inverted pyramids, i.e. downward pointing.

The cube corner geometry parameter is given in Figure 89.

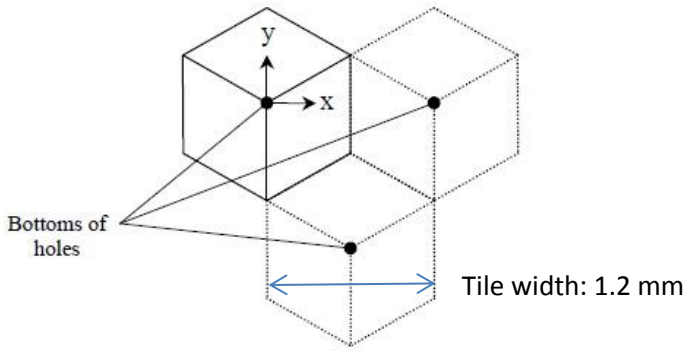

Figure 89: Cube corner pattern texture is only specified in terms of tile width because of its geometry.

Screenshots from the RepTile functions for inverted pyramids and cube corners are shown in Figure 90.

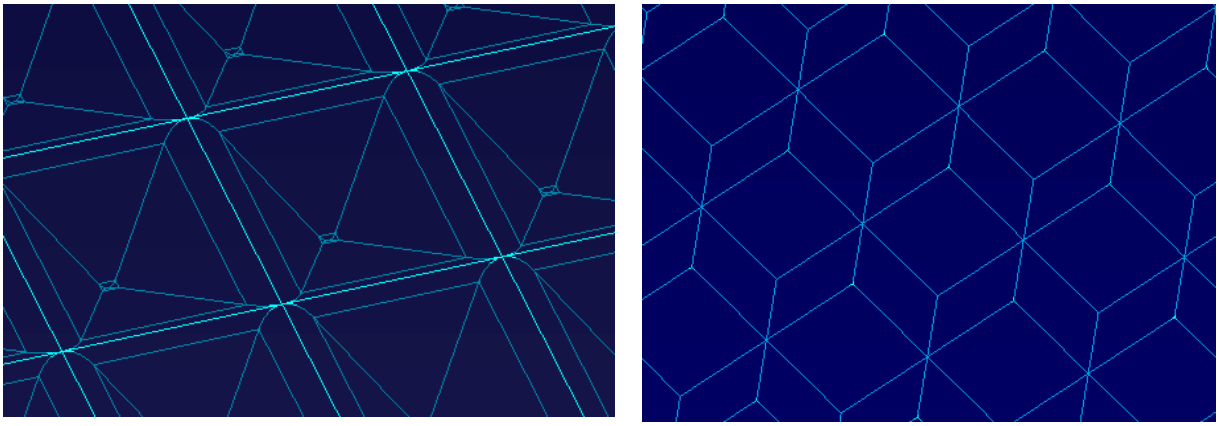

Figure 90: Screenshots from the RepTile functions in Tracepro for inverted pyramids (left) and cube corners (right).

Both rough glass and thin film ARC are homogenous in the surface plane. Table 9 summarizes the dimensions for the glass cover surface features and the simulation results are given in chapter 6.

Table 9: Geometrical dimensions for the glass cover surface features in this thesis.

Feature	Model	Dimensions	
Pyramidal grooves	Solid CAD	Glass thickness: 4 mm Groove length: 11 mm	Period:2.6 mm Height: 1.4 mm
Inverted pyramids	RepTile function	Glass thickness: 4 mm X width: 2.6 mm Y width: 2.6 mm Depth: 0.9 mm Peak radius 0: 0.15 mm Peak radius 1: 0.15 mm	X_0 angle: 34.7° X_1 angle: 34.7° Y_0 angle: 40.3° Y_1 angle: 40.3° Through radius 0: 0.5 mm Through radius 1: 0.5 mm
Cube corners	RepTile function	Glass thickness: 3.2 mm	Tile width: 1.2 mm
Rough glass	BSDF	Glass thickness: 3.2 mm BRDF A: 6.107e-06 BRDF B: 3.408e-07 BRDF g: 3.759 Absorptance: 0.0394	RMS roughness: 110 µm BTDF A: 0.02899 BTDF B: 0.00262 BTDF g: 2.513
Thin film ARC	Thin film stacks	Glass thickness: 3.2 mm Thickness: 101 nm	

6 Simulation results

Numerical simulation results from the respective photovoltaic and irradiance models are presented here. The direct irradiance model shows how parallel rays with varying solar spectrum and light incidence angle affect the optical performance of the PV panel, while the diffuse irradiance models describe the performance under multidirectional light, under varying or constant solar spectrum. The performance is measured by the light transmission factor (LTF) and I_{sc} per incident flux (I_{sc}/P_{in}).

The reader should note that the generated current is expressed in terms of I_{sc}/P_{in} because generated current depends strongly on irradiance, which depends on many factors. This thesis does not study how much irradiance is incident on a panel, but how well different glass textures perform with a given irradiance.

6.1 Comparison of the simple model and the extended simple model

In chapter 4 three optical models of a solar panel were developed; the complex model, the simple and the extended simple model. One of the goals of this thesis was to compare the simple solar panel model and the complex solar panel model, and thereby evaluate what level of complexity is necessary to accurately portray a solar panel in an optical simulation. As mentioned in section 4.3 technical issues prevented any full simulations from being performed with the complex solar panel model, hence only the simple and the extended simple model are investigated here.

A comparison between the simple model and the extended simple model under direct irradiance is shown in Figure 91. Only the results for plain glass and cube corner textured glass is shown here, to demonstrate that these two models return similar results.

The LTF for plain glass and the textured glass is shown for both models, as a function of angle of incidence. The % difference in LTF for the simple model relative to the extended simple model is shown for both plain glass and textured glass. Also shown is the % gain in LTF for the use of textured glass relative to plain glass for both models.

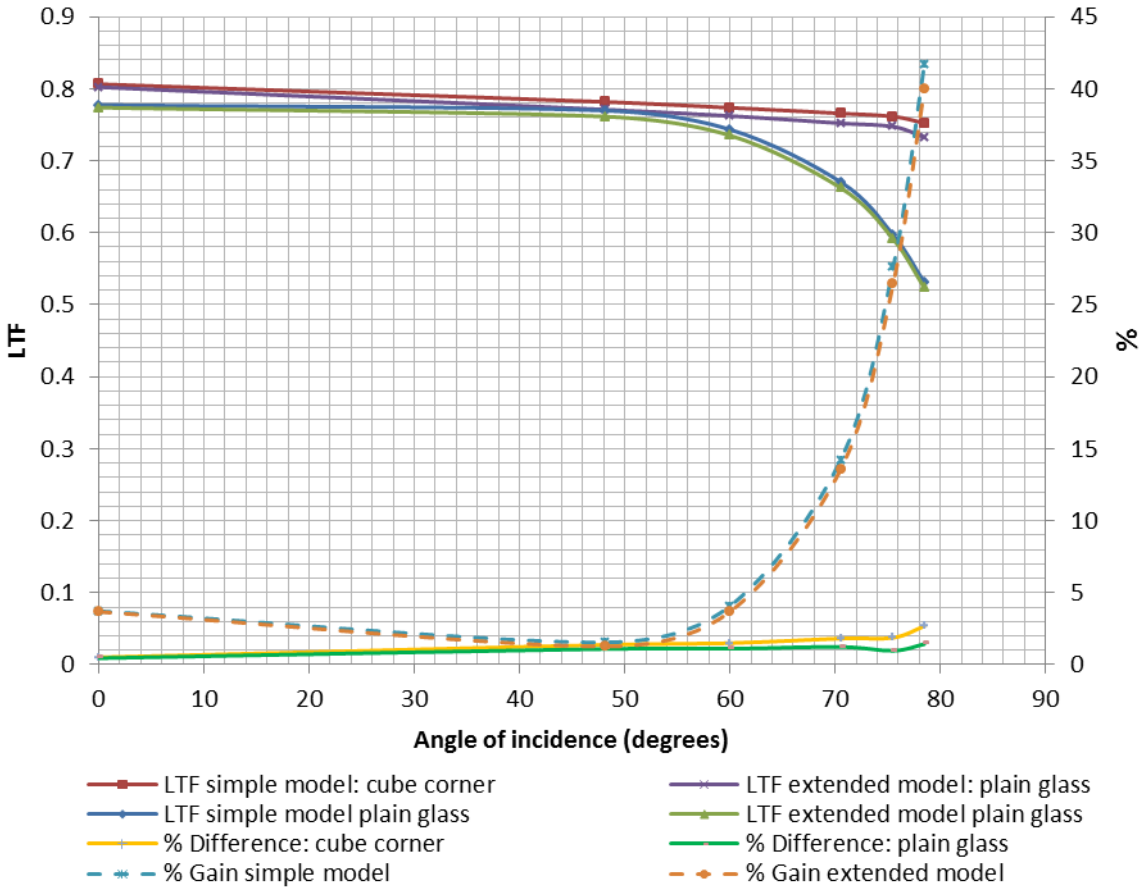

Figure 91: LTF for Simple model and extended simple model with a plain glass cover and a textured glass with cube corner geometry (e.g. SolarExcel).

It can be seen that the difference between the models increases with increasing angle of incidence, from 0.5% for both plain and textured glass, to respectively 1.3% and 2.8%. However, using textured glass relative to plain glass returns the same gain for both models at all angles of incidence. For this reason, it is assumed that the extension of the model is redundant, and that the simple model is representative.

6.2 Simulation of different glass covers using the simple solar panel model

6.2.1 Direct irradiance model

For the glass covers with non-rotationally symmetrical texture the angular effects depend on the azimuth angle as well as the angle of incidence, therefore in this thesis the average LTF between 0 degrees and 45 degrees azimuth angle is calculated for each textured glass cover. In Figure 92 the LTF dependency on the two azimuth angles with the averaged LTF is shown for the 3 textured glasses.

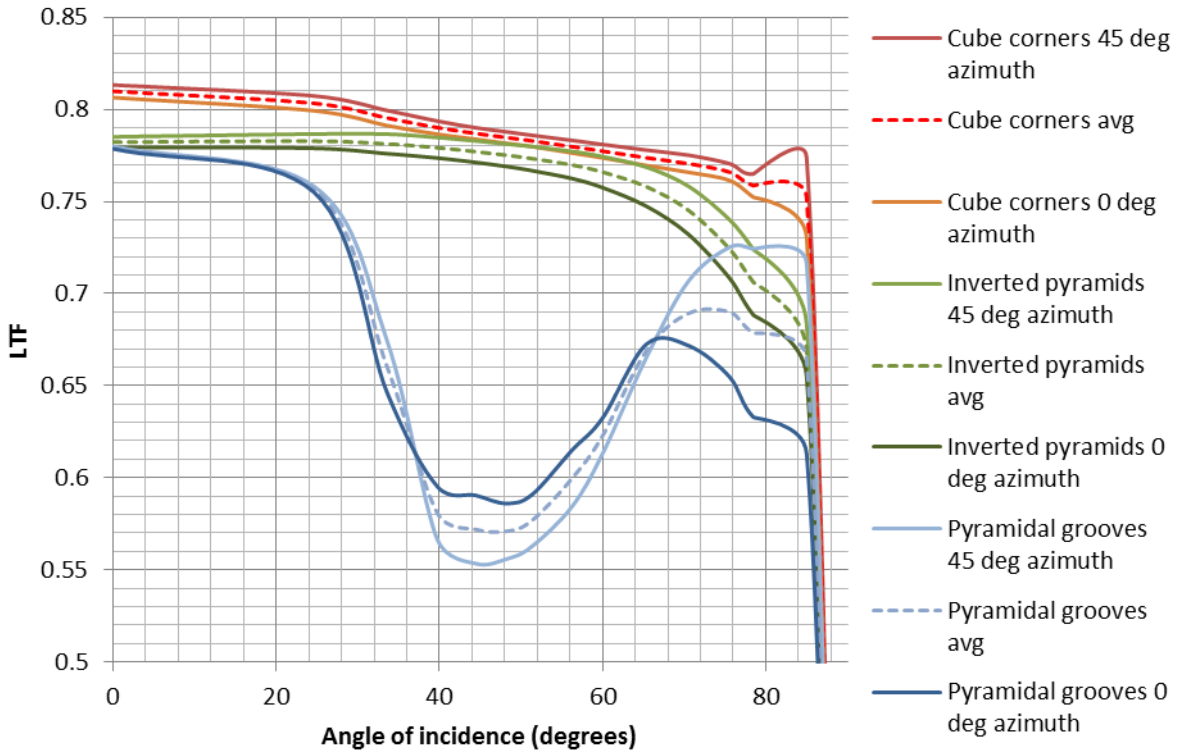

Figure 92: Light transmission factor for the three geometrical textures which depend on the azimuth angle as well as the angle of incidence. The averages of 0 and 45 degrees azimuth angles are shown.

It can be noticed some deviations in the LTF at normal incidence between 0 and 45 degrees azimuth orientation for both Albarino P and SolarExcel. This deviation could be caused by the fact that for the 45 degrees azimuth orientation the panel is rotated 45 degrees about the normal axis, and the light source is reduced in size, as shown in the right image of Figure 93. In the left image light is irradiant on the optical model at 0 degrees azimuth orientation. Reflection effects at the panel edges can potentially be the source of the minor deviation at normal incidence in Figure 92.

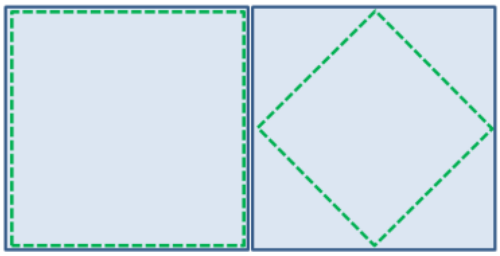

Figure 93: Area covered by the incident light (green dotted lines) on the solar panel (blue box) for 0 degrees azimuth angle (left) and 45 degrees azimuth angle (right).

The LTF for all glass covers described in chapter 5, as well as the IAM factor, is shown in Figure 94.

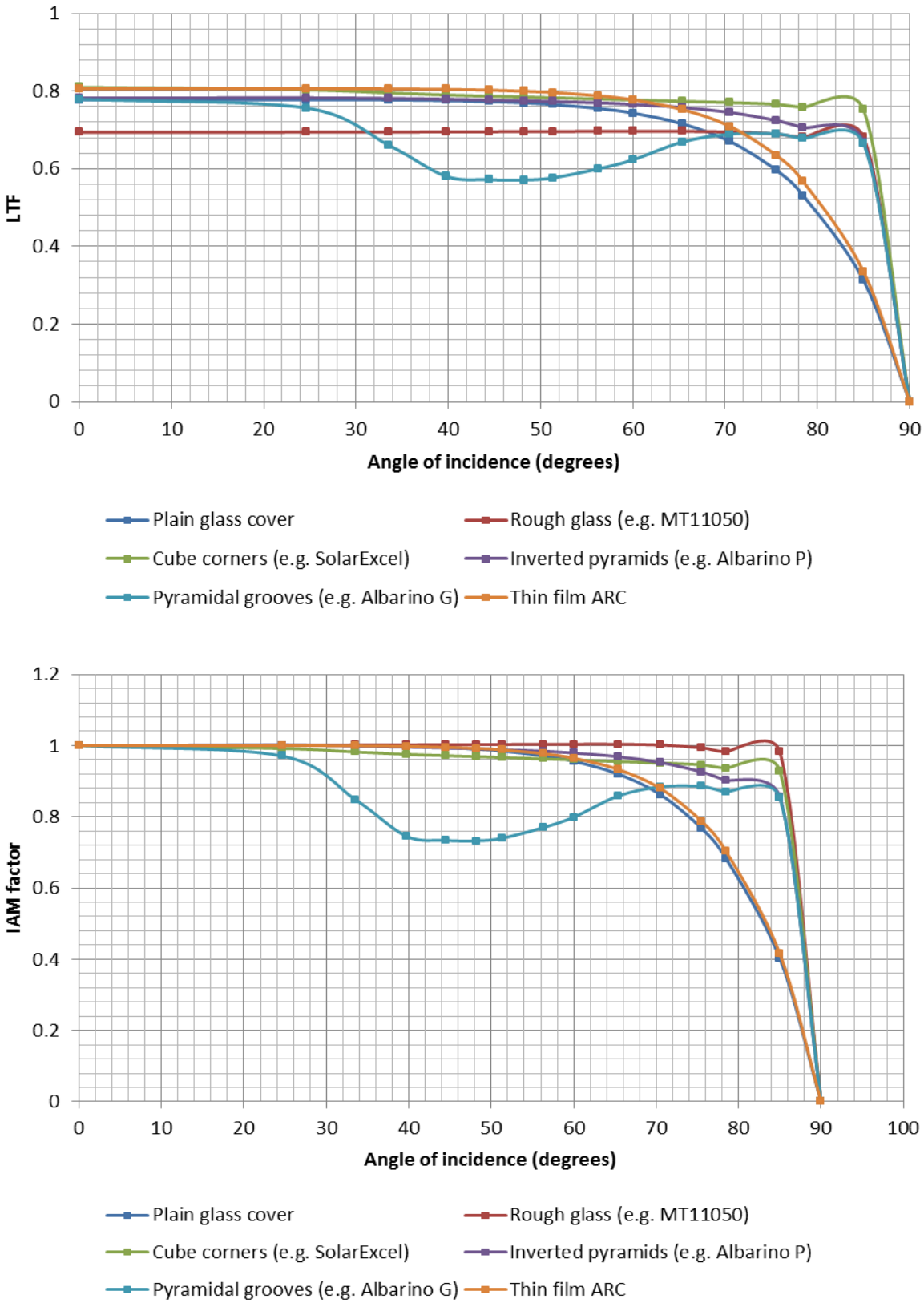

Figure 94: LTF (top) and IAM factors (bottom) for a photovoltaic panel with the different glass covers described in chapter 5. The IAM factor is equal to the LTF normalized to the value at normal irradiance.

It is shown in Figure 94 that thin film ARC performs well across all angles of incidence while textured glass performs particularly well at angles above 60 degrees, except for the pyramidal grooves

textured glass (e.g. Albarino G) and the rough glass. The rough glass performs poorly below 70 degrees angles of incidence. The pyramidal grooves textured glass texture performs poorly between 20 and 70 degrees angle of incidence. This result was rather surprising, given the claimed performance by the manufacturer of such glass. Therefore a test was set up for comparison to investigate the accuracy of the results for pyramidal grooves in Figure 94. Oblong pyramidal grooves are textures that have been investigated in several publications. Kolås et al.(2012) investigated the use of such texture with 90 degree angles as shown in Figure 95 [79].

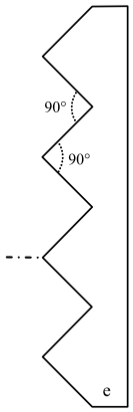

Figure 95: Oblong pyramidal grooves in profile view as shown by Kolås et al. (2012)[79].

As the pyramidal grooves described in chapter 5 are a combination of similar grooves, only distributed in repetitive square tiles, the test investigated the LTF as a function of angle of incidence for 0 degrees and 90 degrees azimuth angle for a panel with glass textured as shown in Figure 95. The texture was modelled by RepTile in Tracepro, and the result is shown in Figure 96.

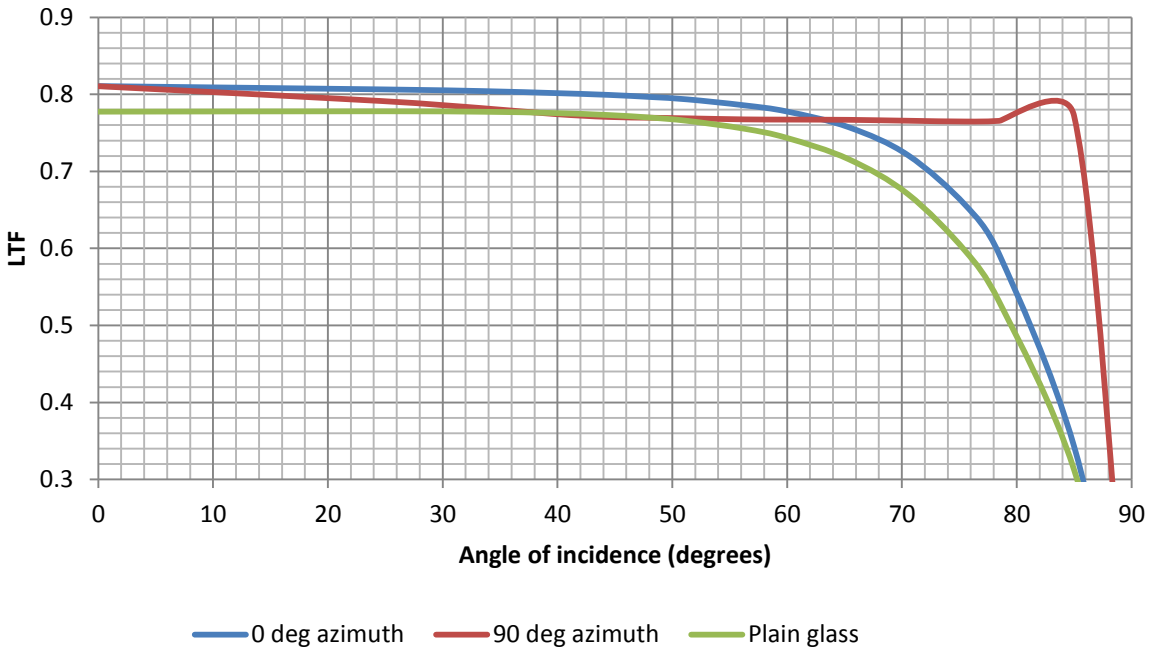

Figure 96: LTF as a function of angle of incidence for oblong pyramidal grooved textured glass with direct irradiance sources at 0 and 90 degrees azimuth angles. It can be seen that for both these azimuthal orientations the textured glass performs better than the reference plain glass.

It is seen in Figure 96 that the oblong pyramidal grooves textured glass performs better than plain glass for all angles of incidence and for both azimuthal orientations. Even though the test was based on “perfect” pyramids without round edges, this contradicts the poor results for the pyramidal grooved texture described in chapter 5. It should be noted that the pyramidal grooves is the only glass texture to be modelled in CAD software and imported into the ray tracing software.

The spectral dependence of the short circuit current density is visible in Figure 97, it shows how the light is absorbed throughout the PV panel structure for plain glass. As predicted by the absorption coefficients covered in chapter 4, at short wavelengths the absorption in the EVA and glass is most significant, especially from 0.3 to 0.4 µm. Above 0.4 µm these absorption losses are low. These absorption losses are shown as a function of angle of incidence for each panel in Figure 99. The absorbed flux is per 1000 W irradiance at the glass cover surface.

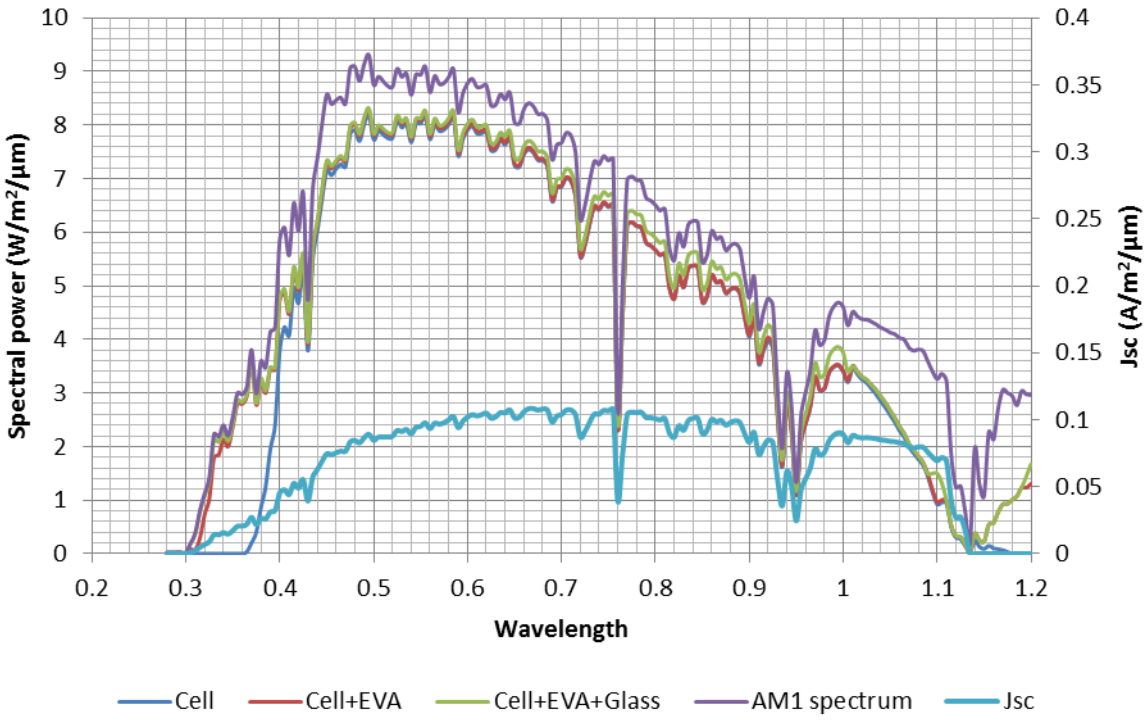

Figure 97: Spectral absorbed flux (W) in the solar panel structure as well as the corresponding short circuit current density per wavelength at AM1 for plain glass covered PV panel. The absorption in the glass and EVA material is significant in the region 0.3 to 0.4 µm, but low in the rest of the spectrum. The spectral dependence for the short circuit current density is evident.

The short circuit current can be obtained from the optically absorbed flux in the cell in accordance with Eq. (5), the result is shown in Figure 98. The I_{SC} is for a 155x155 mm^2 PV cell. As the direct irradiance model has different spectra at different angles of incidence, the I_{SC} per irradiance increases slightly relative to normal incidence because the weighting of the spectrum shifts upwards at higher angles of incidence. For rough glass and cube corners this spectrum-angular effect surpasses the effect of increased reflection. This effect also is very clear in the clear sky diffuse irradiance model.

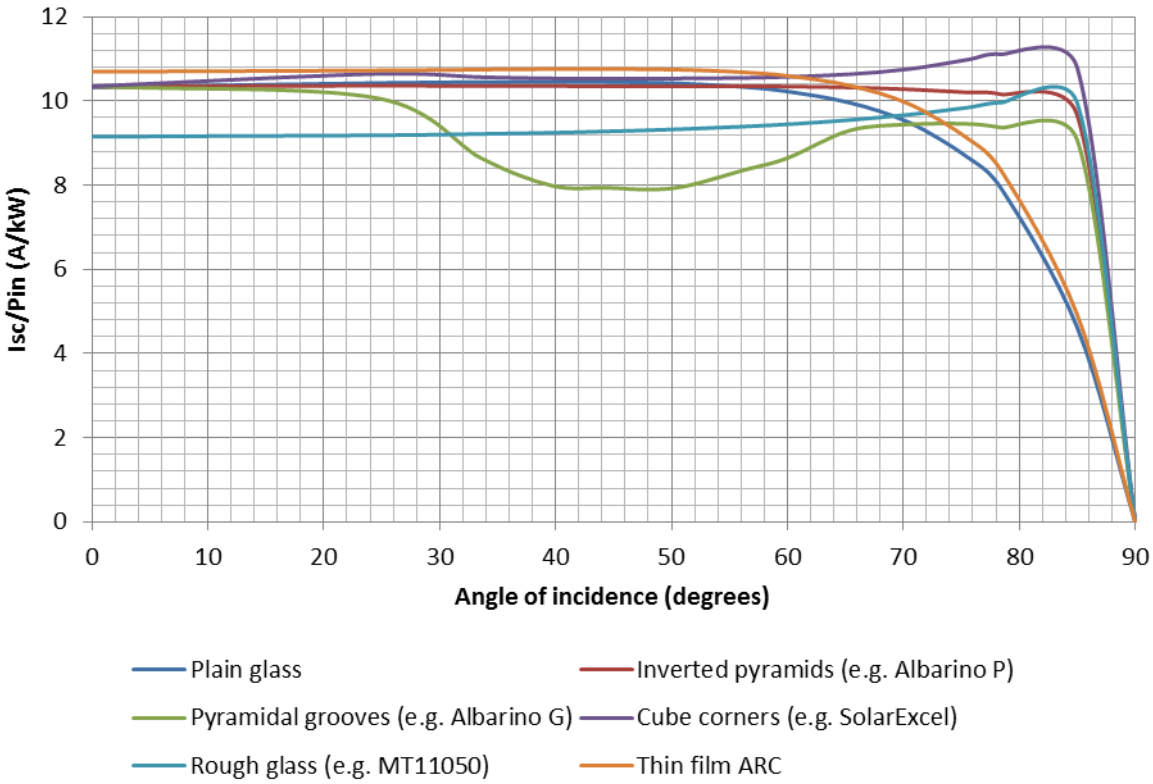

Figure 98: Short circuit current per irradiance for a PV cell as a function of angle of incidence. The increase at high angles of incidence for some panels reflects the dependence on irradiance spectrum for short circuit current and light transmission.

Light absorption in the glass and the EVA as a function of angle of incidence is shown in Figure 99 for each glass.

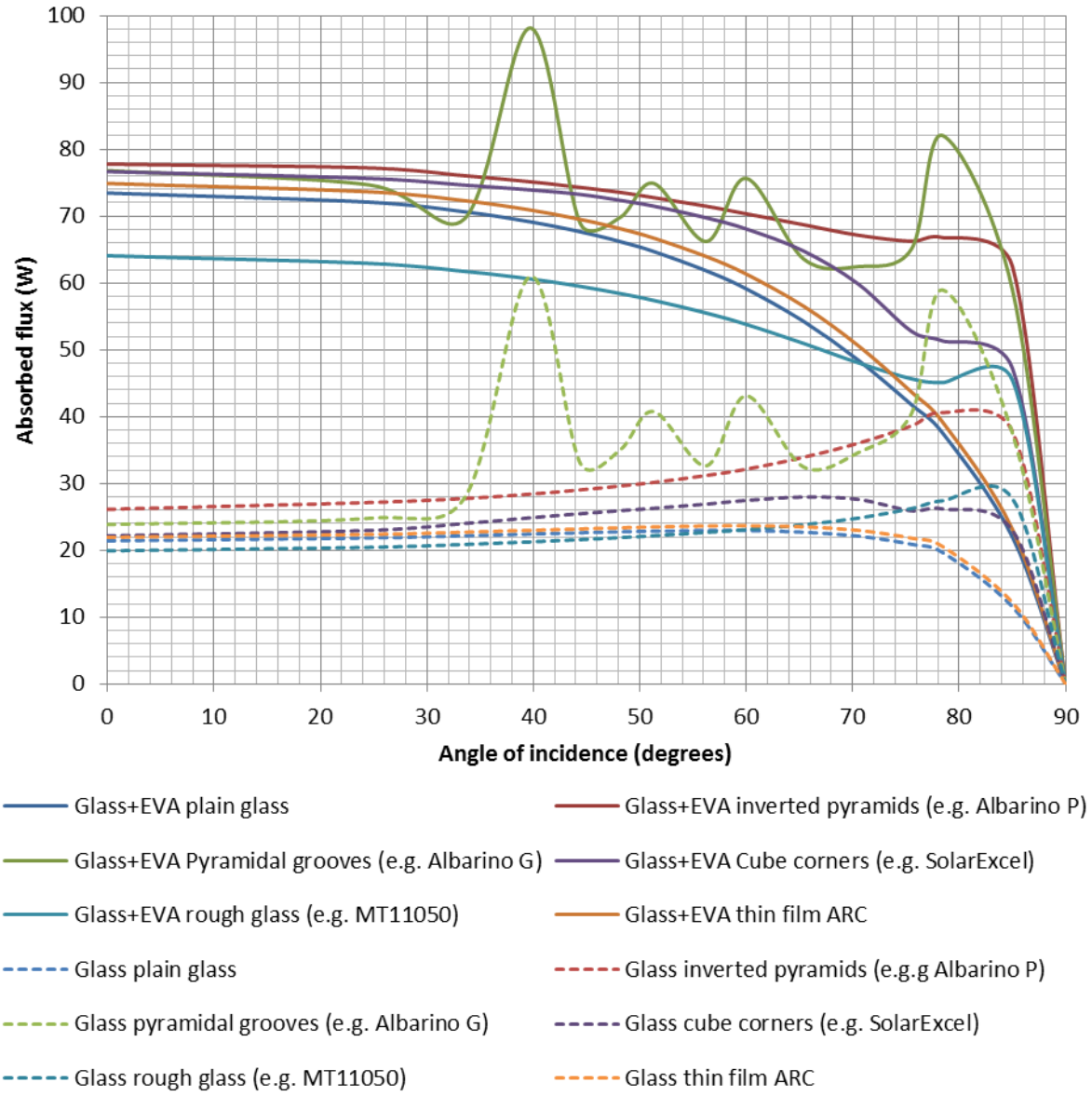

Figure 99: Optical absorption losses in the glass and the EVA as a function of angle of incidence per 1000 W irradiance on the glass cover surface. The absorbed flux (W) in the glass cover and glass+EVA is shown. The absorbed flux in the EVA is the difference between the two.

At low angles of incidence EVA is the largest contributor to absorption losses. As the angle of incidence increases the EVA's absorption losses decreases and glass becomes the largest loss contributor. This is a result of changing spectrum and the increasing path length.

Also seen in Figure 99 the pyramidal grooves texture behaves differently compared to the other textured glasses. Even though the texture absorbs significantly more at some angles of incidence, for example at 40 degrees, this amount of absorbed watts is not enough to explain the poor results shown in Figure 98 at the same angle of incidence and there seems to be no relationship between the graphs. The test performed with the oblong grooved texture from Kolås et al. (2012) showed promising results, hence one can question whether the pyramidal grooved texture described in chapter 5 is a good anti-reflective texture or if the optical model of it is a good approximation.

6.2.2 Diffuse irradiance models

The LTFs under the diffuse irradiance models are shown in Figure 100.

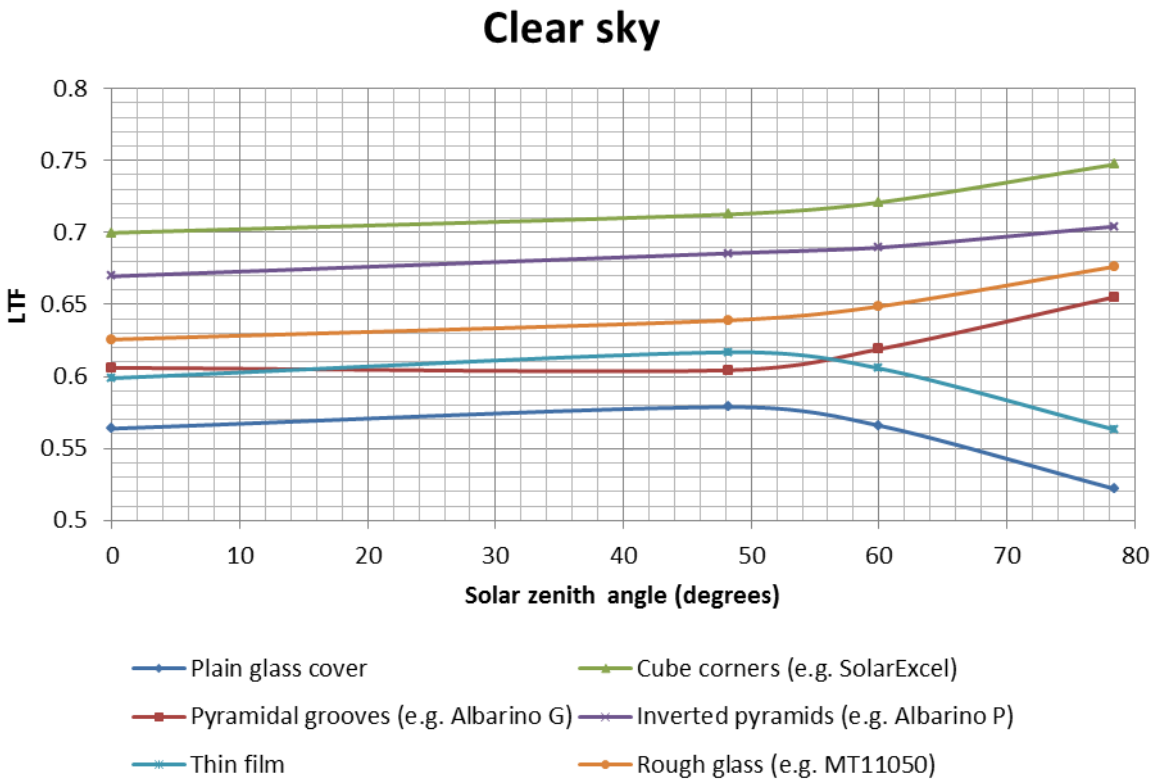

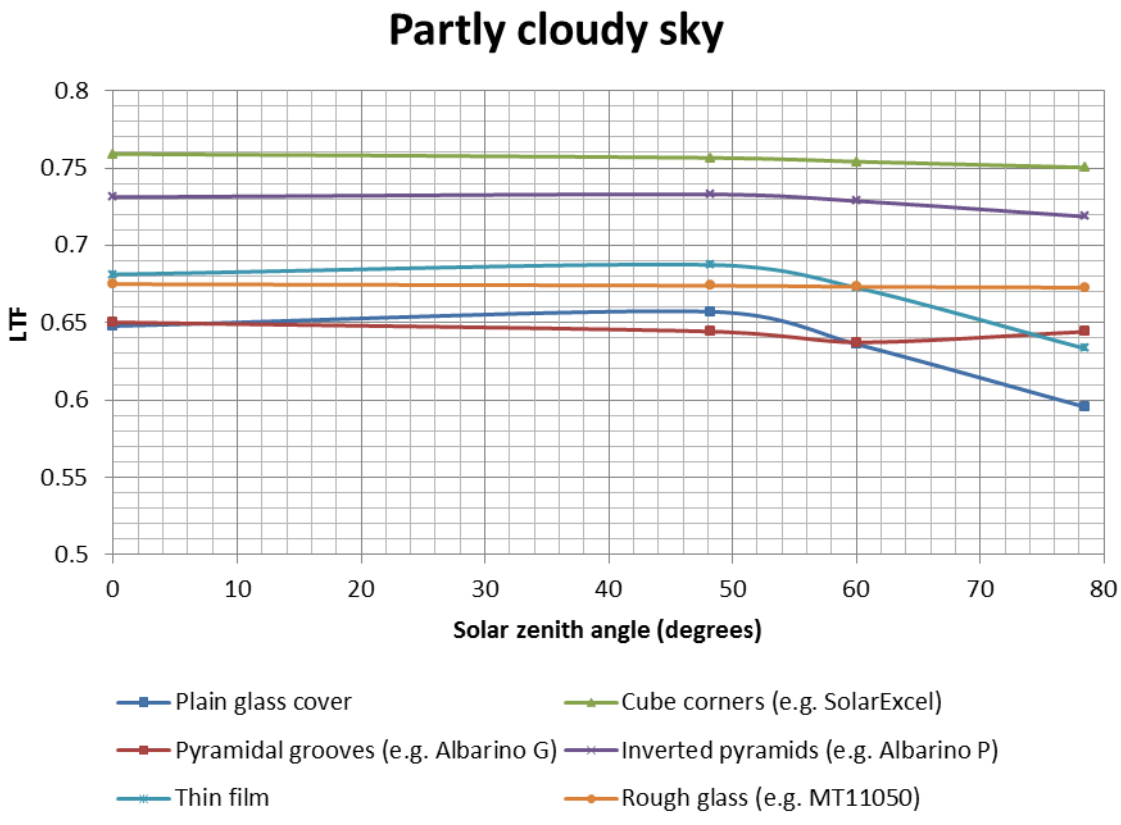

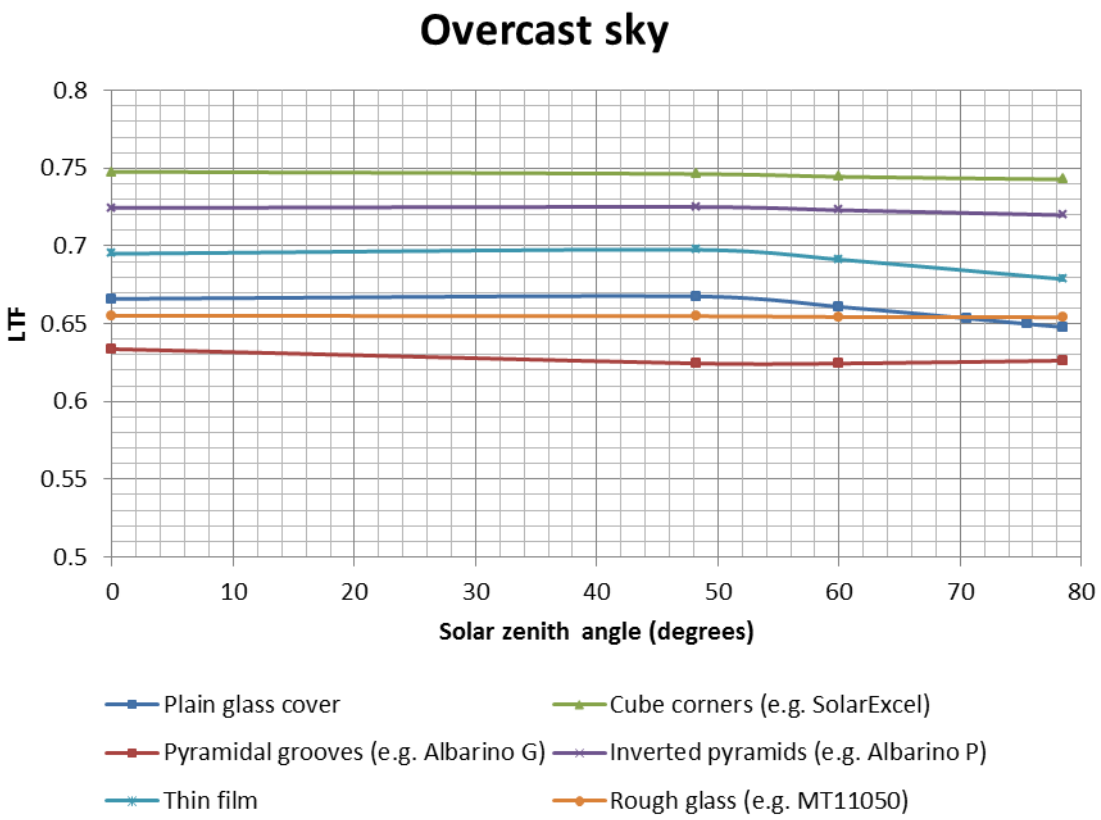

Figure 100: LTF under diffuse irradiance for a photovoltaic panel with the different glass covers described in chapter 5. The clear sky diffuse irradiance model stands out, with increasing fraction of absorbed flux at increasing solar zenith angles. Clear sky is also the only model to have different solar spectrum for each solar zenith angle.

As expected there is a weaker dependence for the photovoltaic panel's performance under diffuse irradiance on the solar zenith angle than the dependence for the panel's performance under direct irradiance on the angle of incidence. This is because of the multidirectional nature of diffuse irradiance.

The results from the clear sky model stand out. The LTF increases at higher solar zenith angles for the panels with textured glass cover. As mentioned in chapter 3, the clear sky model is also the only diffuse irradiance model with different solar spectrum for each solar zenith angle. This supports the fact that measured or derived spectra should be included for each solar zenith angle for each diffuse irradiance model. Also at solar zenith there are differences in LTF magnitude for each glass. This can be caused by:

1. Different spectra
2. Different intensity distributions, or
3. A combination of both.

Considering all the results from this section, the solar spectrum seems to be most important factor. The short circuit current is calculated from the LTF data, and shown in Figure 101.

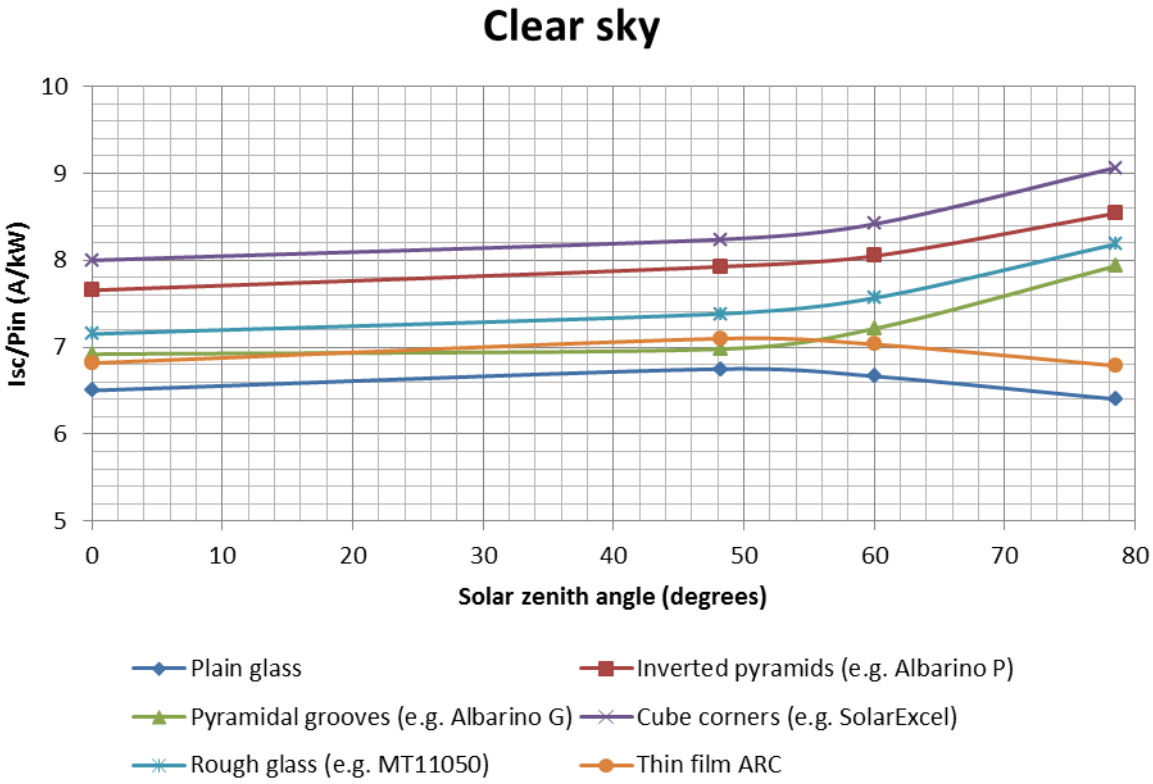
Clear sky
Isc/Pin (A/kW)
10
9
8
7
6
5
0
10
20
30
40
50
60
70
80
Solar zenith angle (degrees)
Plain glass
Inverted pyramids (e.g. Albarino P)
Pyramidal grooves (e.g. Albarino G)
Cube corners (e.g. SolarExcel)
Rough glass (e.g. MT11050)
Thin film ARC

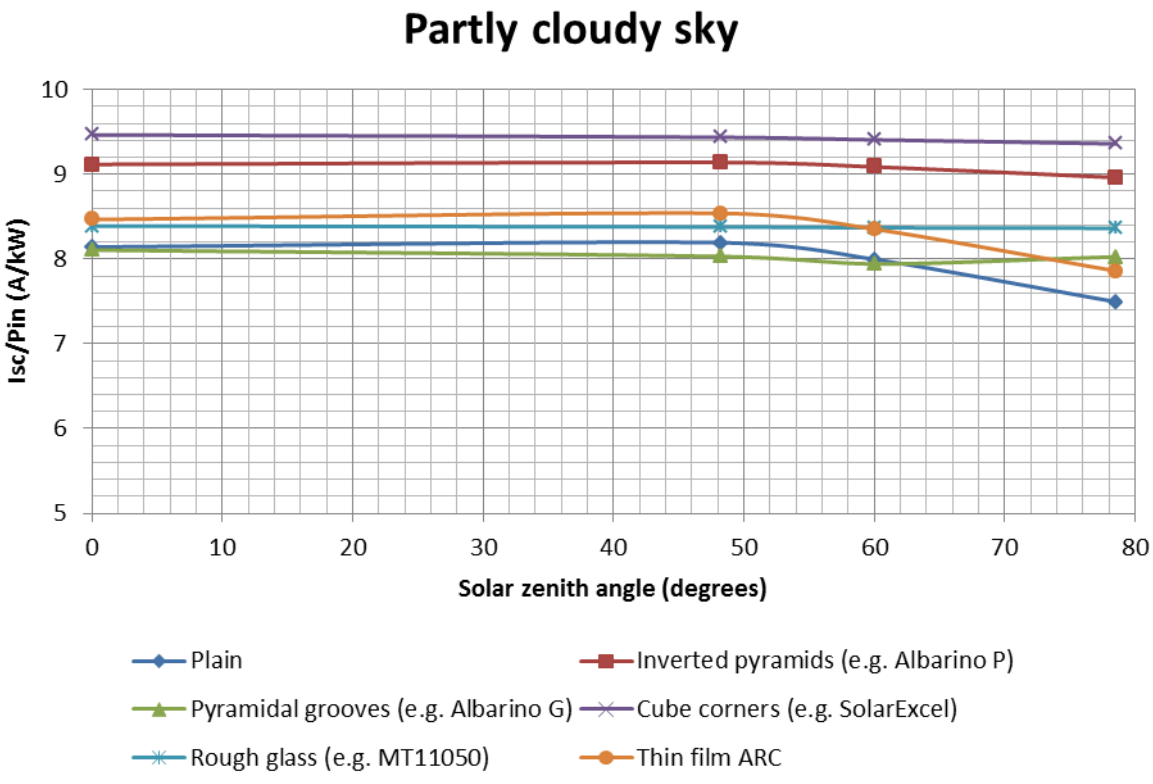
Partly cloudy sky
Isc/Pin (A/kW)
10
9
8
7
6
5
0
10
20
30
40
50
60
70
80
Solar zenith angle (degrees)
Plain
Inverted pyramids (e.g. Albarino P)
Pyramidal grooves (e.g. Albarino G)
Cube corners (e.g. SolarExcel)
Rough glass (e.g. MT11050)
Thin film ARC

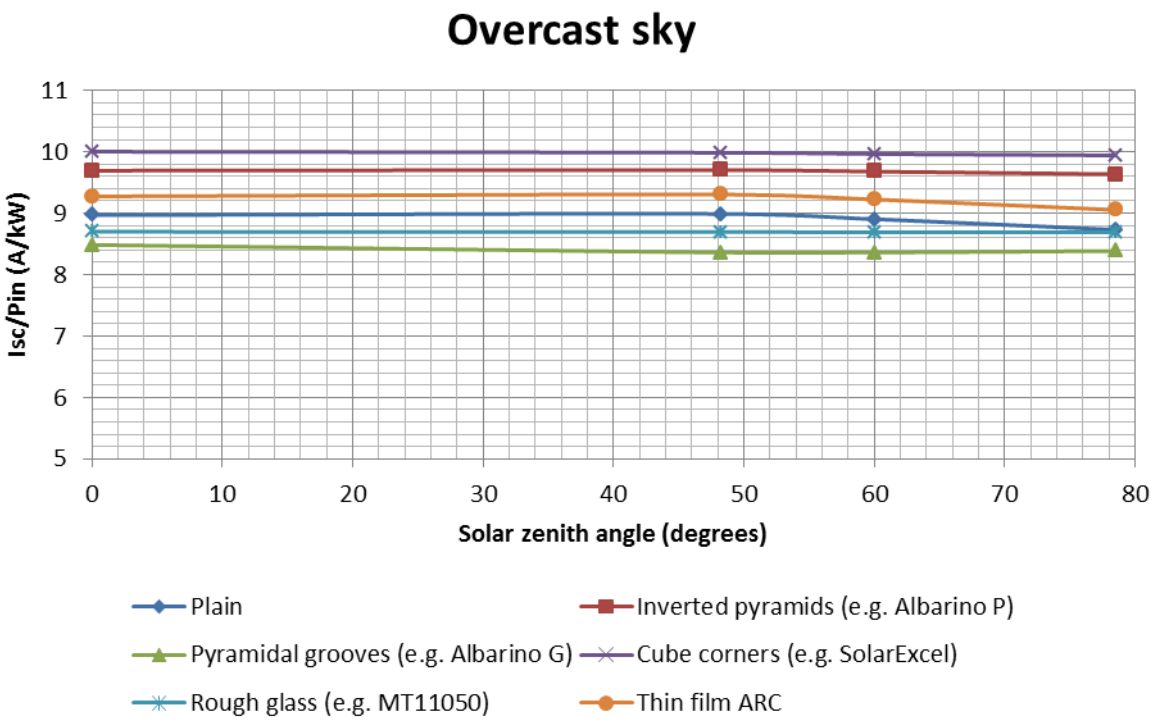

Figure 101: Short circuit current per irradiance for a PV cell as a function of solar zenith angle. The clear sky irradiance model shows that the change in solar spectrum at higher angles of incidence is a stronger factor than the increase in reflection at higher angles of incidence for textured surfaces. The effect is weaker, but evident, for smooth surfaces (plain glass and thin film ARC). For partly cloudy and overcast sky, which have constant solar spectrum, the change in absorbed flux and I_{sc} is weaker at increasing angles of incidence.

As seen in Figure 101 the general shape of the I_{SC}/P_{in} curves are similar to those of LTF for the same irradiance models. Again, the clear sky model shows that the performance is highly dependent on the solar spectrum.

The partly cloudy sky model, with constant solar spectrum, shows that optical performance (transmittance or generated current) for textured glass cover PV panels has a weak dependence on the solar zenith angle. The thin film ARC and the plain glass display higher dependence on the solar zenith angle than the textured surfaces. However, it is still quite low.

The overcast sky model, the most uniform diffuse irradiance model and with constant solar spectrum, displays very weak dependence on the solar zenith angle for all PV panels.

The gain in LTF relative to a panel with plain glass cover is shown for all panels in Figure 102 as a function of solar zenith angle, both under direct and diffuse irradiance. The diffuse irradiance is represented by overcast sky conditions. For the direct irradiance cases, the solar zenith angle corresponds to the angle of incidence.

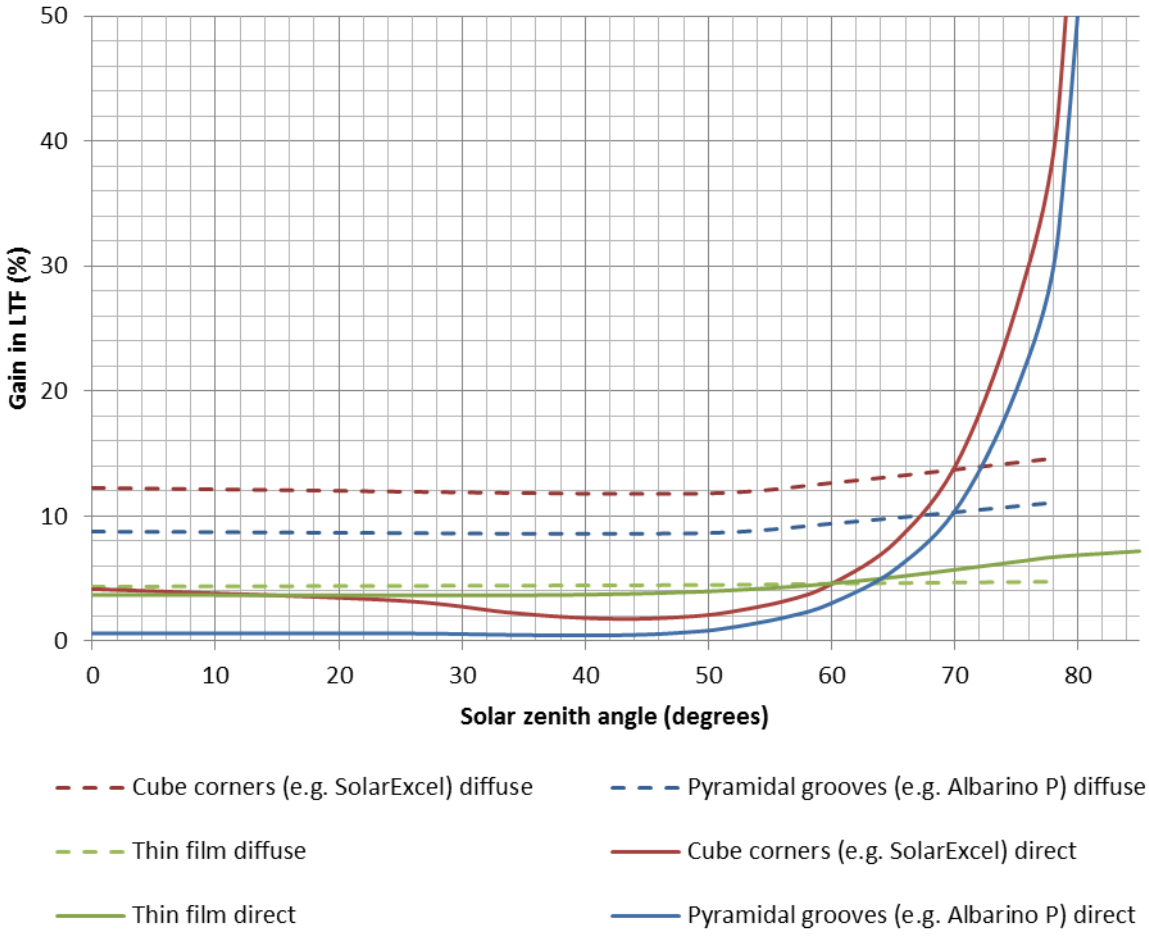

Figure 102: Gain in LTF relative to plain glass for the different glass covered PV panels. Textured glass covers perform better at high angles of incidence, and therefore perform particularly well at diffuse irradiance.

As predicted there is a considerable gain in LTF under diffuse irradiance for textured glass surfaces, and this gain is relatively constant for any solar zenith angle. The direct irradiance shows particularly high gains at high angles of incidence for the textured glasses, while the gain for the thin film ARC does not vary much with angle of incidence. The cube corner textured glass shows the highest gain for both diffuse and direct irradiance.

Figure 102 can be compared to Figure 75, which describes manufacturers claimed gains for inverted pyramids as a function of angle of incidence. The results from this study show an almost constant gain of 8% for all solar zenith angles while the manufacturer found a constant gain of 4%. This difference could be caused by e.g. different reference glasses.

6.2.3 Annual energy simulations

6.2.3.1 PVsyst

The selected location for the annual energy simulations is Singapore since the direct irradiance model is based on a panel normal to AM 1 irradiation. The parameters for the annual energy simulations in PVsyst must be determined in terms of produced power per incident power following the equations in chapter 2.

All parameters not described here which affect the results are kept equal for all the simulations, and can be found in Appendix A together with detailed simulation reports. The cell is 155 x 155 mm^2. There are 36 cells in series in each module and there are 40 modules in series. For each panel, the 2 variables are:

- Performance at normal irradiance
- The IAM factor (from Figure 94)

To mimic realistic conditions the incident normal irradiance consists of diffuse and direct components. The normal irradiance is calculated by integrating the diffuse and direct portions of the AM1 global solar spectrum from SMARTS2 and the fractions are calculated to be 22.2% and 77.8%, respectively. The LTF data under direct and diffuse (clear sky) irradiance are combined with these fractions for each glass covered panel and subsequently the performance can be calculated for 1000W irradiance.

The performance at normal irradiance is given in terms of the V_{mpp}, I_{mpp}, I_{sc}, V_{oc} and FF, which are calculated based on the LTF data.

The results from the simulations are shown in Table 10.

Table 10: Simulation results from PVsyst. The annual energy production is shown as well as % gain relative to the performance for plain glass cover.

	Annual energy production (kWh)	% Gain
Plain glass	2133.1	0
Inverted pyramids (e.g. Albarino P)	2264.5	6.16
Pyramidal grooves (e.g. Albarino G)	1297.0	-39.20
Cube corners (e.g. SolarExcel)	2273.0	6.56
Thin film ARC	2223.0	4.21
Rough glass (e.g. MT11050)	2082.3	-2.38

Neither pyramidal grooves nor rough glass result in any gain in efficiency relative to plain glass cover in these simulations. However, inverted pyramids, cube corners and thin film ARC increase the annual energy production considerably. More detailed outputs for the whole year are shown in Appendix A.

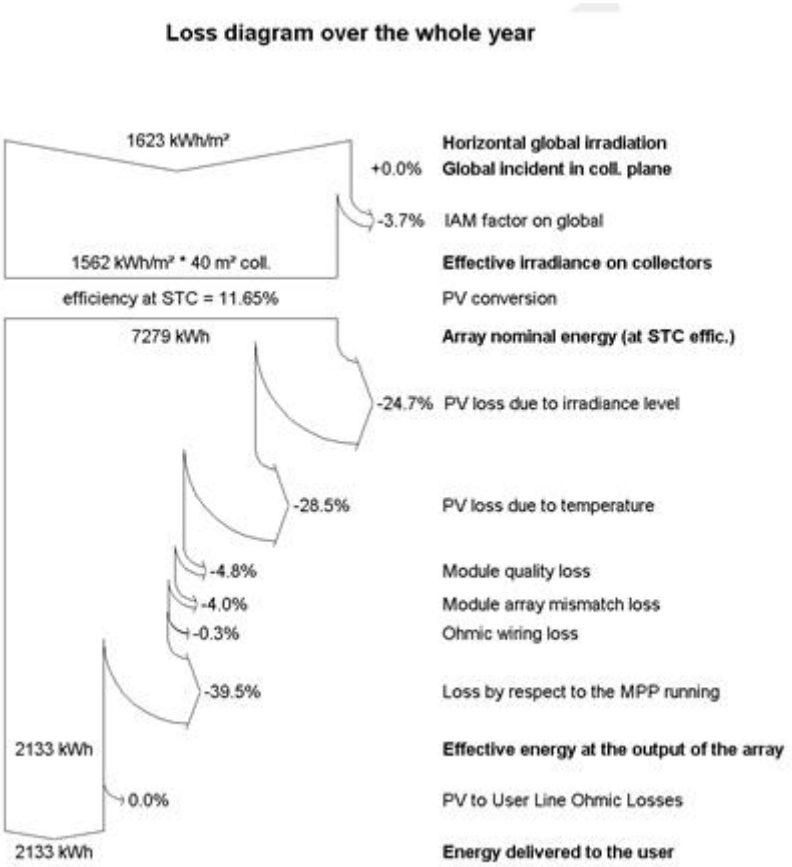

Figure 103: Annual energy simulation results from PVsyst for Singapore. As the solar panel is modelled close to ideal, ohmic losses, etc. are kept at a minimum. The panel tilt is zero.

6.2.3.2 TP Solar Utility

The annual energy productions simulations were also conducted in TP Solar Utility. For comparison purposes Singapore is chosen as location.

Simulations for each day throughout a year is time consuming, so 4 days spaced 3 months apart are used as basis for the simulation. The annual energy production is extrapolated from these integrated daily values. The 4 days are representing each quarter of a year are:

- January – March: 15th February
- April – June: 15th May
- July – September: 15th August
- October – December: 15th November

The simulations are run at 30 minutes intervals between each ray trace simulation. The solar panel is a quarter of a typical solar cell, i.e. 77.5 x 77.5 mm^2. The results are shown in Table 11. These results are the integrated absorbed flux in the cell ($P_{in,cell}$ x EQE) over time, giving the energy production.

Table 11: Simulation results from TP Solar Utility. The annual energy production is shown as well as % gain relative to the performance for plain glass cover. The pyramidal grooved texture resulted in technical issues during simulations and had had to be excluded.

	Annual energy production (kWh)	% Gain relative to plain glass
Plain glass	11.09	0
Inverted pyramids (e.g. Albarino P)	11.21	1.1
Pyramidal grooves (e.g. Albarino G)	N/A	N/A
Cube corners (e.g. SolarExcel)	11.47	3.3
Thin film ARC	11.44	3.1
Rough glass (e.g. MT11050)	10.00	-9.9

The differences in results between TP Solar Utility and PVsyst are summarized in Figure 104. PVsyst results in higher annual gains than TP Solar Utility. This could be caused by several factors, including e.g.:

1. The way light absorption is linked to power generation in PVsyst
2. Diffuse irradiance is included in PVsyst but not in TP Solar Utility

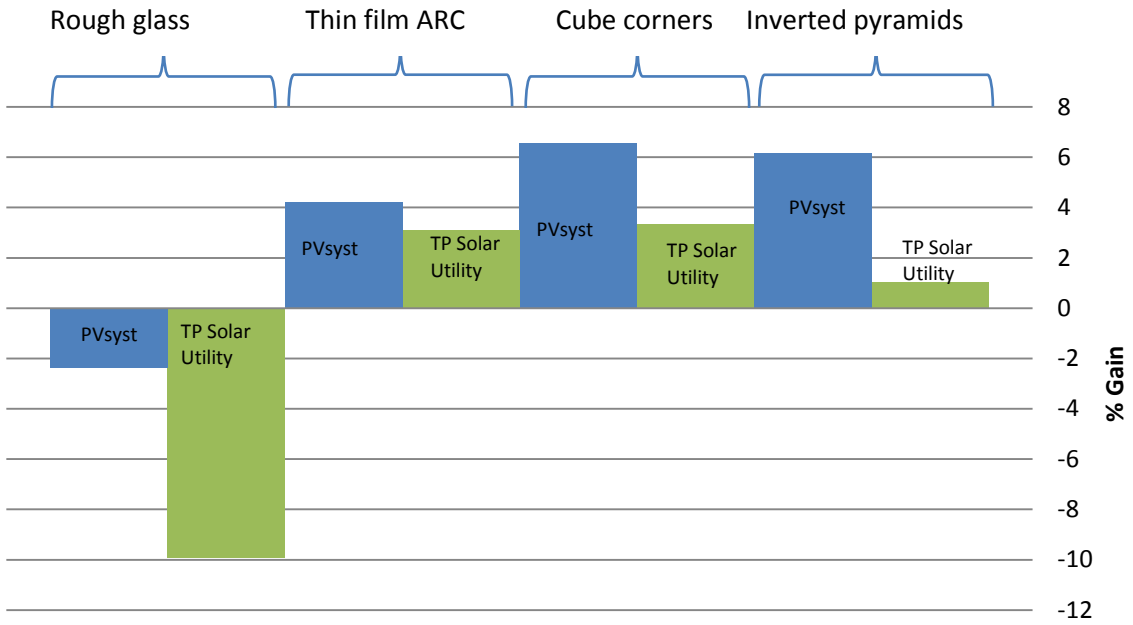

Figure 104: Annual gain in energy production for PVsyst and TP Solar Utility. There is in general quite poor agreement between the two, but PVsyst tends to consistently result in higher gain than TP Solar Utility.

7 Discussion

This study presents a novel approach to evaluate a PV panel's performance under direct and diffuse irradiance. This study is limited to optical simulation. Other physical effects experienced by a PV panel operating in the terrestrial environment, e.g. non-uniform temperature, dust, degradation, etc. are not considered

The values presented in Chapter 6 cannot directly be applied, and are not intended to, evaluate the performance of actual solar panels with anti-reflective glasses. The results should be viewed as how well the anti-reflective glasses perform with respect to each other and plain glass, henceforth evaluating which glass is the best for a given location.

The results are strongly limited by the PV panel tested. The simple solar cell model described in chapter 4 does not consider absorption as function of the angle of incidence. This effect was shown by a comparison between the simple cell model and the complex cell model in Figure 61 - 63. Furthermore, the simple cell model reflects light following a Lambertian distribution and all losses are modeled as reflection losses. Thus there is more light within the panel to be internally reflected back onto the cell after being "lost" as reflection. However these effects will be the same for all the glasses, including the reference plain glass. Therefore the PV panel model should be a good tool to investigate the general performance of anti-reflective glasses compared with each other.

The complex PV model was intended to take most optical effects into account, and thereby both serve as a realistic PV model to do performance simulations and as a validation tool for simple models. However, during this study the complex model resulted in computational error in the ray tracing software. Hence the simple model was only partly validated against the complex bare cell model based on polished textured surfaces. This is far from representing the complexity of a real PV module, but it was shown that that the complex cell model reflects light at normal incidence similar to a commercial cell in the wavelength region from 300 nm to 1100 nm (ref Figure 60). However neither the reflection at oblique angles of incidence nor the scattering distribution has been validated. Correcting the software error and run simulations with the complex cell model and add the corresponding optical elements (e.g EVA, glass, scattering surfaces, Tedlar) forming a PV panel would be valuable for future studies.

The results presented in Chapter 6 shows gains mostly in excess of the claimed gains for similar anti-reflective glasses found in the literature review (see Figure 1)). The reason for this is unclear. The geometrical shapes of the optically modeled anti-reflective glasses are based on the authors' approximations of commercial products available today. It was also considered that the textured surfaces showed a specular behavior. Such perfectly smooth surfaces and geometrical approximations could be a factor.

Also shown in chapter 6 two of the textured glasses, pyramidal grooved texture and rough glass, performs for some angles of incidence poorer than plain glass. The rough glass tested is not specifically designed for use with PV panels which might explain its poor performance. Also the rough glass is modeled as ABg function in the ray tracing software with fixed transmittance and reflection fractions which are independent of angle of incidence. This explains the constant LTF of the rough glass for different angles of incidence.

Optical modeling can produce inaccurate results, as might be the case with pyramidal grooved texture. Several studies, presented in the literary review, report on favorable performance (around 2% gain) using this type of texture. The results presented in chapter 6 do not correspond with these results, instead leading to negative gain at most angles of incidence, which could be caused by poor optical modeling of the glass structure. The test performed with sharp pyramidal grooves for comparison in Figure 96, as well as irregular absorption values in Figure 99, seems to support this. However, this could also be seen as an example of how important it is to regard the reflectance at all angles of incidence, and not only regard a PV panel's performance at normal irradiance. The pyramidal grooves perform similar to that of plain glass at normal irradiance, but the performance between 20 and 70 degrees speaks for its own.

The importance of having an optical direct irradiance model that, like the one presented in this study, takes angle of incidence into account is therefore evident. In this study the normal irradiance was AM1 spectrum. This must be adapted according to location. In 40° latitude, where solar zenith is not experienced, a 40° tilted panel would receive AM1.3 spectrum at normal incidence, and so on. For future studies, the direct irradiance model presented in this thesis can be adapted to any location by just tilting the panel orientation.

Both angular and spectral effects were demonstrated in the results from the three diffuse irradiance models. Under diffuse irradiance the LTF, and hence the I_{SC}, has a weak dependence on solar zenith angle. This finding indicates that for future studies, only one or two solar zenith angles has to be included in diffuse irradiance models. However, the importance of using the correct solar spectrum for the relevant sky conditions was indicated. E.g. at normal irradiance plain glass resulted in LTF of 0.56 and 0.67 under clear sky and overcast sky, respectively, which is a 20 % difference. The weak dependence for LTF on solar zenith angle leads on to conclude that this is caused by spectral effects. Only the clear sky irradiance model has different diffuse solar spectrum at each solar zenith angle, and it can be seen in Figure 100that the LTF even increases at high solar zenith angles for some glasses.

Having calculated the LTF for the different glass covers as a function of angle of incidence, this data can be directly combined with irradiance data for a location containing annual insolation on a horizontal surface as a function of angle of incidence. This will return annual energy production from the ray tracing models and can be compared to annual energy production calculated in PVsyst in future studies whenever the abovementioned data are available.

Figure 102 combined with Figure 104 summarizes the contribution made by this thesis. Both figures demonstrate that measuring gains at normal incidence or STC is not sufficient practice for choosing appropriate anti-reflective glass. In Figure 102 it is shown that thin film performs better compared with inverted pyramids under direct irradiance up to 63 degrees angles of incidence, for higher angles inverted pyramids significantly outperforms thin film. Under diffuse irradiance inverted pyramids performs better for all angles of incidence. The contrasting performance characteristics can be further analyzed by assessing the energy production results from PVsyst, shown in Figure 104. For the given location with the given irradiance conditions (77.8% direct and 22.2% diffuse) inverted pyramids produces approximately 2% more energy over a year compared with thin film. Had the decision on witch anti-reflective glass been made on normal incidence or STC measurements solely the panel would not harvest light at its full potential.

8 Conclusions

The type of glass cover is an important factor influencing the performance of photovoltaic panels, and can turn out to be an active component in the design of PV panels in different locations. Optical modelling and ray tracing were used in this study to investigate the effects of anti-reflecting glass covers on PV panel performance under direct and diffuse irradiance. Universities and manufacturers of such products have reported different gains based on a wide range of different conditions, as summarized in Figure 1. In this study a selection of such anti-reflective glass covers are evaluated under the same simulation conditions.

A simple optical model for a PV panel was evaluated against a more complex optical model, and used as basis for the simulations. The PV model was investigated with six different glass covers, one with plain float glass and five with different anti-reflecting textures or coating. Four irradiance models were presented to investigate the performance of the PV panels; one direct and three diffuse. The direct irradiance model takes into account how the atmosphere changes the solar spectrum as a function of the perceived irradiation angle. In addition, three diffuse irradiance models mimic the multidirectional irradiance under three sky conditions, namely clear, partly cloudy and overcast sky.

The light transmission factor (LTF) was calculated, as well as the generated short circuit current I_{SC} per irradiance (A/W) for each glass cover under each irradiance model. The commercial software PVsyst was fed with performance results from the simulations for each glass cover (IAM factor and "nominal" power) to investigate the gain in annual energy production relative to using plain glass. As a trial these results were compared to gain in annual energy production from optical ray tracing based solely on direct irradiance in Tracepro Solar Utility.

The simulation results show in general a gain in PV panel performance when using anti-reflecting glass covers relative to plain float glass. Textured glass surface is particularly effective under high angles of incidence, and therefore also diffuse irradiance, which indicates that it can be of extra value in locations experiencing high share of overcast sky conditions. Performance gains as high as 12 % were found for cube corner textured glass under overcast sky conditions.

Thin film ARC were shown to performs better than inverted pyramids texture under normal irradiance (3.7% versus 0.6%), however the textured glass return more gain in annual energy production from PVsyst because of the performance under diffuse irradiance (6.2% and 4.2% for inverted pyramids and thin film ARC, respectively). The diffuse fraction of global irradiance varies from one location to the next, and hence an optimal glass cover could be chosen for a given location.

One of the glass cover textures, pyramidal grooves, performed remarkably poorly. It is also the only model to be modelled in CAD software, which may have caused error. Rough glass also resulted in lower energy production than plain glass.

For future studies it is recommended to use the full complex PV panel models, combined with the irradiance models be adapted to a specific location.

If annual isolation as a function of angle of incidence on a horizontal surface is available for a location, this data can be combined with the LTF (per angle of incidence) for each glass cover, and return the annual energy production. This would be valuable to compare with PVsyst results. It would

also be a step closer to determining the optimal glass cover for a specific location. It was found that the LTF has weak dependence on solar zenith angle under diffuse irradiance. Based on this finding it is proposed for future studies to settle with only one or two solar zenith angles, provided the correct solar spectrum is used. With location adapted models, optimization of the glass cover for different locations is feasible.

References

[1] J. L. Torres and L. M. Torres, *Modeling solar radiation at the Earth's surface: recent advances*. Springer, 2008, p. 427.

[2] M. Duell, M. Ebert, M. Muller, B. Li, M. Koch, T. Christian, R. F. Perdichizzi, B. Marion, S. Kurtz, and D. M. J. Doble, "Impact of Structured Glass on Light Transmission, Temperature and Power of PV Modules," in *25th European Photovoltaic Solar Energy Conference and Exhibition / 5th World Conference on Photovoltaic Energy Conversion*, 2010, no. September.

[3] J. Wohlgemuth, D. Cunningham, J. Shaner, A. Nguyen, S. Ransome, and A. Artigao, *Crystalline silicon photovoltaic modules with anti-reflective coated glass*, no. 1. IEEE, 2005, pp. 1015–1018.

[4] D. Neumann, W. A. Nositschka, M. Prast, M. Neander, and K. Werner, "Outdoor Monitoring of Antireflective and Textured Cover Glasses for Solar Modules at Different Sites in Germany, Spain and China of Up to 3 Years," in *24h European Photovoltaic Solar Energy Conference and Exhibition, 21-25 September 2009, Hamburg, Germany*, 2009, no. September, pp. 3359–3362.

[5] S. R. Williams, T. R. Betts, R. Gottschalg, D. Neumann, M. O. Prast, and A. Nositschka, "Evaluating the Outdoor Performance of PV Modules with Different Glass Textures," 2011.

[6] P. Sanchez-Friera, D. Montiel, J. F. Gil, J. A. Montanez, and J. Alonso, "Daily power output increase of over 3% with the use of structured glass in monocrystalline silicon PV modules," *2006 IEEE 4th World Conference on Photovoltaic Energy Conference*, vol. 2, pp. 2156–2159, 2006.

[7] C. Ulbrich, A. Gerber, K. Hermans, A. Lambertz, and U. Rau, "Analysis of short circuit current gains by an anti-reflective textured cover on silicon thin film solar cells," *Progress in Photovoltaics Research and Applications*, 2012.

[8] M. Tachikawa, Y. Nozaki, T. Nishioka, and T. Yamada, "Enhancement of pv module efficiency using reduced reflection-loss surface," in *16th European Photovoltaic Solar Energy Conference*, 2000, pp. 2110–2112.

[9] J. Escarré, K. Söderström, M. Despeisse, S. Nicolay, C. Battaglia, G. Bugnon, L. Ding, F. Meillaud, F.-J. Haug, and C. Ballif, "Geometric light trapping for high efficiency thin film silicon solar cells," *Solar Energy Materials and Solar Cells*, vol. 98, pp. 185–190, 2012.

[10] J. Son, M. Sakhuja, A. J. Danner, C. S. Bhatia, and H. Yang, "Large scale antireflective glass texturing using grid contacts in anodization methods," *Solar Energy Materials and Solar Cells*, vol. 116, pp. 9–13, Sep. 2013.

[11] A. Nositschka, D. Neumann, M.-O. Prast, and M. Bonnet-Eymard, "Temperature Effect of Textured (Light-Trapping) Cover Glasses for Solar Modules for Reduced Voc Losses Tested Indoor and Outdoor," in *25th European Photovoltaic Solar Energy Conference and Exhibition / 5th World Conference on Photovoltaic Energy Conversion*, 2010.

[12] Alfasolar, "Whitepaper: Higher yield by texturing the surface of the module glass," no. December, pp. 49–50, 2009.

[13] P. Grunow, D. Sauter, V. Hoffmann, D. Huljić, B. Litzenburger, and L. Podlowski, “The influence of textured surfaces of solar cells and modules on the energy rating of PV systems.”

[14] M. A. Green, “Self-consistent optical parameters of intrinsic silicon at 300K including temperature coefficients,” *Solar Energy Materials and Solar Cells*, vol. 92, no. 11, pp. 1305–1310, 2008.

[15] M. A. Green, *Silicon solar cells: Advanced principles & practice*. Centre for photovoltaic devices and systems, University of New South Wales, 1995.

[16] J. A. Mazer, *Solar cells: An introduction to crystalline photovoltaic technology*. Kluwer Academic Publishers, 1997.

[17] M. A. Quintana, D. L. King, B. R. Hansen, and J. A. Kratochvil, “Dark current-voltage measurements on photovoltaic modules as a diagnostic or manufacturing tool,” in *26th IEEE Photovoltaic Specialists Conference*, 1997, no. September.

[18] S. R. Wenham, M. A. Green, M. A. Watt, R. Corkish, and A. Sproul, *Applied photovoltaics*, 3rd ed. Earthscan, 2011.

[19] D. L. King, W. E. Boyson, and J. A. Kratochvil, “Photovoltaic array performance model,” Albuquerque, New Mexico, 2004.

[20] T. Yamada, H. Nakamura, T. Sugiura, K. Sakuta, and K. Kurokawa, “Reflection loss analysis by optical modeling of PV module,” vol. 67, pp. 405–413, 2001.

[21] E. J. Wiggelinkhuizen, “Building integration of photovoltaic power systems using amorphous silicon modules : irradiation loss due to non- conventional orientations,” no. December, pp. 1–40, 2001.

[22] N. R. E. Laboratory, “Solar spectra: Air mass zero,” *U.S. Department of Energy*, 2009. [Online]. Available: http://rredc.nrel.gov/solar/spectra/am0/. [Accessed: 25-Feb-2013].

[23] J. Twidell and T. Weir, *Renewable energy resources*, 2nd Editio. London, England: Taylor & Francis, 2006, pp. 85–114.

[24] D. R. Myers, K. Emery, and C. Gueymard, “Revising and validating spectral irradiance reference standards for photovoltaic performance,” in *ASESASME Solar Energy Conference*, 2002, pp. 367–376.

[25] C. Wehrli, “Extraterrestrial solar spectrum,” Davos Dorf, Switzerland, 1985.

[26] R. McGuire, “U.S. Standard atmosphere 1976,” *United States Comittee on Extension to the Standard Atmosphere (COESA)*, 1976. [Online]. Available: http://modelweb.gsfc.nasa.gov/atmos/us_standard.html. [Accessed: 25-Feb-2013].

[27] E. Shettle and R. Fenn, “Models of the atmospheric aerosol and their optical properties,” in *AGARD Conf. No. 183: Optical Propagation in the Atmosphere; Electronic Wave Propagation Panel Symposium*, 1975.

[28] "Rayleigh scattering," *Encyclopedia Britannica*, 2013. [Online]. Available: http://www.britannica.com/EBchecked/topic/492483/Rayleigh-scattering. [Accessed: 27-Feb-2013].

[29] D. R. Myers, "Terrestrial solar spectral distributions derived from broadband hourly solar rediation data," Golden, Colorado, USA, Aug. 2009.

[30] NREL, "NREL's Spectral Solar Radiation Data Base: FSEC - Florida Solar Energy Center," 1986. [Online]. Available: http://rredc.nrel.gov/solar/old_data/spectral/fsec/. [Accessed: 01-Mar-2013].

[31] S. Darula and R. Kittler, "CIE general sky standard defining luminance distributions," Bratislava, Slovakia, 2002.

[32] H. Nakamura and Y. Hayashi, "Luminance distribution of intermediate sky," Nagoya, Japan, 1985.

[33] R. Perez, R. Seals, P. Ineichen, R. Stewart, and D. Menicucci, "A new simplified version of the Perez diffuse irradiance model for tilted surfaces," *Solar Energy*, vol. 39, no. 3, pp. 221–231, 1987.

[34] Y. Uetani, "Spatial distribution of daylight-CIE standard general sky," Vienna, Austria, 2003.

[35] E. Vartiainen, "A new approach to estimating the diffuse irradiance on inclined surfaces," *Renewable Energy*, vol. 20, pp. 45–64, 2000.

[36] A. Mermoud, "PVSyst contextual help." University of Geneva, Institute of the Sciences of the Environment, Geneva, Switzerland, 2013.

[37] B. Y. H. Liu and R. C. Jordan, "The interrelationship and characteristic distribution of direct, diffuse and total solar radiation," Minnesota, USA, 1960.

[38] A. M. Noorian, I. Moradi, and G. A. Kamali, "Evaluation of 12 models to estimate hourly diffuse irradiation on inclined surfaces," *Renewable Energy*, vol. 33, no. 6, pp. 1406–1412, Jun. 2008.

[39] C. Gueymard, *"SMARTS2: a simple model of the atmospheric radiative transfer of sunshine: algorithms and performance assessment"*. Cocoa, FL, USA: Florida Solar energy Center, 1995.

[40] K. R. McIntosh, J. N. Cotsell, J. S. Cumpston, A. W. Norris, N. E. Powell, and B. M. Ketola, "An optical comparison of silicone and EVA encapsulants for conventional silicon PV modules: A ray-tracing study," *Photovoltaic Specialists Conference PVSC 2009 34th IEEE*, pp. 000544–000549, 2009.

[41] M. Rubin, "Optical properties of soda lime silica glasses," *Solar Energy Materials*, vol. 12, no. 4, pp. 275–288, Sep. 1985.

[42] P. Warren, G. Nichol, and L.-M. Deslandes, "The influence of the glass substrate on the manufacture of thin film PV modules," in *Proceedings of the 5th world conference on photovoltaic energy conversion*, 2010.

[43] J. K. Goodyear and V. L. Lindberg, “Low absorption float glass for back surface solar reflectors,” *Solar energy materials*, vol. 3, pp. 57–67, 1980.

[44] SNE Research, “Low-iron glass for Solar Cell.” [Online]. Available: http://www.sneresearch.com/eng/info/show.php?c_id=4948&pg=6&s_sort=&sub_cat=&s_type=&s_word=. [Accessed: 30-May-2013].

[45] K. R. McIntosh and S. C. Baker-Finch, “OPAL.” 2012.

[46] A. W. Czanderna and F. J. Pern, “Encapsulation of PV modules using ethylene vinyl acetate copolymer as a pottant: A critical review,” *Solar energy materials and solar cells*, vol. 43, no. 2, pp. 101–181, 1996.

[47] K. R. McIntosh, J. N. Cotsell, A. W. Norris, N. E. Powell, and B. M. Ketola, “An optical comparison of silicone and EVA encapsulants under various spectra,” in *Photovoltaic specialists conference PVSC 2010 35th IEEE*, 2010, pp. 000269–000274.

[48] Microsol, “Picture of mono c-Si photovoltaic solar cell.” [Online]. Available: http://www.directindustry.com/prod/microsol-international/monocrystalline-photovoltaic-solar-cells-54440-370450.html. [Accessed: 02-Jun-2013].

[49] J. Jaus, H. Pantsar, J. Eckert, M. Duell, H. Herfurth, and D. Doble, *Light management for reduction of bus bar and gridline shadowing in photovoltaic modules*. IEEE, 2010, pp. 000979–000983.

[50] B. Thaidigsmann, A. Wolf, and D. Biro, “Accurate determination of the IQE of screen printed silicon solar cells by accounting for the infinite reflectance of metal contacts,” in *Proceedings of the 24th EPVSEC*, 2009, no. September, pp. 2056–2059.

[51] J. Gjessing and E. S. Marstein, “Optical performance of solar modules,” in *The 3rd International Conference on Silicon Photovoltaics Hameln, Germany 25-27 March*, 2013, vol. 00.

[52] M. DeBergalis, G. Snow, D. D. May, and W. J. Gambogi, “The Third Generation of DuPont ™ Tedlar® PVF Films in Photovoltaic Module Backsheets,” in *26th European Photovoltaic Solar Energy Conference and Exhibition*, 2011, pp. 3162–3164.

[53] K. R. McIntosh, “Tracey.” 2012.

[54] A. Bidiville, K. Wasmer, R. Kraft, and C. Ballif, “Diamond wire-sawn silicon wafers - from the lab to the cell production,” 2009, no. September.

[55] K. Wasmer, A. Bidiville, F. Jeanneret, J. Michler, C. Ballif, M. Van der Meer, and P. M. Nasch, “Effects of edge defects induced by multi-wire sawing on the wafer strength,” 2008, no. September, pp. 1–5.

[56] S. C. Baker-Finch and K. R. McIntosh, “A freeware program for precise optical analysis of the front surface of a solar cell,” *Photovoltaic Specialists Conference PVSC 2010 35th IEEE*, pp. 2184–2187, 2010.

[57] S. C. Baker-finch and K. R. Mcintosh, “Reflection of normally incident light from silicon solar cells with pyramidal texture,” *Progress in Photovoltaics Research and Applications Photovolt: Research and Applications*, vol. 19, no. 4, pp. 406–416, 2010.

[58] R. Santbergen, “Optical absorption factor of solar cells for PVT systems,” Technische Universiteit Eindhoven, 2008.

[59] J. Balenzategui and F. Chenlo, “Measurement and analysis of angular response of bare and encapsulated silicon solar cells,” *Solar Energy Materials and Solar Cells*, vol. 86, no. 1, pp. 53–83, Feb. 2005.

[60] J. Hylton and A. Burgers, “Light trapping in alkaline texture etched crystalline silicon wafers,” 2000.

[61] H. Park, S. Kwon, J. S. Lee, H. J. Lim, S. Yoon, and D. Kim, “Improvement on surface texturing of single crystalline silicon for solar cells by saw-damage etching using an acidic solution,” *Solar Energy Materials and Solar Cells*, vol. 93, no. 10, pp. 1773–1778, 2009.

[62] S. C. Baker-finch and K. R. Mcintosh, “Reflection distributions of textured monocrystalline silicon: implications for silicon solar cells,” vol. 2, 2012.

[63] S.-Y. Lien, C.-H. Yang, C.-H. Hsu, Y.-S. Lin, C.-C. Wang, and D.-S. Wuu, “Optimization of textured structure on crystalline silicon wafer for heterojunction solar cell,” *Materials Chemistry and Physics*, vol. 133, no. 1, pp. 63–68, 2012.

[64] M. Edwards, S. Bowden, U. Das, and M. Burrows, “Effect of texturing and surface preparation on lifetime and cell performance in heterojunction silicon solar cells,” *Solar Energy Materials and Solar Cells*, vol. 92, no. 11, pp. 1373–1377, 2008.

[65] Lambda Research Corporation, “Scattering and surface property editor - Introduction.” [Online]. Available: http://www.lambdares.com/webinars/. [Accessed: 02-May-2013].

[66] Lambda Research Corporation, *Tracepro Users’s Manual release 7.0*. 2010.

[67] “Illustration of a steradian.” [Online]. Available: http://www.astarmathsandphysics.com/a_level_physics_notes/principles_dimensions_units_error_analysis_etc/a_level_physics_notes_the_steradian_or_unit_of_solid_angle.html. [Accessed: 02-Jun-2013].

[68] S. A. Boden, “Biomimetic nanostructured surfaces for antireflection in photovoltaics,” University of Southampton, 2009.

[69] B. S. Richards, “Novel uses of titanium dioxide for silicon solar cells,” UNSW, 2002.

[70] R. Barrio, N. González, J. Cárabe, and J. J. Gandía, “Optimisation of NaOH texturisation process of silicon wafers for heterojunction solar-cells applications,” *Solar Energy*, vol. 86, no. 3, pp. 845–854, Mar. 2012.

[71] A. Nositschka, “Sun-light harvesting with surface patterned glass for photovoltaics,” in *Usage of Solar Energy*, 2008.

[72] A. S. Shikoh, T. R. Betts, S. R. Williams, R. Gottschalg, D. Neumann, M. O. Prast, and W. A. Nositschka, “Representation of optical losses in PV system yield estimates,” 2012.

[73] B. Slager, “Method for producing a textured plate for a photovoltaic device,” U.S. Patent 201200314892012.

[74] C. Ulbrich, A. Gerber, K. Hermans, A. Lambertz, and U. Rau, “Analysis of short circuit current gains by an anti-reflective textured cover on silicon thin film solar cells,” *Progress in Photovoltaics Research and Applications*, 2012.

[75] M. Fonrodona, J. Escarre, F. Villar, D. Soler, J. Asensi, J. Bertomeu, and J. Andreu, “PEN as substrate for new solar cell technologies,” *Solar Energy Materials and Solar Cells*, vol. 89, no. 1, pp. 37–47, Oct. 2005.

[76] I. G. E. Renhorn and G. D. Boreman, “Analytical fitting model for rough-surface BRDF,” *Optics express*, vol. 16, no. 17, pp. 12892–12898, Aug. 2008.

[77] D. S. Hobbs, B. D. Macleod, J. R. Riccobono, T. Llc, and A. Street, “Update on the development of high performance anti-reflecting surface relief micro-structures,” Burlington, Massachusetts, USA, 2007.

[78] E. Wolf and M. Born, *Principles of optics*, 7th ed. Cambridge, UK: Cambridge University Press, 1999, pp. 96–97.

[79] T. Kolås and A. Røyset, “Solar reflection losses in cover glass with asymmetric v-grooves for vertical south oriented PV-module,” in *Optical Instrumentation for Energy and Environmental Applications, Eindhoven, Netherlands*, 2012.

Appendix A – PVsyst simulation reports

Plain glass

PVSYST V6.05		05/05/13	Page 1/3

DC Grid System: Simulation parameters

Project : **DC Grid Project at Singapore**

Geographical Site	**Singapore Airp.**			Country	**Singapore**
Situation		Latitude	1.4°N	Longitude	104.0°E
Time defined as		Legal Time	Time zone UT+8	Altitude	9 m
		Albedo	0.20		
Meteo data:	**Singapore Airp.**	Synthetic	Meteonorm 6.1		

Simulation variant : **New simulation variant3**

Simulation date 05/05/13 16h52

Simulation parameters

Collector Plane Orientation		Tilt	0°	Azimuth	0°
Models used		Transposition	Perez	Diffuse	Measured
Horizon		Free Horizon			
Near Shadings		No Shadings			

PV Array Characteristics

PV module	Si-mono	Model	**Simple module**		
		Manufacturer	Teknova		
Number of PV modules		In series	40 modules	In parallel	1 strings
Total number of PV modules		Nb. modules	40	Unit Nom. Power	100 Wp
Array global power		Nominal (STC)	**4000 Wp**	At operating cond.	3745 Wp (50°C)
Array operating characteristics (50°C)		U mpp	575 V	I mpp	6.5 A
Total area		Module area	**40.0 m²**	Cell area	0.9 m²

PV Array loss factors

Thermal Loss factor	Uc (const)	20.0 W/m²K	Uv (wind)	0.0 W/m²K / m/s
=> Nominal Oper. Coll. Temp. (G=800 W/m², Tamb=20°C, Wind=1 m/s.)			NOCT	56 °C
Wiring Ohmic Loss	Global array res.	1450 mOhm	Loss Fraction	1.5 % at STC
Module Quality Loss			Loss Fraction	3.0 %
Module Mismatch Losses			Loss Fraction	2.5 % (fixed voltage)

Incidence effect, user defined pr

User defined profile

0°	48°	56°	60°	65°	71°	76°	79°	90°
1.00	0.99	0.98	0.96	0.92	0.86	0.77	0.68	0.00

System Parameter		System type	**DC Grid System (public transports)**		
Grid Nominal Voltage	Operating (nominal supply)		**600 V**	Max. Allowable	900 V
Grid Line Resistances		PV field to user	0 mOhm	Supply to user	0 mOhm

User's needs : Unlimited load (grid)

DC Grid System: Main results

Project : **DC Grid Project at Singapore**

Simulation variant : **New simulation variant3**

Main system parameters					
	System type	**DC Grid System (public transports)**			
PV Field Orientation	tilt	0°	azimuth	0°	
PV Array	Nb. of modules	40	Pnom total	**4000 Wp**	
DC Grid	Nominal Voltage	600 V	Overvoltage regulation	Cut of module strings	
User's needs	Unlimited load (grid)				

Main simulation results

System Production	**Produced Energy**	**2133 kWh/year**	Specific prod.	533 kWh/kWp/year
	Performance Ratio PR	32.9 %	Solar Fraction SF	100.0 %

Normalized productions (per installed kWp): Nominal power 4000 Wp

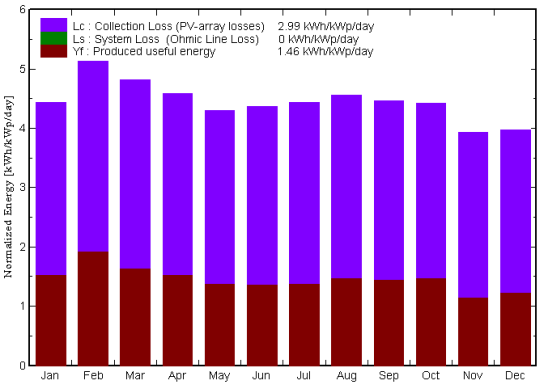

Performance Ratio PR

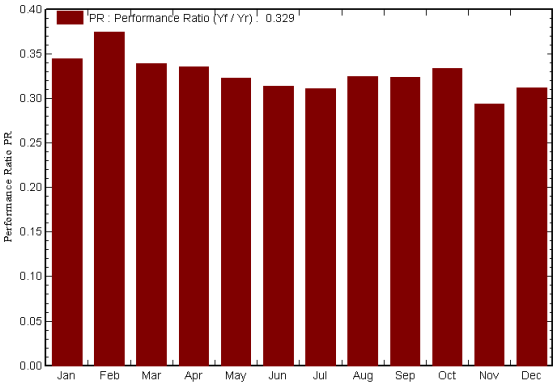

New simulation variant3

Balances and main results

	GlobHor kWh/m²	T Amb °C	GlobInc kWh/m²	GlobEff kWh/m²	EArrMPP kWh	EArray kWh	E User kWh
January	137.5	26.81	137.5	132.0	305.3	189.7	189.7
February	143.8	27.51	143.8	138.6	327.5	215.4	215.4
March	149.4	28.01	149.4	143.9	330.5	203.0	203.0
April	137.5	28.31	137.5	132.5	301.5	184.6	184.6
May	133.1	28.91	133.1	128.3	286.3	171.8	171.8
June	131.0	28.61	131.0	126.2	281.6	164.5	164.5
July	137.6	28.21	137.6	132.4	297.1	171.4	171.4
August	141.3	28.01	141.3	135.9	309.5	183.7	183.7
September	133.9	28.01	133.9	129.0	291.1	173.6	173.6
October	136.9	27.81	136.9	131.9	299.9	182.7	182.7
November	118.0	27.41	118.0	113.2	249.4	138.9	138.9
December	123.3	26.91	123.3	118.4	264.1	153.8	153.8
Year	1623.3	27.88	1623.3	1562.4	3543.7	2133.1	2133.1

Legends:

GlobHor	Horizontal global irradiation	EArrMPP	Array virtual energy at MPP
T Amb	Ambient Temperature	EArray	Effective energy at the output of the array
GlobInc	Global incident in coll. plane	E User	Energy supplied to the user
GlobEff	Effective Global, corr. for IAM and shadings		

DC Grid System: Loss diagram

Project : **DC Grid Project at Singapore**

Simulation variant : **New simulation variant3**

Main system parameters	System type	**DC Grid System (public transports)**		
PV Field Orientation	tilt	0°	azimuth	0°
PV Array	Nb. of modules	40	Pnom total	**4000 Wp**
DC Grid	Nominal Voltage	600 V	Overvoltage regulation	Cut of module strings
User's needs	Unlimited load (grid)			

Loss diagram over the whole year

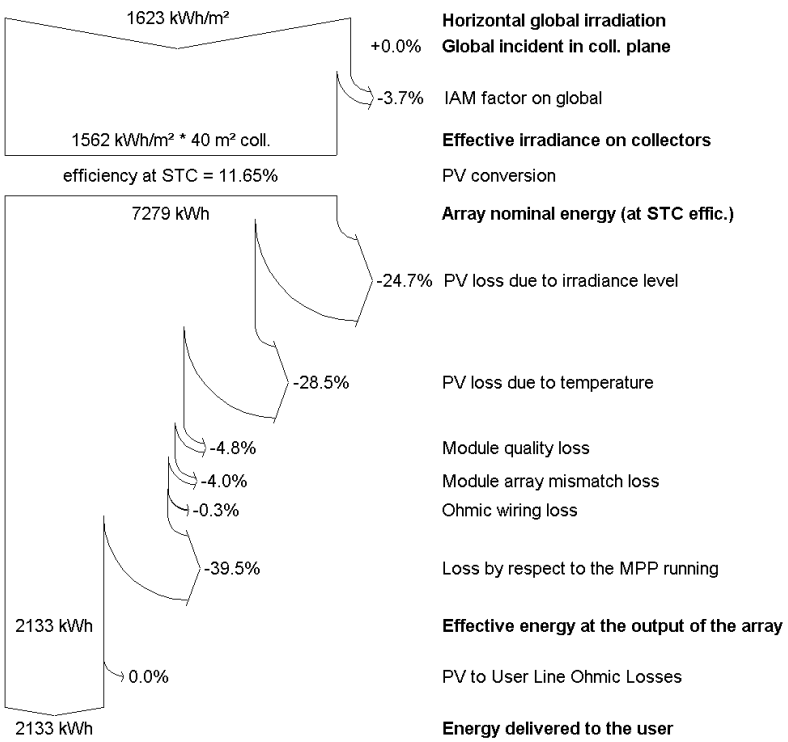

Inverted pyramids

PVSYST V6.05		05/05/13	Page 1/3

DC Grid System: Simulation parameters

Project : **DC Grid Project at Singapore**

Geographical Site	**Singapore Airp.**			Country	**Singapore**
Situation		Latitude	1.4°N	Longitude	104.0°E
Time defined as		Legal Time	Time zone UT+8	Altitude	9 m
		Albedo	0.20		
Meteo data:	**Singapore Airp.**	Synthetic	Meteonorm 6.1		

Simulation variant : **New simulation variant3**

Simulation date 05/05/13 19h47

Simulation parameters

Collector Plane Orientation		Tilt	0°	Azimuth	0°
Models used		Transposition	Perez	Diffuse	Measured
Horizon		Free Horizon			
Near Shadings		No Shadings			

PV Array Characteristics

PV module	Si-mono	Model	**Simple module**		
		Manufacturer	Teknova		
Number of PV modules		In series	40 modules	In parallel	1 strings
Total number of PV modules		Nb. modules	40	Unit Nom. Power	100 Wp
Array global power		Nominal (STC)	**4000 Wp**	At operating cond.	3847 Wp (50°C)
Array operating characteristics (50°C)		U mpp	575 V	I mpp	6.7 A
Total area		Module area	**40.0 m²**	Cell area	0.9 m²

PV Array loss factors

Thermal Loss factor		Uc (const)	20.0 W/m²K	Uv (wind)	0.0 W/m²K / m/s
=> Nominal Oper. Coll. Temp. (G=800 W/m², Tamb=20°C, Wind=1 m/s.)				NOCT	56 °C
Wiring Ohmic Loss		Global array res.	1413 mOhm	Loss Fraction	1.5 % at STC
Module Quality Loss				Loss Fraction	3.0 %
Module Mismatch Losses				Loss Fraction	2.5 % (fixed voltage)

Incidence effect, user defined pr
User defined profile

0°	48°	56°	60°	65°	76°	85°	85°	90°
1.00	0.99	0.98	0.97	0.96	0.91	0.84	0.84	0.00

System Parameter		System type	**DC Grid System (public transports)**		
Grid Nominal Voltage	Operating (nominal supply)		**600 V**	Max. Allowable	900 V
Grid Line Resistances		PV field to user	0 mOhm	Supply to user	0 mOhm

User's needs : Unlimited load (grid)

DC Grid System: Main results

Project : **DC Grid Project at Singapore**

Simulation variant : **New simulation variant3**

Main system parameters					
	System type	**DC Grid System (public transports)**			
PV Field Orientation	tilt	0°	azimuth	0°	
PV Array	Nb. of modules	40	Pnom total	**4000 Wp**	
DC Grid	Nominal Voltage	600 V	Overvoltage regulation	Cut of module strings	
User's needs	Unlimited load (grid)				

Main simulation results

System Production	**Produced Energy**	**2264 kWh/year**	Specific prod.	566 kWh/kWp/year
	Performance Ratio PR	34.9 %	Solar Fraction SF	100.0 %

Normalized productions (per installed kWp): Nominal power 4000 Wp

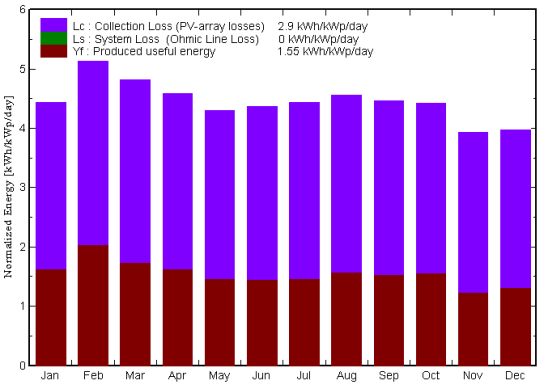

Performance Ratio PR

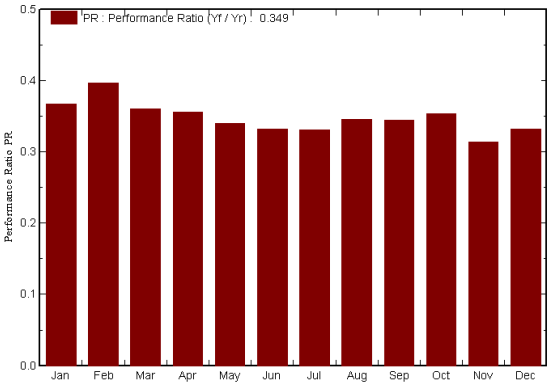

New simulation variant3

Balances and main results

	GlobHor kWh/m²	T Amb °C	GlobInc kWh/m²	GlobEff kWh/m²	EArrMPP kWh	EArray kWh	E User kWh
January	137.5	26.81	137.5	134.9	321.5	202.0	202.0
February	143.8	27.51	143.8	141.3	344.0	228.2	228.2
March	149.4	28.01	149.4	146.8	347.6	215.8	215.8
April	137.5	28.31	137.5	135.2	316.6	195.5	195.5
May	133.1	28.91	133.1	130.8	300.6	181.4	181.4
June	131.0	28.61	131.0	128.7	295.8	174.2	174.2
July	137.6	28.21	137.6	135.1	312.3	182.0	182.0
August	141.3	28.01	141.3	138.7	325.6	195.3	195.3
September	133.9	28.01	133.9	131.6	305.9	184.5	184.5
October	136.9	27.81	136.9	134.6	315.1	193.9	193.9
November	118.0	27.41	118.0	115.8	262.9	148.1	148.1
December	123.3	26.91	123.3	121.0	278.2	163.6	163.6
Year	1623.3	27.88	1623.3	1594.6	3726.1	2264.5	2264.5

Legends:

GlobHor	Horizontal global irradiation	EArrMPP	Array virtual energy at MPP
T Amb	Ambient Temperature	EArray	Effective energy at the output of the array
GlobInc	Global incident in coll. plane	E User	Energy supplied to the user
GlobEff	Effective Global, corr. for IAM and shadings		

DC Grid System: Loss diagram

Project : **DC Grid Project at Singapore**

Simulation variant : **New simulation variant3**

Main system parameters	System type	**DC Grid System (public transports)**		
PV Field Orientation	tilt	0°	azimuth	0°
PV Array	Nb. of modules	40	Pnom total	**4000 Wp**
DC Grid	Nominal Voltage	600 V	Overvoltage regulation	Cut of module strings
User's needs	Unlimited load (grid)			

Loss diagram over the whole year

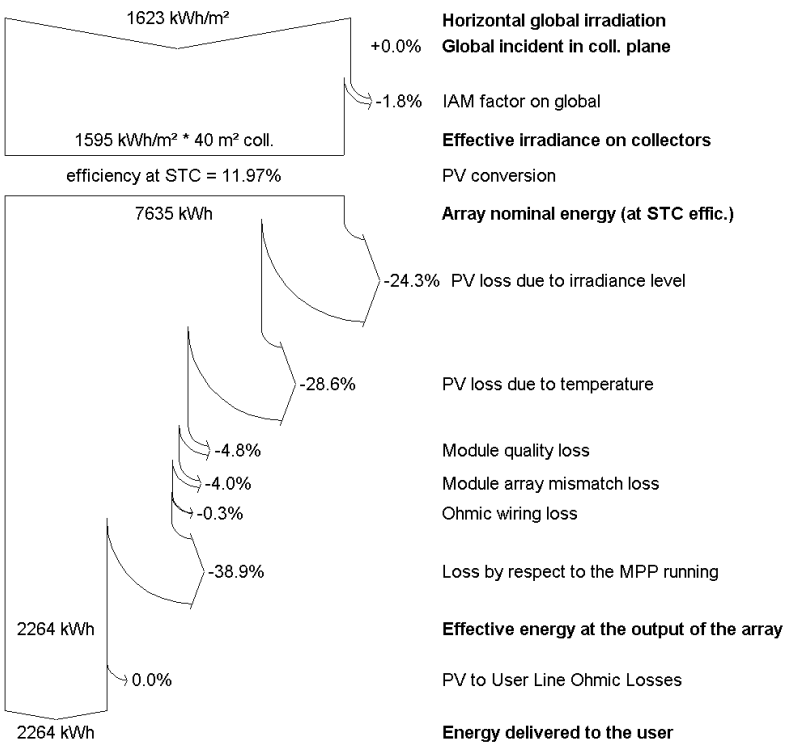

Pyramidal grooves

PVSYST V6.05		06/05/13	Page 1/3

DC Grid System: Simulation parameters

Project : **DC Grid Project at Singapore**

Geographical Site	**Singapore Airp.**			Country	**Singapore**
Situation		Latitude	1.4°N	Longitude	104.0°E
Time defined as		Legal Time	Time zone UT+8	Altitude	9 m
		Albedo	0.20		
Meteo data:	**Singapore Airp.**	Synthetic	Meteonorm 6.1		

Simulation variant : **New simulation variant3**

Simulation date 06/05/13 09h46

Simulation parameters

Collector Plane Orientation		Tilt	0°	Azimuth	0°
Models used		Transposition	Perez	Diffuse	Measured
Horizon		Free Horizon			
Near Shadings		No Shadings			

PV Array Characteristics

PV module	Si-mono	Model	**Simple module**		
		Manufacturer	Teknova		
Number of PV modules		In series	40 modules	In parallel	1 strings
Total number of PV modules		Nb. modules	40	Unit Nom. Power	100 Wp
Array global power		Nominal (STC)	**4000 Wp**	At operating cond.	3786 Wp (50°C)
Array operating characteristics (50°C)		U mpp	575 V	I mpp	6.6 A
Total area		Module area	**40.0 m²**	Cell area	0.9 m²

PV Array loss factors

Thermal Loss factor		Uc (const)	20.0 W/m²K	Uv (wind)	0.0 W/m²K / m/s
=> Nominal Oper. Coll. Temp. (G=800 W/m², Tamb=20°C, Wind=1 m/s.)				NOCT	56 °C
Wiring Ohmic Loss		Global array res.	1435 mOhm	Loss Fraction	1.5 % at STC
Module Quality Loss				Loss Fraction	3.0 %
Module Mismatch Losses				Loss Fraction	2.5 % (fixed voltage)

Incidence effect, user defined pr

User defined profile

0°	48°	56°	60°	65°	76°	85°	85°	90°
1.00	0.75	0.79	0.81	0.86	0.84	0.79	0.78	0.00

System Parameter		System type	**DC Grid System (public transports)**		
Grid Nominal Voltage	Operating (nominal supply)		**600 V**	Max. Allowable	900 V
Grid Line Resistances		PV field to user	0 mOhm	Supply to user	0 mOhm

User's needs : Unlimited load (grid)

DC Grid System: Main results

Project : **DC Grid Project at Singapore**

Simulation variant : **New simulation variant3**

Main system parameters					
	System type	**DC Grid System (public transports)**			
PV Field Orientation	tilt	0°	azimuth	0°	
PV Array	Nb. of modules	40	Pnom total	**4000 Wp**	
DC Grid	Nominal Voltage	600 V	Overvoltage regulation	Cut of module strings	
User's needs	Unlimited load (grid)				

Main simulation results

System Production	**Produced Energy**	**1297 kWh/year**	Specific prod.	324 kWh/kWp/year
	Performance Ratio PR	20.0 %	Solar Fraction SF	100.0 %

Normalized productions (per installed kWp): Nominal power 4000 Wp

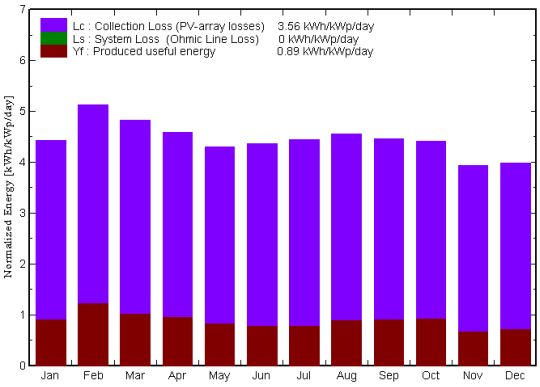

Performance Ratio PR

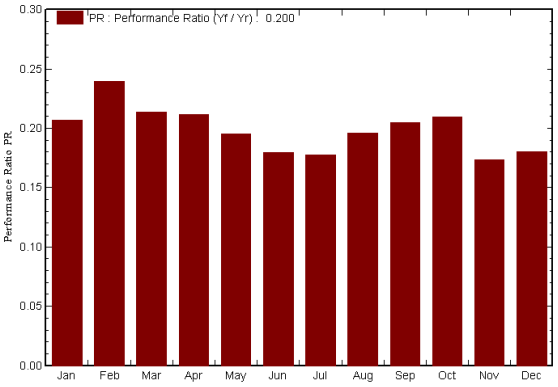

New simulation variant3

Balances and main results

	GlobHor kWh/m²	T Amb °C	GlobInc kWh/m²	GlobEff kWh/m²	EArrMPP kWh	EArray kWh	E User kWh
January	137.5	26.81	137.5	107.5	232.4	113.6	113.6
February	143.8	27.51	143.8	113.2	252.7	137.6	137.6
March	149.4	28.01	149.4	118.4	256.5	127.6	127.6
April	137.5	28.31	137.5	108.9	233.3	116.3	116.3
May	133.1	28.91	133.1	104.2	217.2	104.0	104.0
June	131.0	28.61	131.0	102.1	211.7	93.9	93.9
July	137.6	28.21	137.6	107.5	224.8	97.7	97.7
August	141.3	28.01	141.3	111.1	237.1	110.8	110.8
September	133.9	28.01	133.9	106.5	226.6	109.8	109.8
October	136.9	27.81	136.9	108.1	231.4	114.8	114.8
November	118.0	27.41	118.0	92.5	189.7	81.9	81.9
December	123.3	26.91	123.3	96.1	199.4	89.0	89.0
Year	1623.3	27.88	1623.3	1276.2	2712.7	1297.0	1297.0

Legends:

GlobHor	Horizontal global irradiation	EArrMPP	Array virtual energy at MPP
T Amb	Ambient Temperature	EArray	Effective energy at the output of the array
GlobInc	Global incident in coll. plane	E User	Energy supplied to the user
GlobEff	Effective Global, corr. for IAM and shadings		

DC Grid System: Loss diagram

Project : **DC Grid Project at Singapore**

Simulation variant : **New simulation variant3**

Main system parameters	System type	**DC Grid System (public transports)**		
PV Field Orientation	tilt	0°	azimuth	0°
PV Array	Nb. of modules	40	Pnom total	**4000 Wp**
DC Grid	Nominal Voltage	600 V	Overvoltage regulation	Cut of module strings
User's needs	Unlimited load (grid)			

Loss diagram over the whole year

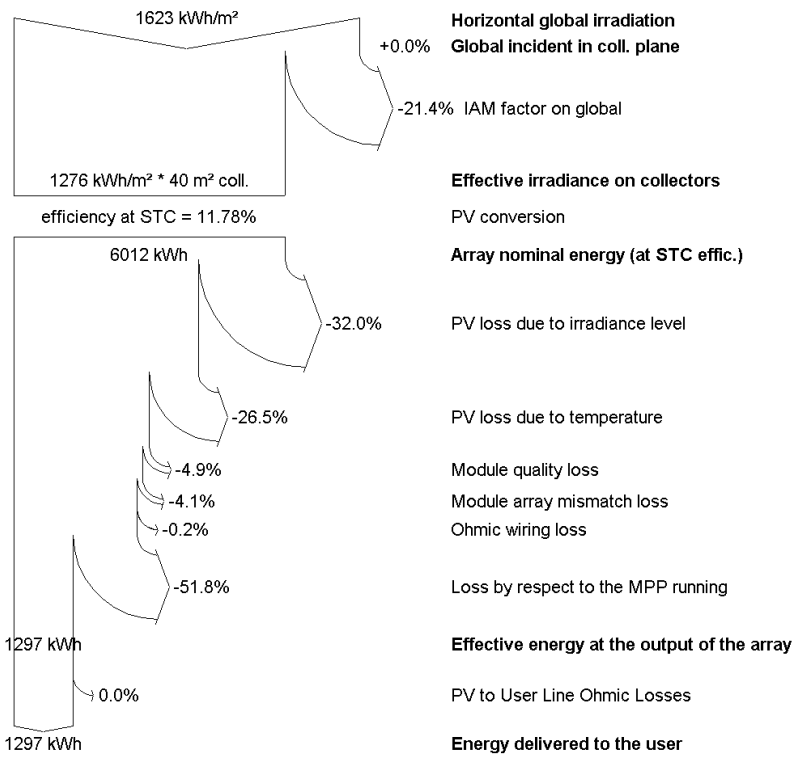

PVSYST V6.05		05/05/13	Page 1/3

DC Grid System: Simulation parameters

Project : **DC Grid Project at Singapore**

Geographical Site		**Singapore Airp.**		Country	**Singapore**
Situation		Latitude	1.4°N	Longitude	104.0°E
Time defined as		Legal Time	Time zone UT+8	Altitude	9 m
		Albedo	0.20		
Meteo data:	**Singapore Airp.**	Synthetic	Meteonorm 6.1		

Simulation variant : **New simulation variant3**

Simulation date 05/05/13 18h13

Simulation parameters

Collector Plane Orientation		Tilt	0°	Azimuth	0°
Models used		Transposition	Perez	Diffuse	Measured
Horizon		Free Horizon			
Near Shadings		No Shadings			

PV Array Characteristics

PV module	Si-mono	Model	**Simple module**		
		Manufacturer	Teknova		
Number of PV modules		In series	40 modules	In parallel	1 strings
Total number of PV modules		Nb. modules	40	Unit Nom. Power	100 Wp
Array global power		Nominal (STC)	**4000 Wp**	At operating cond.	3984 Wp (50°C)
Array operating characteristics (50°C)		U mpp	575 V	I mpp	6.9 A
Total area		Module area	**40.0 m²**	Cell area	0.9 m²

PV Array loss factors

Thermal Loss factor	Uc (const)	20.0 W/m²K	Uv (wind)	0.0 W/m²K / m/s
=> Nominal Oper. Coll. Temp. (G=800 W/m², Tamb=20°C, Wind=1 m/s.)			NOCT	56 °C
Wiring Ohmic Loss	Global array res.	1365 mOhm	Loss Fraction	1.5 % at STC
Module Quality Loss			Loss Fraction	3.0 %
Module Mismatch Losses			Loss Fraction	2.5 % (fixed voltage)

Incidence effect, user defined pr

User defined profile

0°	65°	76°	85°	85°	90°
1.00	0.95	0.94	0.91	0.91	0.00

System Parameter		System type	**DC Grid System (public transports)**		
Grid Nominal Voltage	Operating (nominal supply)		**600 V**	Max. Allowable	900 V
Grid Line Resistances	PV field to user		0 mOhm	Supply to user	0 mOhm

User's needs : Unlimited load (grid)

DC Grid System: Main results

Project : **DC Grid Project at Singapore**

Simulation variant : **New simulation variant3**

Main system parameters					
	System type	**DC Grid System (public transports)**			
PV Field Orientation	tilt	0°	azimuth	0°	
PV Array	Nb. of modules	40	Pnom total	**4000 Wp**	
DC Grid	Nominal Voltage	600 V	Overvoltage regulation	Cut of module strings	
User's needs	Unlimited load (grid)				

Main simulation results

System Production	**Produced Energy**	**2273 kWh/year**	Specific prod.	568 kWh/kWp/year
	Performance Ratio PR	35.0 %	Solar Fraction SF	100.0 %

Normalized productions (per installed kWp): Nominal power 4000 Wp

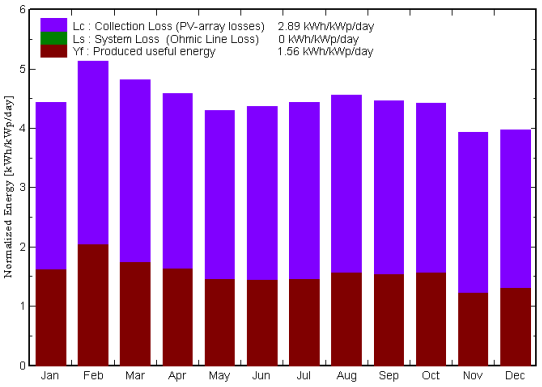

Performance Ratio PR

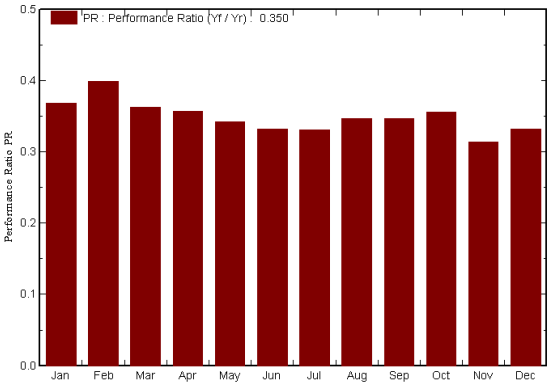

New simulation variant3

Balances and main results

	GlobHor kWh/m²	T Amb °C	GlobInc kWh/m²	GlobEff kWh/m²	EArrMPP kWh	EArray kWh	E User kWh
January	137.5	26.81	137.5	133.0	326.1	202.5	202.5
February	143.8	27.51	143.8	139.5	349.5	229.8	229.8
March	149.4	28.01	149.4	144.9	353.1	217.1	217.1
April	137.5	28.31	137.5	133.4	321.6	196.7	196.7
May	133.1	28.91	133.1	129.0	304.8	182.1	182.1
June	131.0	28.61	131.0	126.9	299.7	174.2	174.2
July	137.6	28.21	137.6	133.2	316.6	182.1	182.1
August	141.3	28.01	141.3	136.9	330.4	195.9	195.9
September	133.9	28.01	133.9	129.9	310.8	185.6	185.6
October	136.9	27.81	136.9	132.8	320.0	195.1	195.1
November	118.0	27.41	118.0	114.2	266.6	148.4	148.4
December	123.3	26.91	123.3	119.3	281.8	163.6	163.6
Year	1623.3	27.88	1623.3	1573.0	3780.9	2273.0	2273.0

Legends:

GlobHor	Horizontal global irradiation	EArrMPP	Array virtual energy at MPP
T Amb	Ambient Temperature	EArray	Effective energy at the output of the array
GlobInc	Global incident in coll. plane	E User	Energy supplied to the user
GlobEff	Effective Global, corr. for IAM and shadings		

DC Grid System: Loss diagram

Project : **DC Grid Project at Singapore**

Simulation variant : **New simulation variant3**

Main system parameters	System type	**DC Grid System (public transports)**		
PV Field Orientation	tilt	0°	azimuth	0°
PV Array	Nb. of modules	40	Pnom total	**4000 Wp**
DC Grid	Nominal Voltage	600 V	Overvoltage regulation	Cut of module strings
User's needs	Unlimited load (grid)			

Loss diagram over the whole year

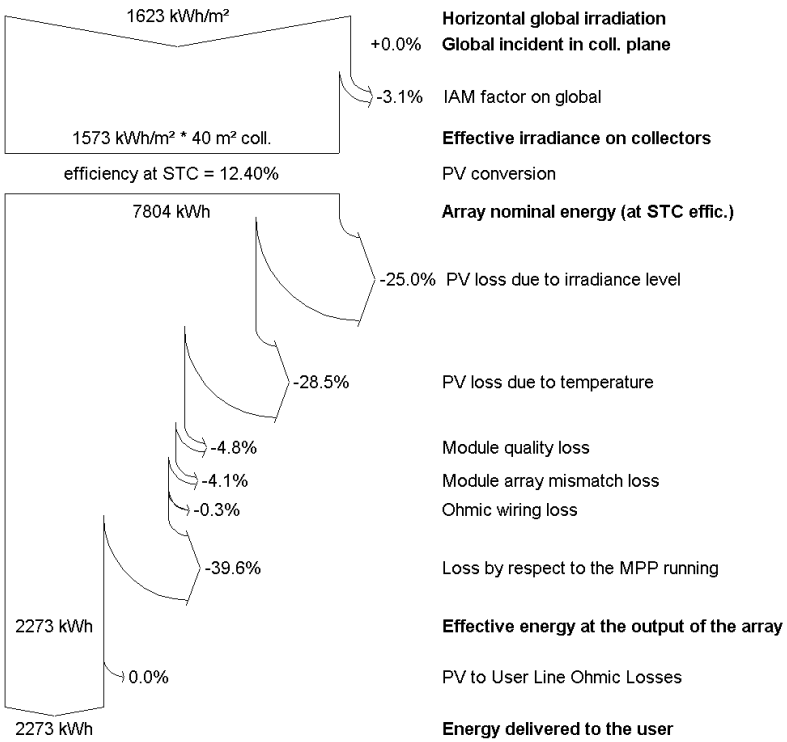

Rough glass

DC Grid System: Simulation parameters

Project : **DC Grid Project at Singapore**

Geographical Site	**Singapore Airp.**			Country	**Singapore**
Situation		Latitude	1.4°N	Longitude	104.0°E
Time defined as		Legal Time	Time zone UT+8	Altitude	9 m
		Albedo	0.20		
Meteo data:	**Singapore Airp.**	Synthetic	Meteonorm 6.1		

Simulation variant : **New simulation variant3**

Simulation date 06/05/13 10h00

Simulation parameters

Collector Plane Orientation		Tilt	0°	Azimuth	0°
Models used		Transposition	Perez	Diffuse	Measured
Horizon		Free Horizon			
Near Shadings		No Shadings			

PV Array Characteristics

PV module	Si-mono	Model	**Simple module**		
		Manufacturer	Teknova		
Number of PV modules		In series	40 modules	In parallel	1 strings
Total number of PV modules		Nb. modules	40	Unit Nom. Power	100 Wp
Array global power		Nominal (STC)	**4000 Wp**	At operating cond.	3452 Wp (50°C)
Array operating characteristics (50°C)		U mpp	574 V	I mpp	6.0 A
Total area		Module area	**40.0 m²**	Cell area	0.9 m²

PV Array loss factors

Thermal Loss factor	Uc (const)	20.0 W/m²K	Uv (wind)	0.0 W/m²K / m/s
=> Nominal Oper. Coll. Temp. (G=800 W/m², Tamb=20°C, Wind=1 m/s.)			NOCT	56 °C
Wiring Ohmic Loss	Global array res.	1571 mOhm	Loss Fraction	1.5 % at STC
Module Quality Loss			Loss Fraction	3.0 %
Module Mismatch Losses			Loss Fraction	2.5 % (fixed voltage)

Incidence effect, user defined pr

0°	48°	56°	60°	65°	76°	85°	85°	90°
1.00	1.00	1.00	1.00	1.00	0.99	0.98	0.98	0.00

User defined profile

System Parameter System type **DC Grid System (public transports)**

Grid Nominal Voltage	Operating (nominal supply)	**600 V**	Max. Allowable	900 V
Grid Line Resistances	PV field to user	0 mOhm	Supply to user	0 mOhm

User's needs : Unlimited load (grid)

DC Grid System: Main results

Project : **DC Grid Project at Singapore**

Simulation variant : **New simulation variant3**

Main system parameters					
	System type	**DC Grid System (public transports)**			
PV Field Orientation	tilt	0°	azimuth	0°	
PV Array	Nb. of modules	40	Pnom total	**4000 Wp**	
DC Grid	Nominal Voltage	600 V	Overvoltage regulation	Cut of module strings	
User's needs	Unlimited load (grid)				

Main simulation results

System Production	**Produced Energy**	**2082 kWh/year**	Specific prod.	521 kWh/kWp/year
	Performance Ratio PR	32.1 %	Solar Fraction SF	100.0 %

Normalized productions (per installed kWp): Nominal power 4000 Wp

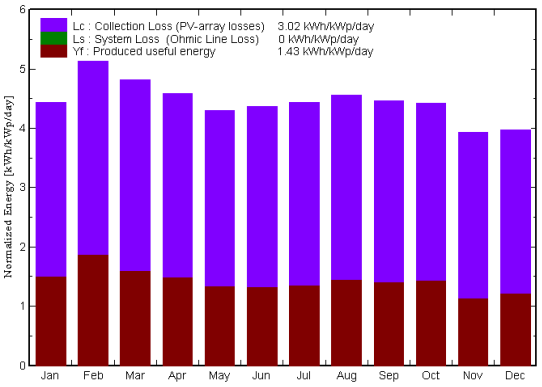

Performance Ratio PR

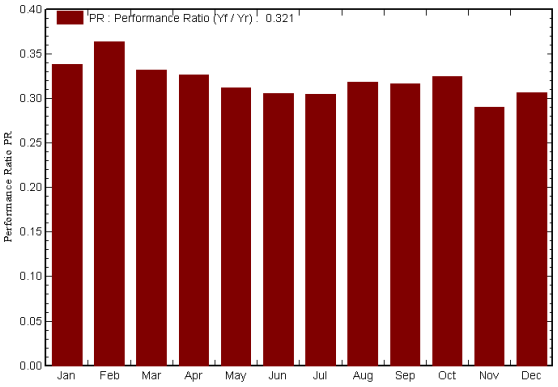

New simulation variant3

Balances and main results

	GlobHor kWh/m²	T Amb °C	GlobInc kWh/m²	GlobEff kWh/m²	EArrMPP kWh	EArray kWh	E User kWh
January	137.5	26.81	137.5	137.2	295.9	186.4	186.4
February	143.8	27.51	143.8	143.5	315.4	209.2	209.2
March	149.4	28.01	149.4	149.1	319.3	198.5	198.5
April	137.5	28.31	137.5	137.2	290.5	179.4	179.4
May	133.1	28.91	133.1	132.9	276.0	166.1	166.1
June	131.0	28.61	131.0	130.7	271.9	160.0	160.0
July	137.6	28.21	137.6	137.3	287.2	167.5	167.5
August	141.3	28.01	141.3	141.0	299.3	179.8	179.8
September	133.9	28.01	133.9	133.6	280.9	169.4	169.4
October	136.9	27.81	136.9	136.6	289.3	178.0	178.0
November	118.0	27.41	118.0	117.8	242.4	136.9	136.9
December	123.3	26.91	123.3	123.1	256.2	151.1	151.1
Year	1623.3	27.88	1623.3	1620.2	3424.2	2082.3	2082.3

Legends:

GlobHor	Horizontal global irradiation	EArrMPP	Array virtual energy at MPP
T Amb	Ambient Temperature	EArray	Effective energy at the output of the array
GlobInc	Global incident in coll. plane	E User	Energy supplied to the user
GlobEff	Effective Global, corr. for IAM and shadings		

DC Grid System: Loss diagram

Project : **DC Grid Project at Singapore**

Simulation variant : **New simulation variant3**

Main system parameters	System type	**DC Grid System (public transports)**		
PV Field Orientation	tilt	0°	azimuth	0°
PV Array	Nb. of modules	40	Pnom total	**4000 Wp**
DC Grid	Nominal Voltage	600 V	Overvoltage regulation	Cut of module strings
User's needs	Unlimited load (grid)			

Loss diagram over the whole year

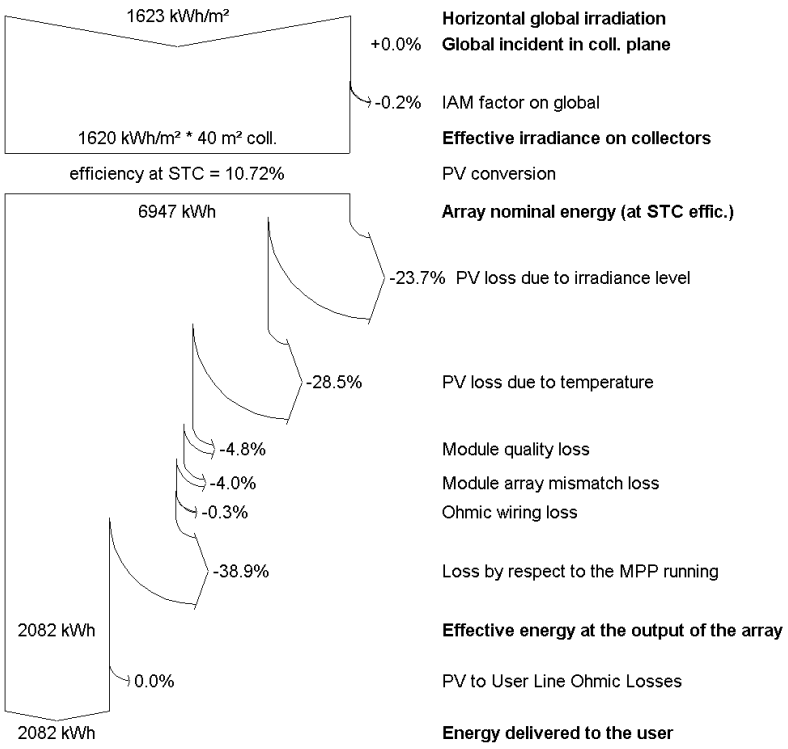

Thin film ARC

DC Grid System: Simulation parameters

Project : **DC Grid Project at Singapore**

Geographical Site	**Singapore Airp.**			Country	**Singapore**
Situation		Latitude	1.4°N	Longitude	104.0°E
Time defined as		Legal Time	Time zone UT+8	Altitude	9 m
		Albedo	0.20		
Meteo data:	**Singapore Airp.**	Synthetic	Meteonorm 6.1		

Simulation variant : **New simulation variant3**

Simulation date 05/05/13 20h13

Simulation parameters

Collector Plane Orientation		Tilt	0°	Azimuth	0°
Models used		Transposition	Perez	Diffuse	Measured
Horizon		Free Horizon			
Near Shadings		No Shadings			

PV Array Characteristics

PV module	Si-mono	Model	**Simple module**		
		Manufacturer	Teknova		
Number of PV modules		In series	40 modules	In parallel	1 strings
Total number of PV modules		Nb. modules	40	Unit Nom. Power	100 Wp
Array global power		Nominal (STC)	**4000 Wp**	At operating cond.	3881 Wp (50°C)
Array operating characteristics (50°C)		U mpp	575 V	I mpp	6.8 A
Total area		Module area	**40.0 m²**	Cell area	0.9 m²

PV Array loss factors

Thermal Loss factor		Uc (const)	20.0 W/m²K	Uv (wind)	0.0 W/m²K / m/s
=> Nominal Oper. Coll. Temp. (G=800 W/m², Tamb=20°C, Wind=1 m/s.)				NOCT	56 °C
Wiring Ohmic Loss		Global array res.	1400 mOhm	Loss Fraction	1.5 % at STC
Module Quality Loss				Loss Fraction	3.0 %
Module Mismatch Losses				Loss Fraction	2.5 % (fixed voltage)

Incidence effect, user defined profile

0°	48°	56°	60°	65°	71°	79°	85°	90°
1.00	0.99	0.98	0.96	0.93	0.88	0.70	0.41	0.00

System Parameter System type **DC Grid System (public transports)**

Grid Nominal Voltage	Operating (nominal supply)	**600 V**		Max. Allowable	900 V
Grid Line Resistances	PV field to user	0 mOhm		Supply to user	0 mOhm

User's needs : Unlimited load (grid)

DC Grid System: Main results

Project : **DC Grid Project at Singapore**

Simulation variant : **New simulation variant3**

Main system parameters					
	System type	**DC Grid System (public transports)**			
PV Field Orientation	tilt	0°	azimuth	0°	
PV Array	Nb. of modules	40	Pnom total	**4000 Wp**	
DC Grid	Nominal Voltage	600 V	Overvoltage regulation	Cut of module strings	
User's needs	Unlimited load (grid)				

Main simulation results

System Production	**Produced Energy**	**2223 kWh/year**	Specific prod.	556 kWh/kWp/year
	Performance Ratio PR	34.2 %	Solar Fraction SF	100.0 %

Normalized productions (per installed kWp): Nominal power 4000 Wp

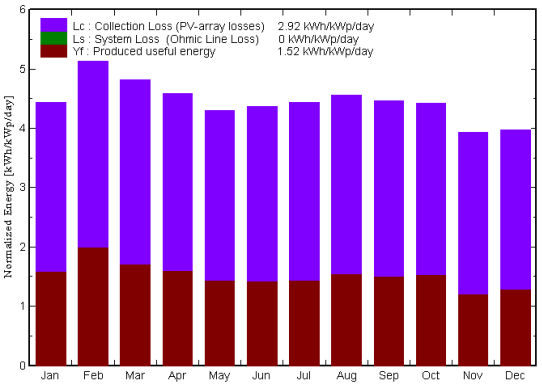

Performance Ratio PR

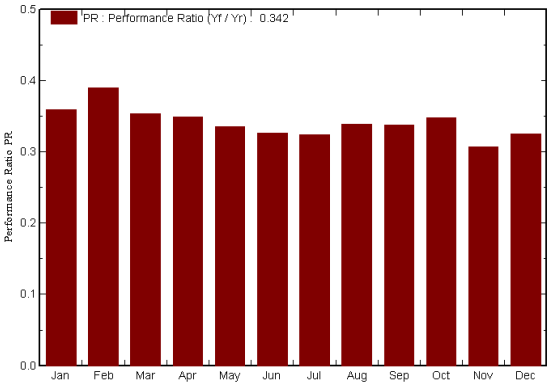

New simulation variant3

Balances and main results

	GlobHor kWh/m²	T Amb °C	GlobInc kWh/m²	GlobEff kWh/m²	EArrMPP kWh	EArray kWh	E User kWh
January	137.5	26.81	137.5	132.5	317.1	197.7	197.7
February	143.8	27.51	143.8	139.0	340.2	224.4	224.4
March	149.4	28.01	149.4	144.3	343.3	211.6	211.6
April	137.5	28.31	137.5	133.0	313.1	192.4	192.4
May	133.1	28.91	133.1	128.7	297.3	179.0	179.0
June	131.0	28.61	131.0	126.6	292.4	171.4	171.4
July	137.6	28.21	137.6	132.8	308.5	178.6	178.6
August	141.3	28.01	141.3	136.3	321.5	191.4	191.4
September	133.9	28.01	133.9	129.4	302.3	181.0	181.0
October	136.9	27.81	136.9	132.3	311.5	190.5	190.5
November	118.0	27.41	118.0	113.6	259.0	144.8	144.8
December	123.3	26.91	123.3	118.8	274.3	160.3	160.3
Year	1623.3	27.88	1623.3	1567.5	3680.6	2223.0	2223.0

Legends:

GlobHor	Horizontal global irradiation	EArrMPP	Array virtual energy at MPP
T Amb	Ambient Temperature	EArray	Effective energy at the output of the array
GlobInc	Global incident in coll. plane	E User	Energy supplied to the user
GlobEff	Effective Global, corr. for IAM and shadings		

DC Grid System: Loss diagram

Project : **DC Grid Project at Singapore**

Simulation variant : **New simulation variant3**

Main system parameters	System type	**DC Grid System (public transports)**		
PV Field Orientation	tilt	0°	azimuth	0°
PV Array	Nb. of modules	40	Pnom total	**4000 Wp**
DC Grid	Nominal Voltage	600 V	Overvoltage regulation	Cut of module strings
User's needs	Unlimited load (grid)			

Loss diagram over the whole year

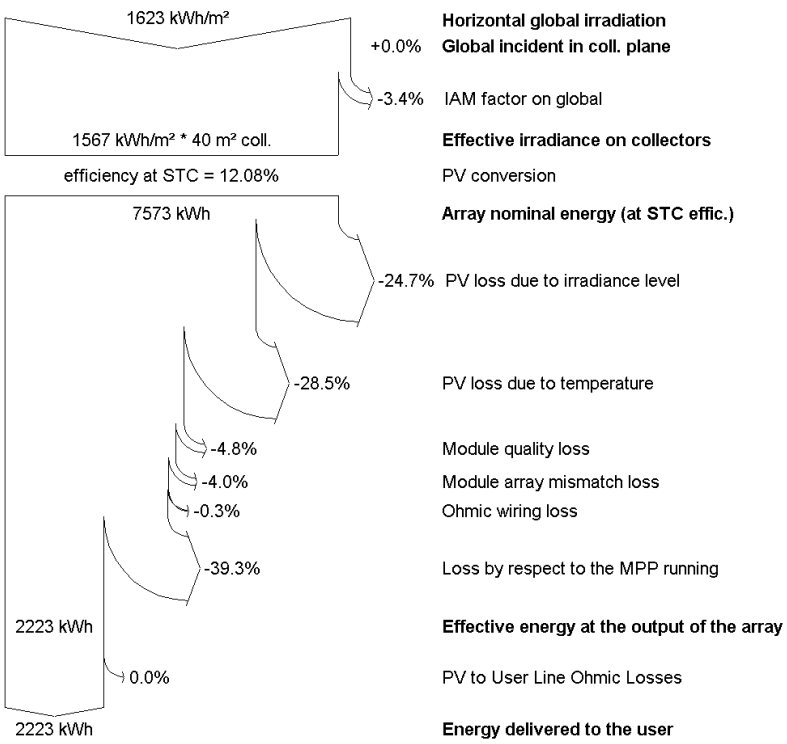

Appendix B – KhepriCoat brochure

KhepriCoat® – the best-performing
anti-reflective coating for solar cover glass

HEALTH · NUTRITION · MATERIALS

DSM
BRIGHT SCIENCE. BRIGHTER LIVING.

Boost module efficiency

Maximize light transmission by minimizing reflection

Over recent years, global demand for sustainable energy has grown steadily – and is certain to continue growing. As a result, solar energy systems will play an increasingly central role in the energy economy of the future. And as the technology becomes more efficient, their role will become even more critical. To help boost the price/performance ratio of solar energy systems, DSM is developing new breakthrough technologies – technologies such as KhepriCoat®. Set to contribute significantly to the hunt for grid parity, KhepriCoat® is the best-performing anti-reflective coating technology for solar cover glass on the market. By transmitting more light, it boosts module efficiency significantly.

Advantages at a glance:

- KhepriCoat® maximizes light transmission by minimizing reflection.
- KhepriCoat® is tough, durable and easy to clean.
- KhepriCoat® adds significant value by improving the price/performance ratio, thus lowering the cost/Wp.
- KhepriCoat® can be used on both rolled (patterned) and float glass, and can be applied on one or both sides of the glass.
- KhepriCoat® can be used in a wide range of solar applications, including solar thermal modules, crystalline-silicon modules and thin-film photovoltaic modules.
- KhepriCoat® can be applied using a range of deposition technologies, such as roll, spray, slot-die and dip coating.
- KhepriCoat® does not need an additional curing step if the glass is tempered.

Minimum reflection, maximum transmission

Wherever glass meets air, about 4% of the light hitting the glass at a perpendicular angle is reflected. And that percentage rises steeply as the light's angle of incidence increases. Obviously, for solar energy systems, reflected light represents a wasted opportunity. KhepriCoat® minimizes this effect. In fact, it delivers a record-breaking performance in terms of light transmission, outperforming all other AR coatings on the market today. Plus, it is mechanically robust and highly durable – essential properties for this outdoor application.

Why KhepriCoat® is different

AR coatings – turning particles into pores

KhepriCoat® is a unique technology, developed and patented by DSM. To achieve this breakthrough, DSM has turned the structure of traditional nano-porous sol-gel coatings "inside out", by turning solid particles into light-transmitting nano-pores. It is this structure that enables KhepriCoat® to deliver a unique combination of mechanical and optical properties.

Traditional coatings

The cost price of solar panels is under constant pressure. As a result, when it comes to AR coatings, manufacturers must use single-layer systems to remain cost-effective. Whilst traditional single-layer AR coatings can be applied in a single-step process, they are limited in the optical benefits they can deliver, due to the way they are structured. Traditional single-layer AR coatings consist of solid silica nano-particles "glued" together with a binder so that the spaces between the particles act as nano-pores (see figure 1). Use too much binder, and this reduces the nano-porosity – and thus the AR performance – of the coating. Use too little binder, and this leads to poor mechanical strength and low durability. What's more, the structure's open surface (see figure 1) makes the silica layer of the coating vulnerable to hydrolysis when exposed to extreme weather conditions. And this can cause a sharp deterioration of both the optical and mechanical properties.

Why KhepriCoat® is different

AR coatings – turning particles into pores

KhepriCoat® avoids this trade-off between optical and mechanical properties by turning the structure of the coating inside out. Instead of being formed in the spaces between solid nano-particles, the nano-pores in KhepriCoat® are actually hollow particles.

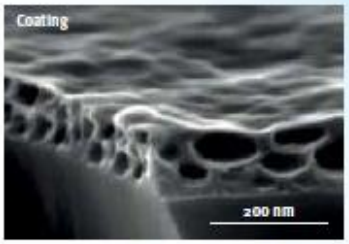

Figure 3: SEM picture of KhepriCoat® showing the closed modified silica surface and high proportion of nano-pores

DSM uses core-shell particles that have a polymer core and a silica-based shell. In the coating stage, a 100-150 nanometer layer of these particles is deposited on the surface of the glass. The spaces between the core-shell particles are at the same time filled with a modified silica binder. The binder immediately forms a solid network between the core-shell particles. During the curing step, the polymer cores of the particles are removed, leaving a glass layer with a high internal porosity (figure 2).

Furthermore, because the coating layer and its glass substrate have similar compositions, the adhesion of the coating layer to the glass surface is excellent.

The optimized nano-pore/binder ratio ensures KhepriCoat® delivers both outstanding optical and mechanical properties. And because it has a smooth, "closed" surface (see figure 3), the risk of hydrolysis is sharply reduced, enabling KhepriCoat® to withstand extreme weather conditions and making it ideal for solar-cell cover glass. In addition, this prevents dirt from penetrating the coating's surface, making it very easy to clean.

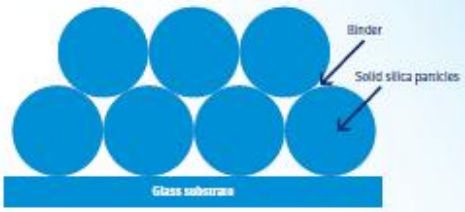

Figure 1: The structure of a traditional sol-gel nano-porous AR coating

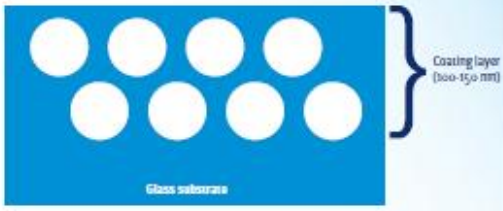

Figure 2: The structure of a single layer of KhepriCoat®

Breaking records in light transmission

Make huge gains when the sun is high...

Solar cover glass that is coated with KhepriCoat® will transmit, on average, around 3% more, per coated side, of the light hitting it at a perpendicular angle of incidence, see figure 4 for single and double sided coated float glass and figure 5 for patterned glass.

...and even larger gains when the sun is low

And when the light's angle of incidence is not perpendicular, the average gain in transmittance can be as high as 8% per coated side (see figure 6).

Leading to larger energy yields

The increase in light transmission leads to a comparable rise in the energy yield of the solar module. In fact, the increase in a module's output can exceed 20%, especially at low angles of incidence (figure 7).

In practice, the actual improvement in energy yield depends on several parameters: for example, on the type of cover glass, on the type of solar cell and on the local cycle of the sun. The typical daily improvement in module efficiency will be in the range of 4% for PV modules and 6-8% for solar thermal modules.

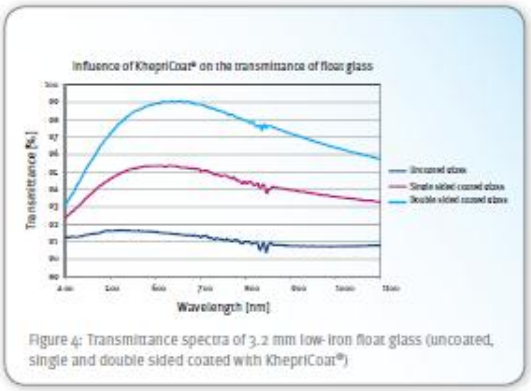

Figure 4: Transmittance spectra of 3.2 mm low-iron float glass (uncoated, single and double sided coated with KhepriCoat®)

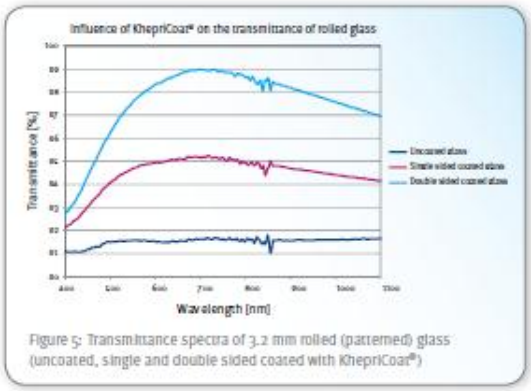

Figure 5: Transmittance spectra of 3.2 mm rolled (patterned) glass (uncoated, single and double sided coated with KhepriCoat®)

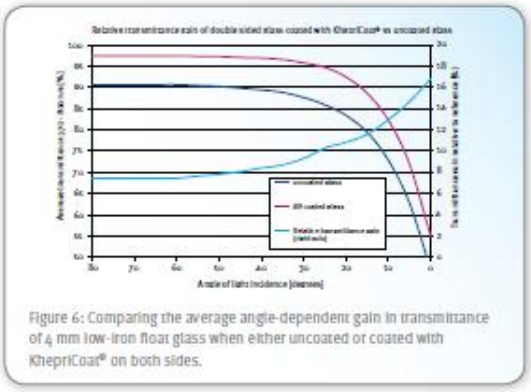

Figure 6: Comparing the average angle-dependent gain in transmittance of 4 mm low-iron float glass when either uncoated or coated with KhepriCoat® on both sides.

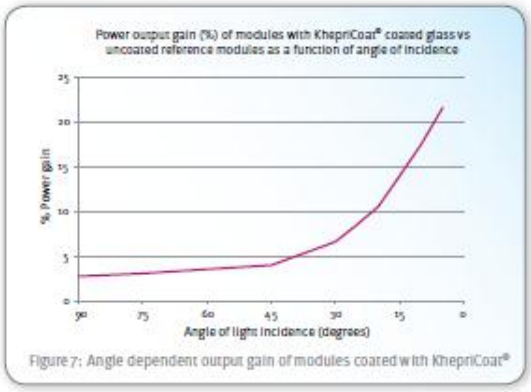

Figure 7: Angle dependent output gain of modules coated with KhepriCoat®

Add proven value to your products

The best light transmission

The strongest proof that KhepriCoat® is the best AR coating available today is that it was used by independent research institute ECN to help set a new world record for conversion efficiency in multi-crystalline solar panels. DSM can enable you to break your own record, by helping you to optimize your KhepriCoat® coatings to match the absorption spectrum of the specific cells you use.

Demonstrable durability

The durability of solar cover glass coated with KhepriCoat® has been evaluated extensively. It has been subjected to extended damp-heat tests, humidity-freeze tests, thermal cycling tests (all according to IEC 61215) and to abrasion-resistance tests. KhepriCoat® surpassed all test criteria, with only minor changes in transmission being observable following these tests.

Suitable for cSi and thin-film modules

By optimizing the coating's thickness, its properties can be tailored to suit a variety of different module types, including both wafer-based and thin-film modules.

Apply KhepriCoat® on one – or both – sides

One-sided coatings of KhepriCoat® can be applied using various coating technologies, such as roll coating, spray coating and slot-die coating.

Figure 8: Roll coating unit in DSM's Technology Development Center

In the solar glass industry, roll coating is the most commonly used deposition technology for AR-coatings. KhepriCoat® can be applied in both the forward and the reverse coating mode. At its Application Technology Development Center in The Netherlands, DSM has a commercial-scale roll coater that it uses during product development and for producing samples for customers (figure 8).

In addition, DSM has adapted existing slot-die-coating technology for the high-speed deposition of optical coatings on rigid substrates. This new system can even carry out in-line coating at speeds as high as 20 meters per minute. Using this technology, DSM has achieved a coating thickness of 100–150 nm with a thickness tolerance of just ± 2 nm. Patents are pending for this process, and a pilot line is available for customer trials at DSM (see figure 9).

When it comes to solar-thermal applications, AR glass is usually coated on both sides. A two-sided coating of KhepriCoat® can be applied using standard dip-coating equipment, or by using a single-sided coating process to apply each layer separately in turn.

Tempered glass? No pre-curing, drying step or chemicals needed

If your solar cover glass is thermally tempered, there is no need for a separate thermal treatment (such as pre-curing or drying) or for a chemical curing step. As a result, you do not need to invest in special ovens, and there is no additional variable cost. And because you don't need to handle chemicals for curing, DSM's KhepriCoat® technology is very safe and environmentally friendly.

The expert support you need

If you are not yet coating glass in-house, DSM can supply you with a complete engineering package and the technical support you need to construct and get started with coating facilities. Drawing on its technical support teams and application development labs based in Europe and China, DSM can offer this technical support globally. Get in touch, and we will help you prepare for the future.

Figure 9: DSM's pilot slot-die coating line

Choose KhepriCoat®

To make your products truly stand out

As pressure from governments and from public opinion is expected to grow in the future, project developers will increasingly ask for ever more efficient solar modules in their hunt for grid-parity. In order to help you answer this demand, KhepriCoat® can enable you to further differentiate your business, and tailor your products to suit the rapidly growing solar cover glass market.

An investment that pays

With a license from DSM, you can produce and sell high-performance AR solar cover glass coated with KhepriCoat®, using coating formulation that is produced by DSM in-house and delivered to you directly. The coating equipment requires a relatively low capital investment. And most importantly, this investment will provide you with optimized returns, as the proven added value of glass coated with KhepriCoat® fully justifies a premium price.

DSM also licenses the technology to thin -film module producers, who can apply the coating to the cover glass before the active layers are deposited on the glass. Depending on the process conditions, a separate (pre) curing step may be necessary.

KhepriCoat® in summary:

- Offers excellent optical properties in a single-layer coating.
- Can be applied 1- or 2-sided on all types of glass, using a range of deposition technologies.
- Increases the output of PV modules by up to 4%.
- Is highly robust, withstands extreme weather conditions and is easy to clean.
- Meets the durability criteria as specified in IEC61215 and is TÜV certified.
- Can be tailored to suit a variety of different cells and types of solar cover glass.
- Offers you a quick return on investment.
- Is supported by a high level of design and engineering services.
- Helps you to maintain or improve your position in a fast growing market by providing a differentiated product offering.

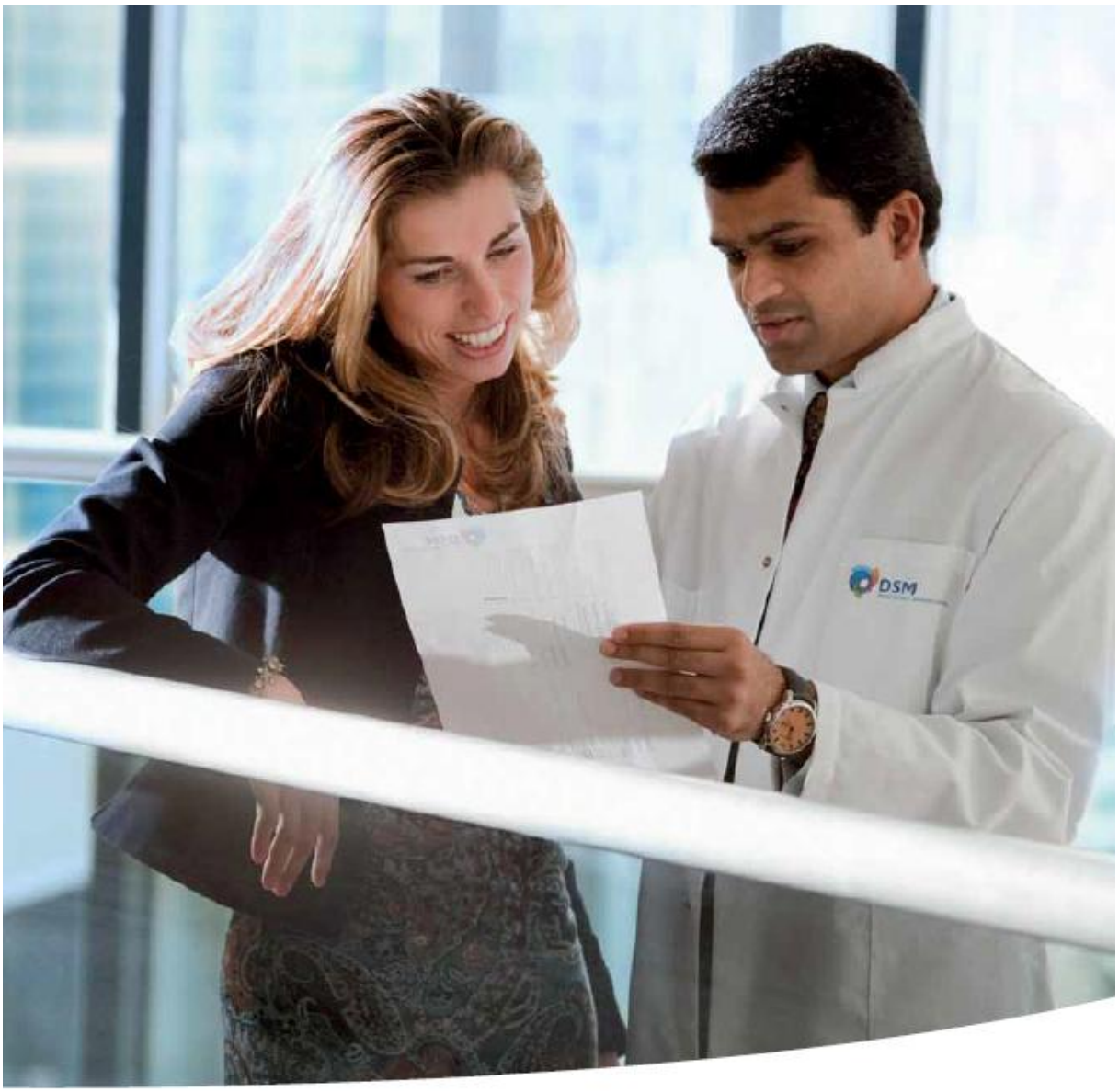

DSM – Bright Science. Brighter Living.™

Royal DSM is a global science-based company active in health, nutrition and materials. By connecting its unique competences in Life Sciences and Materials Sciences, DSM is driving economic prosperity, environmental progress and social advances to create sustainable value for all stakeholders. DSM delivers innovative solutions that nourish, protect and improve performance in global markets such as food and dietary supplements, personal care, feed, pharmaceuticals, medical devices, automotive, paints, electrical and electronics, life protection, alternative energy and bio-based materials. DSM's 22,000 employees deliver annual net sales of about €9 billion. The company is listed on NYSE Euronext. More information can be found at www.dsm.com

Khepri is the name of one of the major Gods in ancient Egyptian mythology. He was believed to push the sun across the sky and is responsible for the dawn. This name was chosen as sunrise and sunset are the times when the benefits of KhepriCoat® offer the highest yield increase versus normal solar glass.

DSM Advanced Surfaces

If you'd like to know more about
KhepriCoat® and how it can help
your business contact us today.

Email: info.advancedsurfaces@dsm.com
www.dsm.com/khepricoat

Europe
DSM Advanced Surfaces
P.O. Box 1163
6160 BD Geleen
The Netherlands
Phone: +31 46 4763128

China
DSM China Ltd.
Advanced Surfaces
476, Li Bing Road,
Zhangjiang High-Tech Park,
Pudong New District, Shanghai 201203
China
Phone: +86 21- 61418035

Version 12.001

Appendix C – Rough glass data

Correspondance with M. Gauvin at TracePro regarding Mold-Tech rough glass data:

Dear Ashborn:

One more thing, we have just measured multiple diffuser platelets created by Moldtech and these are available from the website and I have attached these diffuser definitions. You can import them into your TracePro surface database by hitting the F11 key while running TracePro and browsing for the attached txt file. We also can measure these surfaces for you and create TracePro surface properties. Let me know if you are interested and I will be glad to quote you on this.

Sincerely,

Michael Gauvin
VP Sales & Marketing
Lambda Research Corporation
www.lambdares.com
Tel: 978-486-0766 x 37
Fax: 978-486-0755

Please ask about our customized onsite training at your facility to make you successful!

"A. Stoveland" <asbjorn_stoveland@hotmail.com> wrote:

> Thank you, Jack!
>
> Now I need to model glass surface, that is: rough glass.
> This could be matt/frosted/random micro textures etc. Thomas J. J. Meyer
> referred advised me to ask you about these features in TracePro, I
> understand it has been done before, or that TracePro has properties for this
> in the database?
>
> Regards,
>
> Asbjorn

Appendix D – SEM images of mono c-Si KOH etched wafer taken at UiA

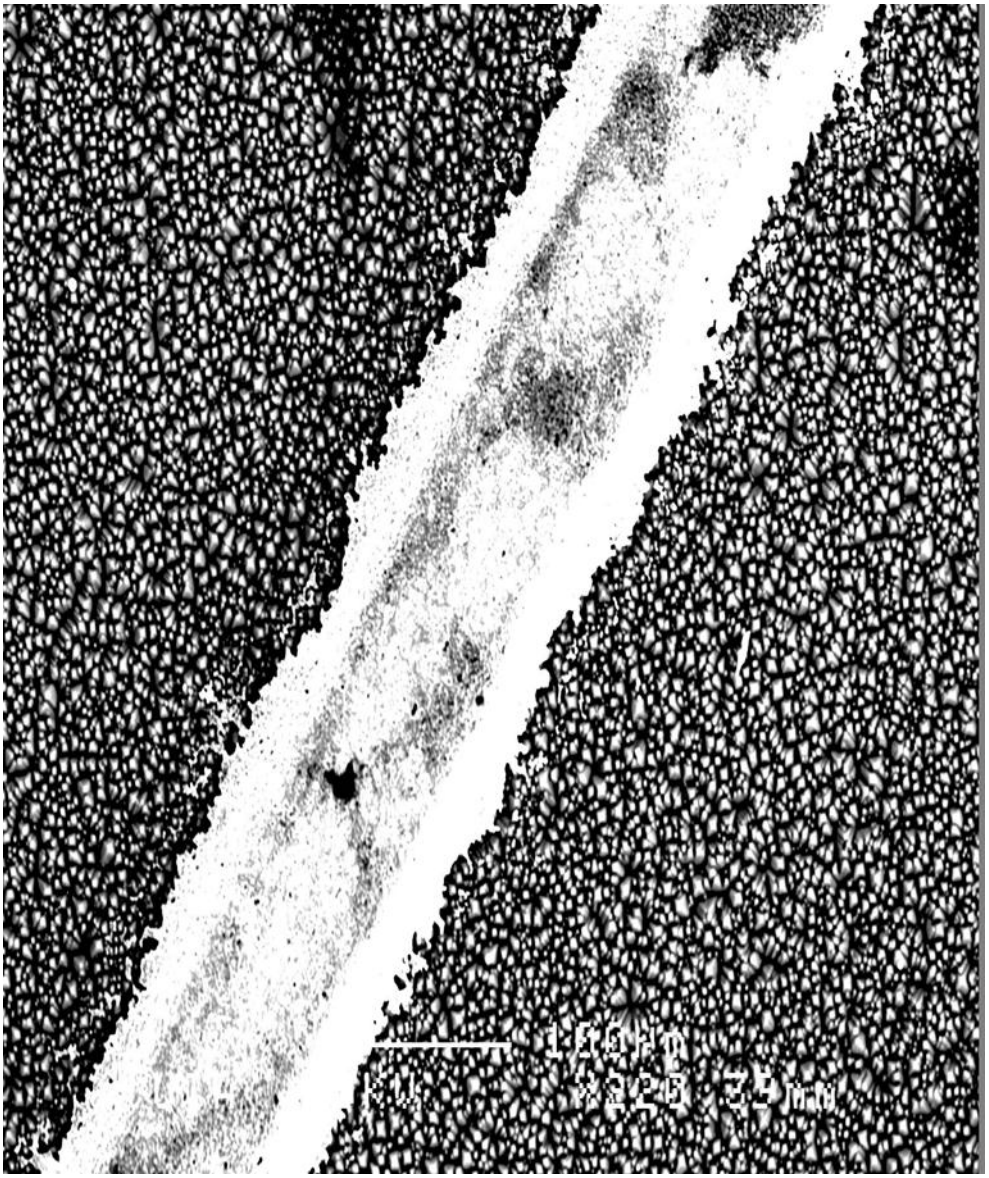

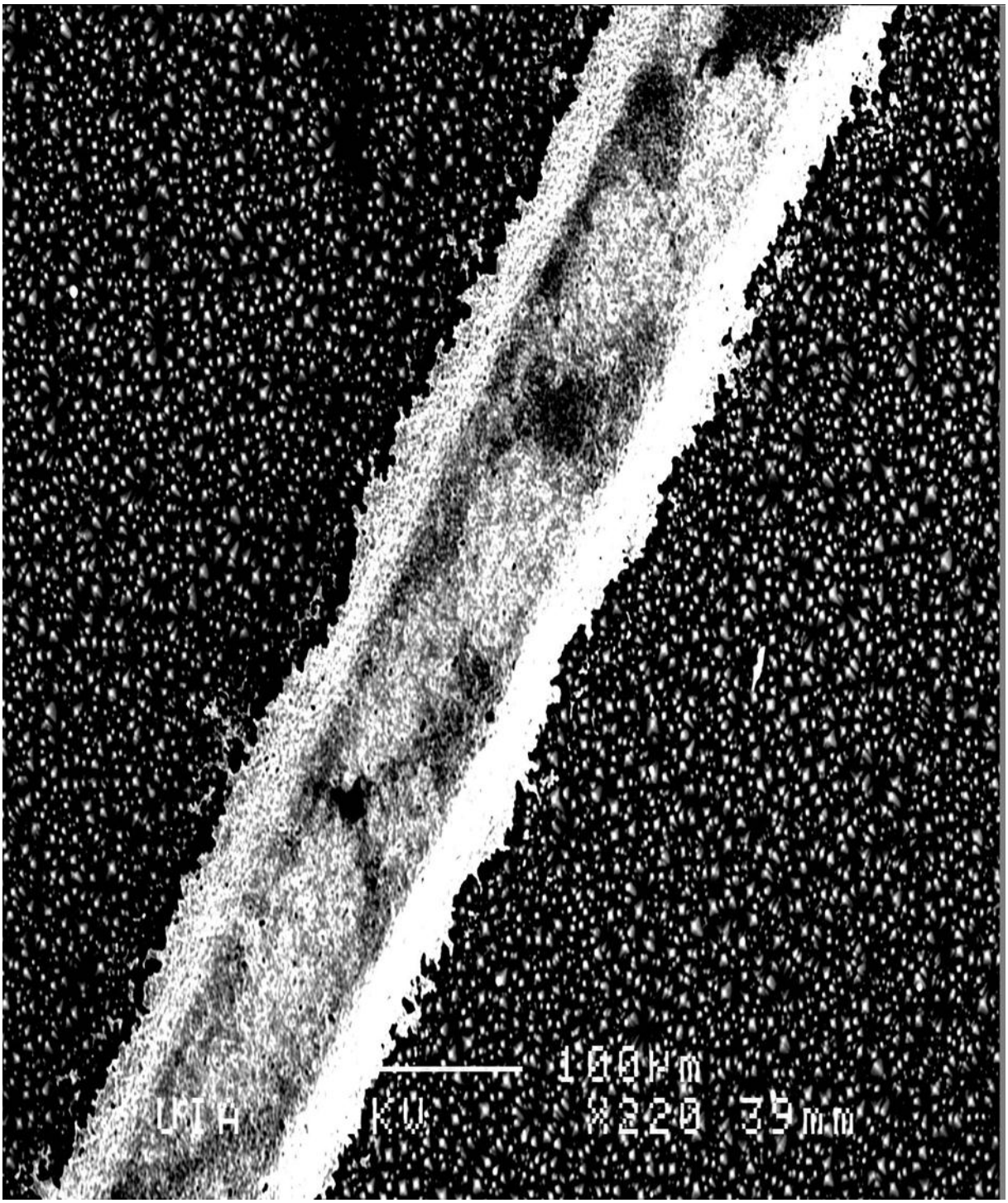
100nm
UTA
KV
X220 39mm

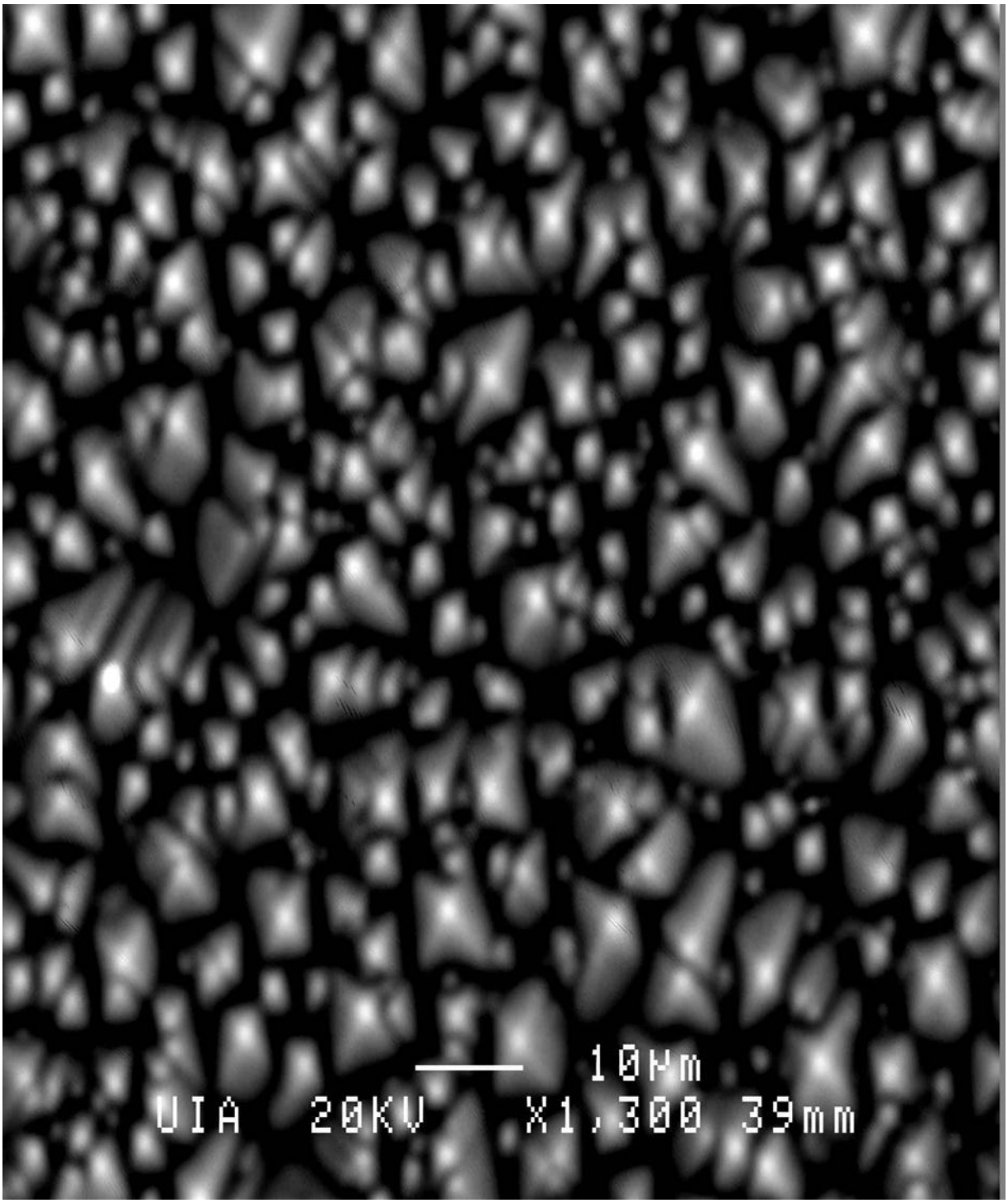
10μm
UIA 20KV X1,300 39mm

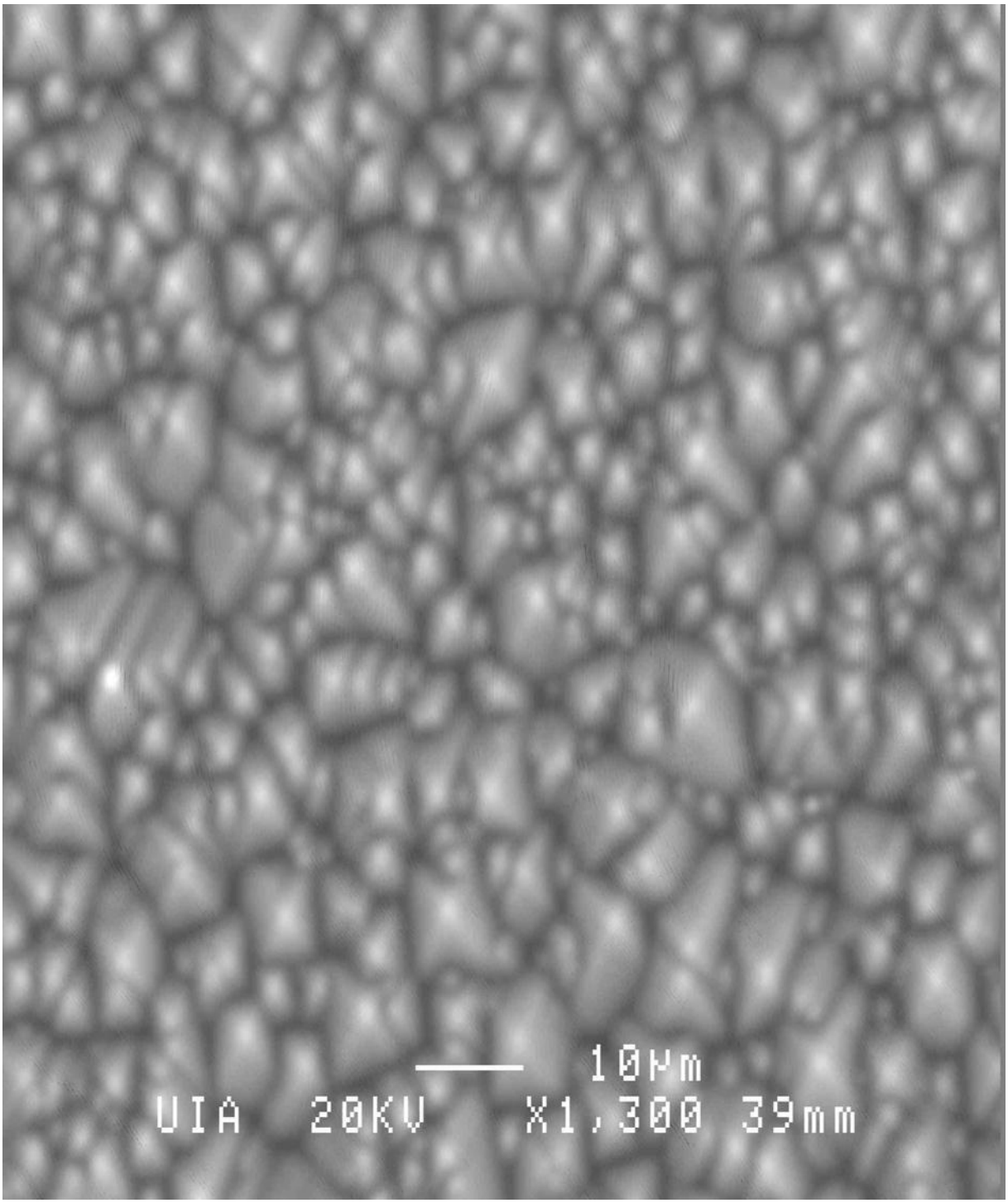
10μm
UIA 20KV X1,300 39mm

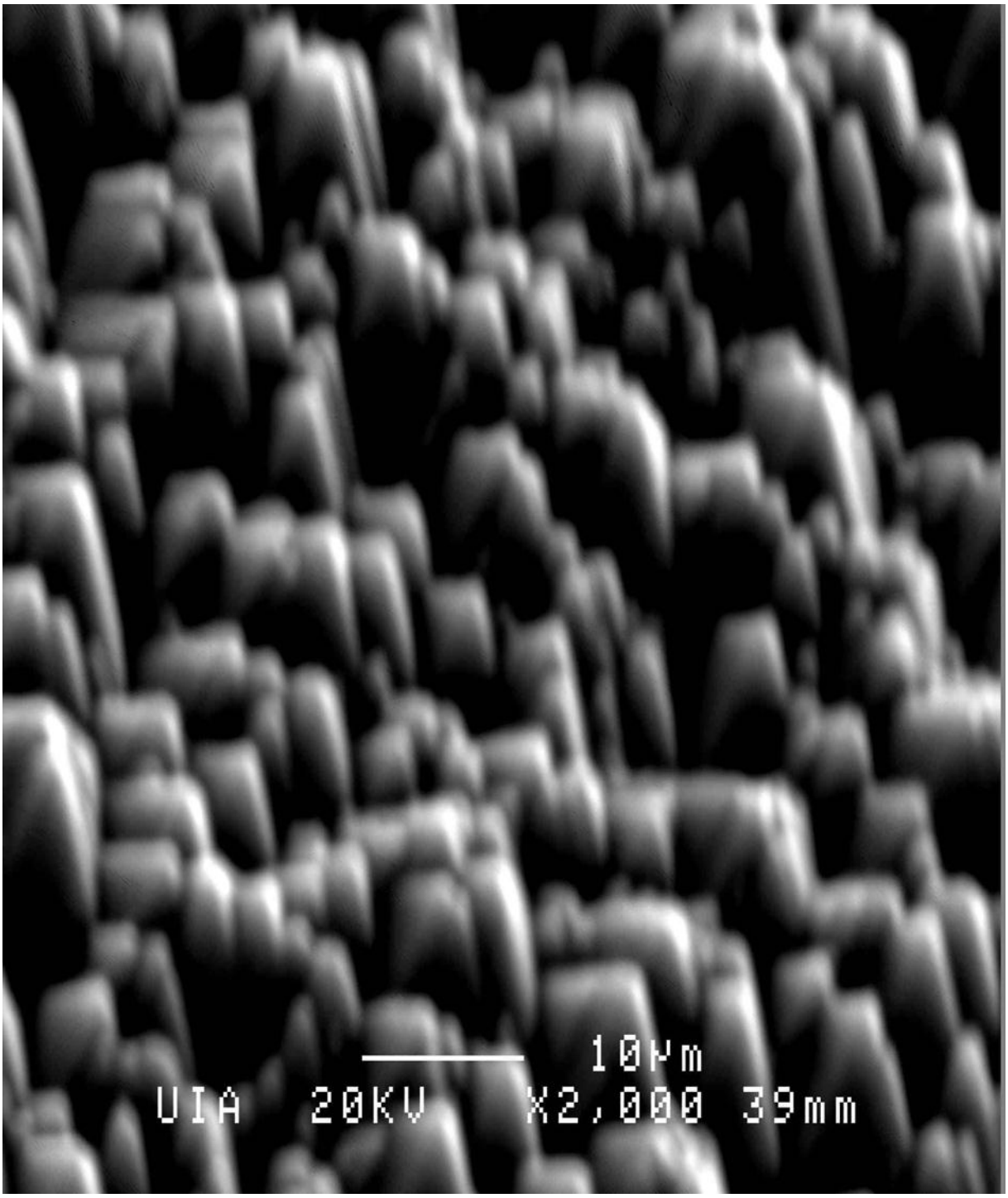
10μm
UIA 20KV X2,000 39mm

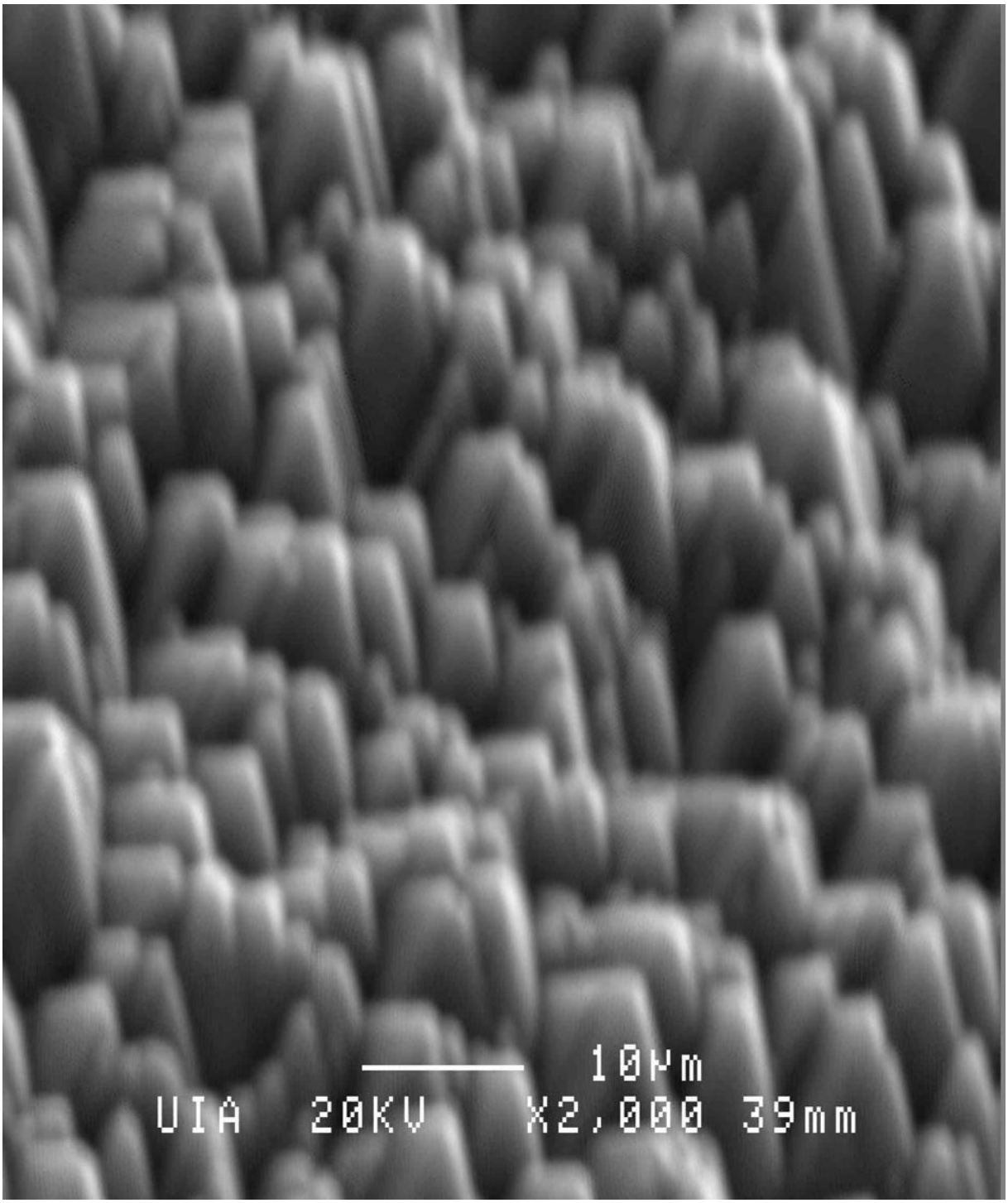
10μm
UIA 20KV X2,000 39mm

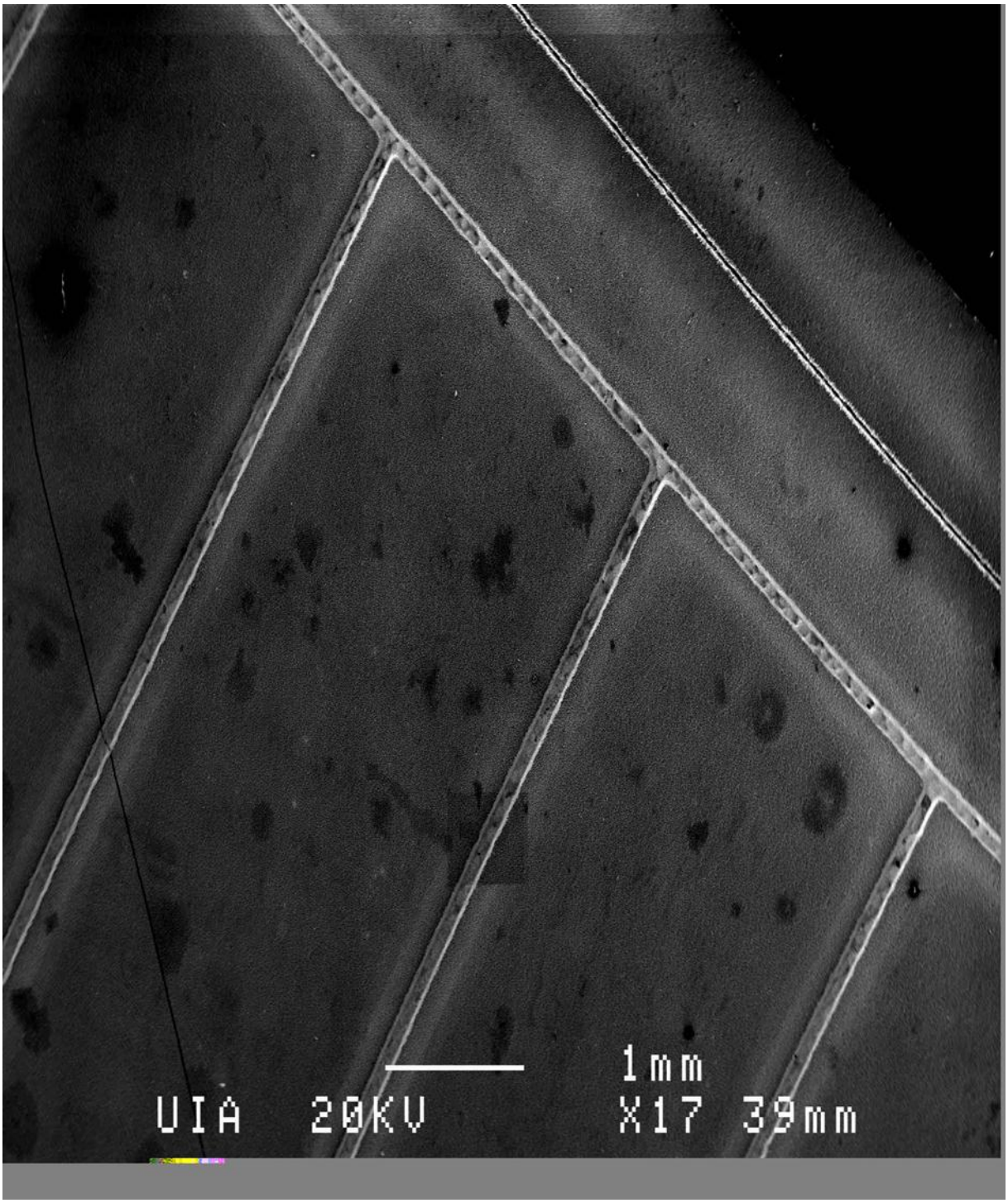
1mm
UIA 20KV X17 39mm